UNIVERSITY OF LONDON THESIS

Degree PhD Year 2005 Name of Author RAMANLAL J.

SPECIAL NOTE

This item is tightly bound and while every effort has been made to reproduce the centres force would result in damage.

The Spectroscopy of H_3^+: Low Energy to Dissociation

A Thesis submitted for the Degree

of

Doctor of Philosophy of the University of London

by

Jayesh Ramanlal

Department of Physics & Astronomy

University College London

February 2005

The H_3^+ ion is the simplest and most fundamental of polyatomic molecules consisting of three protons and two electrons. H_3^+ is an important molecule playing a key role in many areas of Physics, Chemistry and Astronomy. The astrophysical importance of H_3^+ lies in the fact that most of the universe is made up of hydrogen, and molecular hydrogen in the cool regions. H_3^+ is rapidly formed by the reaction

$$H_2 + H_2^+ \rightarrow H_3^+ + H \tag{1}$$

Thus H_3^+ is usually the dominant ion in environments containing molecular hydrogen. Further more, multiply deuterated species have been observed in the interstellar medium recently. These species are thought to have been formed via deuterium fractionation effects, in which the isotopomers H_2D^+ and D_2H^+ play a significant role.

More than two decades have passed since Carrington and co-workers produced a remarkably rich spectrum of the H_3^+. Over 27,000 absorption lines in a region between 872cm^{-1} to 1094cm^{-1}. This experiment still remains largely unexplained. This work calculates intensities of transitions of states near dissociation. Thus will help illuminate the Carrington spectrum.

Within this work I present a method of calculating line strengths for the H_3^+ system. Several improvements on previous methods are presented, including the use discrete variable representation, symmetry and a parallel algorithm. The implementation of this method on massively parallel computers is also discussed.

Several applications of the synthetic spectra of H_3^+ and isotopomers are presented. This will include where possible how they have aided other work and the results of this other work.

Contents

List of Figures

List of Tables

Acknowledgements

I thank Jonathan Tennyson for his tireless enthusiasm, knowledge, encouragement and for generally being an excellent supervisor.

I thank my many collaborators, they have made this PhD far more diverse and interesting then I could have hoped. I am grateful to Hamse Mussa for the PDVR3DJ and PROTLEV3 programs, and for our many useful conversations.

I thank Callum Wright and the HPCx team for all their help with high performance computing.

I have made many friends in the TAMPA group, who have helped me in a multitude of ways; my life is all the richer for them. I especially thank James Munro for our endless conversation and his infectious enthusiasm.

I thank Philip Holtom for proofreading this thesis.

Finally I wish to thank my family and friends for their support and encouragement.

Chapter 1

Introduction

The initial purpose of theoretical spectroscopy calculations was perhaps to test theory against experiment, with the hope that the calculations, if sufficiently accurate, could aid experiment. With advances in theory and the development of computers, *ab initio* calculations are now able to provide much more. The ability to compute large datasets, far greater than is feasible with experiment, enable the calculations to move from microscopic spectroscopy to the macroscopic level of modelling the interstellar medium, stellar evolution, the Earth's atmosphere, and various other chemical processes. Furthermore the nature of an experimental spectrum can be illuminated by theoretical calculations, where individual contributions can be separated and their contribution assessed. Thus from the combination of experiment and theoretical calculations the maximum amount of information may be obtained from a given spectrum.

1.1 Astrophysics

Most of the universe is made of hydrogen. H_3^+ is usually formed through the reaction

$$H_2^+ + H_2 \rightarrow H_3^+ + H \tag{1.1}$$

which is very rapid and exothermic by approximately 1.7 eV. Thus H_3^+ is produced whenever a hydrogen molecule and its ion collide, therefore H_3^+ can be expected to exist in any environment where molecular hydrogen is ionised. H_3^+ has been found to be present in a number of different astronomical environments: The gas giant planets of the solar system [24–26]; dense molecular clouds [27]; diffuse molecular clouds [28, 29];

and also possibly in supernova [30]. It is also predicted to be present in low mass zero metallicity stars [31];

Detection of interstellar molecules via high resolution spectroscopy gives knowledge about the conditions where the molecules are found. H_3^+ is a universal protonator and has been known for some time to be the initiator of a network of ion–neutral reactions which give rise to the formation of most interstellar molecules [32, 33], and as such an understanding of the chemistry of H_3^+ in the interstellar medium is of great importance.

H_3^+ has been detected in both diffuse [28, 29] and dense [34] molecular clouds, in unexpectedly high amounts in the former. Dense molecular clouds, which are opaque to visible light, can be observed in the infra-red, as this radiation is able to penetrate the cloud. The H_3^+ chemistry in these dense clouds is largely understood [34]; it is in diffuse clouds where the "Enigma of H_3^+" [35] exists. H_3^+ was not thought to be important in diffuse molecular clouds because it would be rapidly destroyed by dissociative recombination with electrons, which are abundant in diffuse molecular clouds. However, observations of diffuse molecular clouds in fact show similar amounts of H_3^+ in diffuse clouds to dense clouds [28, 36], in contradiction to the models. There are three factors which determine the abundance of H_3^+ in diffuse clouds: the cosmic ray ionisation rate, the electron fraction, and the recombination rate for H_3^+.

It has been long expected that fractionation effects at low temperature would enhance the relative abundances of the H_3^+ deuterated isotopomers in low temperature environments such the interstellar medium [37]. The primary fractionation reaction is

$$H_3^+ + HD \rightarrow H_2D^+ + H_2 \tag{1.2}$$

which is exothermic by approximately 230 K, that is the difference in zero point energies between the reactants and products. Similar zero point effects result in the production D_2H^+ and D_3^+. Many others species become deuterated [38–40] through reaction chains involving these deuterated isotopomers.

1.2 Spectroscopy of H_3^+

At equilibrium H_3^+ forms an equilateral triangle with the protons separated by $1.65a_\circ$. An unconventional bonding structure is formed by the three protons sharing the two electrons. H_3^+ and D_3^+ are members of the D_{3h} point group. At non-linear geometries it has three vibrational modes. (figure 1.1). One is a totally symmetric "breathing" mode,

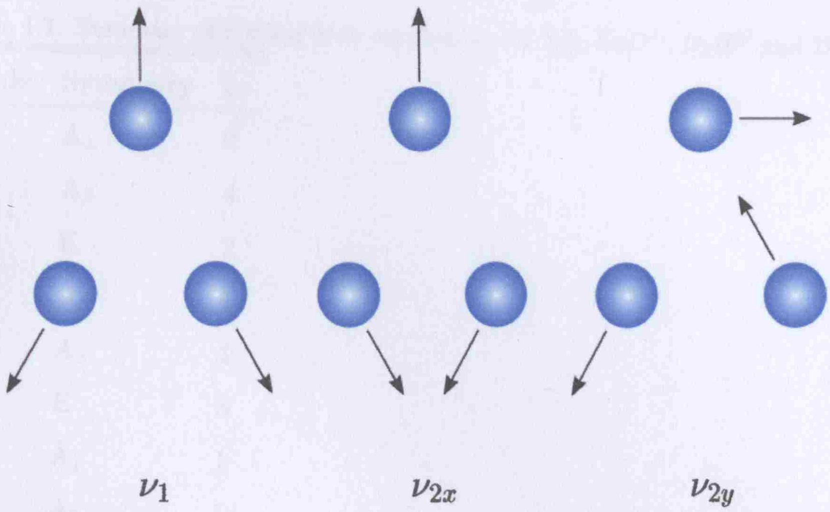

Figure 1.1: The harmonic vibrational modes of H_3^+. The ν_1 breathing mode and the doubly degenerate ν_2 bending mode.

in which all the internuclear distances expand and contract in unison. This A_1 symmetry mode is refereed to as ν_1. The other mode is the doubly degenerate (E) bending mode, ν_2. The ν_2 mode possesses vibrational angular momentum, l, which has allowed values from $-\nu_2$ to $+\nu_2$ in steps of *two*. These states are often labelled ν_2^l. Vibrational states for which l is not divisible by 3 are two-fold degenerate and thus have E symmetry, while states for which l is divisible by 3 are split into A_1 and A_2 pairs. States with $l = 0$ have A_1 symmetry only.

For the deuterated isotopomers H_2D^+ and D_2H^+ the degenerate ν_2 mode is split by the lower symmetry ($C_{2\nu}$) into a bending mode and an asymmetric stretch: ν_2 and ν_3 respectively. The symmetry of the vibrations determines the nuclear spin statistical weights, g_i. These statistical weights are outlined in table 1.1.

1.2.1 Quantum numbers

There are two schemes by which quantum numbers are assigned to H_3^+ and D_3^+, those of Watson [16] and of McCall [41] . H_3^+ (D_3^+) is a symmetric top, thus if J is the rotational angular momentum then its projection onto the molecular axis is given by K. K is normally regarded as a good quantum number. However, in the case of H_3^+ one has to take into account that l, the vibrational angular momentum, is also projected along the molecular axis.

Under the Watson [16] scheme the conserved quantity is $|k - l|$, denoted by G; k is

Table 1.1: Summary of nuclear spin weights, g_i for H_3^+, H_2D^+, D_2H^+ and D_3^+. [16, 17]

Molecule	Symmetry	g_i
H_3^+	A_1	0
	A_2	4
	E	2
D_3^+	A_1	10
	A_2	1
	E	8
H_2D^+	A_1	1
	A_2	1
	B_1	3
	B_2	3
D_2H^+	A_1	3
	A_2	3
	B_1	6
	B_2	6

the signed projection of J onto the molecular axis. For the cases where l is non-zero a further quantum number U, is required, this has the value $+|l|$ and $-|l|$ for the upper and lower level respectively. Thus rotational-vibrational levels can be labelled by (J, G, U).

The total angular momentum, F, and the parity, P, are the only completely rigorous quantum numbers for any molecule. For H_3^+ the total angular momentum is the sum of the total spin angular momentum, I, and the rotational angular momentum, J. H_3^+ consists of three spin 1/2 protons and thus I can be 1/2 (*ortho*) or 3/2 (*para*). As the coupling between the spin of the nuclei and the motion of the nuclei for H_3^+ is extremely small, I and J can be regarded as good quantum numbers. For energy levels which have the same values of I, J, and P an additional quantity, n, is required. This is an index for levels with the same I, J, and P, ordered by energy. Therefore under the McCall scheme rotational-vibrational levels are labelled by (I, J, P, n) [41].

Theoretical calculations of energy levels only provide the quantum numbers J and P, and occasionally I. The assignment of the Watson approximate quantum numbers must therefore be done manually. This assignment becomes progressively more subjective as

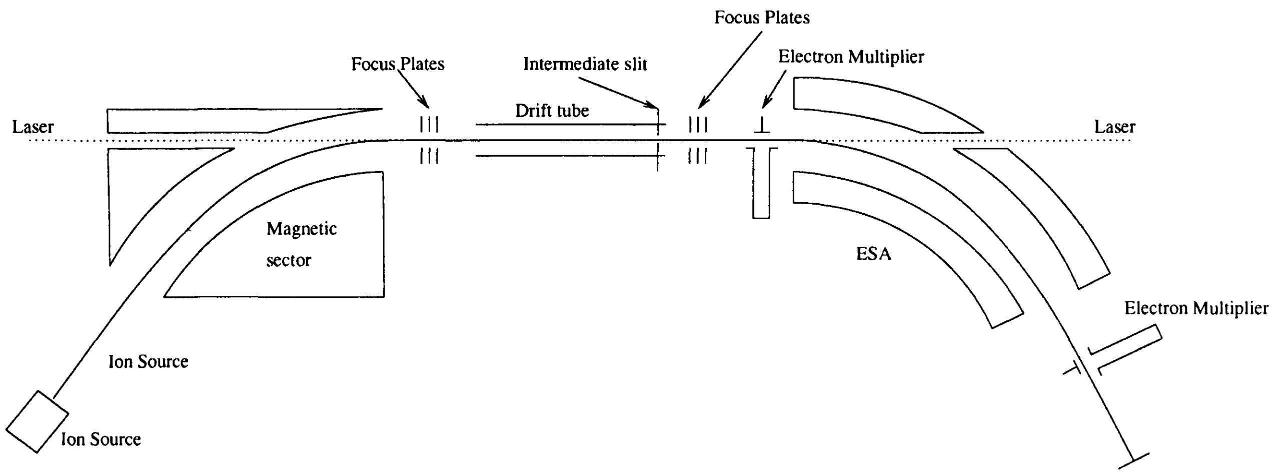

Figure 1.2: A simplified diagram showing the Carrington-Kennedy dissociation experimental apparatus [1]. Ions enter on the left, are mass/charge selected and then enter the drift chamber. A laser excites the ion and the dissociation products are mass selected in the ESA, which also determines their kinetic energy.

the energy of the levels increases, and near impossible near the barrier linearity (~10000 cm^{-1}). Therefore the McCall scheme is useful for theoretical calculations, especially at high energy.

H_2D^+ and D_2H^+ are asymmetric top molecules and thus the energy levels are labelled by J, K_A and K_C, where K_A is the projection of J onto the A axis and K_C is the projection of J onto the C axis. The value of K_A goes from 0 to J; while K_c takes values $K_C = J - K_A$ and $J - K_A + 1$. K_A and K_C are only valid within the rigid rotor model and thus must regarded only as approximate quantum numbers. More fundamentally, K_A and K_C are two components of the total angular momentum J. As the operators for the x, y and z components of J do not commute between themselves, only one component can be known at any one time.

1.3 Carrington-Kennedy Spectrum

One of the major motivations for the work presented here has been an attempt to interpret the near-dissociation spectrum of H_3^+, first measured by Carrington *et al* [1]. This spectrum is remarkable in that a window of only 220 cm^{-1}, approximately 27000 lines were detected.

Carrington *et al* used an ion beam set-up illustrated schematically in figure 1.2. The H_3^+ ions are produced hot by e^- bombardment of molecular hydrogen. The H_3^+ ions are then accelerated through a magnetic sector which is set to transmit H_3^+ ions. The H_3^+ beam now enters the drift tube; a line tunable CW carbon dioxide laser operated with $^{12}CO_2$ or $^{13}CO_2$ is directed along the drift tube. The laser sweeps the frequency range from 872 cm^{-1} to 1094 cm^{-1}. Any H^+ ions released by dissociation are detected by the multiplier. In order to separate the H^+, H_2^+ and the parent H_3^+ ions an electrostatic analyser, ESA, is employed. The ESA has sufficient resolution to be able to determine the kinetic energy of the fragments. To ensure that the fragments detected in the ESA emanated from the tube, a bias voltage was applied. H^+ and H_2^+ fragments are detected when the laser beam is not present; this is due to collision induced dissociation. This set-up provides a very sensitive method of detection.

A spectral line is detected when the laser frequency causes an increase in the number of H^+ ions detected. The near-dissociation mechanism is such that the laser excites the H_3^+ ion in the drift tube into a metastable state; this state leads to dissociation. The fragments of this dissociation are detected. The method of detecting spectral lines is dependent on monitoring fragments from the H_3^+ parent ion beam, and presuming that these fragments are produced from the dissociation of H_3^+, this may not be the case. However as long as any secondary process which fragments the H_3^+ beam is minor in comparison to the outlined H_3^+ dissociation process, these effects should be small. The presence of metastable states through which the transitions take place is implied by the kinetic energy of the H^+ fragments. As this kinetic energy is observed to be as high as 4000 cm^{-1} and as the laser only produces excitations between 874 cm^{-1} and 1094 cm^{-1} the final spectrum must be produced via metastable states between the initial and final states.

The centre of mass kinetic energy of the of the H^+ can be measured by the ESA. The ESA may be utilised in two different modes. Firstly the ESA may be used such that an energy window is established, such that only ions of a certain energy are transmitted. Secondly the ESA may be used to scan the kinetic energy. This allows the variation of centre of mass kinetic energy for a particular transition to be studied. The second mode required a prohibitive amount of time (approximately one hour per transition) thus only small sections of the spectrum were observed in this manner. The 27000 lines refers to those transitions where the kinetic energy released is zero. For the higher kinetic energy releases fewer, more intense lines are observed.

The nature of the experimental set up produces more information regarding the near-dissociation spectrum. The ions produced in the ion source must have a sufficiently long lifetime to reach the drift tube irradiated by the laser. This gives the minimum lifetime of the initial states which Carrington *et al* [42] determined to be 10^{-6} s. They were able to give a maximum lifetime of the excited states of 10^{-7} s from the requirement that dissociation needed to take place in the drift chamber. Furthermore, lifetimes greater then 10^{-9} give lines too broad to be observed and thus provide a lower limit for the excited state lifetime.

The H^+ ions were monitored against a background fragmentation source of H^+. There are a number of sources for this background: collisional dissociation with the residual gas in the analyser; transfer in population at resonance resulting in an increase or decrease in fragmentation. This is dependent on the initial population of the states involved, spontaneous near-dissociation and weak continuous photo-dissociation. This background determined the noise level against which the lines were detected. A spectral line was recorded if the signal to noise ratio was greater than 2:1.

1.4 Aims of this work

The primary aim of this work is to investigate the Carrington-Kennedy spectrum [1]. It is hoped that a calculation of H_3^+ dipole transition intensities near-dissociation could help to illuminate this spectrum. In order to tackle the calculation of transition intensities in the high energy regime a number of preliminary tasks will need to be undertaken. This includes the development and optimisation of the DVR3DRJZ suite of Tennyson *et al* [43], the development and optimisation of the parallel version of the DVR3DRJZ suite, and testing the convergence of calculations near-dissociation. This will allow the near-dissociation calculations to be carried out and subsequently analysed. In the course of developing the DVR3DRJZ suite of programs it became apparent that a new algorithm for the calculation of dipole transitions moments which more fully exploited the symmetry of the H_3^+ was needed. This algorithm would substantially reduce computational costs. This algorithm will be developed.

Additionally there are a number of applications for H_3^+ and isotopomer calculations. During the course of this work deuterium chemistry in the interstellar medium has become an area of renewed interest for many groups. Broadly, this interest is split into two areas: those who wish to observe H_3^+ and its deuterated isotopomers; and those who wish to model various astrophysical processes. Synthetic spectra can help to identify possible transitions for observations, such spectra will be calculated in this work. Partition functions and zero point energies together with reaction energies and equilibrium constants involving H_3^+ and its deuterated isotopomers are invaluable to models of the chemistry in the interstellar medium. These quantities will be calculated.

Theoretical calculations are also able to significantly aid H_3^+ experiments; for example, by giving optimal frequency ranges for measurement. The calculations for applications will be able to take advantage of developments in the DVR3DRJZ suite.

Chapter 2

Theory

Within the Schrödinger formulation of quantum mechanics, the state of a many-particle system is described by the wavefunction

$$\Psi(\underline{q}, t) = \Psi(q_1, q_2, q_3, \ldots, q_n, t) \tag{2.1}$$

where $q_1, q_2, q_3, \ldots q_n$ are the generalised coordinates of the particles at a time t. The evolution of the system is given by the time-dependent Schrödinger equation

$$-i\hbar\frac{\partial\Psi}{\partial t} = \hat{H}\Psi \tag{2.2}$$

where $\hat{H}$ is the Hamiltonian operator, the form of which will be discussed in more detail in sections 2.8 and 2.9. A solution to equation 2.2 proves too difficult for all but the simplest cases, therefore simplifying assumptions have to made.

One simplification that can be made is the removal of the temporal dependence in equation 2.2. If the potential of the system is not dependent on time, the Schrödinger equation admits stationary state solutions of the form

$$\Psi(\underline{q}, t) = \psi(\underline{q})\phi(t) \tag{2.3}$$

Where $\psi(\underline{q})$, the spatial wavefunction, and $\phi(t) = \exp(-iEt/\hbar)$, the phase factor, satisfy the time-independent Schrödinger equation

$$\hat{H}\psi = E\psi \tag{2.4}$$

If we consider a molecule of N electrons of mass m_e, charge e, and positions r_i $(i =$

1,...,N); L nuclei of mass m_j; charge Z and positions R_j ($j = 1,...,L$). Then the Hamiltonian is given by

$$H = -\sum_{i=1}^{N} \frac{\hbar^2}{2m_e}\nabla_i^2 - \sum_{j=1}^{L} \frac{\hbar^2}{2m_j}\nabla_j^2 + V(R_j, r_i) \tag{2.5}$$

$\Psi(R_j, r_i)$ is the molecular wavefunction and $V(R_j, r_i)$ is the potential as given by the sum of all coulomb pair potentials:

$$V(R_j, r_i) = \sum_{A<A'}^{L} \frac{ZZ'e^2}{|R_j - R_{j'}|} - \sum_{A=1}^{L}\sum_{i=1}^{N} \frac{Ze^2}{|R_j - r_i|} + \sum_{i<i'}^{N} \frac{e^2}{|r_{i'} - r_i|} \tag{2.6}$$

2.1 Variational Calculations

The time-independent Schrödinger equation can be solved using the variational method as proposed by Rayleigh and Ritz [44, 45]. The method provides useful means of obtaining approximately the bound state energies and wavefunction states of a time-independent Hamiltonian.

H is a time-independent Hamiltonian whose eigenvalues are E_n with corresponding orthonormal eigenvectors of Ψ_n. Let ϕ be some arbitrary function which is normalisable and square integrable. The expectation value of H may be written

$$\langle E \rangle = \frac{\int \phi^* H \phi d\tau}{\int \phi^* \phi d\tau} \tag{2.7}$$

where integration extends over all of coordinate space.

The arbitrary function ϕ may be an expansion of the eigenvector Ψ_n

$$\phi = \sum_n C_n \Psi_n \tag{2.8}$$

Substituting equation (2.8) into equation (2.7)

$$\langle E \rangle = \frac{\int \sum_n C_n^* \Psi_n^* H \sum_m C_m \Psi_m d\tau}{\int \sum_n C_n^* \Psi_n^* \sum_m C_m \Psi_m d\tau} \tag{2.9}$$

The eigenvectors form an orthonormal set, thus

$$\sum_{n,m} \Psi_n^* \Psi_m = \delta_{nm} \tag{2.10}$$

substituting

$$\langle E \rangle = \frac{\sum_{n,m} C_n^* C_m \int \Psi_n^* H \Psi_m d\tau}{\sum_{n,m} C_n^* C_m \int \Psi_n^* \Psi_m d\tau} \tag{2.11}$$

$$= \frac{\sum_{n,m} C_n^* C_m \int \Psi_n^* H \Psi_m d\tau}{\sum_{n,m} C_n^* C_m \delta_{nm}} \tag{2.12}$$

as $H\Psi_n = E_n\Psi_n$ where E_n is the eigen energy of the i^{th} state

$$\langle E \rangle = \frac{\sum_{n,m} C_n^* C_m \int \Psi_n^* E_n \Psi_m d\tau}{\sum_{n,m} C_n^* C_m \delta_{nm}} \quad (2.13)$$

$$= \frac{\sum_{n,m} C_n^* C_m E_n \delta_{nm}}{\sum_{n,m} C_n^* C_m \delta_{nm}} \quad (2.14)$$

$$= \frac{\sum_n |C_n|^2 E_n}{\sum_n |C_n|^2} \quad (2.15)$$

If E_0 is the ground state; then clearly the expectation energy which is the average energy is greater than the lowest energy

$$\langle E \rangle = \frac{\sum_n |C_n|^2 E_0}{\sum_n |C_n|^2} \quad (2.16)$$

$$\langle E \rangle \geq E_0 \quad (2.17)$$

This proof shows that the approximate energy of the ground state is greater than or equal to the true ground state E_0. Thus minimising $\langle E \rangle$ we can obtain the best possible approximation of the ground state energy. The above proof can be extended to excited state energies E_i [46] such that

$$E_i \leq \langle E^i_{n+1} \rangle \leq \langle E^i_n \rangle \leq \langle E^{i+1}_n \rangle \quad (2.18)$$

where $\langle E^i_{n+1} \rangle$ uses one more basis set expansion function than $\langle E^i_n \rangle$.

The value of $\langle E \rangle$ is dependent on the goodness of the arbitrary function ϕ which can be expanded in terms of the basis set. Thus in using the variational method to solve the Schrödinger equation numerically, the size and quality of this basis set determines how closely related the approximated energy is to the true energy. The criteria for a basis set are such that the set be as complete as possible, spans the correct space, the integrals are readily evaluated and the basis set represent the physics of the situation as closely as possible.

2.2 Born-Oppenheimer approximation

A further simplification to the Schrödinger equation is to adopt the Born-Oppenheimer approximation [47, 48], which exploits the mass difference between electrons and nuclei. This allows the nuclear and electronic motion to be separated as the electrons are assumed to respond instantaneously to any movement of the nuclei. Thus the wavefunction may be written as,

$$\Psi_{ne} = \Psi_n(q_n)\Psi_e(q_e) \quad (2.19)$$

where q_n and q_e are the nuclear and electronic coordinates respectively. The Hamiltonian can then be written as,

$$\hat{H} = \hat{T}_n(q_n) + \hat{H}_e(q_e, q_n) \tag{2.20}$$

where $\hat{T}_n$ is the nuclear kinetic energy and $\hat{H}_e$ is the clamped-nucleus electronic Hamiltonian.

2.2.1 Adiabatic Correction

The Born-Oppenheimer approximation, that is the separation of nuclear and electronic motion, can be improved by adding a correction. If equation (2.19) is substituted into (2.20) and manipulated one obtains:

$$(\hat{T}_n(q_n) + E_e(q_n) + U(q_n))\psi_n = E\psi_n \tag{2.21}$$

where $E_e(q_n)$ is the eigenvalue to the clamped-nucleus electronic Hamiltonian, E is the eigen energy of the molecule and $U(q_n)$ is the Born-Oppenheimer diagonal correction (BODC), which is neglected in the Born-Oppenheimer approximation. The addition of the BODC to the Born-Oppenheimer approximation is referred to as the adiabatic approximation. It is usually argued that $U(q_n)$ is dependent on the electronic wavefunction ψ_e and can be considered as being a function $|q_n - q_e|$ [49]; its magnitude is of the order $(m_e/m_n)E_e(q_n)$ and hence is usually neglected. However with light nuclei, such as in H_3^+, this term becomes significant [50]. The simplest method to evaluate this term is to use the formula of Handy: [51–53]

$$U(q_n) = -\frac{1}{2}\sum_i \frac{1}{m_{n_i}} \langle\psi_e| \frac{\partial^2}{\partial q_{n_i}} |\psi_e\rangle \tag{2.22}$$

where m_{n_i} is the mass of the ith nuclei.

2.3 Potential Energy Surface

As a consequence of using the Born-Oppenheimer approximation the molecular dynamics problem has been separated into two parts: electronic and nuclear dynamics. The potential energy surface is the potential that determines the motion of the nuclei; thus it determines the rotation-vibration spectrum, the structure of the molecule and as such chemical reaction pathways.

The potential energy surface can be determined either by fitting an analytical form to the result of some experiment which measures the dynamical processes of the nuclei within the molecule, or one can calculate the potential *ab initio*. The former of these approaches produces an empirical potential. The major problem with this approach is that the experiment may produce data which does not give complete coverage of the surface, therefore extrapolation which may not be valid is needed to cover a significant portion of the nuclear configuration space. The *ab initio* approach involves solving the Schrödinger equation for the electrons for a grid of nuclear geometries. This approach requires that the Schrödinger equation be solved a sufficient number of times to give an adequate representation of the surface. To do this to the requisite accuracy requires significant computational effort.

Two potential energy surfaces have been employed in this work: the Born-Oppenheimer corrected surface of Polyansky and Tennyson [2] and the global *ab initio* potential surface of Polyansky *et al* [3]. The Born-Oppenheimer corrected surface used the Born-Oppenheimer electronic structure calculations of Cencek *et al* [54]. Cencek *et al* also calculated corrections. These include a electronic relativistic correction to the Schrödinger equation and a mass dependent adiabatic correction to the Born-Oppenheimer approximation. Polyansky *et al* use the electronic data and the corrections to fit a new potential energy surface (refer to figure 2.1). This surface with non-adiabatic corrections (section 2.12) is able, at low energy, to reproduce the energy levels of H_3^+ and isotopomers to within a few hundredth of a wavenumber.

At higher energy the Born-Oppenheimer corrected potential energy surface is not extensive enough, instead the global *ab initio* potential surface of Polyansky *et al* [3] is used. This global Born-Oppenheimer surface used an energy switching function to encompass three different energy regimes and the respective associated electronic structure calculations. At low energy, 69 points from Cencek *et al* [54] were employed, which have an absolute accuracy of 0.05 cm^{-1}. At high energy, 492 points lying below 75,000 cm^{-1} from Schinke *et al* [55] were used to constrain the high energy region. The accuracy of these points is approximately 300 cm^{-1}, several orders of magnitude below that of Cencek *et al.* Polyansky *et al* computed a further 134 *ab initio* points in the intermediate region to an accuracy of 3 cm^{-1}. Because of the differing accuracies of the points in the three regimes the fit weighted the points on accuracy, with the more accurate points given more importance. Two fits were produced. The first fit produced a "shoulder" in the potential for some geometries near 50,000 cm^{-1} and above. This can be seen in figure 2.2. A second fit was performed, Fit 2; this is a poorer fit to the data but

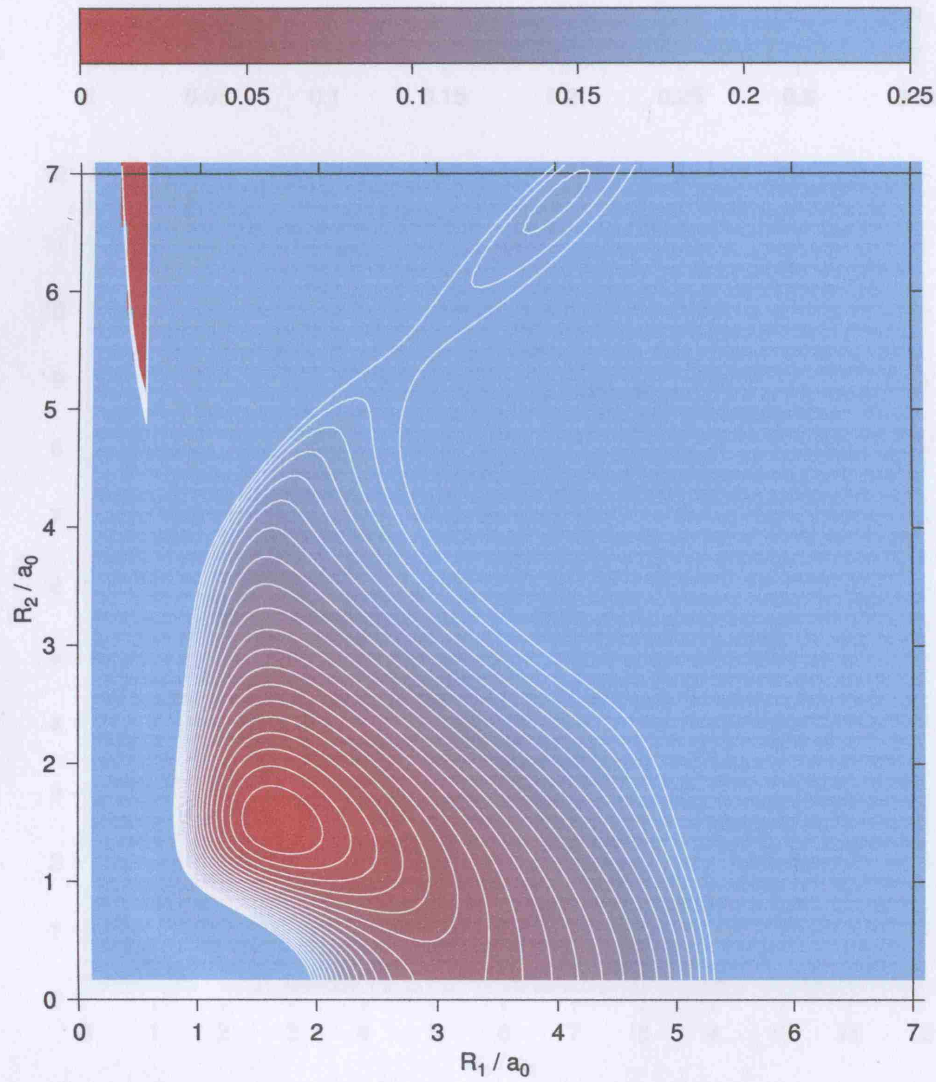

Figure 2.1: The Born-Oppenheimer corrected potential energy surface of Polyansky *et al* [2] in Jacobi coordinates with $\theta = 90°$. Contours drawn from 0.01 E_h to 0.2 E_h with 0.01 E_h increments. Note the unphysical behaviour at high energies.

removes the unphysical "shoulder", figure 2.3. This potential is accurate to within a few wavenumbers up to the dissociation energy.

2.4 Dipole Surface

The dipole surface of a molecule is obtained by calculating the dipole moment at various nuclear geometries; the points are then fitted to a continuous surface. The surface used throughout this work is that of Röhse *et al* [56]. Röhse *et al* give the accuracy of the dipole moment fit as 0.00013 atomic units. The dipole surface returns the μ_x and μ_z

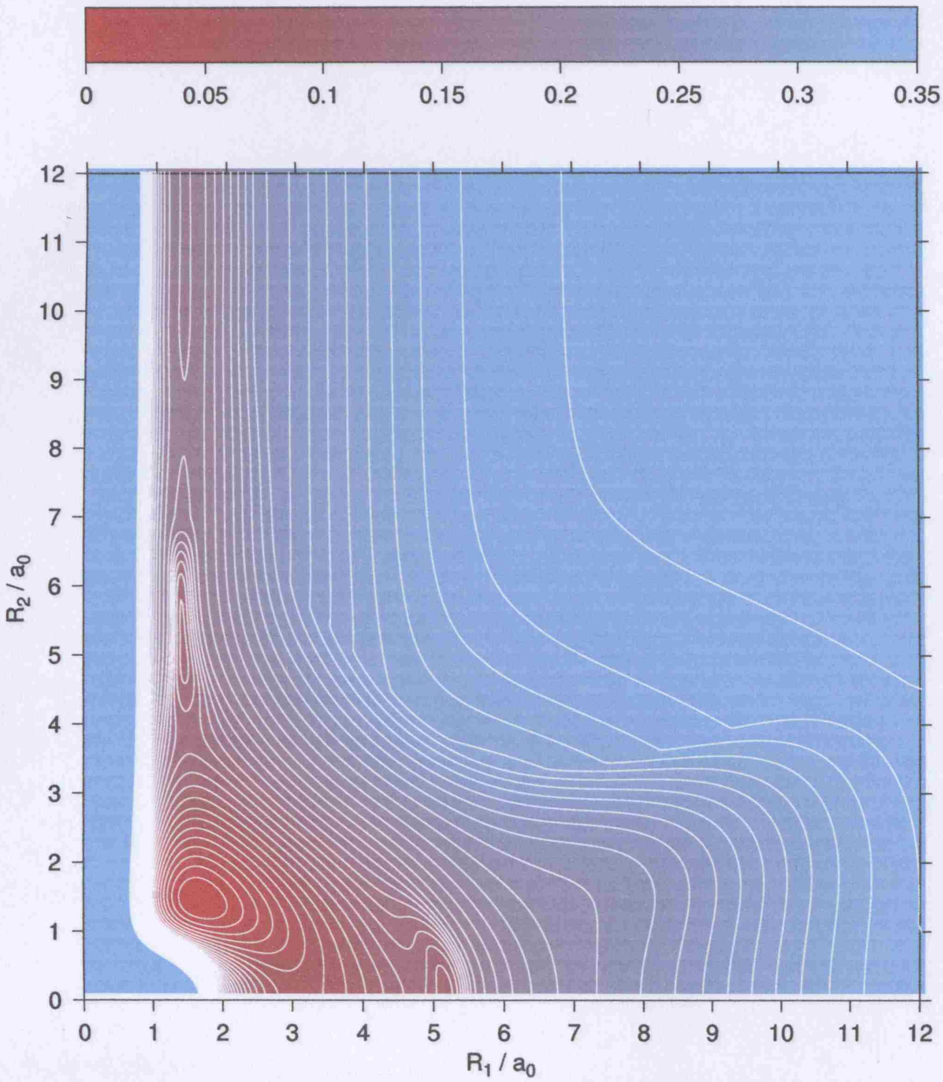

Figure 2.2: The **Fit 1** potential energy surface of Polyansky *et al* [3] in Jacobi coordinates with $\theta = 90°$. Contours drawn from 0.01 E_h to 0.35 E_h with 0.01 E_h increments. Note the shoulder for large values of R_1

components of the dipole as defined by Botswina *et al* [57]. These coordinates are not mutually orthogonal and thus converted to axes where the z component lies along the r_2 coordinate in Jacobi coordinates. The x component lies in the plane of the molecule while the y component is perpendicular to molecular plane, such that they form a right-handed set.

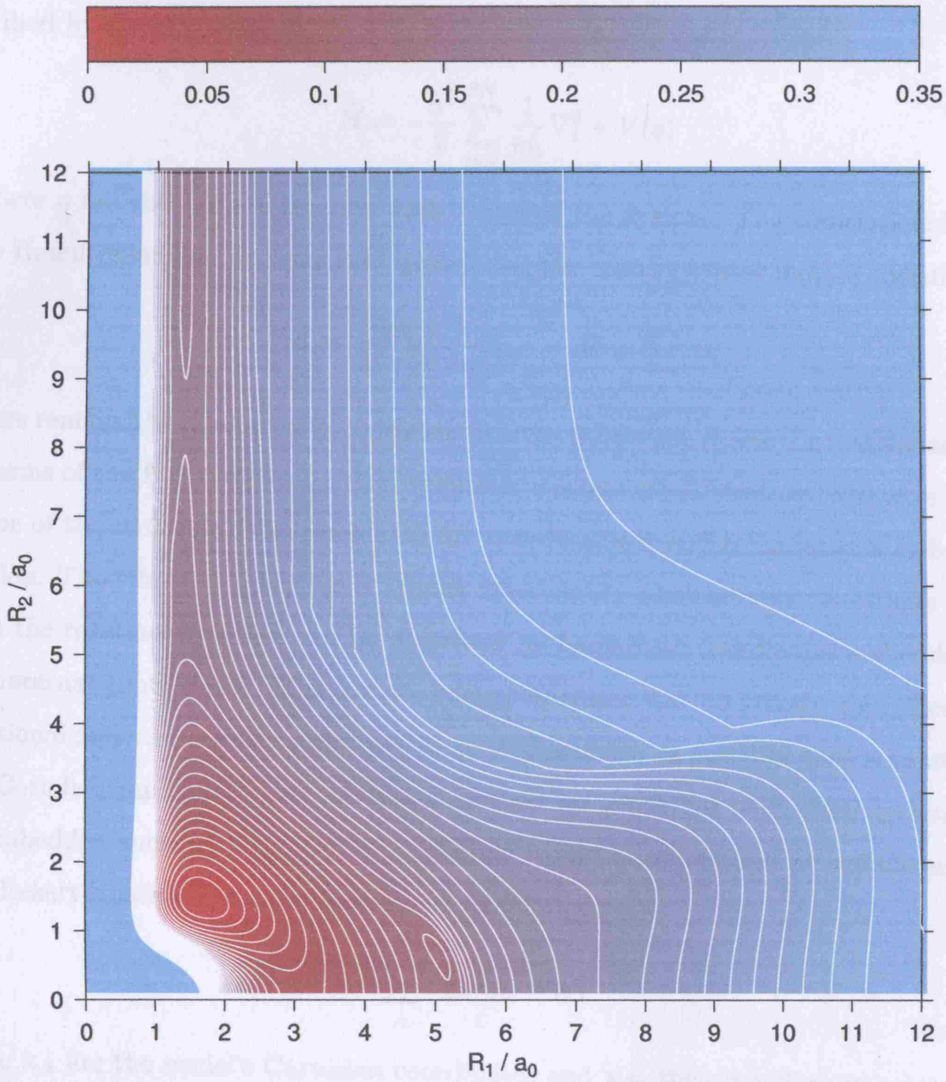

Figure 2.3: The **Fit 2** potential energy surface of Polyansky *et al* [3] in Jacobi coordinates with $\theta = 90°$. Contours drawn from 0.01 E_h to 0.35 E_h with 0.01 E_h increments.

2.5 Coordinate systems

In solving any problem an important step in the process is defining the problem. Defining the problem involves describing the system using coordinates. Judicious choice of coordinates can simplify the mathematics of the problem significantly which can consequently reduce the computational cost of the calculation, thus implicitly the calculation time.

Within the Born-Oppenheimer approximation, the motion of N nuclei can be described by the Hamiltonian

$$\hat{H} = -\frac{\hbar^2}{2}\sum_{i=1}^{3N}\frac{1}{m_i}\nabla_i^2 + V(q) \tag{2.23}$$

Where q are the $3N-6$ internal coordinates of the system. The translational part of the Hamiltonian can be separated by defining the centre of mass motion coordinate

$$\boldsymbol{X} = \frac{1}{M}\sum_i \frac{1}{m_i}x_i, \qquad M = \sum_i m_i \tag{2.24}$$

There remain $3N-3$ internal coordinates. Three of these can define the rotational motion in terms of the Euler angles (α, β, γ) required to rotate the laboratory fixed axes into the frame of the molecule. The remaining $3N$ coordinates describe the internal/vibrational motion. The vibrational motion is usually described by some internal coordinate system, then the rotational motion can be described by body-fixed coordinates embedded onto the internal coordinates. The kinetic energy operator can be greatly simplified if the rotational and vibrational motion are separated as much as possible, that is to minimise the Coriolis coupling. Eckart devised a method by which the body-fixed system could be embedded such that the Coriolis coupling would be minimised at equilibrium [58]. The Eckart conditions can be formulated as follows:

$$\sum_A M_A \mathbf{x}_{Ae} \times \mathbf{x}_A \tag{2.25}$$

where $\mathbf{x}_A$ are the nuclei's Cartesian coordinates and $\mathbf{x}_{Ae}$ their equilibrium values. It is apparent that the Eckart embedding becomes undefined at equilibrium, as the conditions vanish for $\mathbf{x}_A = \mathbf{x}_{Ae}$. Therefore at equilibrium there are an infinite number ways to embedded the body-fixed axes.

It is not always possible to use the Eckart embedding as the kinetic energy operator can become prohibitively complex [59, 60]. Furthermore the Eckart embedding is unable to deal with the problem of a homonuclear molecule becoming linear. This is because it is no longer possible to relate each of the nuclei with their equilibrium positions, and thus meet the Eckart conditions (2.25).

2.5.1 Inter-nuclear coordinates

One of the simplest coordinates systems is inter-nuclear coordinates. The system is described by the distances between the three atoms, A_1, A_2 and A_3, as shown in figure 2.4. This allows the body-fixed coordinates to be placed along the Eckart axes so as to

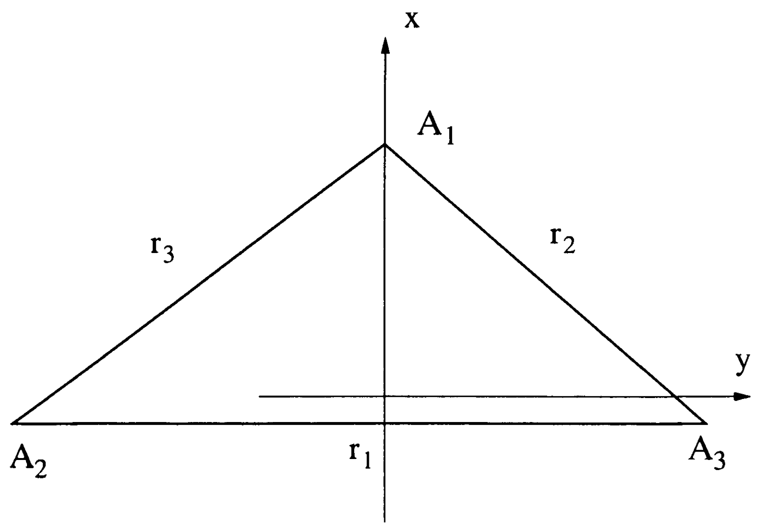

Figure 2.4: The inter-nuclear coordinate system. The body-fixed y-axis is placed parallel to r_1, the x axis bisects r_1 in the plane of the molecule, and the z-axis is defined to give a right-handed set [4].

minimise Coriolis coupling [58]. These coordinates are able to reflect the high symmetry of a molecule with three identical atoms.

This system has been employed successfully by Špirko *et al* [61] and Watson [4]. The problem of using inter-nuclear coordinates is the coupled nature of the integration ranges. This coupling may be overcome with Pekeris coordinates [62–65]; but problems arise when molecules sample linear geometries, which is a particularly important issue for H_3^+.

2.5.2 Radau coordinates

The Radau coordinate systems uses two lengths and an angle, (r_1, r_2, θ), figure 2.5. The distances r_1 and r_2 are the distances of A_1 and A_2 from the point P and the angle θ is the angle between r_1 and r_2. The point P is defined as the canonical point which satisfies the condition that $\overline{PD}^2 = \overline{A_3D}.\overline{CD}$.

If atoms A_1 and A_2 are identical, and the body-fixed x-axis is embedded along the line of symmetry, $\frac{\theta}{2}$ (bisector embedding) then the S_2 permutation symmetry of the AB_2 molecule can be exploited. This make the Radau coordinate system particularly suited to AB_2 molecules such as H_2O [66, 67]. Unfortunately the Radau coordinate system can not fully exploit the higher permutation symmetry S_3 associated with B_3 molecules. Thus the full symmetry of the H_3^+ cannot be exploited. However the Radau coordinate system has been successfully used to represent the H_3^+ system for rotation-vibration

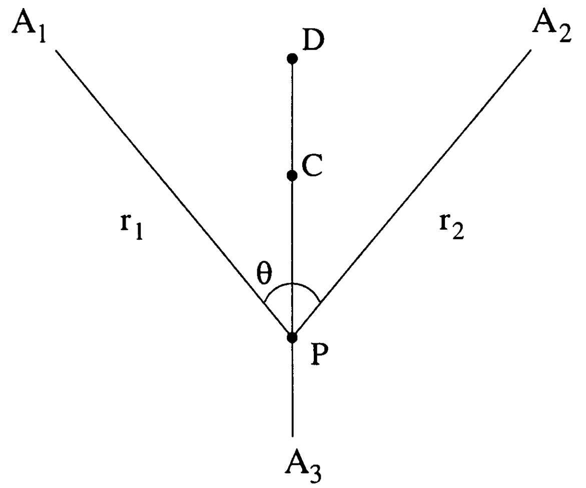

Figure 2.5: The Radau coordinate System. D is the centre of mass of atoms A_1 and A_2, C is the triatomic centre of mass, and P is a canonical point satisfying the condition $\overline{PD}^2 = \overline{A_3D}.\overline{CD}$

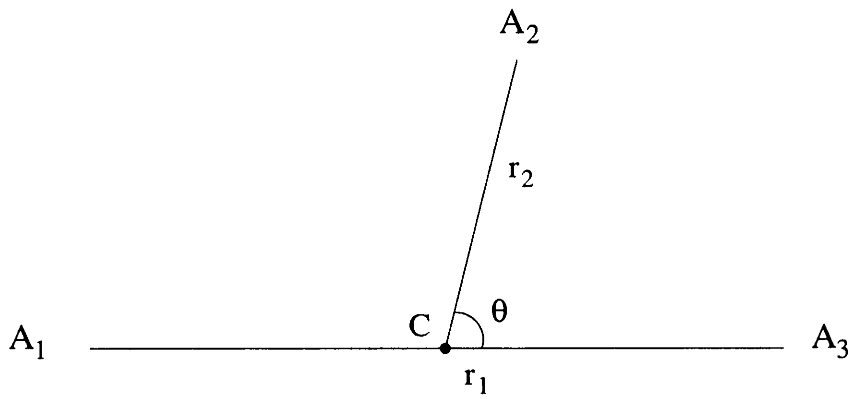

Figure 2.6: The Jacobi Coordinate System [5]. C is the centre of mass of the "diatom".

calculation [68, 69].

2.5.3 Jacobi coordinates (Scattering)

The Jacobi or Scattering coordinate system again uses two lengths and an angle, (r_1, r_2, θ), figure 2.6. r_1 represents the distance between the two atoms, A_2 and A_3, the "diatom," and r_2 represents the distance from the centre of mass of the diatom to the third atom, A_1. θ is the angle between r_1 and r_2.

If atoms A_1 and A_3 are identical, then the line of symmetry about $\theta = 90°$ can be exploited. This is particularly suited to molecules associated with the S_2 permutation symmetry group. Unfortunately the symmetry of the Jacobi coordinates, like Radau coordinates, does not extend to the S_3; thus does not fully represent the D_{3h} symmetry of H_3^+ system. This means the full symmetry of H_3^+ is not represented and thus cannot be

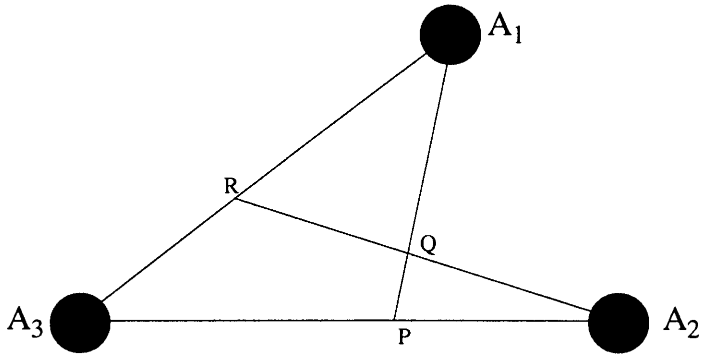

Figure 2.7: Generalised internal coordinate system for a triatomic molecule [6]: A_i represents atom i. The coordinates, r_1, r_2, and θ are given by $r_1 = \overline{A_2R}$, $r_2 = \overline{A_1P}, \theta = A_1\hat{Q}A_2$. The positions of P and R are determined from the particular choice of coordinate system and the masses of A_i.

exploited during computing, making it less efficient. Also the assignment of symmetry to a particular energy level becomes problematic as the states with E symmetry are non-degenerate. Practical problems with this are discussed in chapter 4.

2.5.4 Hyperspherical coordinates

The symmeterised hyperspherical coordinate system [70] uses a distance and two angles, ρ, θ, ϕ, to represent a molecule. The major advantage of these coordinates are that the full S_3 permutation symmetry can be exploited and all energy levels can be assigned to a symmetry block trivially. These coordinates have been used successfully to calculate vibrational and rotational energy levels of H_3^+ [71–74]. These coordinates have been found to be less well suited for molecules which do not have three-fold permutation symmetry [73], such as H_2D^+ and D_2H^+; it is thought that for these lower symmetry molecules coordinates such as Jacobi may be preferable. Hyperspherical coordinates are also very inefficient at large ρ, this is particularly undesirable for a molecule such as H_3^+ which undergoes large amplitude motion.

2.5.5 Coordinate system used in this work

The internal coordinate system for a triatomic molecule can be described by Sutcliffe-Tennyson generalised coordinates, figure 2.7 [6]. Points A_1, A_2 and A_3 denote the positions of the three atoms. The geometric parameters g_1 and g_2 are defined as,

$$g_1 = \frac{A_3 - P}{A_3 - A_2} \tag{2.26}$$

$$g_2 = \frac{A_3 - R}{A_3 - A_1} \tag{2.27}$$

There are several variations on figure 2.7 that produce coordinate systems which could be employed to describe the H_3^+ system. They include Jacobi, Radau, and bond length-bond angle coordinates, which are parameterised by g_1 and g_2. In terms of these parameters we can define the Radau coordinate system as follows,

$$g_1 = 1 - \frac{\alpha}{\alpha + \beta - \alpha\beta}, \qquad g_2 = 1 - \frac{\alpha}{1 - \beta + \alpha\beta} \tag{2.28}$$

$$\alpha = \left(\frac{m_3}{m_1 + m_2 + m_3}\right)^{\frac{1}{2}}, \qquad \beta = \frac{m_2}{m_1 + m_2}$$

where m_1, m_2, and m_3 are the masses or the three atoms. Similarly the Jacobi coordinate system can be defined as follows,

$$g_1 = \frac{m_2}{m_2 + m_3}, \qquad g_2 = 0 \tag{2.29}$$

The parameters g_1 and g_2 for A_3 molecule such as H_3^+ and D_3^+ simplify to $g_1 = \frac{1}{2}, g_2 = 0$ and $g_1 = g_2 = \frac{\sqrt{3}}{1+\sqrt{3}}$ for the Jacobi and Radau coordinate systems respectively. For AB_2 molecules such as H_2D^+ and D_2H^+ where $A_2 = A_3$, g_1 and g_2 are $g_1 = \frac{1}{2}$, $g_2 = 0$ and $g_1 = g_2 = 1 + \frac{M_3}{M_1} - \sqrt{\left(1 + \frac{M_3}{M_1}\right)^2 - 1}$ for the Jacobi and Radau coordinate systems respectively.

Both Radau and Jacobi coordinates are orthogonal, that is the kinetic energy operator in the Hamiltonian is diagonal, which leads to a simpler Hamiltonian then one derived from non-orthogonal coordinates.

There are a number of ways that the body-fixed axes may be embedded in Jacobi and Radau coordinates; some of the embeddings are shown in figures 2.8 and 2.9. In the Jacobi coordinate system there is only one Coriolis term if the body-fixed axis is embedded along either the r_1 or r_2 coordinate. In Radau coordinates the coupling is more complicated. The manner by which coupling between rotation and vibration is reduced is to adopt the Eckart conditions [58] when choosing the embedding of the body-fixed axis; it has been shown that for the H_3^+ system this means that the z-axis should be perpendicular to the frame of the molecule [4, 41].

There are three linear saddle points for H_3^+. In Jacobi coordinates, these occur for $\theta = 0$, $\theta = \pi$ and $r_2 = 0$. The third case, where r_2 goes to zero, causes the

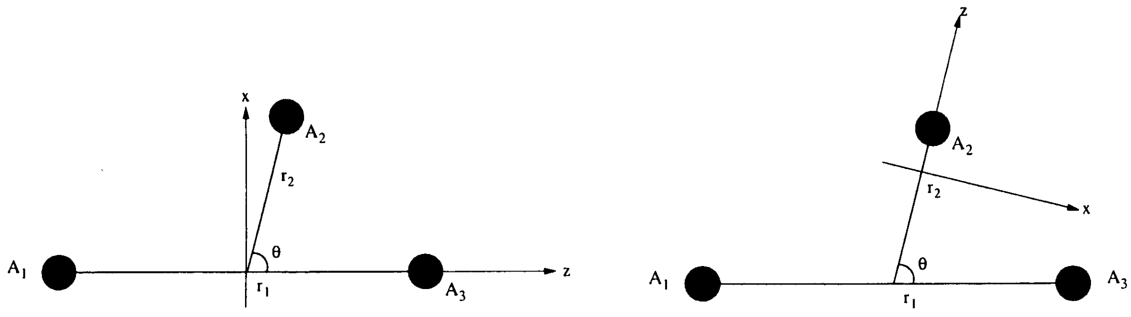

Figure 2.8: The different embeddings of the body-fixed axis system with the Jacobi coordinates. From left to right: The z-axis is parallel to r_1, the x-axis is in the plane of the molecule, while the y-axis is such to defined a right-handed set; The z-axis is parallel to r_2, again the x-axis is in the plane, while the y-axis is such to defined a right-handed set.

most problems as consequently θ becomes undefined [15, 75, 76]. In Radau coordinates the linear case is treated simply when $\theta = 0$ and $\theta = \pi$. The case where r_1 or r_2 is 0 can also treated easily. However the Hamiltonian in Radau coordinates [68] is considerably more complicated than that for Jacobi coordinates (section 2.9). This leads to complex behaviour relating to the convergence, especially with rotational excitation [68]. Throughout this work the Jacobi coordinate system has been employed with the body-fixed z-axis embedded parallel to the r_1 axis (figure 2.8). This is the most sensible embedding as the r_2 coordinate becomes zero for linear geometries, hence embedding the z-axis along r_2 would mean that the z-axis would become undefined at linear geometries.

2.6 Finite Basis Representation

An arbitrary normalised eigenfunction $\Psi(q)$ of a Hamiltonian can be expanded in terms of basis functions $\psi(q)$ which are linear in the parameter c_i; this is known as the Finite basis representation, FBR.

$$\begin{aligned}\Psi(q) &= c_1\psi_1(q) + c_2\psi_2(q) + c_3\psi_3(q) + \ldots + c_N\psi_N(q) \\ \Psi(q) &= \sum_i c_i\psi_i(q) \qquad (2.30)\end{aligned}$$

The vibrational motion can be described by three coordinates, such that the wavefunction can be represented as a sum of products of suitable one dimensional functions $\psi(q)$,

$$\Psi(q_1, q_2, q_3) = \sum_{i,j,k} c_{i,j,k}\psi_i(q_1)\psi_j(q_1)\psi_k(q_1) \qquad (2.31)$$

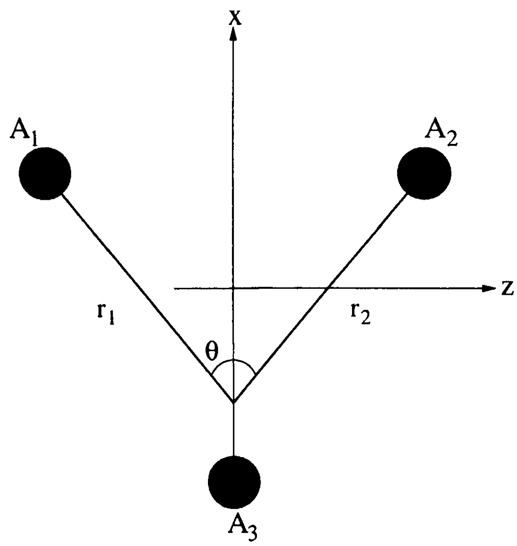

Figure 2.9: The Radau bisector embedding. The x-axis is parallel to $\frac{\theta}{2}$, the z-axis is in the plane of the molecule and the y-axis is such to make a right-handed set.

where q_1, q_2, q_3 are internal coordinates of the system and $c_{i,j,k}$ are coefficients to be determined from diagonalising the Hamiltonian matrix.

The extent to which the FBR represents the *true* wavefunction is dependent on the number of basis functions used; the greater the number of functions, the better the representation. This applies to the eigen energies of the system, which are subject to the variational principle. Although strictly the variational principle optimises the eigen energy only, there is a correlation with the quality of the associated wavefunction. The size of the Hamiltonian matrix is directly dependent on the number of basis functions used. The number of functions tends to increase as the complexity of the motion which the wavefunction describes increases. Thus the number of basis functions needed to converge the wavefunctions of very high lying states to the required accuracy can become computationally prohibitive.

2.7 Discrete Variable Representation

In order to alleviated the problems of the Finite Basis Representation, Light *et al* [77] rediscovered the Discrete Variable Representation, DVR.

The DVR moves from an FBR where the wavefunctions are expressed as a set of orthogonal polynomials to amplitudes represented at the Gaussian quadrature points of these polynomials [78]. If the functions used are a set of $j + 1$ orthogonal polynomials, then there is an orthogonal transformation to a representation at $j + 1$ weighted Gausspolynomial quadrature points.

A 1D DVR transformation of a coordinate expressed as FBR orthogonal polynomials to η points and weights, ω_η, of the associated N-point Gaussian quadrature is given by the unitary transformation [79]

$$T_t^\eta = (\omega_\eta)^{\frac{1}{2}} |t(\eta)\rangle \tag{2.32}$$

Thus the DVR wavefunction consists of a basis of discrete points resulting in a compact representation. There are advantages and disadvantages of using a DVR. The disadvantages are that the DVR Hamiltonian is not strictly variational. The DVR points and the basis set size are linked such that the only way to improve the accuracy of the integrals is to increase the number of points and thus the size of the problem. Within the FBR, a quadrature scheme can be chosen to give the integrals to the required accuracy without consequence to the size of the problem. This means that converged FBR calculations tend to be more accurate than the corresponding DVR calculation. Also it is difficult to perform small DVR calculations as the numerical quadrature with too few points is unreliable and thus unlikely to give meaningful results.

The advantages are that due to the quadrature approximation, the potential elements in the DVR are diagonal (section 2.9); the DVR is particularly conducive to parallel computing as the wavefunction is represented on a grid of points which can be distributed across a series of processors; this is discussed in chapter 5. The grid representation also lends itself to evaluating dipole transition moments, as this is the sum of discrete points within the DVR as opposed to over non-localised functions in an FBR, dipole transitions are discussed in chapter 3. In addition the DVR Hamiltonian is solved by a series of diagonalisations and truncations for each of the three coordinates in turn. Thus the Hamiltonian can be solved via diagonalisations of a 1D, 2D and finally a full 3D Hamiltonian matrix [79] which reduces the size and thus computational cost of the calculation considerably. This is discussed further in section 2.9.1.

2.8 Finite Basis Representation Hamiltonian

Using the Jacobi coordinate systems with the body-fixed z-axis parallel to either the r_1 or the r_2 coordinate, the Coriolis decoupled Hamiltonian matrix, $\hat{H}^{J,k}$, for the finite basis representation may be written [43]

$$\begin{aligned}\langle m,n,j,J,k|\hat{H}^{J,k}|m',n',j',J',k'\rangle &= \langle m|\hat{h}^{(1)}|m'\rangle\delta_{n,n'}\delta_{j,j'} \\ &+ \langle n|\hat{h}^{(2)}|n'\rangle\delta_{m,m'}\delta_{j,j'} \\ &+ (\langle m|\hat{g}^{(1)}|m'\rangle\delta_{n,n'}\delta_{j,j'} + \langle n|\hat{g}^{(2)}|n'\rangle\delta_{m,m'}\delta_{j,j'})j(j+1)\delta_{jj'} \\ &+ \langle m,n,j|V(r_1,r_2,\theta)|m',n',j'\rangle \\ &+ \langle t|\hat{g}^{(i)}|t'\rangle\delta_{j,j'}\delta_{s,s'}(J(J+1)-2k^2) \qquad (2.33)\end{aligned}$$

where $\langle m|$ and $\langle n|$ are the radial basis functions for the r_1 and r_2 coordinates respectively, $\langle j|$ are the angular basis functions, J is the total angular momentum of the system, and k is projection of J onto the body-fixed z-axis. This Coriolis decoupled Hamiltonian assumes that k is a good quantum number, that is the Coriolis couplings are neglected.

The Hamiltonian for fully Coriolis coupled vibration-rotation within the finite basis representation can be expressed as [43]

$$\begin{aligned}\langle m,n,j,J,k,p|\hat{H}|m',n',j',J',k',p'\rangle &= \delta_{k,k'}\langle m,n,j|\hat{H}^{J,k}|m',n',j'\rangle \\ &- (1+\delta_{k,0}+\delta_{k',0})^{-\frac{1}{2}}\delta_{k',k\pm1}\langle t|\hat{g}^{(i)}|t'\rangle\delta_{j,j'}\delta_{s,s'}C^{\pm}_{J,k'}C^{\pm}_{j,k'} \\ & k = p, p+1, ..., J, \quad p = 0,1 \qquad (2.34)\end{aligned}$$

If the body-fixed z-axis is taken parallel to $\underline{r}_1$ then $|t\rangle = |m\rangle$, $s = n$ and $i = 1$; and if the z-axis is taken parallel to $\underline{r}_2$ then $|t\rangle = |n\rangle$, $s = m$ and $i = 2$. The angular factors are given by

$$C^{\pm}_{l,k'} = (l(l+1) - k(k\pm1))^{\frac{1}{2}} \qquad (2.35)$$

where V is the potential and the radial kinetic integrals are given by

$$\langle t|\hat{h}^{(i)}|t'\rangle = \langle t| - \frac{\hbar^2}{2\mu_i}\frac{\partial^2}{\partial r_i^2}|t'\rangle \qquad (2.36)$$

$$\langle t|\hat{g}^{(i)}|t'\rangle = \langle t| - \frac{\hbar^2}{2\mu_i r_i^2}|t'\rangle \qquad (2.37)$$

The reduced masses are give by [6]

$$\frac{1}{\mu_1} = \frac{g_2}{m_1} + \frac{1}{m_2} + \frac{(1-g_2)^2}{m_3} \qquad (2.38)$$

$$\frac{1}{\mu_2} = \frac{1}{m_1} + \frac{g_1^2}{m_2} + \frac{(1-g_1)^2}{m_3} \qquad (2.39)$$

The variables g_1, g_2, m_1, m_2 and m_3 are as described in section 2.5.

2.9 Discrete Variable Representation Hamiltonian

The Coriolis decoupled Hamiltonian, Equation (2.33), may be transformed to the Discrete Variable Representation, DVR, via a unitary transformation of the Finite Basis Representation, FBR, to some quadrature scheme associated with polynomials used in the FBR. A 1D transformation for any of the three coordinates r_1, r_2 or θ to η points with weights ω_η of the N-point Gaussian quadrature associated with the orthogonal polynomials used for the FBR in that coordinate can achieved using equation (2.32), where $t = m, n, j$ for $\eta = \alpha, \beta, \gamma$ respectively.

The product of the three transformations, one for each coordinate, will give the composite transformation

$$\underline{T} = T^{\alpha,\beta,\gamma}_{m,n,j} = T^{\alpha}_{m} T^{\beta}_{n} T^{\gamma}_{j} \tag{2.40}$$

The three dimensional DVR Hamiltonian $H^{J,k}_{\alpha,\alpha',\beta,\beta',\gamma,\gamma'}$ can be obtained from the three dimensional FBR by applying the transformation as

$$\underline{T}^T \langle m, n, j, J, k | \hat{H}^{J,k} | m', n', j', J', k' \rangle \underline{T} \tag{2.41}$$

$$\begin{aligned} H^{J,k}_{\alpha,\alpha',\beta,\beta',\gamma,\gamma'} &= K^{(1)}_{\alpha,\alpha'} \delta_{\beta,\beta'} \delta_{\gamma,\gamma'} + K^{(2)}_{\beta,\beta'} \delta_{\alpha,\alpha'} \delta_{\gamma,\gamma'} + L^{(1)}_{\alpha,\alpha'} \delta_{\gamma,\gamma'} \delta_{\beta,\beta'} + L^{(2)}_{\beta,\beta'} \delta_{\gamma,\gamma'} \delta_{\alpha,\alpha'} \\ &+ (J(J+1) - k^2) M^{(i)}_{\alpha,\alpha',\beta,\beta'} \delta_{\gamma,\gamma'} \\ &+ V(r_{1\alpha}, r_{2\beta}, \theta_{\gamma},) \delta_{\alpha,\alpha'} \delta_{\beta,\beta'} \delta_{\gamma,\gamma'} \end{aligned} \tag{2.42}$$

It can be seen from equation (2.42) that the potential energy operator is diagonal, this is due to the quadrature approximation [78, 79]

$$\sum_{m,n,j} \sum_{m',n',j'} T^{\alpha,\beta,\gamma}_{m,n,j} \langle m, n, j | V(r_1, r_2, \theta) | m', n', j' \rangle T^{\alpha',\beta',\gamma'}_{m',n',j'} \simeq V(r_{1\alpha}, r_{2\beta}, \theta_\gamma) \delta_{\alpha,\alpha'} \delta_{\beta,\beta'} \delta_{\gamma,\gamma'} \tag{2.43}$$

$r_{1\alpha}, r_{2\beta}, \theta_\gamma$ are the values of r_1, r_2, θ at α, β, γ. Thus the potential is diagonal in all coordinates and therefore requires no integration. A consequence of this approximation is that the DVR Hamiltonian is not strictly variational, as the number of basis functions is linked to the number of points.

The kinetic energy terms in the Hamiltonian (2.42) are given by

$$K^i_{\eta,\eta'} = \sum_{t,t'} T^n_t \langle t | \hat{h}^{(i)} | t' \rangle T^{n'}_{t'} \tag{2.44}$$

$$L^i_{\eta,\eta',\gamma,\gamma'} = J_{\gamma,\gamma'} \sum_{t,t'} T^n_t \langle t | \hat{g}^{(i)} | t' \rangle T^{n'}_{t'} \tag{2.45}$$

$$= \frac{J_{\gamma,\gamma'} \hbar^2}{2\mu_i r^2_{i\eta}} \delta_{\eta,\eta'} \tag{2.46}$$

by applying the quadrature approximation. $J_{\gamma,\gamma'}$ is given by

$$J_{\gamma,\gamma'} = \sum_j T_j^{\gamma} j(j+1) T_j^{\gamma'} \tag{2.47}$$

The symmetry of AB_2 molecules in Jacobi coordinates can exploited such that $J_{\gamma,\gamma'}$ becomes the $J_{\gamma,\gamma',q}$ and is given by

$$J_{\gamma,\gamma',q} = \sum_j^{N/2-1} T_{2j+q}^{\gamma} j(j+q) j(2j+q+1) T_{2j+q}^{\gamma'} \qquad q = 0, 1 \tag{2.48}$$

Where q identifies the even and odd symmetry blocks for AB_2 molecules with $q = 0$ the ortho block and $q = 1$ the para block.

2.9.1 Solution Scheme

One of the advantages of using a DVR is that the Hamiltonian can be solved through a series of diagonalisation and truncations, which reduces the computational cost of the solution [80, 81]. If we assume that the coordinate order of the solution is $\theta \to r_1 \to r_2$, that is γ first and α last. The 1D problem is solved for each α and β

$$^{(1D)}H_{\gamma,\gamma'}^{\alpha,\beta} = L_{\alpha,\alpha',\gamma,\gamma'}^{(1)} + L_{\beta,\beta',\gamma,\gamma'}^{(1)} + V(r_{1\alpha}, r_{2\alpha}, \theta_\gamma) \tag{2.49}$$

The amplitudes for the h^{th} level, with eigenvalues $\epsilon_h^{\alpha,\beta}$, are given at each grid point, α, β by $C_{\gamma,h}^{\alpha,\beta}$. Eigenvalues are then selected and used to solve the 2D problem for each β. The manner of selection can either be determined by the size of the 2D Hamiltonian or by energy, $\epsilon_h^{\alpha,\beta} \leq E_{max}^{1D}$.

$$^{(2D)}H_{\alpha,\alpha',h,h'}^{\beta} = \epsilon_h^{\alpha,\beta} \delta_{\alpha,\alpha'} \delta_{h,h'} + \sum_\gamma C_{\gamma,h}^{\alpha,\beta} C_{\gamma,h'}^{\alpha',\beta} K_{\alpha\alpha'}^{(1)} \tag{2.50}$$

Amplitudes for the l^{th} level, with eigenvalue ϵ_l^{β} are given by $C_{\alpha,l,h}^{\beta}$ for each point β. These eigenvalues are selected to be used to solve the full 3D problem. Again they may be selected by the size of the 3D Hamiltonian, N, or by energy $\epsilon_l^{\beta} \leq E_{max}^{2D}$

$$^{(3D)}H_{\beta,\beta',l,l'} = \epsilon_l^{\beta} \delta_{\beta,\beta'} \delta_{l,l'} + \sum_{\alpha h,h'} C_{\alpha,l,h}^{\beta} C_{\alpha,l',h'}^{\beta'} \sum_{\gamma,h} C_{\gamma,h}^{\alpha\beta} C_{\gamma,h'}^{\alpha\beta'} K_{\beta,\beta'}^{(2)} \tag{2.51}$$

Eigenvalues and eigenfunctions coefficients, ϵ_i and $C_{\beta,i,l}$, of this, the Coriolis decoupled Hamiltonian, $\hat{H}^{J,k}$, for $J > 0$ can be used to construct and solve the full rotation-vibration Hamiltonian, $\hat{H}$. The first term in (2.42) is simply ϵ_i and the Hamiltonian matrix construction becomes one of calculating terms off-diagonal in k.

The coefficients of eigenvectors of this 3D Hamiltonian need to be expressed as amplitudes of the wavefunction at the original DVR grid points. These wavefunctions can be put to a number of uses in addition to solving the fully Coriolis coupled Hamiltonian.

The wavefunction amplitude for the i^{th} eigenstate at the DVR grid points is

$$\Psi^{i}_{\alpha,\beta.\gamma} = \sum_{i,h} C_{\beta il} C^{\beta}_{\alpha lh} C^{\alpha\beta}_{\gamma h} = \sum_{i} C_{\beta il} \sum_{h} C^{\beta}_{\alpha lh} C^{\alpha\beta}_{\gamma h} \tag{2.52}$$

Where the $\theta \to r_1 \to r_2$ ordering is assumed.

The quadrature approximation allows matrix element $\langle t|\hat{g}^{(i)}|t'\rangle$ to be diagonal in a DVR. However the angular contribution is diagonal in an FBR. Therefore to solve the fully coupled Hamiltonian the DVR wavefunctions of $\hat{H}^{J,k}$ are transformed to an FBR in θ by,

$$\psi^{J,k,h}_{\alpha,\beta,j} = \sum_{\gamma} T^{\gamma}_{j} \psi^{J,k,h}_{\alpha,\beta,\gamma} \tag{2.53}$$

Thus Hamiltonian matrix in DVR^2 - FBR^1 representation becomes

$$\begin{aligned} \langle h,k,p|\hat{H}|h',k',p\rangle &= \delta_{h,h'}\delta_{k,k'}\epsilon^{J,k}_{h} \\ &- (1+\delta_{k,0}\delta_{k',0})^{\frac{1}{2}}\delta_{k',k\pm1} \\ &\times \sum_{\alpha,\beta,\gamma} \psi^{J,k,h}_{\alpha,\beta,j}\psi^{J,k',h'}_{\alpha,\beta,j} C^{\pm}_{J,k'} C^{\pm}_{j,k'} M^{(i)}_{\alpha,\alpha',\beta,\beta'} \\ k = p, p+1, ..., J, \qquad p = 0,1 & \end{aligned} \tag{2.54}$$

Where for z embedded along r_1 $(i=1)$, the $\underline{M}$-matrix it is diagonal in β and given by

$$M^{(1)}_{\alpha,\alpha'} = \sum_{m,m'} T^{\alpha}_{m}\langle m|\hat{g}^{(1)}|m'\rangle T^{\alpha'}_{m'} \simeq \delta_{\alpha\alpha'}\frac{\hbar^2}{2\mu_1 r^2_{1\alpha}} \tag{2.55}$$

If z is embedded along r_2 $(i=2)$, it is diagonal in β

$$M^{(2)}_{\beta,\beta'} = \sum_{n,n'} T^{\beta}_{m}\langle n|\hat{g}^{(2)}|n'\rangle T^{\beta'}_{n'} \simeq \delta_{\beta\beta'}\frac{\hbar^2}{2\mu_1 r^2_{2\beta}} \tag{2.56}$$

Solving $\hat{H}^{J,k}$ gives eigenvalues, η_l, and eigenfunctions, $\psi^{J,l}_{k,i}$. The eigenvalues represent the energy levels of the system and the eigenfunctions are the accompanying wavefunctions. The wavefunctions can be transformed back to a DVR using

$$d^{J,l}_{k,\alpha,\beta,j} = \sum_{h} \psi^{J,l}_{k,i}\psi^{J,k,h}_{\alpha,\beta,j} \tag{2.57}$$

The DVR wavefunctions $d^{J,l}_{k,\alpha,\beta,j}$ may then be used to calculate dipole transition strengths, this is described in detail in chapter 3.

2.10 Basis functions

In choosing basis functions one must consider both whether these functions will adequately represent the motion of the molecule and how computationally workable they are, that is to say the cost of evaluating the relevant integrals using them must be reasonable.

The angular coordinate θ is represented by associated Legendre polynomials. For the radial coordinates either Spherical Oscillator [82] or Morse Oscillator-like functions [83] can be used. The Morse Oscillator-like functions are defined as:

$$|n\rangle = H_n(r) = \beta^{\frac{1}{2}} N_{n\alpha} \exp(-\frac{y}{2}) y^{\frac{\alpha+1}{2}} L_n^{\alpha}(y) \tag{2.58}$$

$$y = A \exp[-\beta(r - r_e)],$$

where

$$A = \frac{4D_e}{\omega_e}, \beta = \omega_e \left(\frac{\mu}{2D_e}\right)^{\frac{1}{2}}, \alpha = integer(A). \tag{2.59}$$

With μ, r_e, ω_e and D_e representing the reduced mass, equilibrium separation, fundamental frequency and dissociation energy of the relevant coordinate respectively. The parameters r_e, ω_e and D_e can be adjusted to give optimal results.

The Spherical Oscillator functions are defined by:

$$|n\rangle = H_n(r) = 2^{\frac{1}{2}} \beta^{\frac{1}{4}} N_{n\alpha+\frac{1}{2}} \exp(-\frac{y}{2}) y^{\frac{\alpha+1}{2}} L_n^{\alpha+\frac{1}{2}}(y) \tag{2.60}$$

$$y = \beta r^2$$

where

$$\beta = (\mu\omega_e)^{\frac{1}{2}} \tag{2.61}$$

and α and ω_e are treated as variational parameters.

2.11 Quadrature approximation

Henderson *et al* [15] found a particular failure of the quadrature approximation when evaluating the r_2^{-2} integrals. Within the Jacobi coordinate system it is possible that the r_2 coordinate becomes equal to, or very close to zero when the molecule is near linear geometry. If Spherical oscillator-like functions are used to represent the r_2 coordinate then quadrature approximation has to be abandoned for the r_2^{-2} integral because the integral exhibits non-polynomial behaviour as $r_2 \to 0$.

An alternative procedure was developed which alters the construction of the 3D DVR Hamiltonian, ${}^{3D}H_{\beta,\beta',l,l'}$. The altered Hamiltonian ${}^{3D}\tilde{H}_{\beta,\beta',l,l'}$ is given below,

$$ {}^{3D}\tilde{H}_{\beta,\beta',l,l'} = {}^{3D}H_{\beta,\beta',l,l'} + \sum_{\alpha,k,k'} C^{\beta}_{\alpha,l,k} C^{\beta'}_{\alpha,l',k'} (\tilde{M}^{(2)}_{\beta,\beta'} - M^{(2)}_{\beta,\beta'}) \sum_{\gamma,\gamma'} C^{\alpha,\beta}_{\gamma,k} C^{\alpha,\beta'}_{\gamma',k'} J_{\gamma\gamma'} \quad (2.62) $$

where ${}^{3D}H_{\beta,\beta',l,l'}$ is given by equation (2.51) and $\tilde{M}^{(2)}_{\beta,\beta'}$ is given by

$$ \tilde{M}^{(2)}_{\beta,\beta'} = \sum_{n,n'} T^{\beta}_{n} \langle n|\hat{g}^{(2)}|n'\rangle T^{\beta'}_{n'} \quad (2.63) $$

This is evaluated analytically and is given by [82]

$$ \langle n|\hat{g}^{(2)}|n'\rangle = \frac{\hbar^2 \beta}{(2\alpha+1)\mu_2} \left(\frac{n!\,\Gamma(n'+\alpha+\frac{3}{2})}{n'!\,\Gamma(n'+\alpha+\frac{3}{2})} \right)^{\frac{1}{2}} \qquad n \geq n' \quad (2.64) $$

2.12 Non-Adiabatic correction

An additional correction to the Born-Oppenheimer approximation can be made based on the work of Bunker and Moss [84] on diatomics which introduces non-adiabatic corrections; separate reduced masses are employed for the vibrational and rotational terms in the Hamiltonian, μ^V and μ^R respectively. The distinction of the reduced mass leads to an extra term in the Sutcliffe-Tennyson Hamiltonian, $\hat{K}_{\mathrm{NBO}}$:

$$ \hat{K}_{\mathrm{NBO}} = \delta_{k,k'} k^2 \langle j',k| \sin^{-2}\theta |j,k\rangle \left(\frac{\hbar^2}{2r_1^2} \left(\frac{1}{2\mu_1^R} \frac{1}{2\mu_1^V} \right) + \left(\frac{1}{2\mu_2^R} \frac{1}{2\mu_2^V} \right) \right) \quad (2.65) $$

Polyansky and Tennyson [2] found for the H_3^+ system that μ^R was close to the nuclear mass while μ^V differed slightly from the nuclear masses. The vibrational reduced mass, μ^V, could be calculated from a isotopomer independent scaling term.

2.13 Coordinate Ordering

Henderson *et al* [81] performed numerical experiments with the order of the coordinates in a DVR calculation. They found that for a given DVR calculation placing the coordinate with the largest number of grid points last requires considerably less computational time and converges faster, that is with fewer grid points. For the systems they studied this last coordinate was also the one with the greatest density of vibrational states.

2.14 Computational Implementation (Serial Program)

The suite of programs by Tennyson *et al* [43] implements the method of determining rotation-vibration energy levels and wavefunctions outlined.

The program DVR3DRJZ solves the Coriolis decoupled Hamiltonian, $\hat{H}^{J,k}$ (equation 2.42) producing eigenvalues η_i and eigenfunctions $\psi^{J,k,h}_{\alpha,\beta,\gamma}$. These are vibrational energy levels and wavefunctions for $J = 0$; for $J > 0$ they are used by the programs ROTLEV3 to solve the full Coriolis coupled Hamiltonian. ROTLEV3 transforms the DVR eigenfunctions $\psi^{J,k,h}_{\alpha,\beta,\gamma}$ to the DVR^2-FBR^1 representation using equation (2.53), $\psi^{J,k,h}_{\alpha,\beta,j}$. A certain number of the lowest solutions to $\hat{H}^{J,k}$ and the accompanying DVR^2-FBR^1 eigenfunctions are used in equation 2.54. The solutions to the full Coriolis Hamiltonian are the rotational-vibrational energy levels, η_l, and wavefunctions $\psi^{J,l}_{k,i}$. These wavefunctions are transformed to the DVR representation, $d^{J,l}_{k,\alpha,\beta,j}$ using equation (2.57). These wavefunctions are then used by DIPOLE3 to calculate dipole transitions (refer to chapter 3).

Chapter 3

Dipole transition calculations

3.1 Jacobi Dipole calculation

A general formula for the dipole transition line strength using a DVR is outlined below. This derivation starts from the formalism of Miller *et al* [85] which derived the dipole transition line strength using a wavefunction represented by an FBR.

The derivation is valid for both the Jacobi coordinate system with the body fixed z-axis fixed to either the r_1 or r_2 coordinate and the Radau coordinate system with the body fixed z-axis fixed to either r_1, r_2 or along the bisector. J is the total angular momentum, with k the projection of J onto the z-axis. M spans the magnetic sub levels of the wavefunction. The angular part of the wavefunction is represented by the angular basis given by

$$|J_M, k, j, p\rangle = \left(\frac{2J+1}{8\pi^2}\right)^{1/2} \Theta_{j0}(\theta) D^J_{M0}(\alpha\beta\gamma)^* \qquad k = 0, p = 0 \tag{3.1}$$

$$|J_M, k, j, p\rangle = (-1)^k \left(\frac{2J+1}{8\pi^2}\right)^{1/2} (1/2)^{1/2} \times \left(\Theta_{jk}(\theta) D^J_{M-k}(\alpha\beta\gamma)^* + (-1)^p \Theta_{jk}(\theta) D^J_{Mk}(\alpha\beta\gamma)^*\right) \qquad k > 0, p = 0, 1 \tag{3.2}$$

The Radial part of the wavefunction is represented by $\phi_m(r_1)\phi_n(r_2)$

$$|m, n\rangle = \phi_m(r_1)\phi_n(r_2) \tag{3.3}$$

The lth eigenfunction of the Jth angular momentum level with parity p is given by

$$|J_M, p, l\rangle = \sum_{k=p}^{J} \sum_{mnj} d_{kmnj}^{JMpl} |J_M, k, m, n, j, p\rangle \quad (3.4)$$

The line strength S($f - i$) for a particular transition from an initial state i to a final state f is given by

$$S(f-i) = \sum_{M'M''\tau} (T_{if}^{M'M''\tau})^2 \quad (3.5)$$

where

$$T_{if}^{M'M''\tau} = \langle J'_{M'}, p', l' | \boldsymbol{\mu}_\tau^{\mathbf{s}} | J''_{M''}, p'', l'' \rangle \quad (3.6)$$

and μ_τ^s is the τ component of the space-fixed dipole moment. Due to the nature of the body fixed coordinates, only the z and x components are non-zero. The body-fixed dipole moment, $\boldsymbol{\mu}^{\mathbf{m}}(r_1, \mathrm{r}_2, \theta)$, transforms to a tensor of rank one into space fixed coordinates.

$$\boldsymbol{\mu}_\tau^{\mathbf{s}} = \sum_{\nu=-1}^{+1} \mu_\nu^m(r_1, r_2, \theta) D_{\tau,\nu}^1(\alpha\beta\gamma)^* \quad (3.7)$$

This gives

$$\begin{aligned} T_{if}^{M'M''\tau} &= \langle J'_{M'}, p', l' | \mu_\nu^m(r_1, r_2, \theta) D_{\tau,\nu}^{1*} | J''_{M''}, p'', l'' \rangle \\ &= \sum_{\nu=-1}^{+1} \sum_{k'=p'}^{J'} \sum_{m'n'j'} \sum_{k''=p''}^{J''} \sum_{m''n''j''} \\ &\quad \langle J'_{M'}, k', m', n', j', p' | \mu_\nu^m(r_1, r_2, \theta) D_{\tau,\nu}^{1*} | J''_{M''}, k'', m'', n'', j'', p'' \rangle \end{aligned} \quad (3.8)$$

This equation can be separated into angular and radial parts. Considering the angular part first

$$\begin{aligned} &\sum_{\nu=-1}^{+1} \sum_{k'=p'}^{J'} \sum_{k''=p''}^{J''} \sum_{j'j''} d_{k'm'n'j'}^{J'M'p'l'} d_{k''m''n''j''}^{J''M''p''l''} \\ \times\ &\langle J'_{M'}, k', j', p' | \mu_\nu^m(r_1, r_2, \theta) D_{\tau,\nu}^{1*} | J''_{M''}, k'', j'', p'' \rangle \end{aligned} \quad (3.9)$$

Substituting in the angular functions (3.2) and multiplying out, we obtain the following (The k=0 special case is treated later).

$$\sum_{\nu=-1}^{+1}\sum_{k'=p'}^{J'}\sum_{k''=p''}^{J''}\sum_{j'j''} d^{J'M'p'l'}_{k'm'n'j'} d^{J''M''p''l''}_{k''m''n''j''}$$
$$\int \frac{(-1)^{k'+k''}}{2}\left(\frac{2J'+1}{8\pi^2}\right)^{1/2}\left(\frac{2J''+1}{8\pi^2}\right)^{1/2}$$
$$\Big[\Theta^*_{j'k'}(\theta)D^{J'}_{M'-k'}(\alpha\beta\gamma)\mu^m_\nu(r_1,r_2,\theta)D^{*1}_{\tau,\nu}\Theta_{j''k''}(\theta)D^{*J''}_{M''-k''}(\alpha\beta\gamma)+$$
$$\Theta^*_{j'k'}(\theta)D^{J'}_{M'-k'}(\alpha\beta\gamma)\mu^m_\nu(r_1,r_2,\theta)D^{*1}_{\tau,\nu}\Theta_{j''k''}(\theta)D^{*J''}_{M''k''}(\alpha\beta\gamma)+$$
$$(-1)^{p'}\Theta^*_{j'k'}(\theta)D^{J'}_{M'k'}(\alpha\beta\gamma)\mu^m_\nu(r_1,r_2,\theta)D^{*1}_{\tau,\nu}\Theta_{j''k''}(\theta)D^{*J''}_{M''-k''}(\alpha\beta\gamma)+$$
$$(-1)^{p'}\Theta^*_{j'k'}(\theta)D^{J'}_{M'k'}(\alpha\beta\gamma)\mu^m_\nu(r_1,r_2,\theta)D^{*1}_{\tau,\nu}(-1)^{p''}\Theta_{j''k''}(\theta)D^{*J''}_{M''k''}(\alpha\beta\gamma)\Big]$$
$$\times \quad d\sin\beta\, d\beta d\alpha d\gamma\, d\cos\theta \tag{3.10}$$

Exploiting the properties of angular algebra as given by Brink and Satchler [86] and given below

$$D^j_{mm'}(\alpha\beta\gamma)^* = (-1)^{m-m'}D^j_{-m-m'}(\alpha\beta\gamma) \tag{3.11}$$

$$\int D^C_{cc'}(\alpha\beta\gamma)D^A_{aa'}(\alpha\beta\gamma)D^B_{bb'}(\alpha\beta\gamma)\sin\beta d\beta d\alpha d\gamma$$
$$= 8\pi^2\begin{pmatrix} A & B & C \\ a & b & c\end{pmatrix}\begin{pmatrix} A & B & C \\ a' & b' & c'\end{pmatrix} \tag{3.12}$$

$T^{M'M''\tau}_{if}$ becomes

$$T^{M'M''\tau}_{if} = \frac{1}{2}(2J'+1)^{1/2}(2J''+1)^{1/2}\sum_{\nu=-1}^{+1}\sum_{k'=p'}^{J'}\sum_{k''=p''}^{J''}\sum_{j'j''}$$
$$d^{J'M'p'l'}_{k'm'n'j'}d^{J''M''p''l''}_{k''m''n''j''}(-1)^{k'+k''}(-1)^{\tau-\nu}\mu^m_\nu\begin{pmatrix} 1 & J'' & J' \\ -\tau & -M'' & M'\end{pmatrix}$$
$$\times\int\Bigg[(-1)^{M''+k''}\begin{pmatrix} 1 & J'' & J' \\ -\nu & k'' & -k'\end{pmatrix}\Theta^*_{j'k'}(\theta)\Theta_{j''k''}(\theta)+$$
$$(-1)^{M''-k''}\begin{pmatrix} 1 & J'' & J' \\ -\nu & -k'' & -k'\end{pmatrix}\Theta^*_{j'k'}(\theta)\Theta_{j''k''}(\theta)+$$
$$(-1)^{M''+k''}(-1)^{p'}\begin{pmatrix} 1 & J'' & J' \\ \nu & k'' & k'\end{pmatrix}\Theta^*_{j'k'}(\theta)\Theta_{j''k''}(\theta)+$$
$$(-1)^{M''-k''}(-1)^{p'+p''}\begin{pmatrix} 1 & J'' & J' \\ -\nu & -k'' & k'\end{pmatrix}\Theta^*_{j'k'}(\theta)\Theta_{j''k''}(\theta)\Bigg]\, d\cos\theta \tag{3.13}$$

3-j symbols are invariant under cyclic permutation of its columns and multiplies by (-1)$^{a+b+c}$ by non-cyclic ones.

$$\begin{pmatrix} a & b & c \\ \alpha & \beta & \gamma \end{pmatrix} = \begin{pmatrix} b & c & a \\ \beta & \gamma & \alpha \end{pmatrix} = (-1)^{a+b+c} \begin{pmatrix} b & a & c \\ \beta & \alpha & \gamma \end{pmatrix} \tag{3.14}$$

also

$$\begin{pmatrix} a & b & c \\ -\alpha & -\beta & -\gamma \end{pmatrix} = (-1)^{a+b+c} \begin{pmatrix} a & b & c \\ \alpha & \beta & \gamma \end{pmatrix} \tag{3.15}$$

Thus

$$\begin{pmatrix} 1 & J'' & J' \\ -\tau & M'' & M' \end{pmatrix} = \begin{pmatrix} J' & 1 & J' \\ M' & -\tau & -M'' \end{pmatrix} = (-1)^{J''+J'+1} \begin{pmatrix} J' & 1 & J'' \\ -M' & \tau & M'' \end{pmatrix} \tag{3.16}$$

Using equations (3.14) and (3.15) equation (3.13) can be rewritten as

$$\begin{aligned} T_{if}^{M'M''\tau} &= \frac{1}{2}(2J'+1)^{1/2}(2J''+1)^{1/2} \sum_{\nu=-1}^{+1} \sum_{k'=p'}^{J'} \sum_{k''=p''}^{J''} \sum_{j'j''} \\ & d_{k'm'n'j'}^{J'M'p'l'} d_{k''m''n''j''}^{J''M''p''l''} (-1)^{k'+k''} (-1)^{\tau-\nu} (-1)^{J''+J'+1} \begin{pmatrix} J' & 1 & J'' \\ -M' & \tau & M'' \end{pmatrix} \\ & \times \int \mu_\nu^m \Theta_{j'k'}^*(\theta) \Theta_{j''k''}(\theta) \Bigg[(-1)^{M''+k''} \begin{pmatrix} J' & 1 & J'' \\ -k' & -\nu & k'' \end{pmatrix} + \\ & (-1)^{M''-k''} \begin{pmatrix} J' & 1 & J'' \\ -k' & -\nu & -k'' \end{pmatrix} + \\ & (-1)^{M''+k''} (-1)^{p'} \begin{pmatrix} J' & 1 & J'' \\ k' & -\nu & k'' \end{pmatrix} + \\ & (-1)^{M''-k''} (-1)^{p'+p''} \begin{pmatrix} J' & 1 & J'' \\ k' & -\nu & -k'' \end{pmatrix} \Bigg] d\cos\theta \end{aligned} \tag{3.17}$$

From the 3-j symbols of second and third terms the following relations can be obtained

$$-k' - \nu - k'' = 0 \tag{3.18}$$

$$k' - \nu + k'' = 0 \tag{3.19}$$

It can be shown that the second and third term are forbidden due to the restriction that k' and k'' must be a positive non-zero integer. Reordering upon ν equation (3.17) now becomes

$$
\begin{aligned}
T_{if}^{M'M''\tau} &= \frac{1}{2}(2J'+1)^{1/2}(2J''+1)^{1/2}\sum_{\nu=-1}^{+1}\sum_{k'=p'}^{J'}\sum_{k''=p''}^{J''}\sum_{j'j''} \\
& d_{k'm'n'j'}^{J'M'p'l'} d_{k''m''n''j''}^{J''M''p''l''}(-1)^{k'+k''}(-1)^{\tau-\nu}(-1)^{J''+J'+1}\begin{pmatrix} J' & 1 & J'' \\ -M' & \tau & M'' \end{pmatrix} \\
\times & \int \mu_\nu^m \Theta_{j'k'}^*(\theta)\Theta_{j''k''}(\theta)\left[(-1)^{M''+k''}\begin{pmatrix} J' & 1 & J'' \\ -k' & \nu & k'' \end{pmatrix}\right. \\
& \left.(-1)^{M''-k''}(-1)^{p'+p''}\begin{pmatrix} J' & 1 & J'' \\ k' & -\nu & -k'' \end{pmatrix}\right] d\cos\theta
\end{aligned} \tag{3.20}
$$

Again using the 3-j symbol property defined by equation (3.15), equation (3.20) can be rewritten

$$
\begin{aligned}
T_{if}^{M'M''\tau} &= \frac{1}{2}(2J'+1)^{1/2}(2J''+1)^{1/2}\sum_{\nu=-1}^{+1}\sum_{k'=p'}^{J'}\sum_{k''=p''}^{J''}\sum_{j'j''} \\
& d_{k'm'n'j'}^{J'M'p'l'} d_{k''m''n''j''}^{J''M''p''l''}(-1)^{k'+k''}(-1)^{\tau-\nu}(-1)^{J''+J'+1}\begin{pmatrix} J' & 1 & J'' \\ -M' & \tau & M'' \end{pmatrix} \\
\times & \int \mu_\nu^m \Theta_{j'k'}^*(\theta)\Theta_{j''k''}(\theta) \\
\times & \left[(-1)^{M''+k''} + (-1)^{M''-k''}(-1)^{p'+p''}(-1)^{J''+J'+1}\right] \\
\times & \begin{pmatrix} J' & 1 & J'' \\ -k' & \nu & k'' \end{pmatrix} d\cos\theta
\end{aligned} \tag{3.21}
$$

Once again using the 3-j symbol properties and defining $k = k''$ we can further simplify.

$$-M' + \tau + M'' = 0 \tag{3.22}$$

$$-k' + \nu + k'' = 0 \tag{3.23}$$

$$
\begin{aligned}
T_{if}^{M'M''\tau} &= \frac{(-1)^{M'}}{2}(2J'+1)^{1/2}(2J''+1)^{1/2}\sum_{\nu=-1}^{+1}\sum_{k=p''}^{J''}\sum_{j'j''} \\
& d_{k'm'n'j'}^{J'M'p'l'} d_{k''m''n''j''}^{J''M''p''l''}(-1)^k \begin{pmatrix} J' & 1 & J'' \\ -M' & \tau & M'' \end{pmatrix} \\
\times & \int \mu_\nu^m \Theta_{j'k'}^*(\theta)\Theta_{j''k''}(\theta) \times \left[(-1)^{J''+J'+1} + (-1)^{p'+p''}\right] d\cos\theta \\
\times & \begin{pmatrix} J' & 1 & J'' \\ -\nu-k & \nu & k \end{pmatrix}
\end{aligned}
\tag{3.24}
$$

The angular integral can be evaluated using a Gaussian quadrature as outlined in Stroud and Secrest [87] of the form,

$$\int_a^b f(x) = \sum_{i=1}^{n} w_i f(x_i) \tag{3.25}$$

Where $f(x)$ is a polynomial of degree m, x_i are points and w_i are weights. The Condon and Shortley functions $\Theta_{j'k'}^*(\theta)$ and $\Theta_{j''k''}(\theta)$ can be expressed as the polynomials $P_{j'k'}^*$ and $P_{j''k''}$ respectively.

$$
\begin{aligned}
T_{if}^{M'M''\tau} &= \frac{(-1)^{M'}}{2}(2J'+1)^{1/2}(2J''+1)^{1/2}\sum_{\nu=-1}^{+1}\sum_{k=-p''}^{J''}\sum_{j'j''} \\
& d_{k'm'n'j'}^{J'M'p'l'} d_{k''m''n''j''}^{J''M''p''l''}(-1)^k \begin{pmatrix} J' & 1 & J'' \\ -M' & \tau & M'' \end{pmatrix} \\
\times & \sum_{i=1}^{n} \mu_\nu^m(x_i) P_{j'k'}^*(x_i) P_{j''k''}(x_i) \\
\times & \left[(-1)^{J''+J'+1} + (-1)^{p'+p''}\right] \\
\times & \begin{pmatrix} J' & 1 & J'' \\ -\nu-k & \nu & k \end{pmatrix}
\end{aligned}
\tag{3.26}
$$

x_i and w_i are determined from the Legendre polynomial of equal order to P_{j0}, ie k=0.

The radial part in an FBR can be expressed as,

$$\sum_{\nu=-1}^{1}\sum_{m'n'}\sum_{m''n''}\langle m'n'|\mu_\tau^s|m''n''\rangle \times d_{k'm'n'j'}^{J'M'p'l'} d_{k''m''n''j''}^{J''M''p''l''} \tag{3.27}$$

We can omit $D^{1*}_{\tau,\nu}$ as it has no radial dependence. A 1D DVR transformation for a coordinate is defined in terms of points, x_i, and weights, w_i, of the N-point Gaussian quadrature associated with the orthogonal polynomials used for the FBR in that coordinate [79].

$$T^{\alpha}_{m} = (w_\alpha)^{1/2}|m_\alpha\rangle \tag{3.28}$$

$$T^{\beta}_{n} = (w_\beta)^{1/2}|n_\beta\rangle \tag{3.29}$$

$$\sum_{\nu=-1}^{1}\sum_{m'n'}\sum_{m''n''} T^{\alpha'}_{m'}T^{\beta'}_{n'}\langle m'n'|\mu^s_\tau|m''n''\rangle T^{\alpha''}_{m''}T^{\beta''}_{n''} \times d^{J'M'p'l'}_{k'm'n'j'}d^{J''M''p''l''}_{k''m''n''j''} \tag{3.30}$$

$$\sum_{\nu=-1}^{1}\sum_{m'n'}\sum_{m''n''} (w_{\alpha'})^{1/2}(w_{\beta'})^{1/2}\langle m'_{\alpha'}n'_{\beta'}|\mu^s_\tau|m''_{\alpha''}n''_{\beta''}\rangle(w_{\alpha'})^{1/2}(w_{\beta'})^{1/2} \times d^{J'M'p'l'}_{k'm'n'j'}d^{J''M''p''l''}_{k''m''n''j''} \tag{3.31}$$

$$\sum_{\nu=-1}^{1}\sum_{m'n'}\sum_{m''n''}\sum_{\alpha'\beta'}\sum_{\alpha''\beta''} (w_{\alpha'})^{1/2}(w_{\beta'})^{1/2}(w_{\alpha'})^{1/2}(w_{\beta'})^{1/2}\mu^s_\tau\delta_{\alpha'\alpha'}\delta_{\beta''\beta''} \times d^{J'M'p'l'}_{k'm'n'j'}d^{J''M''p''l''}_{k''m''n''j''} \tag{3.32}$$

let

$$c^{J'M'p'l'}_{k'j'\alpha\beta} = \sum_{m'n'} (w_{\alpha'})^{1/2}(w_{\beta'})^{1/2}d^{J'M'p'l'}_{k'm'n'j'} \tag{3.33}$$

$$c^{J''M''p''l''}_{k''j''\alpha\beta} = \sum_{m''n''} (w_{\alpha''})^{1/2}(w_{\beta''})^{1/2}d^{J''M''p''l''}_{k''m''n''j''} \tag{3.34}$$

Therefore

$$\sum_{\alpha\beta}\mu^m_\tau c^{J'M'p'l'}_{k'j'\alpha\beta}c^{J''M''p''l''}_{k''j''\alpha\beta} \tag{3.35}$$

Thus combining the radial and angular parts,

$$\begin{aligned}
T_{if}^{M'M''\tau} &= \frac{(-1)^{M'}}{2}(2J'+1)^{1/2}(2J''+1)^{1/2}\sum_{\nu=-1}^{+1}\sum_{k=p''}^{J''}\sum_{j'j''}\sum_{\alpha\beta} \\
& (-1)^k\begin{pmatrix} J' & 1 & J'' \\ -M' & \tau & M'' \end{pmatrix}\begin{pmatrix} J' & 1 & J'' \\ -\nu-k & \nu & k \end{pmatrix} \\
&\times \sum_{i=1}^{n} w_i\mu_\nu^m(x_i)P_{j'k'}^*(x_i)P_{j''k''}(x_i) \\
&\times c_{k'j'\alpha\beta}^{J'M'p'l'}c_{k''j''\alpha\beta}^{J''M''p''l''} \\
&\times \left[(-1)^{J''+J'+1}+(-1)^{p'+p''}\right]
\end{aligned} \tag{3.36}$$

$$\begin{aligned}
S(f-i) &= \frac{1}{4}\left[(2J'+1)(2J''+1)\right] \\
&\times \left[\sum_{\nu=-1}^{+1}\sum_{k=p''}^{J''}\sum_{j'j''}\sum_{\alpha\beta}\right. \\
&\times (-1)^k\begin{pmatrix} J' & 1 & J'' \\ -\nu-k & \nu & k \end{pmatrix} \\
&\times \sum_{i=1}^{n}\mu_\nu^m(x_i)P_{j'k'}^*(x_i)P_{j''k''}(x_i) \\
&\times c_{k'j'\alpha\beta}^{J'M'p'l'}c_{k''j''\alpha\beta}^{J''M''p''l''} \\
&\times \left.\left[(-1)^{J''+J'+1}+(-1)^{p'+p''}\right]\right]^2 \\
& \text{for } k>0, p=0,\ 1 \text{ only}
\end{aligned} \tag{3.37}$$

3.1.1 Special Cases

There are a number of special cases which must be dealt with.

Firstly for $k'=0, p'=0$ to $k''=0, p''=0$ case. Taking the angular basis first, from (3.1) and (3.4),

$$\begin{aligned}
T_{if}^{M'M''\tau} &= \int\left(\frac{2J'+1}{8\pi^2}\right)^{1/2}\left(\frac{2J''+1}{8\pi^2}\right)^{1/2}\sum_{v=-1}^{+1}\sum_{j'j''}d_{k'm'n'j'}^{J'M'p'l'}d_{k''m''n''j''}^{J''M''p''l''} \\
&\times \Theta_{j'0}^*(\theta)\Theta_{j''0}(\theta) \\
&\times D_{M'0}^{J'}(\alpha,\beta,\gamma)\mu_\nu^m(r_1,r_2,\theta)D_{\tau\nu}^{1*}(\alpha,\beta,\gamma)D_{M''0}^{J''*}(\alpha,\beta,\gamma) \\
&\times d\text{sin}\beta\, d\beta d\alpha d\gamma\, d\text{cos}\,\theta
\end{aligned} \tag{3.38}$$

Using the 3-j symbol relations outlines in equations (3.11), (3.12), (3.14) and (3.15).

$$\begin{aligned}
T_{if}^{M'M''\tau} &= \int \left(\frac{2J'+1}{8\pi^2}\right)^{1/2} \left(\frac{2J''+1}{8\pi^2}\right)^{1/2} \sum_{v=-1}^{+1} \sum_{j'j''} d_{k'm'n'j'}^{J'M'p'l'} d_{k''m''n''j''}^{J''M''p''l''} \\
&\times \Theta_{j'0}^{*}(\theta)\Theta_{j''0}(\theta)\mu_{\nu}^{m}(r_1, r_2, \theta) \\
&\times D_{M'0}^{J'}(\alpha,\beta,\gamma)(-1)^{\tau-\nu} D_{-\tau-\nu}^{1}(\alpha,\beta,\gamma)(-1)^{M''} D_{-M''-0}^{J''}(\alpha,\beta,\gamma) \\
&\times d\sin\beta \, d\beta d\alpha d\gamma \, d\cos\theta \qquad (3.39)
\end{aligned}$$

$$\begin{aligned}
T_{if}^{M'M''\tau} &= (2J'+1)^{1/2}(2J''+1)^{1/2} \sum_{v=-1}^{+1} \sum_{j'j''} d_{k'm'n'j'}^{J'M'p'l'} d_{k''m''n''j''}^{J''M''p''l''} \\
&\times (-1)^{\tau-\nu}(-1)^{M''} \begin{pmatrix} 1 & J'' & J' \\ -\tau & -M'' & M' \end{pmatrix} \begin{pmatrix} 1 & J'' & J' \\ -\nu & 0 & 0 \end{pmatrix} \\
&\times \int \Theta_{j'0}^{*}(\theta)\Theta_{j''0}(\theta)\mu_{\nu}^{m}(r_1, r_2, \theta) d\cos\theta \qquad (3.40)
\end{aligned}$$

$$\begin{aligned}
T_{if}^{M'M''\tau} &= (2J'+1)^{1/2}(2J''+1)^{1/2} \sum_{v=-1}^{+1} \sum_{j'j''} d_{k'm'n'j'}^{J'M'p'l'} d_{k''m''n''j''}^{J''M''p''l''} \\
&\times (-1)^{M''}(-1)^{\tau-\nu}(-1)^{J''+J'+1} \begin{pmatrix} J' & 1 & J'' \\ -M' & \tau & M'' \end{pmatrix} \begin{pmatrix} J' & 1 & J'' \\ 0 & -\nu & 0 \end{pmatrix} \\
&\times \int \Theta_{j'0}^{*}(\theta)\Theta_{j''0}(\theta)\mu_{\nu}^{m}(r_1, r_2, \theta) d\cos\theta \qquad (3.41)
\end{aligned}$$

Similarly we can evaluate the angular integral as a Gaussian quadrature.

$$\begin{aligned}
T_{if}^{M'M''\tau} &= (2J'+1)^{1/2}(2J''+1)^{1/2} \sum_{v=-1}^{+1} \sum_{j'j''} d_{k'm'n'j'}^{J'M'p'l'} d_{k''m''n''j''}^{J''M''p''l''} \\
&\times (-1)^{M''}(-1)^{\tau-\nu} \begin{pmatrix} J' & 1 & J'' \\ -M' & \tau & M'' \end{pmatrix} \begin{pmatrix} J' & 1 & J'' \\ 0 & \nu & 0 \end{pmatrix} \\
&\times \sum_{i=1}^{n} w_i P_{j'0}(x_i)^{*} P_{j''0}(x_i)\mu_{\nu}^{m}(x_i) \qquad (3.42)
\end{aligned}$$

Thus incorporating the radial portion we obtain,

$$\begin{aligned}
T_{if}^{M'M''\tau} &= (2J'+1)^{1/2}(2J''+1)^{1/2} \\
&\times \sum_{v=-1}^{+1} \sum_{j'j''} \sum_{\alpha\beta} c_{k'j'\alpha\beta}^{J'M'p'l'} c_{k''j''\alpha\beta}^{J''M''p''l''} \\
&\times (-1)^{M'}(-1)^{-\nu} \begin{pmatrix} J' & 1 & J'' \\ -M' & \tau & M'' \end{pmatrix} \begin{pmatrix} J' & 1 & J'' \\ 0 & \nu & 0 \end{pmatrix} \\
&\times \sum_{i=1}^{n} w_i P_{j'0}(x_i)^{*} P_{j''0}(x_i)\mu_{\nu}^{m}(x_i, \alpha, \beta) \qquad (3.43)
\end{aligned}$$

$$
\begin{aligned}
S(f-i) &= (2J'+1)(2J''+1) \\
&\times \left[\sum_{v=-1}^{+1}\sum_{j'j''}\sum_{\alpha\beta} c_{k'j'\alpha\beta}^{J'M'p'l'} c_{k''j''\alpha\beta}^{J''M''p''l''}\right. \\
&\times (-1)^{-\nu}\begin{pmatrix} J' & 1 & J'' \\ 0 & \nu & 0 \end{pmatrix} \\
&\times \left.\sum_{i=1}^{n} w_i P_{j'0}(x_i)^* P_{j''0}(x_i)\mu_\nu^m(x_i,\alpha,\beta)\right]^2 \\
\text{for} \quad & k'=0, \quad k''=0 \\
& p'=0, \quad p''=0
\end{aligned} \tag{3.44}
$$

For $k' = 0, p' = 0$ to $k'' > 0, p'' = 0, 1$ case. Taking the angular basis first, from (3.1), (3.2) and (3.4),

$$
\begin{aligned}
T_{if}^{M'M''\tau} &= \sum_{v=-1}^{+1}\sum_{k'=p'}^{J'}\sum_{k''=p''}^{J''}\sum_{j'j''}\int(-1)^{k''}\left(\frac{1}{2}\right)^{1/2}\left(\frac{2J'+1}{8\pi^2}\right)^{1/2}\left(\frac{2J''+1}{8\pi^2}\right)^{1/2} \\
&\times d_{k'm'n'j'}^{J'M'p'l'} d_{k''m''n''j''}^{J''M''p''l''} \\
&\times \Big[\Theta_{j'0}^*(\theta)D_{M'0}^{J'}(\alpha,\beta,\gamma)\mu_\nu^m D_{\tau\nu}^{1*}(\alpha,\beta,\gamma)\Theta_{j''k''}D_{M''-k''}^{J''*}(\alpha,\beta,\gamma)+ \\
&(-1)^{p''}\Theta_{j'0}^*(\theta)D_{M'0}^{J'}(\alpha,\beta,\gamma)\mu_\nu^m D_{\tau\nu}^{1*}(\alpha,\beta,\gamma)\Theta_{j''k''}(\theta)D_{M''-k''}^{J''*}(\alpha,\beta,\gamma)\Big] \\
&\times d\sin\beta\, d\beta d\alpha d\gamma\, d\cos\theta
\end{aligned} \tag{3.45}
$$

$$
\begin{aligned}
T_{if}^{M'M''\tau} &= \sum_{v=-1}^{+1}\sum_{k'=p'}^{J'}\sum_{k''=p''}^{J''}\sum_{j'j''}\int(-1)^{k''}\left(\frac{1}{2}\right)^{1/2}(2J'+1)^{1/2}(2J''+1)^{1/2} \\
&\times d_{k'm'n'j'}^{J'M'p'l'} d_{k''m''n''j''}^{J''M''p''l''} \\
&\times \Big[\Theta_{j'0}^*(\theta)\Theta_{j''k''}(\theta)\mu_\nu^m(-1)^{\tau-\nu}(-1)^{M''+k''} \\
&\quad\times\begin{pmatrix} 1 & J'' & J' \\ -\tau & -M'' & M' \end{pmatrix}\begin{pmatrix} 1 & J'' & J' \\ -\nu & k'' & 0 \end{pmatrix} \\
&+ \Theta_{j'0}^*(\theta)\Theta_{j''k''}(\theta)\mu_\nu^m(-1)^{p''}(-1)^{\tau-\nu}(-1)^{M''-k''} \\
&\quad\times\begin{pmatrix} 1 & J'' & J' \\ -\tau & -M'' & M' \end{pmatrix}\begin{pmatrix} 1 & J'' & J' \\ -\nu & -k'' & 0 \end{pmatrix}\Big] \\
&\times d\sin\beta\, d\beta d\alpha d\gamma\, d\cos\theta
\end{aligned} \tag{3.46}
$$

$$\begin{aligned}
T_{if}^{M'M''\tau} &= \sum_{v=-1}^{+1}\sum_{k'=p'}^{J'}\sum_{k''=p''}^{J''}\sum_{j'j''}\int (-1)^{k''}\left(\frac{1}{2}\right)^{1/2}(2J'+1)^{1/2}(2J''+1)^{1/2} \\
&\times\ d_{k'm'n'j'}^{J'M'p'l'}d_{k''m''n''j''}^{J''M''p''l''} \\
&\times\ \Theta_{j'0}^{*}(\theta)\Theta_{j''k''}(\theta)\mu_{\nu}^{m}\begin{pmatrix} 1 & J'' & J' \\ -\tau & -M'' & M' \end{pmatrix}(-1)^{J''+J'+1}(-1)^{\tau-\nu} \\
&\times\ \left[(-1)^{M''+k''}\begin{pmatrix} J' & 1 & J'' \\ 0 & -\nu & k'' \end{pmatrix}+(-1)^{p''}(-1)^{M''-k''}\begin{pmatrix} J' & 1 & J'' \\ 0 & -\nu & -k'' \end{pmatrix}\right] \\
&\times\ d\sin\beta\, d\beta d\alpha d\gamma\, d\cos\theta \qquad (3.47)
\end{aligned}$$

$$\begin{aligned}
T_{if}^{M'M''\tau} &= \sum_{v=-1}^{+1}\sum_{k''=p''}^{J''}\sum_{j'j''}\int \left(\frac{1}{2}\right)^{1/2}(2J'+1)^{1/2}(2J''+1)^{1/2} \\
&\times\ d_{k'm'n'j'}^{J'M'p'l'}d_{k''m''n''j''}^{J''M''p''l''} \\
&\times\ (-1)^{\tau-\nu}(-1)^{M''}\Theta_{j'0}^{*}(\theta)\Theta_{j''k''}(\theta)\mu_{\nu}^{m}\begin{pmatrix} J' & 1 & J'' \\ -M' & -\tau & M'' \end{pmatrix}\begin{pmatrix} J' & 1 & J'' \\ 0 & \nu & k'' \end{pmatrix} \\
&\times\ [(-1)^{J''+J'+1}+(-1)^{p''}]d\cos\theta \qquad (3.48)
\end{aligned}$$

From the 3-j the symbols we obtain the following relations

$$M'' = M'-\tau \qquad (3.49)$$

$$\nu = -k'' \qquad (3.50)$$

Applying the Gaussian quadrature on the angular integration in a similar manner as previously.

$$\begin{aligned}
T_{if}^{M'M''\tau} &= \sum_{v=-1}^{+1}\sum_{k''=p''}^{J''}\sum_{j'j''} d_{k'm'n'j'}^{J'M'p'l'}d_{k''m''n''j''}^{J''M''p''l''} \\
&\times\ (2J'+1)^{1/2}(2J''+1)^{1/2}\left(\frac{1}{2}\right)^{1/2}(-1)^{k''}(-1)^{M'} \\
&\times\ \sum_{i=1}^{n} w_i P_{j'0}^{*}(x_i)P_{j''k''}(x_i)\mu_{\nu}^{m}(\alpha,\beta,x_i) \\
&\times\ \begin{pmatrix} J' & 1 & J'' \\ -M' & -\tau & M'' \end{pmatrix}\begin{pmatrix} J' & 1 & J'' \\ 0 & \nu & k'' \end{pmatrix} \\
&\times\ [(-1)^{J''+J'+1}+(-1)^{p''}] \qquad (3.51)
\end{aligned}$$

Including the previously derived radial portion,

$$
\begin{aligned}
T_{if}^{M'M''\tau} &= \sum_{v=-1}^{+1} \sum_{k''=p''}^{J''} \sum_{j'j''} \sum_{\alpha\beta} c_{k'\alpha'\beta'j'}^{J'M'p'l'} c_{k''\alpha''\beta''j''}^{J''M''p''l''} \\
&\times \quad (2J'+1)^{1/2}(2J''+1)^{1/2} \left(\frac{1}{2}\right)^{1/2} (-1)^{k''+M'} \\
&\times \quad \sum_{i=1}^{n} w_i P_{j'0}^{*}(x_i) P_{j''k''}(x_i) \mu_{\nu}^{m}(\alpha,\beta,x_i) \\
&\times \quad \begin{pmatrix} J' & 1 & J'' \\ -M' & -\tau & M'' \end{pmatrix} \begin{pmatrix} J' & 1 & J'' \\ 0 & \nu & k'' \end{pmatrix} \\
&\times \quad [(-1)^{J''+J'+1} + (-1)^{p''}]
\end{aligned}
\tag{3.52}
$$

$$
\begin{aligned}
S(f-i) &= \left(\frac{1}{2}\right)(2J'+1)(2J''+1) \left[\sum_{v=-1}^{+1} \sum_{k''=p''}^{J''} \sum_{j'j''} \sum_{\alpha\beta} c_{k'\alpha'\beta'j'}^{J'M'p'l'} c_{k''\alpha''\beta''j''}^{J''M''p''l''} \right. \\
&\times \quad (-1)^{k''} \begin{pmatrix} J' & 1 & J'' \\ 0 & \nu & k'' \end{pmatrix} \\
&\times \quad \sum_{i=1}^{n} w_i P_{j'0}^{*}(x_i) P_{j''k''}(x_i) \mu_{\nu}^{m}(\alpha,\beta,x_i) \\
&\times \quad \left. [(-1)^{J''+J'+1} + (-1)^{p''}] \right]^2 \\
&\text{for} \quad \begin{matrix} k'=0 & k''>0 \\ p'=0 & p''=0,1 \end{matrix}
\end{aligned}
\tag{3.53}
$$

Similarly for $k' > 0, p' = 0,1$ to $k'' = 0, p'' = 0$ case, the line strength is given by

$$
\begin{aligned}
S(f-i) &= \left(\frac{1}{2}\right)(2J'+1)(2J''+1) \left[\sum_{v=-1}^{+1} \sum_{k''=p''}^{J''} \sum_{j'j''} \sum_{\alpha\beta} c_{k'\alpha'\beta'j'}^{J'M'p'l'} c_{k''\alpha''\beta''j''}^{J''M''p''l''} \right. \\
&\times \quad \begin{pmatrix} J' & 1 & J'' \\ 0 & \nu & k'' \end{pmatrix} \\
&\times \quad \sum_{i=1}^{n} w_i P_{j'0}^{*}(x_i) P_{j''k''}(x_i) \mu_{\nu}^{m}(\alpha,\beta,x_i) \\
&\times \quad \left. [(-1)^{J''+J'+1} + (-1)^{p''}] \right]^2 \\
&\text{for} \quad \begin{matrix} k'>0 & k''=0 \\ p'=0,1 & p''=0 \end{matrix}
\end{aligned}
\tag{3.54}
$$

3.1.2 General Case

As the DVR[2]-FBR[1] wavefunctions, $c^{JMpl}_{k\alpha\beta j}$, have an angular dependence on k it is necessary to transform them such that all the wavefunctions are on a common DVR grid. This transformation, which places the wavefunctions $c^{J'M'p'l'}_{k'\alpha\beta j'}$ and $c^{J''M''p''l''}_{k''\alpha\beta j''}$ onto a common grid is given by

$$c^{Jpl}_{k\alpha\beta\gamma} = \sum_n (w_n)^{\frac{1}{2}} P_{jk}(x_n) d^{J,k,l}_{\alpha,\beta,j} \tag{3.55}$$

The weights w_i and points x_i are determined from a Gauss-Legendre polynomial of equal order to P_{j0}, ie $k = 0$. The number of angular points on the common grid, γ, is at least one more than the number FBR angular functions, j. The DIPOLE3 program allows γ to be used as input, thus allowing it to be varied. This relatively fast transformation has the effect of removing one of the summations from the line strength expression. The implementation and use of these transformed wavefunctions into the DIPOLE3 program by the author has led to a significant increase in efficiency, and hence a reduction in computational cost.

The above relations can be combined to give a single equation for the transition strength S(f-i).

$$\begin{aligned} S(f-i) &= \frac{1}{4}\left[(2J'+1)(2J''+1)\right]\left[(-1)^{J''+J'+1}+(-1)^{p'+p''}\right]^2 \\ &\times \left[\sum_{\nu=-1}^{+1}\sum_{k=p''}^{J''} a(k+\nu,k)(-1)^k \begin{pmatrix} J' & 1 & J'' \\ -\nu-k & \nu & k \end{pmatrix} \sum_{\alpha\beta\gamma} c^{J'p'l'}_{k'\alpha\beta\gamma} c^{J''p''l''}_{k''\alpha\beta\gamma} \mu^m_\nu(\alpha\beta\gamma)\right]^2, \end{aligned} \tag{3.56}$$

where $\underline{c}^{JMpl}$ is the value of the wavefunction of the l^{th} state with rotational quantum numbers (J, M, p), at grid point $(\alpha\beta\gamma)$.The coefficient $a(\nu, k)$ is given by

$$\begin{aligned} a(0,k) &= 2^{-\frac{1}{2}}b, \\ a(\pm 1,0) &= \mp 2^{-\frac{1}{2}}b, \\ a(\pm 1,k) &= \mp b \end{aligned} \tag{3.57}$$

where the factor b depends on the embedding used:

$$
\begin{aligned}
b &= 1 && \text{for the standard } r_1 \text{ embedding;} \\
b &= (-1)^{\nu} && \text{for the standard } r_2 \text{ embedding;} \\
b &= (-1)^{d} && \text{for the bisector embedding,} \\
d &= integer(\frac{k+p'}{2}) + integer(\frac{k+\nu+p''}{2}) && (3.58)
\end{aligned}
$$

where the *integer* specifies integer arithmetic rounded towards zero.

3.2 Computational Implementation

The calculation of dipole transitions as outlined above has been implemented by the author in the DIPOLE3 program of Tennyson *et al* [43]. The general algorithm of the dipole calculation is as follows

1. Calculate dipole moment at the radial grid points and angular integration points
2. Begin to loop over k
3. Read in wavefunctions, $d^{J',k',l'}_{\alpha,\beta,j'}$, and transform to common grid, giving $c^{J'p'l'}_{k'\alpha\beta\gamma}$
4. Read in wavefunctions, $d^{J'',k'',l''}_{\alpha,\beta,j''}$, and transform to common grid, giving $c^{J''p''l''}_{k''\alpha\beta\gamma}$
5. Evaluate the following part of line strength equation

$$
a(k+\nu,k)(-1)^k \begin{pmatrix} J' & 1 & J'' \\ -\nu-k & \nu & k \end{pmatrix} \sum_{\alpha\beta\gamma} c^{J'p'l'}_{k'\alpha\beta\gamma} c^{J''p''l''}_{k''\alpha\beta\gamma} \mu^m_\nu(\alpha\beta\gamma)
$$

6. Next k, i.e. **goto** 3
7. Calculate S($f-i$) by completing the evaluation of line strength equation (3.56)
8. Calculate A_{if} and $I(\omega_{if})$ (equations (3.60) and (3.61)) and output transitions

This new algorithm is significantly more efficient then that by Lynas-Gray *et al* [88], which uses the expression for the transition strength, S($f-i$), (3.56) given below using

DVR[2]-FBR[1] wavefunctions and the function $b_{\gamma,\nu}^{\alpha,\beta}$ gives the value of the dipole moment for a given α,β, γ and ν.

$$\begin{aligned} S(f-i) &= \frac{1}{4}\left[(2J'+1)(2J''+1)\right] \\ &\times \left[\sum_{\nu=-1}^{+1}\sum_{\gamma=|\nu|}^{J''}\sum_{k=p''}\sum_{j''j'}[(-1)^{J''+J'+1}+(-1)^{p''+p'}]a(\nu,\nu+k,\gamma)[(2j'+1)(2j''+1)]^{\frac{1}{2}}\right. \\ &\times \begin{pmatrix} J' & 1 & J'' \\ -\nu-k & \nu & k \end{pmatrix}\begin{pmatrix} j' & \gamma & j'' \\ 0 & 0 & 0 \end{pmatrix}\begin{pmatrix} j' & \gamma & j'' \\ -\nu-k & \nu & k \end{pmatrix} \\ &\times \left.\sum_{\alpha\beta} b_{\gamma,\nu}^{\alpha,\beta} \times c_{k'j'\alpha\beta}^{J'p'l'} c_{k''j''\alpha\beta}^{J''p''l''}\right]^2 \end{aligned} \tag{3.59}$$

The Lynas-Gray *et al* expression has an extra summation compared to the new expression (3.56). The new form of dipole transition integral can now be expressed in the most computationally efficient form, that is $\sum_I \psi_i(I)\mu(I)\psi_f(I)$, where I runs over integration points. Thus the line strength is calculated simply by summing over grid points of the bra wavefunctions times the dipole operator times the ket wavefunctions. In addition the new expression removes the angular coupling in the Lynas-Gray *et al* expression. This is particularly useful for parallelisation as the whole wavefunction can be split across processors, not just the radial portion (refer to section 5.6).

3.3 Einstein A-coefficient

The Einstein A-coefficient, A_{if} may be calculated from the line strength, S(f − i), as given by equation (3.56),

$$A_{if} = \frac{64\pi^2}{3c^3h}\omega^3\frac{S(f-i)g_i}{2J'+1} \tag{3.60}$$

where ω_{if} is the frequency of the transition, g_i is the nuclear degeneracy factor for lower level, c is the speed of light in a vacuum, and h is Plank's constant.

3.4 Integrated absorption coefficient

The integrated absorption coefficient, $I(\omega_{if})$, in cm^{-3} per molecule can be calculated as a function of frequency, ω_{if},

$$I(\omega_{if}) = \frac{(4.162034\ \text{cm}^{-2}\ \text{Debye}^{-2}) \times 10^{-19}\omega_{if}g_i[\exp(E''/kT) - \exp(E'/kT)]}{Q(T)}S(f-i) \tag{3.61}$$

where T is the temperature, $Q(T)$ is the partition function of the molecule, E' and E'' are the energies of the upper and lower levels respectively, and g_i is the nuclear degeneracy factor for the level.

Chapter 4

H_3^+ low-lying states: Applications

There are a number of important applications for H_3^+ calculations, many of these applications are on going. One such application is deuterium chemistry in the interstellar medium. This has had renewed interest of late, due in part to recent observations of multiply deuterated species in the interstellar medium [38–40]. The cosmic abundance of deuterium with respect to hydrogen at low temperature is approximately 1.4×10^{-5} in the solar neighbourhood [89], but a much higher ratio is observed between molecules and their deuterium baring isotopomers in some environments. The process which leads to enhanced abundance of deuterium baring isotopomers is know as deuterium fractionation. This effect is thought to be primarily through reactions with H_2D^+. Modelling of interstellar deuterium chemistry by Roberts *et al* [90] suggest that all the deuterated H_3^+ isotopomers, not only H_2D^+, have an effect on fractionation. In fact under certain conditions D_3^+ becomes the dominant ion [91]. That is the inclusion of D_3^+ and D_2H^+ enhances fractionation significantly [91]. The deuteration of H_3^+ to form the isotopomers is exothermic dues to differences in zero point energies.

Both theoretical and experimental progress can be made if cooperation exists between theorists and experimentalists; this cooperation can be an important diagnostic tool. To this end a number of calculations have been performed to aid experiment.

Unless otherwise stated all calculations in this chapter use the DVR3D program suite of Tennyson *et al* [43] and the ultra-high accuracy *ab initio* potential energy surface of Polyansky and Tennyson [2] which was based on the electronic structure calculations of Cencek *et al* [54]. The Jacobi coordinate system (r_1, r_2, θ) with the body-fixed z-axis

Table 4.1: Parameters, in atomic units, for the Morse oscillator-like functions used for the radial grid in DVR3D [18].

	r_1			r_2		
	r_e	D_e	ω_e	r_e	D_e	ω
H_3^+	2.1	0.1	0.0118	1.71	0.26	0.009
H_2D^+	1.71	0.1	0.0108	1.65	0.215	0.00895
D_2H^+	1.83	0.09	0.0081	1.62	0.17	0.0105
D_3^+	1.78	0.12	0.009	1.48	0.2	0.009

taken along the r_1 coordinate was used (see figure 2.6). The DVR grid size was 20, 21, and 36 for the r_1, r_2 and θ coordinates respectively. These grids were based on the use of Morse oscillator-like functions for the r_1 and r_2 coordinates, the parameters used are given in table 4.1. Associate Legendre polynomials were used for the angular coordinate. For the vibrational step, a final Hamiltonian of dimension 4000 was used in all cases. For the rotational step a final Hamiltonian of dimension 350×(J+1) was used unless otherwise stated. Vibrational reduced masses of 1.0075372 u and 2.0138140 u were used for hydrogen and deuterium respectively [2]. The rotational masses used for hydrogen and deuterium were 1.00727647 u and 2.0135532 u respectively [2] which correspond to the nuclear masses. Using the above parameters it has been shown that known transition frequencies in the low energy regime can be reproduced to with a few hundredth of a cm^{-1}.

4.1 Zero point energies

The zero point energies of H_3^+ and its isotopomers are needed to accurately model reaction dynamics (see section 4.3). It is believed that H_3^+ in the interstellar medium is the primary driver of ion-molecule chemistry and thus is important in the evolution of both dense and diffuse molecular clouds. In addition, ion-molecule reactions at low temperatures of the isotopomers of H_3^+ lead to enhanced abundances of other deuterium baring molecules with respect to their non-deuterated forms. Thus the H_3^+ isotopomers are important in modelling these molecular clouds. The formation of the isotopomers of H_3^+ is exothermic due to differences in zero point energies.

The zero point energies were calculated by finding the global minimum for the potential energy surface of Polyansky and Tennyson [2] (refer to section 2.3). The calculated

Table 4.2: Comparison of vibrational zero point energies for deuterated H_3^+. Δ(zpe) is the change in zero point energy relative to the lowest $J = 1, K = 1$ level of H_3^+.

Isotopomer	Zero point energy [cm^{-1}]			Δ(zpe) [K]
	Carney	Jensen *et al*	This work	This work
H_3^+	4345.3		4361.7	0.0
H_2D^+	3963.0	3993.3	3978.1	−644.2
D_2H^+	3547.5	3571.5	3561.4	−1243.8
D_3^+	3099.8		3112.3	−1890.0

zero point energies for H_3^+, H_2D^+, D_2H^+, and D_3^+ are presented, table 4.2. The zero point energies which were calculated were compared to the previous work of Carney [92] and Jensen *et al* [93].

4.2 Partition functions

The internal partition functions, z_{int} for H_3^+, D_3^+ and D_2H^+ were computed by explicitly summing the series:

$$z_{int} = \sum_i (2J+1) g_i \exp\left(-\frac{c_2 E_i}{T}\right) \tag{4.1}$$

where J is the rotational quantum number, g_i is the nuclear spin degeneracy factor for state i, c_2 is the second radiation constant and E_i is the associated energy level relative to the $J = 0$ ground state in cm^{-1}. No distinction was made between rotational and vibrational energy levels. H_3^+ has only one bound electronic bound state, thus there was no electronic contribution to the partition functions. All the H_3^+ energy levels were taken relative to the $J = 0$ vibrational ground state. The partition function of H_2D^+ was not calculated as it had been previously calculated along with H_3^+ by Sidhu *et al* [7]. The partition function of H_3^+ was calculated again in this work for the purposes of comparison with that of Sidhu *et al.*

The full partition function, z_{tot} can be written as

$$z_{tot} = z^{trans} z_{int} \tag{4.2}$$

where z_{int} is the internal partition function. The translational contribution to the partition function, z^{trans}, can be estimated using the perfect gas model as all the reactions considered conserve the number of particles in the system. The ratio of their translational partition functions is given by a simple mass factor [94]

$$\frac{z_C^{trans} z_D^{trans}}{z_A^{trans} z_B^{trans}} = \left(\frac{m_C m_D}{m_A m_B}\right)^{3/2} \tag{4.3}$$

where m_X is the mass of species X.

A total of $40\times(J+1)$ energy levels were computed for each J, up to J=14. This procedure gave at least 19119 rotation-vibration energy levels for each molecule and ensured that all energy levels up to 10000 cm^{-1} were included.

D_2H^+ has $C_{2\nu}$ symmetry, this symmetry is fully represent in the DVR3D program by the parity of the basis, q, even and odd; which means that energies with even (g_e =3) and odd (g_o =6) parity are easily identified. H_3^+ and D_3^+ have D_{3h} symmetry, this symmetry is not fully represented by the DVR3D program. Thus energies with E, A_1 and A_2 cannot be so easily identified. The A_1 and A_2 states are represented by DVR3D and have even and odd basis parity respectively. The E symmetry energies are determined by the fact that they are degenerate across even and odd basis parities. The E symmetry states can be identified by hand by examining the complete list of energy levels for both even and odd basis parities. For H_3^+ the nuclear degeneracy factors are 2, 0 and 4 for E, A_1 and A_2 respectively. For D_3^+ the nuclear degeneracy factors are 8, 10 and 1 for E, A_1 and A_2 respectively.

Table 4.3 presents the values obtained by the explicit summation of equation (4.1). It was found that at a temperature of 800 K the inclusion of the J=14 energy levels contributed only 0.02%, 0.77% and 0.35% to the internal partition functions for H_3^+ and D_3^+ and D_2H^+ respectively. Therefore the partition functions are valid up to a temperature of 800 K.

Comparing the H_3^+ partition functions of this work and that of Sidhu *et al* (figure 4.1) we see that the two works are in good agreement. There is some minor disagreement at higher temperatures where in any case the much more comprehensive partition function of Neale and Tennyson [8] should be used. Neale and Tennyson used all levels lying up to 15000 cm^{-1} with $J \leq 20$ so that the partition function could be reliably used to a temperature of 10000 K. Figure 4.2 shows the partition functions of D_2H^+ and D_3^+. There is no data for which this can be compared, but the good agreement shown in figure 4.1 indicates that these partition functions will show similar accuracy.

The partition functions have been fitted to the standard formula, see Irwin [95], in the temperature range 5 K to 800 K using the data in table 4.3. The coefficients a_n for H_3^+ , D_3^+ and D_2H^+ are tabulated in table 4.4.

Table 4.3: Calculated internal partition functions as a function of temperature to 4 significant figures. Powers of ten given in parenthesis

T(K)	H_3^+	D_3^+	D_2H^+
5	5.832(−8)	10.00	6.001
10	6.349(−4)	10.24	6.128
20	0.0826	12.57	7.885
30	0.4654	16.38	11.12
40	1.148	21.19	15.09
50	2.020	26.96	19.59
60	2.995	33.60	24.58
70	4.024	40.99	30.03
80	5.083	49.03	35.92
90	6.158	57.62	42.22
100	7.246	66.73	48.93
150	12.90	118.67	87.61
200	19.10	179.79	133.61
300	33.39	325.28	243.78
400	50.06	498.79	375.3
500	68.97	701.12	527.3
600	90.18	936.59	701.6
700	113.1	1211.29	901.1
800	140.7	1531.36	1129.6

$$\log_{10}(z) = \sum_{n=0}^{6} a_n (\log_{10} T)^n \tag{4.4}$$

Our fit is never more than 1.35%, 0.78%, and 1.22% from the calculated values of z for H_3^+, D_3^+ and D_2H^+ respectively.

It is interesting to note that the partition functions of each molecule tends towards the nuclear spin degeneracy factor of the lowest state in the low temperature limit. This is zero for H_3^+, as the energy levels were taken relative to the Pauli forbidden rotational ground state for which $g_i = 0$. This should be considered when this partition function is used.

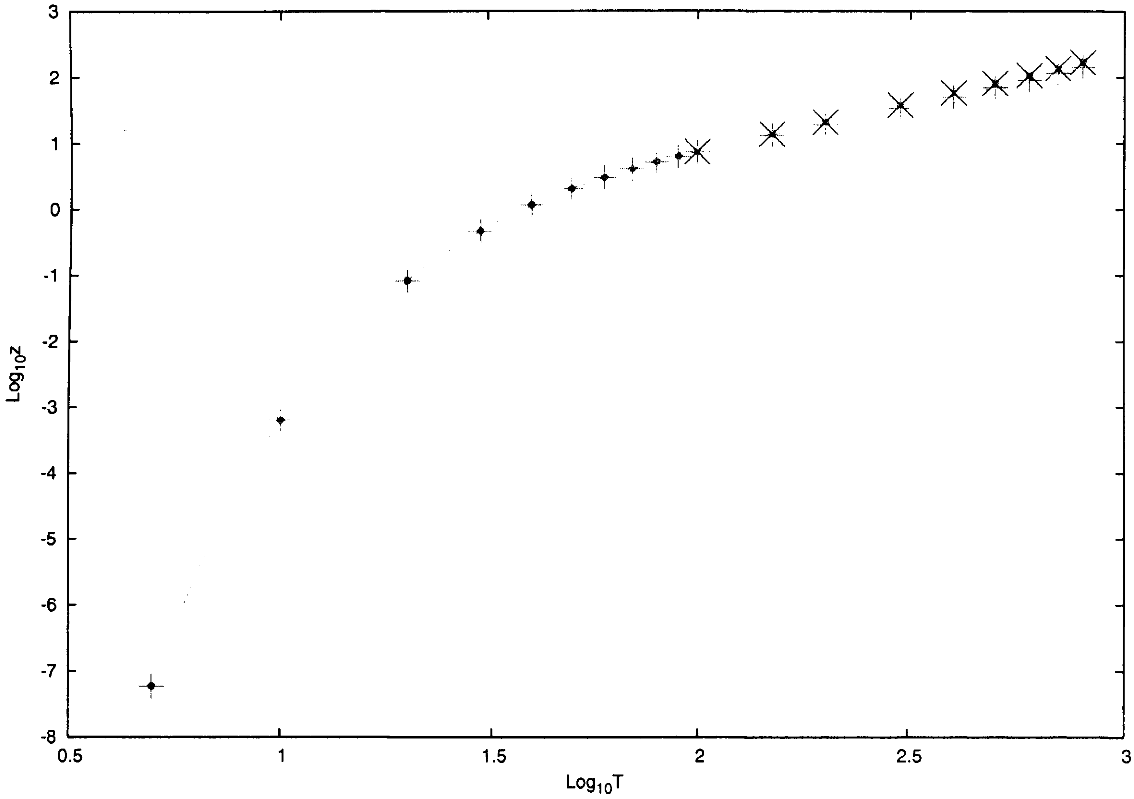

Figure 4.1: H_3^+ partition function, z as a function of temperature, T. *Crosses*, this calculation; *dashed curve*, fit of equation (4.4) to our calculated data; *Circles*, calculation of Sidhu *et al* [7]; *Pluses*, calculation of Neale and Tennyson [8].

	H_3^+	D_3^+	D_2H^+
a_0	−35.10102	−0.388363	−0.975341
a_1	72.2463	5.65495	7.92203
a_2	−66.3543	−8.53925	−13.5834
a_3	35.3938	5.83071	11.0576
a_4	−11.3756	−1.74965	−4.45541
a_5	2.06118	0.205985	0.890251
a_6	−0.160957	−0.00289176	−0.0704028

Table 4.4: Fitting coefficients for the polynomial fit (equation 4.4) to the partition functions of H_3^+, D_3^+ and D_2H^+in the temperature range 5 K to 800 K.

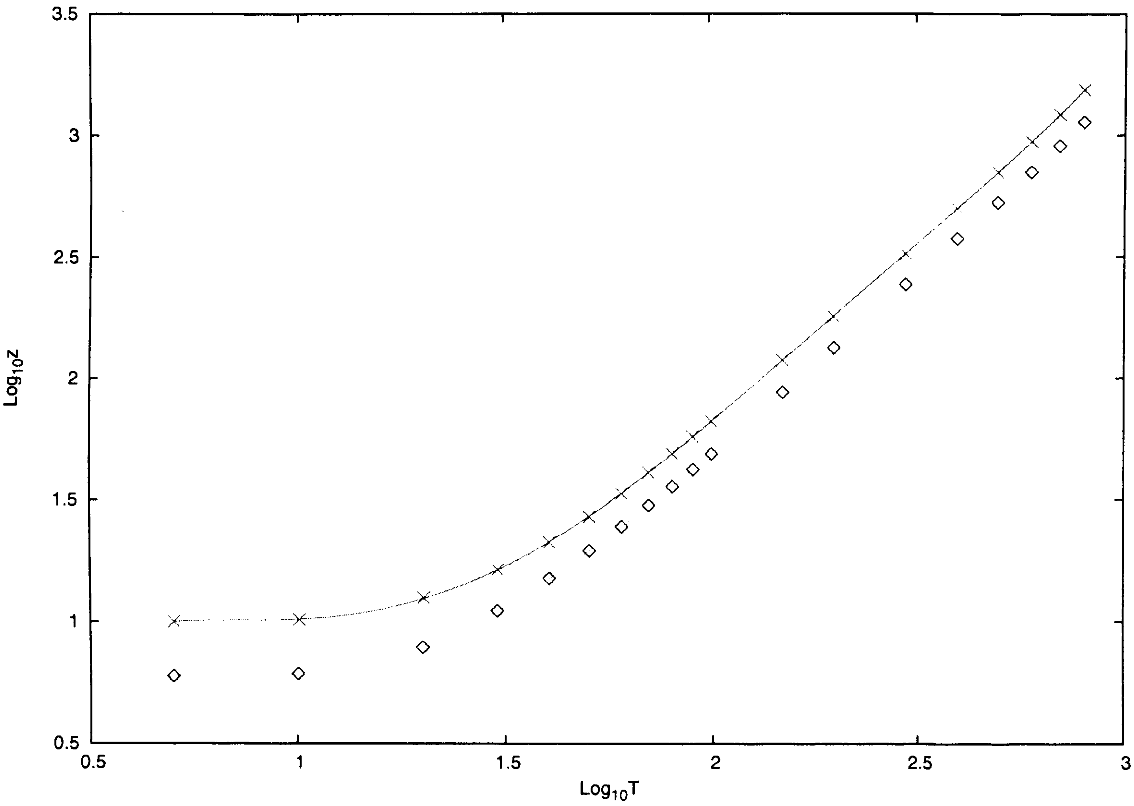

Figure 4.2: D_2H^+ and D_3^+ partition functions, z, as a function of temperature, T. *Diamonds*, D_2H^+ calculation; *dashed curve*, fit of equation (4.4) to D_2H^+ data; *crosses*, D_3^+ calculation; *solid curve*, fit of equation (4.4) to D_3^+ data.

4.3 Reaction Constants

Hydrogenic gas phase reactions involving H_3^+ and the deuterated isotopomers that are regarded to be significant in gas phase deuteration are tabulated in table 4.5. Within the thermodynamic equilibrium regime, the equilibrium constants, K, of these reactions can be calculated from the partition functions and zero point energies of the reactant and product species. It is not possibly to separate the forward and backward rates in these calculations thus comparisons can only been made to the ratio of the forward, k_f, and backward, k_b, rates.

$$K = \frac{k_f}{k_b} \tag{4.5}$$

For reaction

$$\mathrm{A + B \rightarrow C + D} \tag{4.6}$$

the temperature dependent equilibrium constant, $K(T)$, was calculated using the fol-

Table 4.5: The energy released, ΔE, for the reactions of interest

	Reaction	ΔE / K
(a)	$H_3^+ + D \rightarrow H_2D^+ + H$	−597.8
(b)	$H_3^+ + HD \rightarrow H_2D^+ + H_2$	−231.8
(c)	$H_2D^+ + HD \rightarrow D_2H^+ + H_2$	−187.2
(d)	$D_2H^+ + HD \rightarrow D_3^+ + H_2$	−233.8
(e)	$H_3^+ + D_2 \rightarrow H_2D^+ + HD$	−153.0
(f)	$H_3^+ + D_2 \rightarrow D_2H^+ + H_2$	−340.2
(g)	$H_2D^+ + D_2 \rightarrow D_2H^+ + HD$	−108.4
(h)	$H_2D^+ + D_2 \rightarrow D_3^+ + H_2$	−342.2
(i)	$D_2H^+ + D_2 \rightarrow D_3^+ + HD$	−155.0

lowing,

$$K = \frac{z^C_{tot} z^D_{tot}}{z^A_{tot} z^B_{tot}} \exp\left(-\frac{\Delta E}{kT}\right) \tag{4.7}$$

where z_{tot} is the partition function incorporating translational motion and ΔE is the energy released in the reaction. The value ΔE was calculated using

$$\Delta E = E^C_\circ + E^D_\circ - E^A_\circ - E^B_\circ \tag{4.8}$$

where $E^X_\circ$ is the zero point energy of species X as measured on an absolute energy scale. Thus the ΔE for reactions (b) to (i) were calculated in this way. The diatomic zero point energies were calculated using the constants of Huber and Herzberg [19] (table 4.6) and equation 4.12. The zero point energies of H_3^+ and isotopomers were taken from table 4.2. The ground state for H_3^+ is forbidden by the Pauli principle; The lowest state, $J = 1$, $K = 1$, lies some 64.123 cm^{-1} above this ground state. Thus for H_3^+ the so called "rotational zero point energy" was used, which is 4425.823 cm^{-1}. For reaction (a) the difference in ionisation energy between H and D was taken to be 46.4 K [96].

The diatomic partition functions needed for the equilibrium constants were calculated using the formulae given below.

$$z = \sum_{\nu,J} (2J+1) g_J \exp\left(-\frac{F_\nu + G_\nu - G_0}{kT}\right) \tag{4.9}$$

where

$$F_\nu = B_\nu J(J+1) - D_e J^2 (J+1)^2, \tag{4.10}$$

$$B_v = B_e = \alpha_e(\nu + \tfrac{1}{2}), \tag{4.11}$$

$$G_\nu = \omega_e(\nu + \tfrac{1}{2}) - \omega_e x_e (\nu + \tfrac{1}{2})^2 \tag{4.12}$$

Table 4.6: Constants in cm^{-1} used to calculate diatomic partition functions taken from Huber and Herzberg [19]

	H_2	D_2	HD
B_e	60.853	30.443	45.655
α_e	3.06	1.0786	1.986
D_e	0.0471	0.01141	0.02605
ω_e	4401.21	3115.50	3813.15
$\omega_e x_e$	121.33	61.82	91.65
g_e	1	6	6
g_o	3	3	6

The constants used were taken from Huber and Herzberg [19] and are tabulated in table 4.6.

Table 4.7 gives the equilibrium constants, K, for the reactions tabulated in table 4.5 as a function of temperature. The equilibrium constants were calculated using the partition functions previously discussed (section 4.2). The H_2D^+ partition function was taken from Sidhu *et al* [7].

Experiments measuring both the forward and backward rates for the reactions of interest have been conducted by Adams and Smith [21], Giles *et al* [20] and most recently by Gerlich *et al* [97]. Both Adams and Smith and Giles *et al* used a variable temperature selected ion flow arrangement [98], while Gerlich *et al* used a low temperature multipole ion trap.

There have been few experiments where both the forward and backward reaction rates of interest have been measured; so that the equilibrium constant may be deduced for comparison. A comparison of the experimental data available to date is given in tables 4.8, 4.9 and 4.10. Our calculations generally show approximate agreement with the experimental data. The notable exception is the recent experiment of Gerlich *et al* [97] for the H_3^++ HD $\rightarrow$ H_2D^++H_2, which disagrees with our calculations by 12 orders of magnitude (table 4.10). Gerlich *et al* measured the forward and backward rates at a low temperature, 10 K, using a low temperature multipole ion trap. There have been no other experiments carried out at this low temperature, thus no other direct experimental comparison can be made. Smith and Adams using standard extrapolation give an equilibrium constant of $1.7\times10^{+9}$ at 10 K, which is in better agreement with our own result. The previously calculated value of Sidhu *et al* used a ΔE of 139.5 K, this ΔE

Table 4.7: Equilibrium constants, $\log_{10}(K)$, for the reactions given in table 4.5 as a function of temperature. The first line corresponds to reactants while the second line corresponds to products.

T (K)	H_3^++D	H_3^++HD	H_2D^++HD	D_2H^++HD	H_3^++D_2	H_3^++D_2	H_2D^++D_2	H_2D^++D_2	D_2H^++D_2
	H_2D^++H	H_2D^++H_2	D_2H^++H_2	D_3^++H_2	H_2D^++HD	D_2H^++H_2	D_2H^++HD	D_3^++H_2	D_3^++HD
5	59.1951	26.5161	16.1410	19.6059	20.5256	36.6666	10.1505	29.7564	13.6154
10	29.2007	12.4148	8.0189	9.4544	9.8455	17.8644	5.4496	14.9040	6.8851
20	14.1069	5.2661	4.0622	4.3690	4.4023	8.4645	3.1984	7.5674	3.5052
30	9.3591	3.1640	2.5237	2.6552	2.8620	5.3857	2.2218	4.8770	2.3533
40	7.0102	2.1462	1.7791	1.8049	2.1178	3.8969	1.7507	3.5556	1.7765
50	5.6306	1.5816	1.3426	1.3131	1.7047	3.0473	1.4657	2.7787	1.4361
60	4.7257	1.2337	1.0659	0.9998	1.4456	2.5115	1.2777	2.2776	1.2117
70	4.0858	0.9997	0.8802	0.7841	1.2668	2.1471	1.1473	1.9314	1.0512
80	3.6116	0.8337	0.7465	0.6256	1.1377	1.8842	1.0505	1.6760	0.9296
90	3.2462	0.7093	0.6456	0.5030	1.0398	1.6854	0.9761	1.4792	0.8335
100	2.9563	0.6122	0.5664	0.4045	0.9632	1.5296	0.9174	1.3219	0.7555
150	2.1009	0.3270	0.3283	0.0973	0.7441	1.0724	0.7454	0.8426	0.5143
200	1.6813	0.1816	0.2021	-0.0694	0.6415	0.8436	0.6620	0.5925	0.3904
300	1.2660	0.0311	0.0676	-0.2472	0.5457	0.6133	0.5822	0.3350	0.2674
400	1.0602	-0.0445	-0.0014	-0.3386	0.5062	0.5048	0.5493	0.2108	0.2122
500	0.9374	-0.0893	-0.0421	-0.3927	0.4914	0.4493	0.5387	0.1460	0.1880
600	0.8569	-0.1179	-0.0687	-0.4274	0.4904	0.4217	0.5397	0.1123	0.1810
700	0.7999	-0.1380	-0.0866	-0.4507	0.4967	0.4101	0.5481	0.0974	0.1840
800	0.7579	-0.1523	-0.0997	-0.4668	0.5076	0.4079	0.5602	0.0934	0.1931

does not take into account the previously discussed rotational zero point energy. Thus if a ΔE of 231.8 K is used then an equilibrium constant of $7.1\times10^{+12}$, which is more consistent to our own is obtained. At this low temperature only a few energy levels are thermodynamically available. Thus the theoretical calculation of the reaction constant uses only a few low lying states which for the triatomic species are determined to within a few hundredth of a cm^{-1} [2]. Therefore it is difficult to see how our calculation could be incorrect by several orders of magnitude. It seems more likely that the source of the discrepancy is with the experiment. These sources could be that other processes are occurring in the experiment which have not be accounted for or the experiment not being in thermodynamic equilibrium. This is one of the most important reactions with regard to fractionation in the interstellar medium. Most theoretical models of the interstellar medium use the value of either Adams and Smith [21] or Giles *et al* [20]. These models have shown good agreement with observation [90, 99], which is difficult to imagine if the reaction constant of Gerlich *et al* is used.

A comparison of our equilibrium constants with those of Giles *et al* [20] for the reactions of interest are shown in table 4.8. Giles *et al* give relative errors of ± 15% for the equilibrium constants. This values is much lower then the related absolute values on the measured rates; Giles *et al* state that certain systematic errors will cancel when taking the ratio of rates, thus producing lower error bounds. This may be rather optimistic. In general there is better agreement between our calculation and the experiment of Giles *et al* at the higher temperature of 300 K. This is most likely due to the less demanding nature of measuring the reaction rates as higher temperature. Giles *et al* also calculate the equilibrium constants by calculating the partition functions of the reactant and product species, and the ΔE for the reaction. These partition functions were obtained by explicitly summing the energy levels (as equation 4.1) calculated using the rigid rotor approximation and the relevant experimentally determined rotational constants. The rigid rotor approximation is problematic for the H_3^+ system and definitely inferior to our own *ab initio* energy level calculations. However we are generally in better agreement with theoretical equilibrium constants of Giles *et al* than their experimentally derived equilibrium constants.

A comparison of equilibrium constants for the reaction $H_3^+ + HD \rightarrow H_2D^+ + H_2$ to those of Adams and Smith [21] and Herbst [22] for a number of temperatures are given in table 4.9. Adams and Smith estimate their errors on the reaction rates to be ±20%, this gives an error on the equilibrium constants of ±30%. We are generally in good agreement with Adams and Smith. Herbst calculated the reaction constants using his calculated partition functions and ΔE. The partition functions for H_3^+ and H_2D^+ are determined from explicitly doing the sum as in equation 4.1. The energy levels are found by using the spectroscopic constants of Oka [100, 101] and Carney [92] respectively. The constants of Huber and Herzberg [19] were used to calculate the partition functions of HD and H_2. Our calculations are in reasonable agreement with the cruder calculations of Herbst.

The reliability of our equilibrium constants are determined by the quality of the partition functions used. The approximate model used to calculate the diatomic partition functions begins to fail at higher energies; The reliability *ab initio* energy levels used to calculate the triatomic partition functions can also be regarded to decrease with energy. Therefore as energy levels of higher energy become more important at higher temperatures the reliability of the partition functions for both the diatomic and triatomic species are more reliable at low temperatures. Hence the reliability of equilibrium constants decreases with temperature.

4.4 Transitions for Observation

Renewed interest in deuterium chemistry has led to many attempts to observe deuterated species in the interstellar medium [39]; including attempts to observe the deuterated species of H_3^+. This has led to an increase in the demand for synthetic spectra to aid observation. To this end the Einstein A_{if} coefficients of the dipole transitions have been calculated.

The dipole transition intensities for D_3^+, D_2H^+ and H_2D^+ are given in tables 4.13, 4.12 and 4.11 respectively; transitions are given up to $J = 5$ and a maximum frequency of 5000 cm^{-1}; transitions whose relative intensity is less than 0.0001 are neglected. The D_3^+ energy levels are labelled by the notation (ν_1, ν_2, J, G, U) [102]. The quantum numbers ν_1, ν_2, G and U were assigned by referring to the work of [103] and by inspection. The H_2D^+ and D_2H^+ levels are assigned by hand using the standard quantum numbers J, K_a, and K_c.

Table 4.8: A comparison of our Equilibrium constants with those of Giles *et al* [20].

	80K			**300K**		
	Giles *et al* (Expt)	Giles *et al* (Theory)	This work	Giles *et al* (Expt)	Giles *et al* (Theory)	This work
$H_3^+ + HD \rightarrow H_2D^+ + H_2$	3.8 (±0.6)	6.6	6.82	1.80 (±0.3)	2.0	1.07
$H_2D^+ + HD \rightarrow D_2H^+ + H_2$	1.7 (±0.3)	3.6	5.58	0.80 (±0.1)	0.8	1.17
$D_2H^+ + HD \rightarrow D_3^+ + H_2$	1.8 (±0.3)	2.0	4.22	0.40 (±0.1)	0.3	1.00
$H_3^+ + D_2 \rightarrow H_2D^+ + HD$	8.2 (±1.2)	13.2	13.73	5.20 (±0.8)	6.7	3.51
$H_3^+ + D_2 \rightarrow D_2H^+ + H_2$	9.2 (±1.4)	48.3	76.59	5.30 (±0.8)	5.1	4.10
$H_2D^+ + D_2 \rightarrow D_2H^+ + HD$	4.4 (±0.7)	7.2	11.23	1.90 (±0.3)	2.5	3.82
$H_2D^+ + D_2 \rightarrow D_3^+ + H_2$	4.4 (±0.7)	14.5	47.43	0.70 (±0.1)	0.8	2.16
$D_2H^+ + D_2 \rightarrow D_3^+ + HD$	1.7 (±0.3)	4.0	8.50	0.80 (±0.1)	1.0	1.85

Table 4.9: A comparison of Equilibrium constants with Adams and Smith [21] and Herbst [22] for the reaction H_3^++ HD → H_2D^++ H_2.

T(K)	Adams and Smith	Herbst	This work
80	4.48 (±1.3)	5.9	6.82
200	2.35 (±0.7)	2.6	1.52
295	1.96 (±0.6)	2.1[a]	1.07[a]

a. The theoretical value is actually at 300 K

Table 4.10: A comparison of Equilibrium constants at a temperature of 10 K for the reaction H_3^++ HD → H_2D^++ H_2. Powers of ten given in parenthesis.

This Work	2.6(+12)
Gerlich *et al* [97]	7.14
Adams and Smith [21]	1.5(+9)[a]
Sidhu *et al*[7]	7.1(+12)[b]

a. This value is extrapolated from experimental data

b. This value uses the corrected ΔE of 231.8 K

Table 4.11: Einstein A_{if} coefficients for transitions from low-lying levels of H_2D^+. Powers of ten given in parenthesis.

J'	K_a'	K_c'		E' / cm^{-1}	J''	K_a''	K_c''		E'' / cm^{-1}	ω_{if}(calc.) / cm^{-1}	ω_{if}(obs.) / cm^{-1}	A_{if} / s^{-1}
1	1	0	B_1	72.457	1	1	1	A_1	60.027	12.429	-	1.219(-4)
1	0	1	A_2	45.698	0	0	0	A_1	0.000	45.698	-	4.040(-3)
2	1	2	A_2	138.843	1	1	1	A_1	60.027	78.816	-	1.876(-2)
2	0	2	A_1	131.638	1	0	1	A_2	45.698	85.94	-	3.034(-2)
2	1	1	B_1	175.939	1	1	0	B_1	72.457	103.483	-	4.238(-2)
2	2	0	A_1	223.868	1	0	1	A_2	45.698	178.17	-	1.664(-2)
0	0	0	A_1	2205.916	1	0	1	A_2	45.698	2160.218	2160.176[a]	17.545
1	1	0	B_1	2278.465	1	1	1	A_1	60.027	2218.438	2218.393[a]	10.372
1	0	1	A_2	2246.727	0	0	0	A_1	0.000	2246.727	2246.697[a]	1.896
2	0	2	A_1	2318.377	1	0	1	A_2	45.698	2272.68	-	0.352
0	0	0	A_2	2335.338	1	1	1	A_1	60.027	2275.31	2275.403[a]	145.65
1	0	1	A_1	2383.878	1	1	0	B_1	72.457	2311.421	2311.512[a]	83.419
1	1	0	B_1	2409.227	1	0	1	A_2	45.698	2363.529	-	78.984
2	2	0	A_1	2427.119	1	0	1	A_2	45.698	2381.421	2381.367[a]	3.058

continued...

Table 4.11: ...continued

1	1	1	A_2	2402.699	0	0	0	A_1	0.000	2402.699	2402.795[a]	60.938
2	0	2	A_2	2477.681	1	1	1	A_1	60.027	2417.654	2417.734[a]	29.82
2	1	2	A_1	2490.966	1	0	1	A_2	45.698	2445.268	2445.348[a]	58.586
2	2	1	B_1	2568.382	1	1	0	B_1	72.457	2495.925	2496.014[a]	60.067
2	2	0	A_2	2569.489	1	1	1	A_1	60.027	2509.461	2509.541[a]	48.476
0	0	0	A_1	2992.524	1	0	1	A_2	45.698	2946.826	2946.802[b]	53.167
1	1	0	B_1	3063.331	1	1	1	A_1	60.027	3003.304	3003.276[b]	27.509
1	0	1	A_2	3038.198	0	0	0	A_1	0.000	3038.198	3038.177[b]	20.353
2	1	2	A_2	3128.888	1	1	1	A_1	60.027	3068.86	3068.845[b]	20.088
2	0	2	A_1	3123.324	1	0	1	A_2	45.698	3077.626	3077.611[b]	24.757
2	1	1	B_1	3167.147	1	1	0	B_1	72.457	3094.69	3094.671[b]	19.302
2	2	0	A_1	3209.847	1	0	1	A_2	45.698	3164.149	-	1.598
0	0	0	A_1	4287.61	1	0	1	A_2	45.698	4241.912	-	16.953
1	0	1	A_2	4331.45	0	0	0	A_1	0.000	4331.45	-	9.631
2	1	2	A_2	4412.461	1	1	1	A_1	60.027	4352.434	4352.360[c]	14.871
2	0	2	A_1	4407.925	1	0	1	A_2	45.698	4362.227	-	15.450
0	0	0	A_2	4461.832	1	1	1	A_1	60.027	4401.805	-	88.628
2	1	1	A_2	4512.486	1	0	1	A_2	45.698	4466.788	-	0.413
1	1	0	B_1	4536.348	1	0	1	A_2	45.698	4490.65	-	44.342
2	0	2	A_2	4555.88	1	1	1	A_1	60.027	4495.853	4495.881[c]	27.013
1	1	1	A_2	4512.558	0	0	0	A_1	0.000	4512.558	4512.567[c]	41.115
2	1	2	A_1	4563.405	1	0	1	A_2	45.698	4517.707	-	38.458
0	0	0	A_1	4602.746	1	0	1	A_2	45.698	4557.048	-	69.044
2	2	1	B_1	4677.548	1	1	0	B_1	72.457	4605.091	-	38.831
1	2	1	B_1	4677.74	1	1	1	A_1	60.027	4617.713	-	33.563
2	2	0	A_2	4691.531	1	1	1	A_1	60.027	4631.504	-	20.198
1	0	1	A_2	4657.859	0	0	0	A_1	0.000	4657.859	-	9.007
2	0	2	A_1	4761.399	1	0	1	A_2	45.698	4715.701	-	7.752
2	2	0	B_1	4845.211	1	0	1	A_2	45.698	4799.514	-	1.335
0	0	0	A_1	5039.84	1	0	1	A_2	45.698	4994.142	-	10.723

a. Frequencies of Foster *et al* [104]

b. Frequencies of Kozin *et al* [105]

c. Frequencies of Fárník *et al* [23]

Table 4.12: Einstein A_{if} coefficients for transitions from low-lying levels of D_2H^+. Powers of ten given in parenthesis.

J'	K'_a	K'_c		E' / cm^{-1}	J''	K''_a	K''_c		E'' / cm^{-1}	ω_{if}(calc.) / cm^{-1}	ω_{if}(obs.) / cm^{-1}	A_{if} / s^{-1}
1	1	0	B_1	57.993	1	0	1	A_1	34.918	23.075	-	5.091(-4)
1	1	1	A_2	49.255	0	0	0	A_1	0.000	49.255	-	3.303(-3)
2	0	2	A_1	101.716	1	1	1	A_2	49.255	52.461	-	2.070(-3)
2	1	2	A_2	110.259	1	0	1	A_1	34.918	75.341	-	1.060(-2)
2	2	1	B_1	179.173	1	1	0	B_1	57.993	121.18	-	4.450(-2)
2	2	0	A_1	182.074	1	1	1	A_2	49.255	132.819	-	4.463(-2)
0	0	0	A_1	1968.146	1	1	1	A_2	49.255	1918.89	1918.908[a]	52.175
1	0	1	A_1	1998.523	1	1	0	B_1	57.993	1940.53	1940.551[a]	21.990
1	1	0	B_1	2027.034	1	0	1	A_1	34.918	1992.116	1992.130[a]	28.480
2	0	2	A_1	2055.077	1	1	1	A_2	49.255	2005.821	2005.844[a]	6.089
1	1	1	A_2	2014.09	0	0	0	A_1	0.000	2014.09	2014.106[a]	14.364
2	1	2	A_2	2062.923	1	0	1	A_1	34.918	2028.005	2028.024[a]	9.981
0	0	0	A_2	2078.435	1	0	1	A_1	34.918	2043.517	2043.515[a]	21.728
1	1	1	A_1	2128.7	1	1	0	B_1	57.993	2070.707	2070.708[a]	16.782
1	1	0	A_2	2136.248	1	1	1	A_2	49.255	2086.992	2086.990[a]	12.135
2	2	1	B_1	2145.612	1	1	0	B_1	57.993	2087.619	2087.630[a]	11.233
2	2	0	A_1	2149.555	1	1	1	A_2	49.255	2100.299	2100.307[a]	5.992
1	0	1	A_2	2118.589	0	0	0	A_1	0.000	2118.589	2118.588[a]	14.303
2	1	2	A_1	2202.779	1	1	1	A_2	49.255	2153.524	2153.525[a]	21.901
2	0	2	A_2	2194.064	1	0	1	A_1	34.918	2159.146	2159.145[a]	19.827
2	1	1	B_1	2225.161	1	1	0	B_1	57.993	2167.168	2167.166[a]	17.293
2	2	0	A_2	2257.594	1	0	1	A_1	34.918	2222.675	-	0.387
0	0	0	A_1	2736.98	1	1	1	A_2	49.255	2687.724	-	86.183
1	0	1	A_1	2771.523	1	1	0	B_1	57.993	2713.53	-	44.856
1	1	0	B_1	2793.96	1	0	1	A_1	34.918	2759.042	2759.036[b]	44.572
1	1	1	A_2	2785.338	0	0	0	A_1	0.000	2785.338	2785.332[b]	31.182
2	0	2	A_1	2837.556	1	1	1	A_2	49.255	2788.3	2788.300[b]	16.939
2	1	2	A_2	2845.72	1	0	1	A_1	34.918	2810.802	2810.800[b]	29.412
2	2	1	B_1	2912.708	1	1	0	B_1	57.993	2854.716	2854.707[b]	29.321
2	2	0	A_1	2915.616	1	1	1	A_2	49.255	2866.36	2866.350[b]	22.136
0	0	0	A_1	3821.309	1	1	1	A_2	49.255	3772.054	-	6.594
1	0	1	A_1	3851.977	1	1	0	B_1	57.993	3793.984	-	5.085

continued...

Table 4.12: ...continued

1	1	0	B_1	3881.727	1	0	1	A_1	34.918	3846.809	3846.786[c]	3.326
2	0	2	A_1	3909.933	1	1	1	A_2	49.255	3860.677	3860.660[c]	3.048
1	1	1	A_2	3871.398	0	0	0	A_1	0.000	3871.398	3871.377[c]	3.666
2	1	2	A_2	3921.988	1	0	1	A_1	34.918	3887.07	3887.052[c]	5.426
2	2	1	A_1	4010.528	1	1	0	B_1	57.993	3952.535	-	3.641
2	2	0	A_1	4013.18	1	1	1	A_2	49.255	3963.924	-	3.451
0	0	0	A_1	4042.815	1	1	1	A_2	49.255	3993.56	3993.518[c]	47.457
1	0	1	A_1	4058.521	1	1	0	B_1	57.993	4000.528	4000.494[c]	42.900
0	0	0	A_2	4060.822	1	0	1	A_1	34.918	4025.904	4025.873[c]	41.465
2	0	2	A_1	4097.094	1	1	1	A_2	49.255	4047.839	4047.840[c]	21.275
1	1	1	A_2	4062.925	0	0	0	A_1	0.000	4062.925	4062.889[c]	29.138
2	1	2	A_1	4097.933	1	0	1	A_1	34.918	4063.015	4062.983[c]	26.675
1	1	0	A_2	4101.122	1	0	1	A_1	34.918	4066.204	4066.158[c]	23.775
1	0	1	B_1	4119.147	1	1	1	A_2	49.255	4069.891	4069.859[c]	20.300
2	2	1	B_1	4179.804	1	1	0	B_1	57.993	4121.811	-	24.474
1	1	1	A_2	4122.993	0	0	0	A_1	0.000	4122.993	-	1.369(-3)
2	0	2	A_1	4214.033	1	1	1	A_2	49.255	4164.777	-	5.765
2	2	0	A_2	4208.006	1	0	1	A_1	34.918	4173.088	-	0.922
2	1	2	A_1	4229.853	1	1	1	A_2	49.255	4180.597	-	2.424
2	2	1	A_2	4252.4	1	0	1	A_1	34.918	4217.482	-	1.391
0	0	0	A_1	4648.808	1	1	1	A_2	49.255	4599.553	-	10.723
1	0	1	A_1	4673.469	1	1	0	B_1	57.993	4615.476	-	9.138
0	0	0	A_2	4674.96	1	0	1	A_1	34.918	4640.042	-	13.692
2	0	2	A_1	4720.562	1	1	1	A_2	49.255	4671.307	-	4.699
1	1	0	B_1	4706.784	1	0	1	A_1	34.918	4671.866	-	4.944
1	1	1	A_2	4681.85	0	0	0	A_1	0.000	4681.85	-	7.138
1	1	0	A_1	4732.173	1	1	1	A_2	49.255	4682.918	-	6.999
2	1	2	A_2	4723.648	1	0	1	A_1	34.918	4688.73	-	6.633
1	0	1	A_2	4727.065	0	0	0	A_1	0.000	4727.065	-	0.447
2	2	1	B_1	4796.924	1	1	0	B_1	57.993	4738.931	-	6.783
2	2	0	A_1	4798.798	1	1	1	A_2	49.255	4749.542	-	2.177
2	0	2	A_2	4807.782	1	0	1	A_1	34.918	4772.864	-	0.875
2	0	0	B_1	4852.274	1	0	1	A_1	34.918	4817.356	-	0.503

a. Frequencies of Polyansky and McKellar [106]

b. Frequencies of Kozin *et al* [105]

c. Frequencies of Fárník *et al* [23]

4.5 Telescope proposals

4.5.1 Roueff *et al*

It was proposed to observe H_2D^+ and D_2H^+ in a young stellar object. A line strength calculation on the isotopomers H_2D^+ and D_2H^+ in the infrared was carried out for a telescope proposal at United Kingdom Infra-Red Telescope (UKIRT), sited in Hawaii. The principal investigator was Evelyne Roueff of the Observatoire de Paris. The data calculated is shown in tables 4.14 and 4.15. The proposal was awarded 25 hours of telescope time in semester 03A in 2003.

The H_2D^+ transition $1_{11} \leftarrow 0_{00}$ from table 4.14 shows the greatest intensity, thus this transition was chosen for the observation. Observations were carried out on the young stellar object RAFGL7009S. RAFGL7009S is a deeply embedded massive young stellar object with an estimated kinematic distance of 3.0 kpc [107]. Unfortunately bad weather hampered observations; Figure 4.3 shows the spectrum from the best observational run. The radial velocity of the molecular material is approximately 41.5 km s^{-1} [108, 109]. Therefore the H_2D^+ transition $1_{11} \leftarrow 0_{00}$ should occur at approximately 4.1615 μm. It is clear from figure 4.3 that there is no spectral feature near that wavelength. Evelyne Roueff has been awarded a further 25 hours, 5 nights, of telescope time during semester 04A, 2004 (Patt No: u/04a/58).

4.5.2 Ceccarelli *et al*

Walmsley *et al* [91] suggest that under certain conditions in the interstellar medium D_3^+ becomes the dominant ion.

Cecilia Ceccarelli of the Laboratoire d'Astrophysique de l'Observatoire de Grenoble hopes to observe D_3^+ in the interstellar medium. To assist in the observations, *ab initio* calculations were made to determine the transitions which may be good candidates for observation. The typical temperature of the interstellar medium was assumed to be 10 K.

Energy levels up to J=4 were computed. A synthetic spectrum was produced at 10 K up to a frequency of 5000 cm^{-1}, transitions whose relative intensities were less than 0.0001 were neglected. Absolute intensities, $I(\omega_{if})$, and Einstein coefficients A_{if} were

Table 4.13: Einstein A_{if} coefficients for transitions from low-lying levels of D_3^+

J'	$\nu_1'\nu_2'$	G'	U'		E' / cm^{-1}	J'	$\nu_1''\nu_2''$	G''	U''		E'' / cm^{-1}	ω_{if}(calc.) / cm^{-1}	ω_{if}(obs.)^a / cm^{-1}	A_{if} / s^1
0	01	1	1	E'	1834.655	1	00	1	0	E''	32.324	1802.331	1802.349	264.18
1	01	0	-1	A_2''	1884.380	1	00	0	0	$A1'$	43.609	1840.770	1840.789	34.99
1	01	1	1	E'	1878.561	1	00	1	0	E''	32.324	1846.237	1846.256	141.96
1	01	0	1	A_1''	1888.048	0	00	0	0	A_1'	0.000	1888.048	1888.065	252.84
2	01	1	-1	E'	1955.981	1	00	1	0	E''	32.324	1923.657	1923.670	107.50
2	01	0	1	A_2''	1979.203	1	00	0	0	A_2'	43.609	1935.593	1935.609	24.65
2	01	1	1	E'	1968.077	1	00	1	0	E''	32.324	1935.753	-	119.38
1	02	3	2	A_2'	3646.285	1	00	0	0	A_1'	43.609	3602.676	3602.669	234.05
0	02	2	2	E'	3650.700	1	00	1	0	E''	32.324	3618.376	3618.371	231.47
2	02	4	2	E'	3662.342	1	00	1	0	E''	32.324	3630.018	3630.022	140.29
1	02	-3	-2	A_1''	3647.190	0	00	0	0	A_1'	0.000	3647.190	-	193.96
1	02	2	2	E'	3694.893	1	00	1	0	E''	32.324	3662.569	3662.557	114.64
2	02	-3	2	A_2''	3736.400	1	00	0	0	A_2'	43.609	3692.791	3692.785	17.29
2	02	2	2	E'	3783.234	1	00	1	0	E''	32.324	3750.909	3750.879	23.66

a. Frequencies of Amano *et al* [103]

Table 4.14: Infra-Red transitions for H_2D^+

$JK'_aK'_c \leftarrow JK''_aK''_c$	Vibration	E'/cm^{-1}	E''/cm^{-1}	ω_{if}/cm^{-1}	A_{if} / s^{-1}
101 ← 000	v_1	0.000	3038.198	3038.198	20.353
101 ← 000	v_2	0.000	2246.727	2246.727	1.896
111 ← 000	v_3	0.000	2402.699	2402.699	60.937
000 ← 101	v_1	2992.524	45.698	2946.826	53.167
000 ← 101	v_2	2205.916	45.698	2160.218	17.545
202 ← 101	v_1	45.698	3123.324	3077.626	24.758
220 ← 101	v_2	45.698	2427.119	2381.421	3.058

Table 4.15: Infra-Red transitions for D_2H^+

$JK'_aK'_c \leftarrow JK''_aK''_c$	Vibration	E'/cm^{-1}	E''/cm^{-1}	ω_{if}/cm^{-1}	A_{if} / s^{-1}
111 ← 000	v_1	0.000	2785.338	2785.338	31.182
111 ← 000	v_2	0.000	2014.090	2014.090	14.364
101 ← 000	v_3	0.000	2118.589	2118.589	14.303
110 ← 101	v_1	34.918	2793.960	2759.042	44.572
110 ← 101	v_2	34.918	2027.034	1992.116	28.480
212 ← 101	v_1	34.918	2845.720	2810.802	29.412
212 ← 101	v_2	34.918	2062.923	2028.005	9.981

calculated using the partition function described in section 4.2 and assigning symmetry labels by hand [102]. The data calculated is shown in table 4.16.

The 1888.048 cm^{-1} line provides the greatest intensity. However it lies just outside the M window, which ranges from approximately 2050 cm^{-1} to 2260 cm^{-1}. This will make ground based observations of this transition difficult; however it still remains the best candidate for observation.

4.6 Fárník *et al*

Transitions to the overtone $2\nu_2$ and $2\nu_3$, and combination $\nu_2+\nu_3$ vibrations in jet cooled H_2D^+ and D_2H^+ ions were measured for the first time by high-resolution IR spectroscopy [23]. The ion beams were produced in a pulsed, slit jet supersonic discharge. This produces beams of densities $10^{10}/cm^3$ which are rotationally cool. Using a continuous wave Ar^+ (488nm or 514.5nm) laser with dye (R6G) lasers which gives a resolution of $4\times10^{-7}Hz^{-1/2}$. Absorption measurements were also made to determine relative line strengths to an accuracy of approximately 10% (tables 4.17 and 4.18).

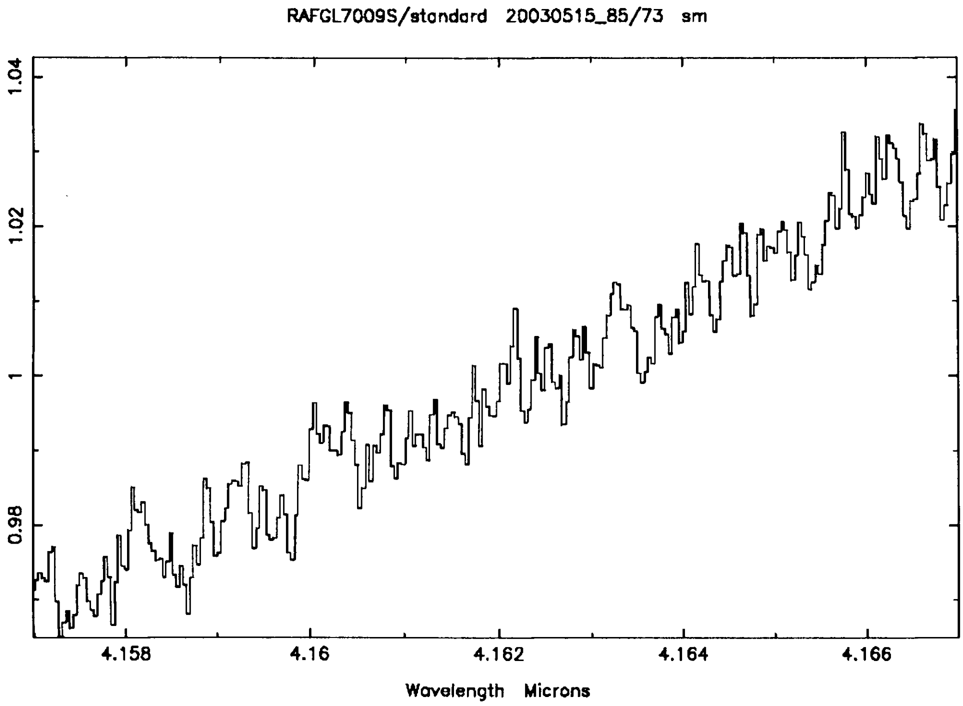

Figure 4.3: Attempted spectrum of H_2D^+ 1_{11}-0_{00} transition at 4.1618 μm at a resolution 10 km s^{-1} from the source RAFGL7009S recorded by Thomas Geballe of the Gemini Observatory in Hilo on UKIRT

Fárník *et al* [23] found that there was some disagreement in observed and calculated line strength transitions for overtone transitions of H_2D^+ and D_2H^+. The source of these disagreements was suggested to be unconverged wavefunctions. It is known that dipole calculations are especially sensitive to the convergence of the wavefunction; excellent agreement was found between theory and experiment with the energy levels. Thus it was thought that the convergence of the *ab initio* calculations in Fárník *et al* should be tested.

As the calculations are variational, performing a new calculation with a larger Hamiltonian size, a variational parameter, should improve convergence. The DVR grid consisted of 20 r_1 points, 21 r_2 points, and 36 θ points. The size of the final Hamiltonian matrix was 2000 by 2000. A comparison of these results are shown in tables 4.17 and 4.18. It is clear that there is no substantial difference and the ratios of observed and calculated line strengths remain unchanged between the two calculations. Thus from these results it may be deduced that convergence was not the source of the line strength discrepancy.

Table 4.16: Transitions of D_3^+ at 10 K, for $J = 0$ to 4 up to a frequency of 5000 cm^{-1}. Einstein coefficients, A_{if} and absolute intensities, $I(\omega_{if})$ are explicitly calculated using the nuclear spin factors given by the symmetry assignment of energy levels. Powers of ten given in parenthesis.

J″	J′	E″/cm^{-1}		E′/cm^{-1}		ω_{if}/cm^{-1}	S(f←i) / D^2	Abs I(ω_{if}))	A_{if} / s^{-1}
0	1	1834.655	E	32.324	E	1802.331	1.4387(-1)	1.0075(-19)	264.176
1	1	1884.380	A_2	43.609	A_2	1840.770	5.3668(-2)	7.5685(-21)	34.994
1	1	1878.561	E	32.324	E	1846.237	2.1578(-1)	1.5479(-19)	141.960
1	0	1888.048	A_1	0.000	A_1	1888.048	3.5935(-1)	2.7590(-17)	252.840
2	1	1955.980	E	32.324	E	1923.657	2.4074(-1)	1.7993(-19)	107.488
2	1	1979.203	A_2	43.609	A_2	1935.593	5.4185(-2)	8.0351(-21)	24.647
2	1	1968.076	E	32.324	E	1935.753	2.6236(-1)	1.9733(-19)	119.368
1	1	3646.284	A_2	43.609	A_2	3602.676	4.7880(-2)	1.3215(-20)	234.048
0	1	3650.700	E	32.324	E	3618.376	1.5578(-2)	2.1901(-20)	231.440
2	1	3662.342	E	32.324	E	3630.018	4.6759(-2)	6.5950(-20)	140.288
1	0	3647.189	A_1	0.000	A_1	3647.190	3.8243(-2)	5.6720(-18)	193.960
1	1	3694.893	E	32.324	E	3662.569	2.2321(-2)	3.1764(-20)	114.640
2	1	3736.400	A_2	43.609	A_2	3692.791	5.4737(-3)	1.5486(-21)	17.289
2	1	3783.234	E	32.324	E	3750.909	7.1482(-3)	1.0418(-20)	23.662
1	0	4111.558	A_1	0.000	A_1	4111.558	4.1335(-5)	6.9110(-21)	0.300

4.7 McNab Experiment

The spectrum of H_3^+ has been reasonably well studied in the low energy regime and has also been well established by Carrington *et al* in the near-dissociation regime. However an area which has remained largely unexplored is that region between the low energy and the near dissociation; that is the region about 20000 cm^{-1}. Iain McNab of the University of Newcastle aimed to perform an ion beam experiment in this region. To aid this we have calculated a synthetic spectrum for D_2H^+.

Energy Levels up to $J = 7$ were computed. The synthetic spectrum was produced at 600 K. Absolute intensities were calculated using the partition function of H_2D^+ + 50% from Sidhu *et al* [7]. The synthetic spectrum is shown in figure 4.4

From figure 4.4 it is clear that H_2D^+ spectrum shows little intensity above approximately a frequency 5000 cm^{-1}; Even below 5000 cm^{-1} there are regions of very low intensity. Thus it would be advisable for the apparatus to be tuned to the areas of the spectrum highest in intensity where measurements would be easiest and good noise to signal ratios obtained.

Table 4.17: Observed line intensities of Fárník *et al*[23] and their deviation form calculated values for D_2H^+

		Fárník *et al*				[23]	This work			
$JK'_aK'_c \leftarrow JK''_aK''_c$		ν_{exp} / cm^{-1}	$S(f\leftarrow i)_{exp}$	$S(f\leftarrow i)_{calc}$	$S_{exp} - S_{calc}$	S_{exp}/S_{calc}	ν_{calc}	$S(f\leftarrow i)_{calc}$	$S_{exp} - S_{calc}$	S_{exp}/S_{calc}
111← 000	$2\nu_2$	3871.3773	6.20(-4)	6.04(-4)	1.63(-5)	1.03	3871.398	0.6044340(-3)	1.59(-5)	1.03
111← 000	$2\nu_3$	4062.8893	4.04(-3)	4.16(-3)	-1.19(-4)	0.97	4062.925	0.4155900(-2)	-1.15(-4)	0.97
202← 111	$2\nu_2$	3860.6596	8.44(-4)	8.44(-4)	-4.59(-5)	0.95	3860.677	0.8443610(-3)	-4.63(-5)	0.95
000← 111	$2\nu_3$	3993.5179	2.39(-3)	2.38(-3)	1.44(-5)	1.01	3993.560	0.2375850(-2)	1.85(-5)	1.01
202← 111	$2\nu_3$	4047.8403	5.27(-3)	5.11(-3)	1.57(-4)	1.03	4047.839	0.5114140(-2)	1.53(-4)	1.03
110← 111	$\nu_2+\nu_3$	4069.8581	2.94(-3)	2.88(-3)	6.12(-5)	1.02	4069.891	0.2880480(-2)	6.07(-5)	1.02
110← 101	$2\nu_2$	3846.7864	7.10(-4)	5.58(-4)	1.52(-4)	1.27	3846.809	0.5588810(-3)	1.51(-4)	1.27
212← 101	$2\nu_2$	3887.0520	1.45(-3)	1.47(-3)	-1.63(-5)	0.99	3887.070	0.1472970(-2)	-1.93(-5)	0.99
000← 101	$\nu_2+\nu_3$	4025.8734	2.12(-3)	2.03(-3)	8.69(-5)	1.04	4025.904	0.2026250(-2)	9.06(-5)	1.04
212← 101	$2\nu_3$	4062.9832	6.16(-3)	6.34(-3)	-1.84(-4)	0.97	4063.015	0.6340630(-2)	-1.85(-4)	0.97
110← 101	$2\nu_3$	4066.1576	3.37(-3)	3.38(-3)	-8.36(-6)	1.00	4066.204	0.3382800(-2)	-1.12(-5)	1.00
101← 110	$2\nu_3$	4000.4940	6.59(-3)	6.41(-3)	1.81(-4)	1.03	4000.528	0.6409550(-2)	1.81(-4)	1.03
211← 110	$\nu_2+\nu_3$	4121.7757	5.42(-3)	5.58(-3)	-1.58(-4)	0.97	4121.811	0.5572020(-2)	-1.50(-4)	0.97
Fundamentals										
111← 000	ν_1	2785.3670	4.70(-2)	1.38(-2)	3.32(-2)	3.41	2785.338	0.1380340(-1)	3.32(-2)	3.41
212← 101	ν_1	2810.8260	1.72(-2)	2.11(-2)	-3.92(-3)	0.81	2810.802	0.2111550(-1)	-3.93(-3)	0.81

Table 4.18: Observed line intensities of Fárník *et al*[23] and their deviation form calculated values for H_2D^+

		Fárník *et al*				[23]	This work			
$JK'_aK'_c \leftarrow JK''_aK''_c$		ν_{exp} / cm^{-1}	$S(f\leftarrow i)_{exp}$	$S(f\leftarrow i)_{calc}$	$S_{exp} - S_{calc}$	S_{exp}/S_{calc}	ν_{calc}	$S(f\leftarrow i)_{calc}$	$S_{exp} - S_{calc}$	S_{exp}/S_{calc}
110← 111	$2\nu_2$	4301.6315	1.08(-3)	1.03(-2)	5.54(-5)	1.05	4301.721	1.03(-3)	5.80(-5)	1.06
212← 111	$2\nu_2$	4352.3589	2.72(-3)	2.88(-3)	-1.55(-4)	0.95	4352.434	2.88(-3)	-1.51(-4)	0.95
202← 111	$\nu_2+\nu_3$	4495.8809	1.42(-3)	4.74(-3)	-3.32(-3)	0.30	4495.853	4.74(-3)	-3.32(-3)	0.30
111← 110	$2\nu_2$	4271.0174	1.75(-3)	1.79(-3)	-3.77(-5)	0.98	4271.096	1.78(-3)	-2.87(-5)	0.98
211← 110	$2\nu_2$	4394.3288	1.66(-3)	1.63(-3)	3.26(-5)	1.02	4394.411	1.63(-3)	2.87(-5)	1.02
101← 110	$\nu_2+\nu_3$	4422.7188	4.72(-3)	6.54(-3)	-1.81(-3)	0.72	4422.711	6.54(-3)	-1.81(-3)	0.72
Fundamentals										
101← 000	ν_1	3038.2200	5.87(-3)	6.95(-3)	-1.07(-3)	0.85	3038.198	6.94(-3)	-1.06(-3)	0.85
202← 101	ν_1	3077.6110	6.12(-3)	1.36(-2)	-7.47(-3)	0.45	3077.626	1.35(-2)	-7.41(-3)	0.45
212← 101	ν_3	2445.3480	2.61(-2)	6.39(-2)	-3.78(-2)	0.41	2445.268	6.39(-2)	-3.78(-2)	0.41
212← 111	ν_1	3068.8450	1.50(-1)	1.11(-2)	3.99(-3)	1.36	3068.860	1.11(-2)	4.01(-3)	1.36
220← 111	ν_3	2509.5410	7.76(-2)	4.89(-2)	2.87(-2)	1.59	2509.461	4.89(-2)	2.87(-2)	1.59
111← 110	ν_1	2978.0450	1.35(-2)	1.05(-2)	2.99(-3)	1.29	2978.059	1.05(-2)	3.00(-3)	1.29
221← 110	ν_3	2496.0140	8.24(-2)	6.16(-2)	2.07(-2)	1.34	2495.925	6.16(-2)	2.07(-2)	1.34
111← 212	ν_1	2911.6350	3.16(-2)	9.35(-2)	-6.19(-3)	0.34	2911.673	9.34(-3)	-6.18(-3)	0.34

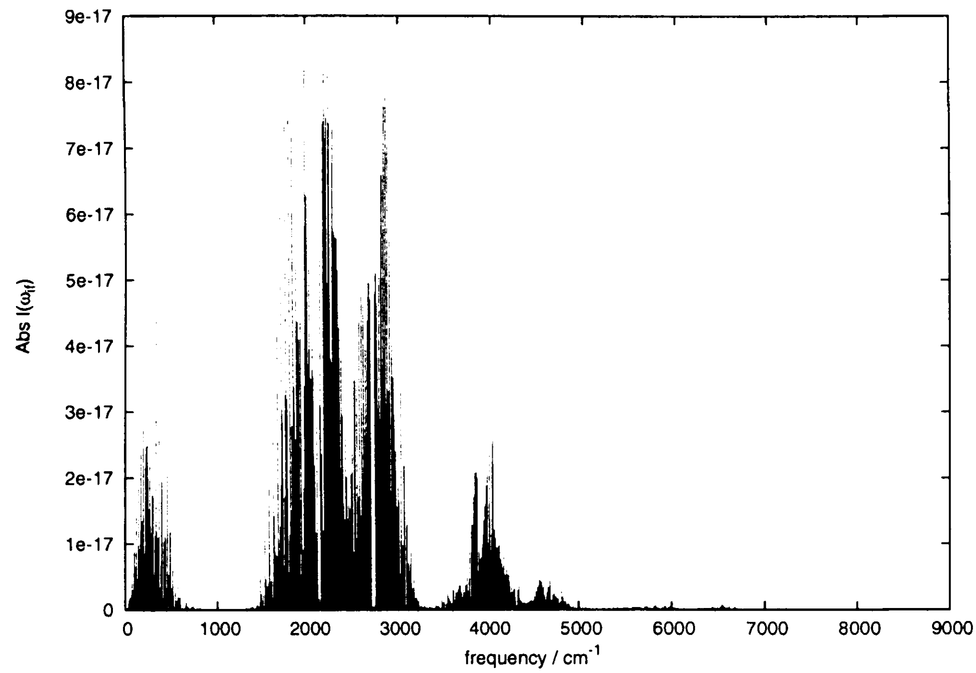

Figure 4.4: *Ab initio* synthetic spectrum of H_2D^+at 600 K, for $J = 0$ to 7. $I(\omega_{if})$ are explicitly calculated using the nuclear spin factors given by the symmetry assignment of energy levels.

4.8 Nesbitt Experiment

H_3^+ represents a very clean acid; the following simple exothermic reaction would enable the quantum states in D_2H^+ to be probed using IR absorption.

$$H_3^+ + D_2 \rightarrow D_2H^+ + H_2 \tag{4.13}$$

David Nesbitt of the University of Colorado looked into the feasibility of performing state resolved proton transfer reaction dynamics with H_3^+ in their IR crossed beam apparatus. As an aid to the feasibility to this study *ab initio* calculations were made of the H_3^+, H_2D^+, D_2H^+ and D_3^+ molecules to determine transitions which may be observed using their IR absorption apparatus.

Energy Levels up to $J = 7$ were computed. The synthetic spectra were produced at 50 K. Absolute intensities were calculated for H_3^+, D_2H^+, and D_3^+ using the partition function from section 4.2. For H_2D^+ the partition function of Sidhu *et al* [7] was used. The synthetic spectra are shown in figures 4.5, 4.6, 4.7, and 4.8

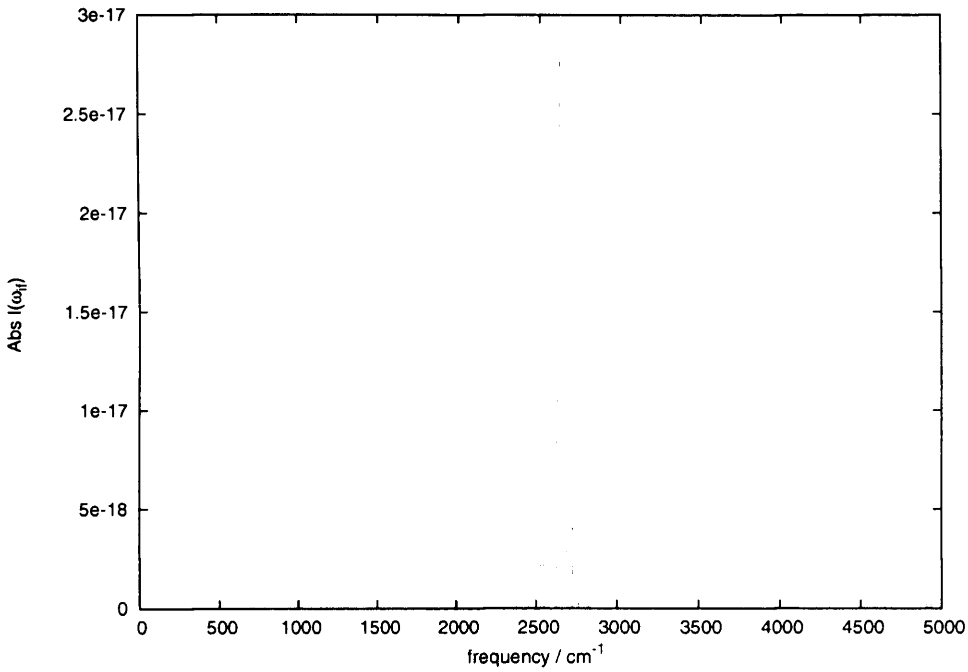

Figure 4.5: *Ab initio* synthetic spectrum of H_3^+ at 50 K, for $J = 0$ to 4 up to a frequency of 5000 cm^{-1}.

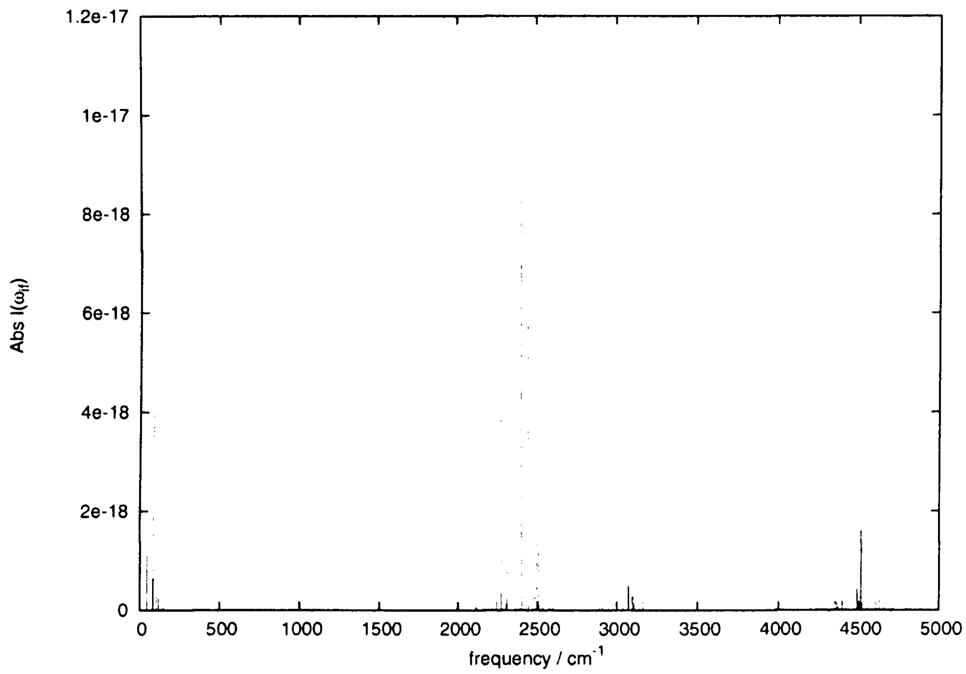

Figure 4.6: *Ab initio* synthetic spectrum of H_2D^+ at 50 K, for $J = 0$ to 4 up to a frequency of 5000 cm^{-1}. $I(\omega_{if})$ are explicitly calculated using the nuclear spin factors given by the symmetry assignment of energy levels.

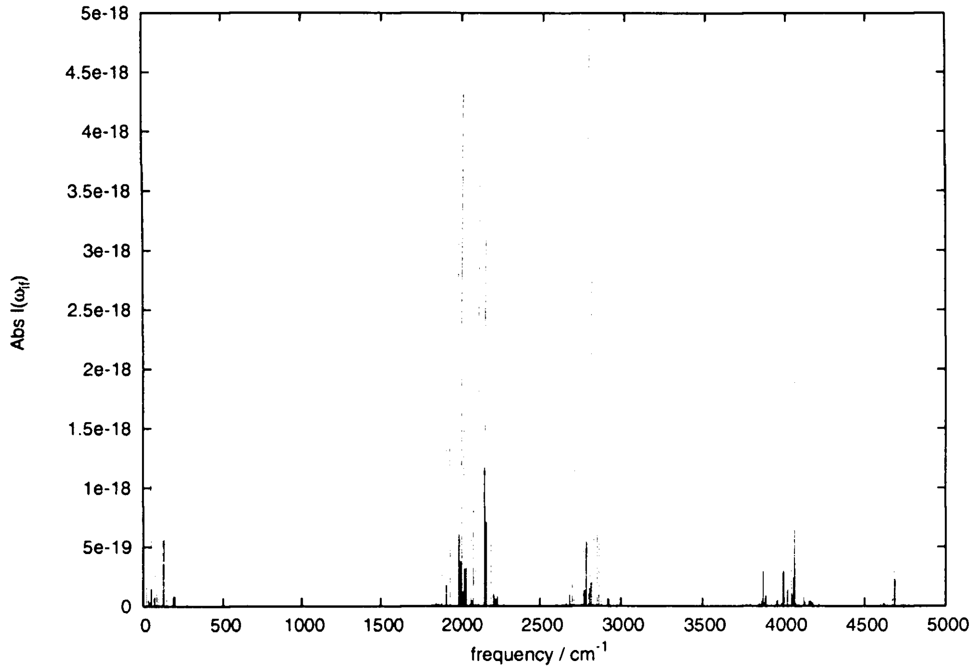

Figure 4.7: *Ab initio* synthetic spectrum of D_2H^+ at 50 K, for $J = 0$ to 4 up to a frequency of 5000 cm^{-1}. $I(\omega_{if})$ are explicitly calculated using the nuclear spin factors given by the symmetry assignment of energy levels.

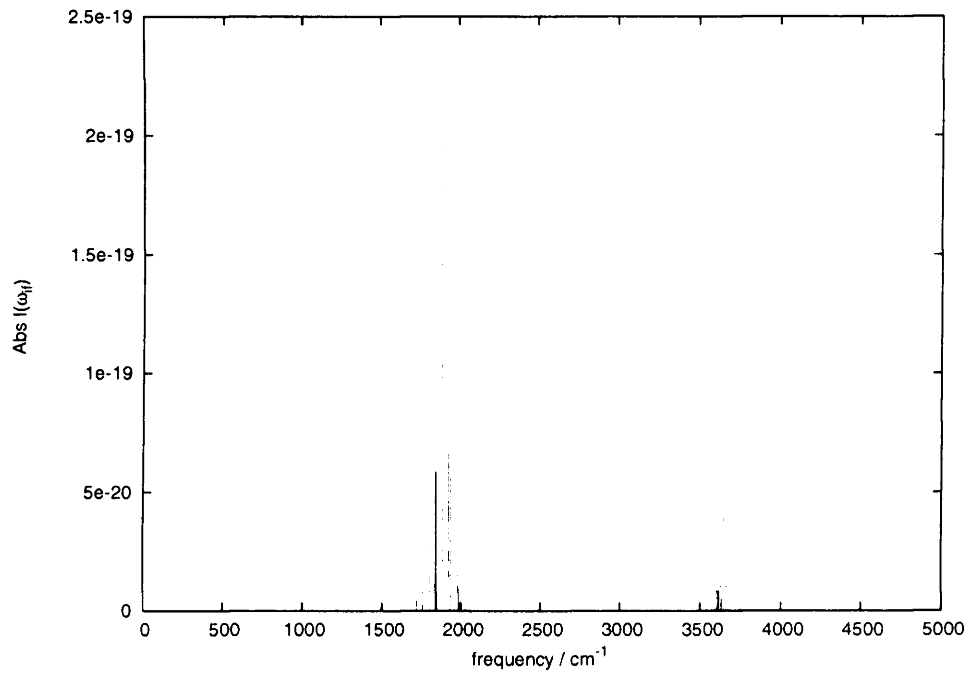

Figure 4.8: *Ab initio* synthetic spectrum of H_3^+ at 50 K, for $J = 0$ to 4 up to a frequency of 5000 cm^{-1}.

Table 4.19: The strongest transitions of D_3^+ at **30 K** in the range 6820 cm^{-1} and 6930 cm^{-1}. Powers of 10 are given in parenthesis.

J″		E″ / cm^{-1}	J′		E′ / cm^{-1}	ω_{if} / cm^{-1}	S(f←i) / D^2	I(ω_{if})	A_{if} / s^{-1}
1	A_1	6865.038	1	A_2	43.609	6821.429	1.722(-5)	3.686(-21)	5.713
0	A_2	6859.664	1	E	32.324	6827.339	5.843(-6)	2.151(-22)	0.583
1	E	6914.978	2	E	85.627	6829.351	1.803(-5)	4.121(-22)	4.803
3	E	6934.339	2	E	85.627	6848.712	2.595(-5)	5.947(-22)	2.987
2	E	6892.375	1	E	32.324	6860.050	1.531(-5)	4.529(-21)	2.479
1	A_2	6870.771	0	A_1	0.000	6870.771	1.092(-5)	1.906(-21)	0.370
1	E	6906.953	1	E	32.324	6874.628	8.428(-6)	2.499(-21)	2.290
2	E	7011.590	2	E	85.627	6925.963	9.093(-6)	2.108(-22)	1.516
2	A_1	6969.995	1	A_2	43.609	6926.386	1.531(-5)	3.328(-21)	3.191

4.9 Ion trap

An attempt to measure populations of D_3^+ in the laboratory of Dieter Gerlich in Chemnitz using an ion trap set-up required *ab initio* spectra to aid observation. In the experiment D_2^+ ions are formed by electron impact in a separate ion source and injected into the trap. D_3^+ is formed as the product of the reaction between the injected D_2^+ ions and D_2 molecules. The D_3^+ ions formed are then probed with a laser. It is hoped that measurement of the population of states of D_3^+ can be made; their dependence on kinetic temperature, temperature of the buffer gas and possibly the ortho/para conversion. The ion trap is cooled to between 6 K and 30K; the laser operates between 6820 cm^{-1} and 6930 cm^{-1}. Thus the strongest transition in this range at a temperature of 30 K were calculated; they are presented in table 4.19.

4.10 Dissociative recombination

Dissociative recombination is the major destruction process of H_3^+ in diffuse interstellar clouds. H_3^+ ions are formed from either the ubiquitous cosmic rays that pervade the universe or stellar radiation. H_3^+ is destroyed by electron recombination,

$$H_3^+ + e^- \rightarrow \begin{array}{c} H + H + H \\ H_2 + H \end{array} \tag{4.14}$$

the rate of the this reaction is given by k_e. During the past 50 years many studies have attempted to determine this reaction rate, k_e, however no agreed value has been found;

often values of k_e disagree over several orders of magnitude. The first measurement of k_e by Biondi and Brown in 1949 [110] gave a value of 2.5×10^{-6} cm^{3}s^{-1}; more recently an experiment by Glosik *et al* in 2001 gives a value of 2×10^{-9} cm^{3}s^{-1} [111]; the value has been as low as below 1×10^{-11} cm^{3}s^{-1} [112, 113]. There have been a number of attempts to measure the rate; however, different experiments have not agreed satisfactorily, especially those between storage ring merged beam experiments and plasma experiments. A possible explanation is based on different vibrational and rotational temperatures, that is vibrational or rotational excited states have a different recombination rate.

4.10.1 Integrated stationary afterglow

An afterglow experiment involves creating a plasma of the species of interest in some inert buffer gas. The time evolution of the plasma can then be monitored to ascertain for example the instance of decay due to recombination, as observed by measuring the electron densities. A stationary afterglow relies on fast detection of the concentration decay, while in the flowing afterglow technique the plasma flows along a flow tube where the concentration decay can be measured along the x-axis. This does not require as fast a detection technique as the stationary afterglow. The typical detector is a Langmuir probe which is on a movable mount for the stationary afterglow. The Langmuir probe technique is satisfactory if all the information required is the electron density and temperature. However is may be desirable to have some knowledge of the quantum states of the ions under study, this requires spectroscopic techniques. Spectroscopic knowledge of the ions would help to resolve the question of differing rates between vibrational and rotational states.

The *Advanced integrated stationary afterglow*, AISA, [114] consists of a vacuum chamber through which the plasma will flow; a Langmuir probe and quadrupole mass spectrometer are used as detectors. A mixture of He, Ar, and H_2 is pumped into the chamber where pulses of microwaves ignite the mixture to create a plasma. Recently a Cavity Ring-Down Spectroscopy, CRDS, probe has been added to the apparatus to resolve the quantum states of the ions. CRDS can be used in three modes. Firstly the discharge is operated continuously and the laser frequency is scanned over the area of interest. From the absorption spectra peaks, the population of the lower energy level can be determined if the strength of the transition is known, for example from *ab initio* calculations. In

Table 4.20: The 10 strongest transitions of D_2H^+ at **100 K** in the range 1 to 1.6 μm (6250 cm^{-1} and 10000 cm^{-1}). Powers of 10 are given in parenthesis.

J″		E″ / cm^{-1}	J′		E′ / cm^{-1}	ω_{if} / cm^{-1}	S(f←i) / D^2	I(ω_{if})	A_{if} / s^{-1}
2	A_2	6570.861	1	A_1	34.918	6535.943	1.303(-4)	2.630(-20)	2.282
1	A_2	6536.301	0	A_1	0.000	6536.301	5.773(-5)	1.926(-20)	1.685
3	A_2	6636.090	2	A_1	101.716	6534.374	1.969(-4)	1.520(-20)	2.461
1	A_1	6524.909	1	B_1	57.993	6466.916	8.531(-5)	1.223(-20)	2.412
1	B_1	6673.664	1	A_2	49.255	6624.409	7.130(-5)	1.187(-20)	2.167
2	A_2	7263.945	1	A_1	34.918	7229.027	4.103(-5)	9.160(-21)	0.972
1	A_2	6661.687	0	A_1	0.000	6661.687	2.677(-5)	9.102(-21)	0.827
2	A_1	6567.766	1	A_2	49.255	6518.511	1.081(-4)	8.852(-21)	1.878
1	B_1	6558.905	1	A_1	34.918	6523.987	4.365(-5)	8.796(-21)	1.267
2	A_2	6745.756	1	A_1	34.918	6710.838	4.124(-5)	8.547(-21)	0.782

the second mode the laser is tuned to a transition and the plasma cavity is pulsed by the microwave discharge to create plasma in pulses. The cavity gets into resonance and ring down occurs, the characteristic time and the time from the nearest microwave pulse are recorded for each ring down. This produces an afterglow time line with absorption and therefore concentration information. The third and final mode is a combination of the other two, A time resolved absorption measurement combined with a scan over frequency. This produces a matrix of absorption values, where each row represents an absorption spectra at a certain time and the columns give the absorption evolution at a certain laser frequency.

To aid this work we calculated the 10 strongest transitions for H_2D^+, D_2H^+, and D_3^+ at a temperature of 100 K and 350 K, tables 4.22 to 4.25. This would help identify possible transition to which the laser could be tuned to look at the time evolution of absorption. The *ab initio* intensity data would also help to estimate the populations of states.

4.10.2 Preliminary experimental results

Some preliminary results for D_3^+ are shown below in table 4.26, and figures 4.11 and 4.12. These results include the first observations of second overtone spectroscopy of D_3^+.

The 6849.110 cm^{-1} transition appears to be significantly better resolved then the 6821.359 cm^{-1} transition. The 6821.359 cm^{-1} transition differs from theory by 0.07

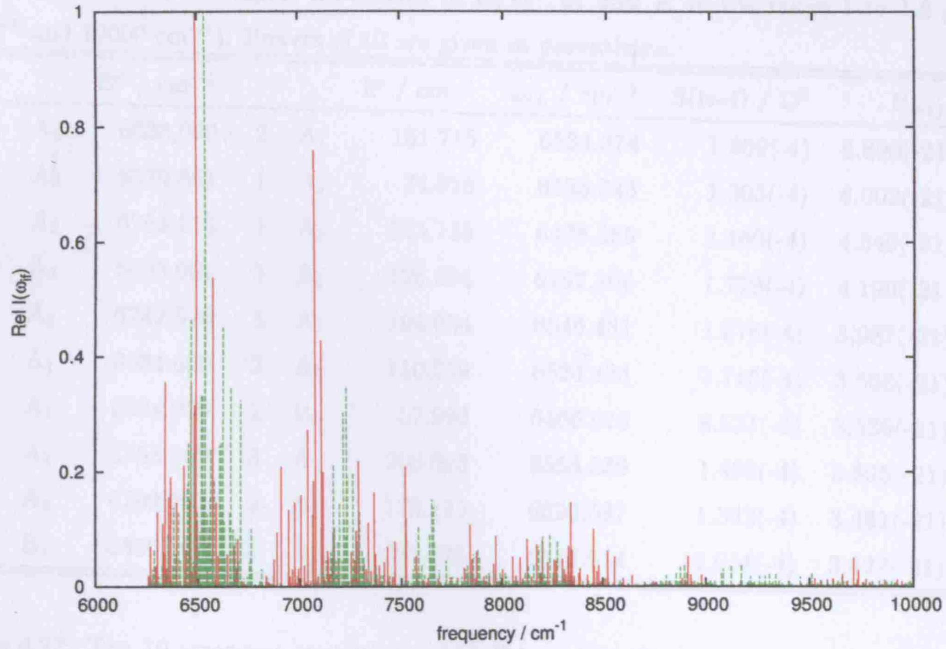

Figure 4.9: *Ab initio* synthetic spectra of H_2D^+ (continuous line) and D_2H^+ (dashed line) at **100 K**, in the range 1 to 1.6 μm (6250 cm^{-1} and 10000 cm^{-1}) up to a frequency of 5000 cm^{-1}.

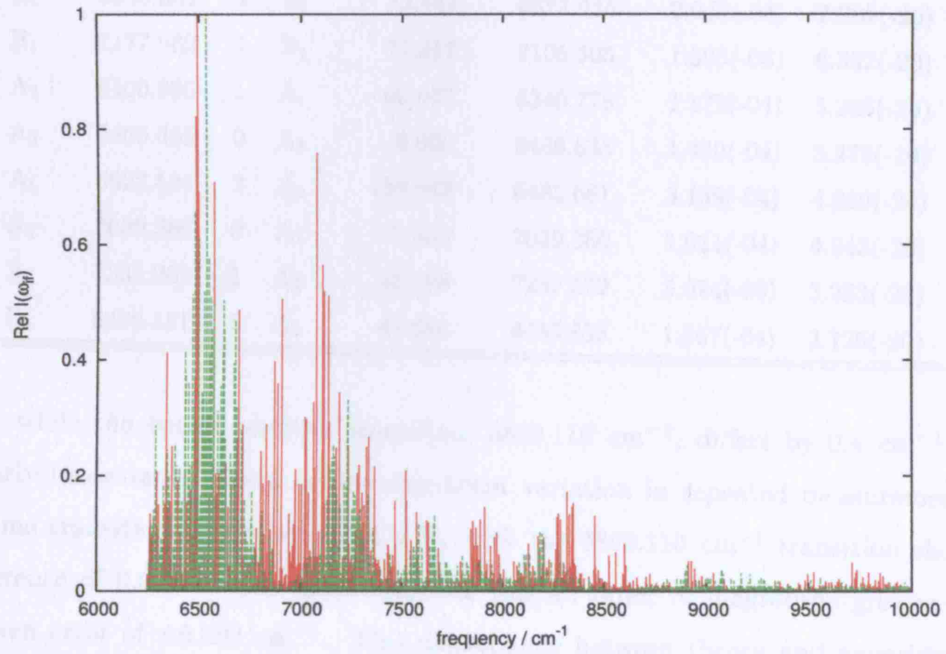

Figure 4.10: *Ab initio* synthetic spectra of H_2D^+ (continuous line) and D_2H^+ (dashed line) at **350 K**, in the range 1 to 1.6 μm (6250 cm^{-1} and 10000 cm^{-1}) up to a frequency of 5000 cm^{-1}.

Table 4.21: The 10 strongest transitions of D_2H^+ at **350 K** in the range 1 to 1.6 μm (6250 cm^{-1} and 10000 cm^{-1}). Powers of 10 are given in parenthesis.

J''		E'' / cm^{-1}	J'		E' / cm^{-1}	ω_{if} / cm^{-1}	S(f←i) / D^2	I(ω_{if})	A_{if} / s^{-1}
3	A_2	6636.090	2	A_1	101.716	6534.374	1.969(-4)	6.890(-21)	2.461
2	A_2	6570.861	1	A_1	34.918	6535.943	1.303(-4)	6.002(-21)	2.282
5	A_2	6794.110	4	A_1	315.725	6478.385	3.160(-4)	4.549(-21)	2.450
4	A_2	6693.901	3	A_1	196.094	6497.806	1.779(-4)	4.199(-21)	1.701
4	A_2	6742.576	3	A_1	196.094	6546.481	1.676(-4)	3.987(-21)	1.639
3	A_1	6634.692	2	A_2	110.259	6524.433	2.115(-4)	3.568(-21)	2.632
1	A_1	6524.909	1	B_1	57.993	6466.916	8.531(-5)	3.536(-21)	2.412
2	A_1	6758.563	3	A_2	200.023	6558.539	1.495(-4)	3.505(-21)	2.645
2	A_2	6799.761	2	B_1	179.173	6620.587	1.342(-4)	3.461(-21)	2.443
4	B_1	6856.267	3	B_1	283.323	6572.944	2.054(-4)	3.427(-21)	2.033

Table 4.22: The 10 strongest transitions of H_2D^+ at **100 K** in the range 1 to 1.6 μm (6250 cm^{-1} and 10000 cm^{-1}). Powers of 10 are given in parenthesis.

J''		E'' / cm^{-1}	J'		E' / cm^{-1}	ω_{if} / cm^{-1}	S(f←i) / D^2	I(ω_{if})	A_{if} / s^{-1}
2	A_1	6537.148	1	A_2	45.698	6491.451	2.614(-04)	1.484(-19)	4.486
2	A_1	7123.258	1	A_2	45.698	7077.560	1.819(-04)	1.126(-19)	4.046
2	B_1	6646.381	1	B_1	72.457	6573.925	2.043(-04)	7.989(-20)	3.640
2	B_1	7177.962	1	B_1	72.457	7105.505	1.503(-04)	6.352(-20)	3.381
0	A_2	6400.805	1	A_1	60.027	6340.778	1.172(-04)	5.285(-20)	9.367
1	A_2	6466.635	0	A_1	0.000	6466.635	1.450(-04)	5.275(-20)	4.100
3	A_1	6622.524	2	A_2	138.843	6483.681	3.159(-04)	4.689(-20)	3.858
1	A_2	7039.366	0	A_1	0.000	7039.366	1.021(-04)	4.043(-20)	3.724
2	A_1	7333.269	1	A_2	45.698	7287.572	5.074(-05)	3.233(-20)	1.232
1	B_1	6479.531	1	A_2	45.698	6433.833	1.667(-04)	3.125(-20)	4.641

cm^{-1}, while the better resolved transition, 6849.110 cm^{-1}, differs by 0.4 cm^{-1}; this is clearly inconstant. There is also significant variation in repeated measurements of the same transitions as shown table 4.26, with the 6849.110 cm^{-1} transition showing a difference of 0.06 between measurements, this an order of magnitude greater than the given error of $\pm$0.002 cm^{-1}. This discrepancy between theory and experiment is contradictory to the results for the overtone and combination band spectroscopy of H_2D^+ and D_2H^+ (section 4.6) where the maximum disagreement is less then 0.1 cm^{-1}. However, if the discrepancy is assumed to be with the theoretical results, then there are

Table 4.23: The 10 strongest transitions of $\mathbf{H_2D^+}$ at **350 K** in the range 1 to 1.6 μm (6250 cm^{-1} and 10000 cm^{-1}). Powers of 10 are given in parenthesis.

J''		E'' / cm^{-1}	J'		E' / cm^{-1}	ω_{if} / cm^{-1}	S(f←i) / D^2	I(ω_{if})	A_{if} / s^{-1}
2	A_1	6537.148	1	A_2	45.698	6491.451	2.614(-4)	1.484(-19)	4.486
2	A_1	7123.258	1	A_2	45.698	7077.560	1.819(-4)	1.126(-19)	4.046
2	B_1	6646.381	1	B_1	72.457	6573.925	2.043(-4)	7.989(-20)	3.640
2	B_1	7177.962	1	B_1	72.457	7105.505	1.503(-4)	6.352(-20)	3.381
0	A_2	6400.805	1	A_1	60.027	6340.778	1.172(-4)	5.285(-20)	9.367
1	A_2	6466.635	0	A_1	0.000	6466.635	1.450(-4)	5.275(-20)	4.100
3	A_1	6622.524	2	A_2	138.843	6483.681	3.159(-4)	4.689(-20)	3.858
1	A_2	7039.366	0	A_1	0.000	7039.366	1.021(-4)	4.043(-20)	3.724
2	A_1	7333.269	1	A_2	45.698	7287.572	5.074(-5)	3.233(-20)	1.232
1	B_1	6479.531	1	A_2	45.698	6433.833	1.667(-4)	3.125(-20)	4.641

Table 4.24: The 10 strongest transitions of D_3^+ at **100 K** in the range 1 to 1.6 μm (6250 cm^{-1} and 10000 cm^{-1}). Powers of 10 are given in parenthesis.

J''		E'' / cm^{-1}	J'		E' / cm^{-1}	ω_{if} / cm^{-1}	S(f←i) / D^2	I(ω_{if})	A_{if} / s^{-1}
1	A_1	6865.038	1	A_1	43.609	6821.429	1.722(-5)	3.912(-21)	5.713
2	A_1	6969.995	1	A_1	43.609	6926.386	1.531(-5)	3.533(-21)	3.191
2	E	6892.375	1	E	32.324	6860.050	1.531(-5)	3.291(-21)	2.479
3	E	6934.339	2	E	85.627	6848.712	2.595(-5)	3.291(-21)	2.987
1	E	6906.953	1	E	32.324	6874.629	8.427(-6)	2.587(-21)	2.290
1	E	6914.978	2	E	85.627	6829.351	1.803(-5)	2.587(-21)	4.803
4	E	6993.979	3	E	159.862	6834.117	3.681(-5)	1.816(-21)	3.275
4	E	6993.893	3	E	159.863	6834.030	3.671(-5)	1.816(-21)	3.267
0	E	6859.664	1	E	32.324	6827.340	5.842(-6)	1.793(-21)	4.665
2	A_1	6988.693	3	E	159.863	6828.830	2.915(-5)	1.793(-21)	5.823

a number of possible sources. The calculations may not be converged. This is unlikely as convergence was tested for with regard to the Fárník *et al* results (section 4.6). Another source could be the various corrections to the potential energy surface, which are mass scaled for the H_3^+ isotopomers. This scaling may not extend adequately to the heaviest isotopomer, D_3^+. This should warrant further investigation.

Table 4.25: The 10 strongest transitions of D_3^+ at **350 K** in the range 1 to 1.6 μm (6250 cm^{-1} and 10000 cm^{-1}). Powers of 10 are given in parenthesis.

J″		E″ / cm^{-1}	J′		E′ / cm^{-1}	ω_{if} / cm^{-1}	S(f←i) / D^2	I(ω_{if})	A_{if} / s^{-1}
4	E	6993.979	3	E	159.862	6834.117	3.6805(-5)	1.062(-21)	3.275
2	E	6988.693	3	E	159.862	6828.831	2.9151(-5)	1.060(-21)	5.823
3	A_1	6934.339	2	E	85.627	6848.712	2.5945(-5)	1.051(-21)	2.987
1	E	6865.038	1	E	43.609	6821.429	1.7217(-5)	1.018(-21)	5.713
3	E	7087.216	3	E	260.474	6826.743	3.9332(-5)	1.018(-21)	5.607
5	A_1	7071.330	4	A_2	254.964	6816.366	4.7885(-5)	1.000(-21)	3.459
2	A_1	6969.995	1	A_2	43.609	6926.386	1.5312(-5)	9.375(-22)	3.191
2	E	6892.375	1	E	32.324	6860.050	1.5305(-5)	9.326(-22)	2.479
1	E	6914.978	2	E	85.627	6829.351	1.8032(-5)	9.326(-22)	4.803
3	A_1	7070.608	4	A_2	254.964	6815.645	3.3860(-5)	9.030(-22)	3.842

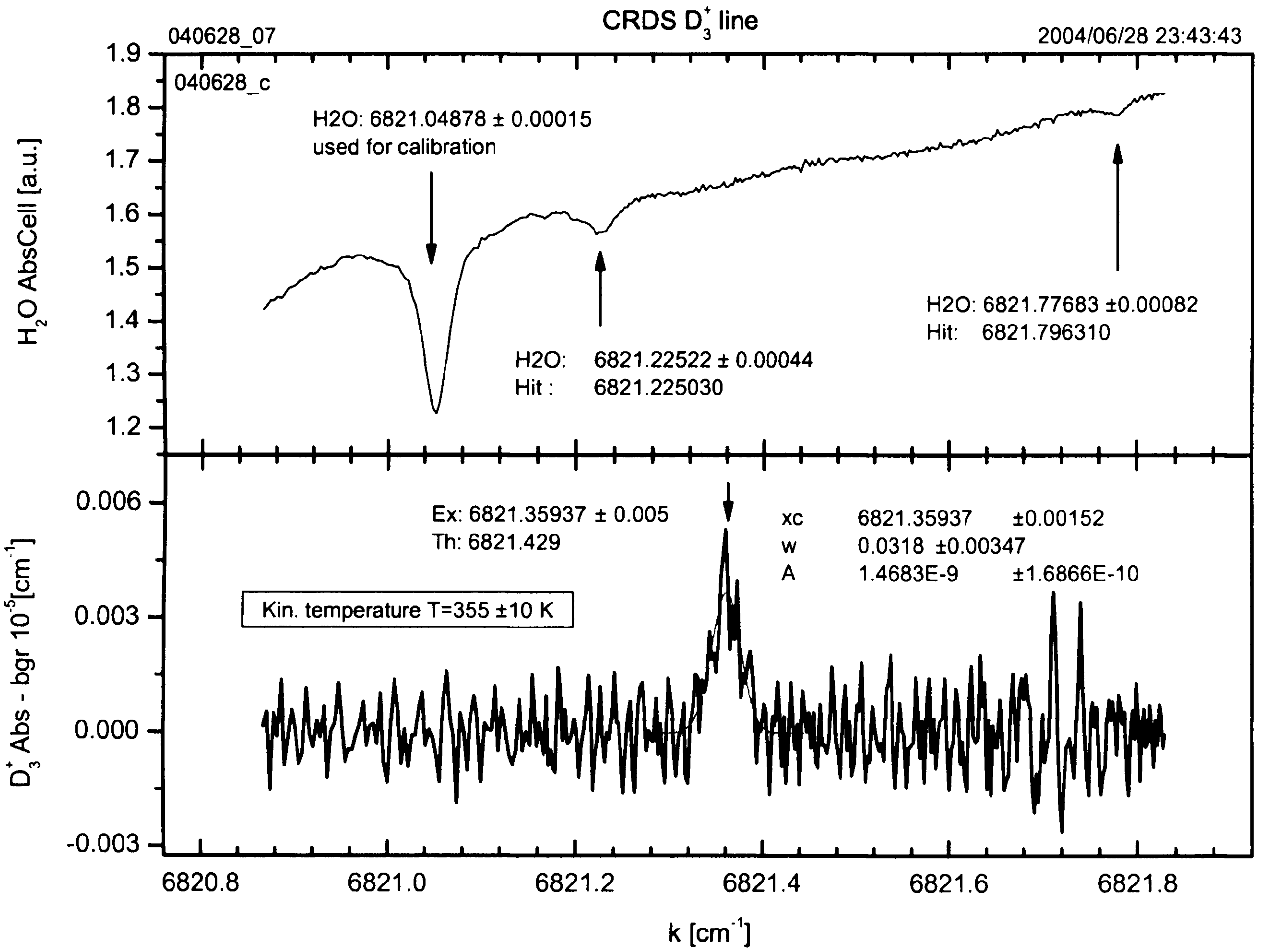

Figure 4.11: Observed D_3^+ spectra showing the 6821.359 cm^{-1} transition [9]

Table 4.26: A comparison between the D_3^+ lines observed by Glosik *et al* [9] and those of this work.

Measurement ID	J′		E′ / cm^{-1}	J″		E″ / cm^{-1}	ω_{if}(calc.) / cm^{-1}	ω_{if}(obs.) / cm^{-1}	calc.-obs. / cm^{-1}
040624_10	1	A_2	6870.771	0	A_1	0.000	6870.771	6870.326 ± 0.030	0.44
040624_18	1	A_2	6870.771	0	A_1	0.000	6870.771	6870.345 ± 0.004	0.43
040624_20	1	A_2	6870.771	0	A_1	0.000	6870.771	6870.348 ± 0.005	0.42
040628_02	2	A_2	6983.620	3	E	159.862	6823.758	6823.938 ± 0.050	-0.18
040628_03	2	A_2	6983.620	3	E	159.862	6823.758	6823.928 ± 0.005	-0.17
040628_04	2	A_2	6983.620	3	E	159.862	6823.758	6823.930 ± 0.005	-0.17
040628_07	1	A_1	6865.038	1	A_2	43.609	6821.429	6821.359 ± 0.005	0.07
040630_17	3	E	6934.339	2	E	85.627	6848.712	6849.047 ± 0.050	-0.34
040630_18	3	E	6934.339	2	E	85.627	6848.712	6849.110 ± 0.005	-0.40

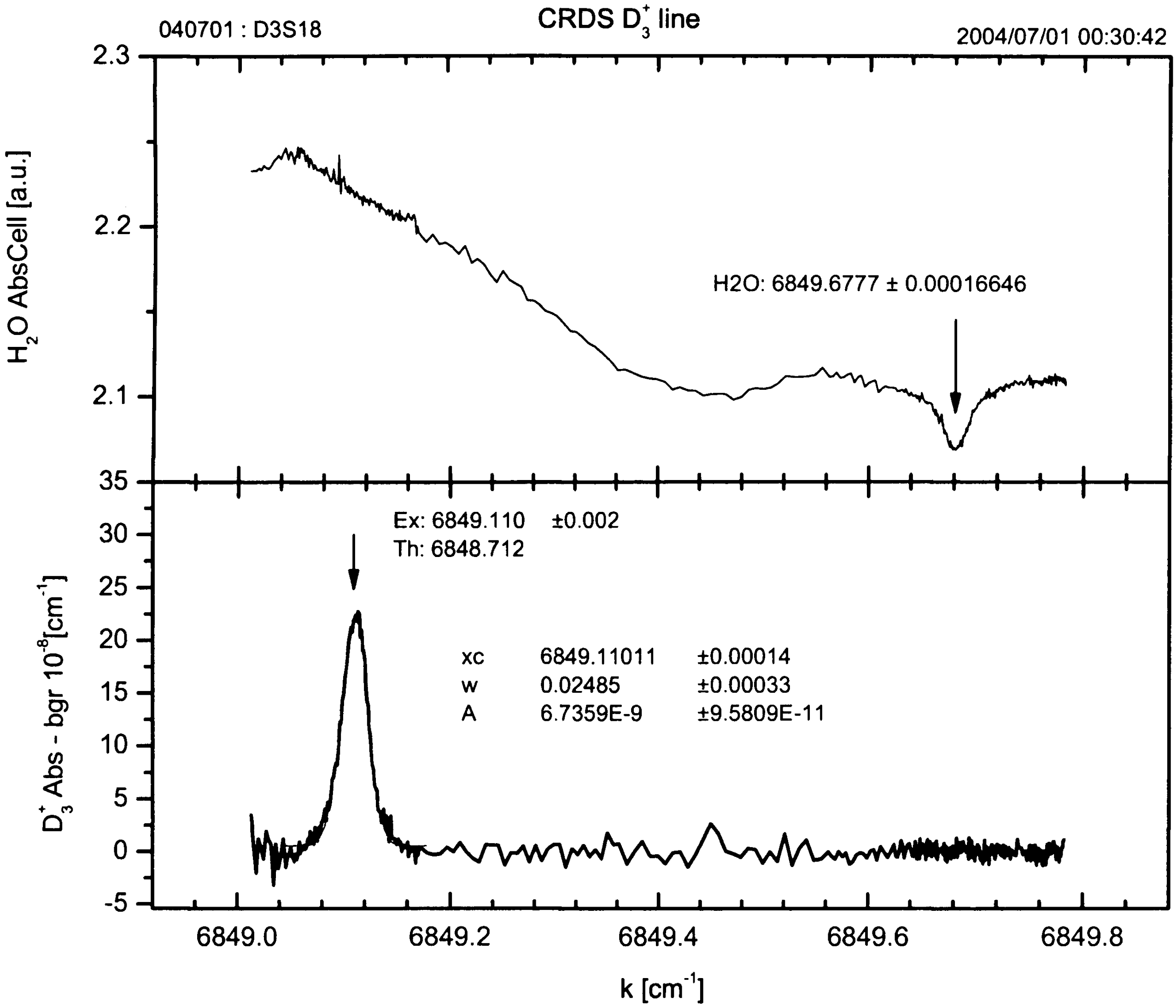

Figure 4.12: Observed D_3^+ spectra showing the 6849.110 cm^{-1} transition [9]

4.10.3 Storage Ring

Experiments with D_2H^+ were performed at the heavy ion Test Storage Ring (TSR) at the Max-Planck-Institut für Kernphysik in Heidelberg to measure the dissociative recombination rate. Molecular ions are produced in a gas discharge ion source and accelerated to 1.4 Mev [115]. These accelerated ions are then injected into the storage ring. This ion beam overlaps with a "cold" electron beam which has the effect of cooling the ion beam down and giving rise to dissociative recombination. The neutral fragments produced exit the storage ring and are recorded on an imaging detector.

As the dissociative recombination rates found by different experiments differed greatly, a thorough investigation of the dissociative recombination process was needed. One possible source of the discrepancy was thought to be that the D_2H^+ was not cold as thought,

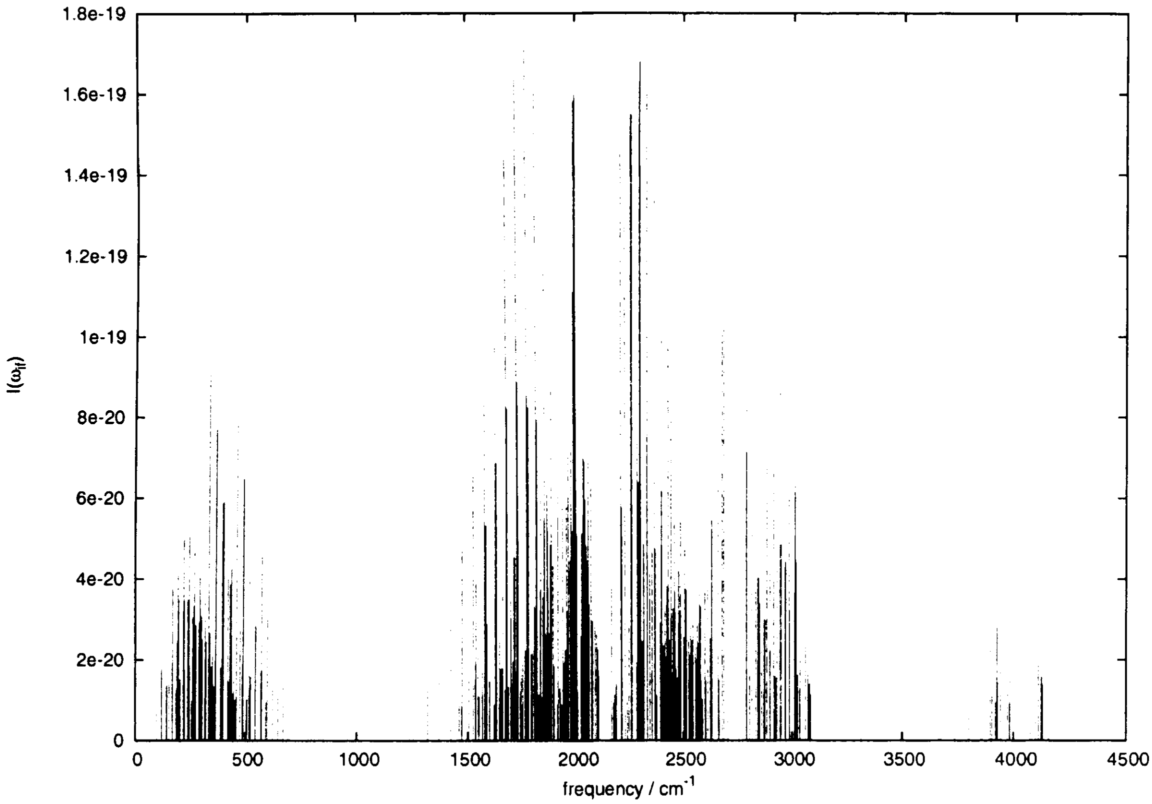

Figure 4.13: *Ab initio* synthetic pure rotational spectrum of D_2H^+ at 1000 K

but rotationally excited. To estimate the amount of rotational excitation, a Monte Carlo simulation was to be constructed with thermally distributed rotational excitations assuming different temperatures. The results of the simulation could then be compared with the results of the experiment.

A calculation at 1000 K to extend the data presented in table 7 of Miller *et al* [85] was performed to provide rotational data which could be used in the Monte Carlo model. The pure rotational transitions were identified by hand. Using a partition function of 1694.3 determined from the data in section 4.2 the absolute intensities were calculated. The spectrum is shown in figure 4.13.

Chapter 5

Parallel Computing

5.1 The case for parallelisation

The parallelisation of any program can be difficult and complex. At the very least the parallel program must be tested throughly to ensure the serial and parallel program produce identical results, this can be time consuming and tedious. Therefore a well reasoned argument must be made for parallelisation before it is undertaken.

There are two main reasons for parallelisation: the problem is too large to be tackled on a single processor or the time for the serial program to produce a solution is too great. The solving of the Hamiltonian matrix is one of the major computational tasks in this work. To simply store a 40000×40000 Hamiltonian requires in excess of 12.2 Gb of memory, this does not take into account workspace, which depending on the chosen algorithm may be several times this amount. The use of this amount of core memory is simply unfeasible on a single processor. For line strength calculations the computational cost is dependent on the size of the DVR grid and J, as is shown by equation 3.56. The objective is to investigate high-lying states pertaining to the very dense spectrum found by Carrington *et al* [1]. To achieve convergence for these states a large DVR grid is needed (refer to chapter 6). Also it is thought that many of these transitions are between highly rotationally excited states [69], therefore high J is needed. Thus only by distributing the work across multiple processors can a full calculation be feasibly performed.

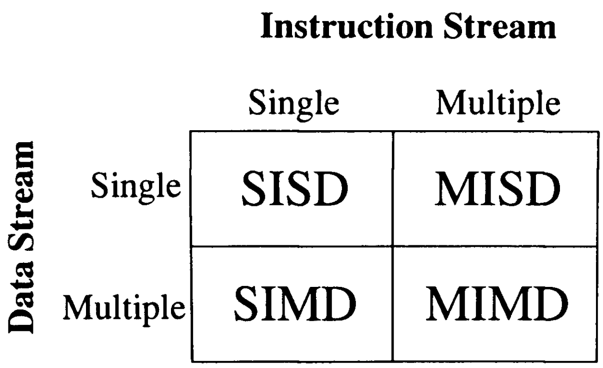

Figure 5.1: Flynn's taxonomy [10]

5.2 Parallel Architecture

5.2.1 Flynn's taxonomy

Flynn's taxonomy [10] classifies parallel architecture on the presence of single or multiple streams of data and instructions, figure 5.1.

SISD single instruction, single data stream, defines a sequential computer, such as the classic workstation.

MISD multiple instruction, single data stream, describes multiple processors applying different instructions to the same datum.

SIMD single instruction, multiple data streams, describes multiple processors performing the same operations on different data. An example would be an array processor such as the Thinking Machine Corporation's CM-200. There is often a control processor which broadcasts instructions, etc.

MIMD multiple instructions, multiple data streams, describes many processors performing diverse operations on diverse data. An example would be a network of workstations communicating through message passing.

The Flynn taxonomy provides a useful means by which computer architecture can be described simply, however it is by no means exhaustive. Many modern day computer architectures which incorporate such standard features as pipelining and multiple cache levels may belong to more that one category.

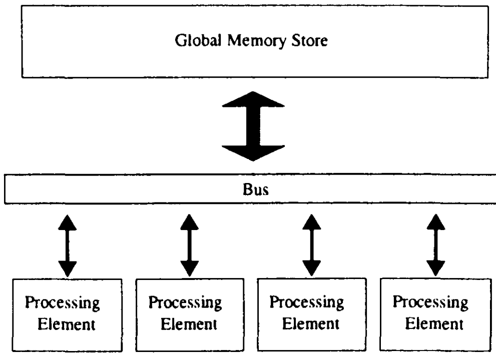

Figure 5.2: Schematic representation of the Shared memory architecture.

5.2.2 MIMD

MIMD architectures typically employ multiple independent processors that can execute individual instruction streams, or possibly with different processors executing different programs. This class of architecture is normally subdivided through the relationship between memory and processors.

Shared memory

Shared memory architecture is illustrated in figure 5.2. Typically, a relatively small number processors have access to some global memory store via some interconnect or bus. Processors communicate via the global memory, that is, one processor will write some data to memory and then another processor is able to read this data. Thus the time to access any piece of data is the same, as all communication goes though the bus.

The advantage of this architecture is that it is easy to develop programs for as all communication is done implicitly. The major disadvantage is that this system does not scale well. The reason for this is that bottlenecks created when a number of processors attempt to access the global memory store at the same time. A method which attempts to resolve this and make the shared memory architecture more scalable is *Non-Uniform Memory Access* (NUMA). Under this system all processors are allowed access to all memory within the system, however some memory may appear slower then other memory. This system tends to shift the problem onto the communication network which connects the local memories.

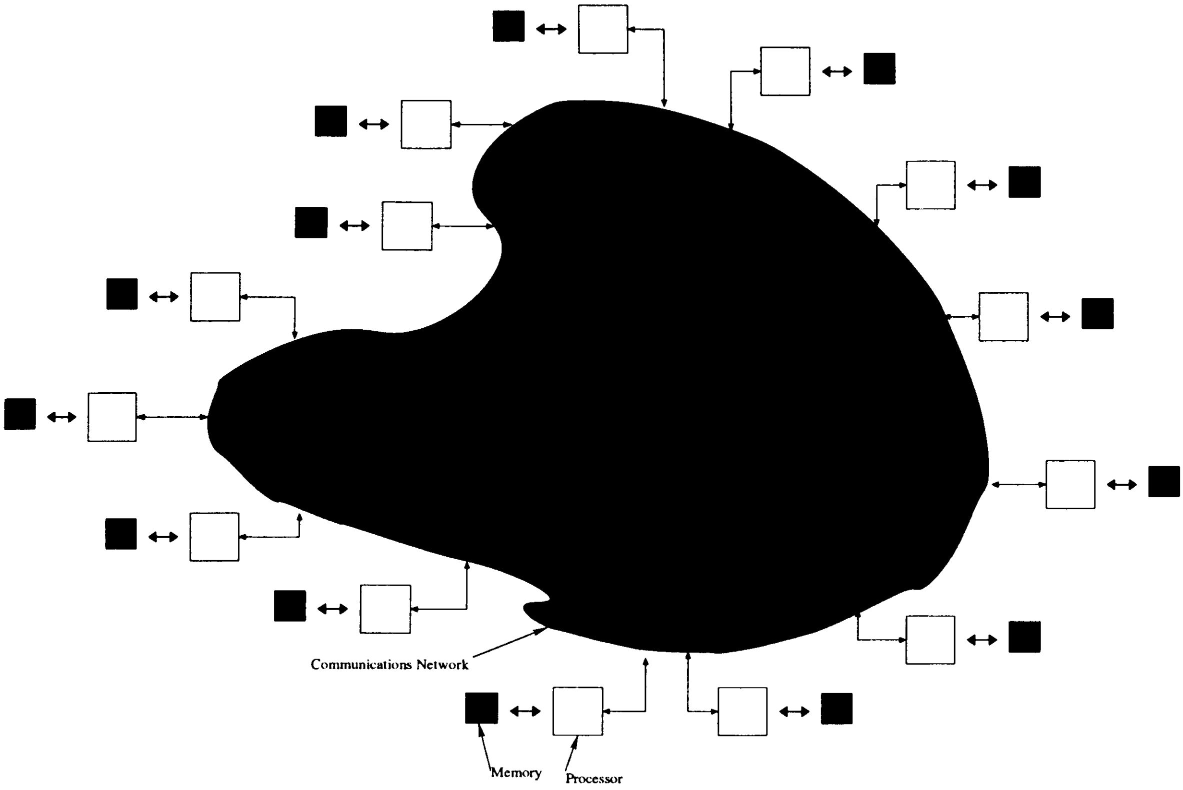

Figure 5.3: Schematic representation of the Distributed memory architecture.

Distributed memory

The distributed memory architecture is such that it is truly scalable. Each processor is attached its own local memory; a processor can only access memory that is directly attached to it. If data from the local memory of one processor is needed by another processor, then that data has to be explicitly transported via a communications network. (figure 5.3). Clearly a processor's access to data on local memory is much faster then that of data in memory in some remote processor; This non-uniform access time can be affected by the manner in which the communications network in implemented.

5.2.3 Communications Network

Fundamentally for large problems, processors must be able to communicate, be this through shared memory or through an explicit communications network. There are a number different interconnect topologies each with advantages and disadvantages in terms of latency, bandwidth, scalability, and ease of construction.

The *Bus* and *Crossbar* architectures are commonly used in shared memory machines (figure 5.2). A bus can be considered as a set of parallel wires which connect processors, memory, etc. This architecture is essentially a broadcast interconnect as all traffic from all components must cross the bus. Thus as the load increases the bus eventually becomes the performance bottleneck. This limits its ability to scale as the number of processors connected to it increases. The crossbar architecture attempts to resolves the bottlenecks caused by the bus architecture by providing multiple independent paths between processors and memory. Any component on the crossbar can access any other component via a path through the crossbar, and multiple paths may be active simultaneously. However the cost of construction of a crossbar becomes prohibitive as the number of processors increases. Both the bus and crossbar cannot scale sufficiently to support thousands of processors, and are restricted to relatively small shared memory machines.

There are a myriad of topologies used for the interconnect in the thousands of processor regime. In this regime it is no longer possible to refer to memory as a single block. There are several steps of communications between the source and destination, thus the objective of the topology is to minimise the number of steps.

5.2.4 Communication libraries

At present there are two major generic communication libraries in use: Message-Passing Interface (MPI) [116] and OpenMP [117], the differences between them is essentially the difference between the data-parallel and message-passing programming models.

The data-parallel model is one where parallelism is attained when a master thread spawns additional threads which may reside on different processors as and when needed. Memory is global with each thread having read and write access (common memory is the defining difference between a *thread* and a *process*). The typical method by which this parallelism is achieved is through parallelising the computationally intensive loops. The data-parallel model is most suited to shared memory machines as the communication is through shared memory and thus becomes particularly inefficient when processors are not sharing local memory and are communicating by some interconnect. Programs which operate with large arrays requiring the same operation are most suited to the data-parallel model. Preferably many of these operations should be independent, that is not depend on the results of previous operations. OpenMP implements the data-parallel model. It is an API (Application Program Interface) for writing multi-threaded programs using compiler directives and library routines. Communication between threads is done via the sharing of variables and thus all communication is implicit.

In the message-passing model each process has local memory and all other processes are unable to access this memory without the use of explicit message passing. Messages are communicated between processes to synchronise and exchange data. The message-passing model is particularly suited to the MIMD architecture (refer to section 5.2.2). MPI implements the message-passing model through a collection of communication primitives. MPI is regarded as the "assembly" code of parallel computing and as such is available on virtually all machines. It includes features like communicators, topologies, communication modes and single-call collective operations. MPI, more specifically MPI-2 has been used through out this work to create parallel programs.

BLACS (Basic Linear Algebra Communication Subprograms) [118] is a communications library developed specifically for linear algebra. It is an array based communications library as the majority of linear algebra problems are solved using arrays. Therefore the BLACS library treats processors as being part of a two dimensional process grid, with each processor being assigned a row and column, as this is conducive to working with arrays. The advantages of BLACS is that it is relatively easy to program with and is available on most platforms. However BLACS is built on top of a message passing library such as MPI, and thus lacks the ability to do low level communications. BLACS provides the communication layer for the ScaLAPACK library, this is discussed in section 5.4.1.

5.2.5 HPCx

The HPCx system can be a considered as a combination of the shared memory and the distributed memory architecture.

Phase 2 HPCx consists of 1600 IBM Power4+ CPUs. Each CPU has a 1.7Gz clock speed with 2 independent 64-bit floating point units, giving a peak performance of 6.8 GFlops. Each CPU has 96 Kb of level 1 cache. Two of these CPUs co-habit the Power4+ chip, figure 5.4. These CPUs share 1.5 Mb of level 2 cache. Each chip is capable of giving a peak performance of 16.6 GFlops. Four chips share 128 Mb level 3 cache upon a Multi-Chip Module (MCM) as shown in figure 5.5. An MCM gives 54.4 GFlops at peak performance. A P690+ frame is made of four of these MCMs. These can be considered as 32-way shared memory nodes consisting of 32 CPUs and 32 Gb of main memory per frame, giving a peak performance of 217.6 GFlops. Each frame runs

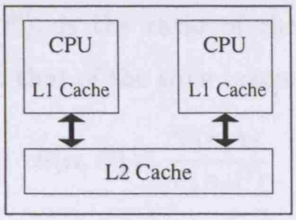

Figure 5.4: The Power4+ chip consisting of two CPUs sharing level 2 cache.

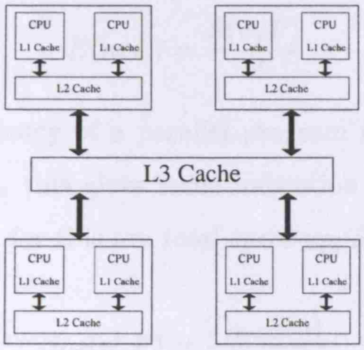

Figure 5.5: Multi-Chip Module consisting of four Power4+ chips sharing level 3 cache.

a separate copy of the operating system.

The frames are able to communicate via the IBM High Performance Switch (HPS). Each frame has four switch connections. The interconnect is built in a series of stages like a conventional Butterfly network but each stage consists of an 8×8 crossbar rather then the classic 2×2. This arrangement gives a latency of 11 μs (MPI) and 600 Mbs^{-1} through each connection. A hierarchical communications system is produced due the differing way the constituents are connected. For example communications between two CPUs on the same chip and that of two CPUs on different frames.

Thus the full system consists of 50 P690+ frames, that is 1600 CPUs and 1600 Gb main memory. This is capable of give a peak performance of 10.88 TFlops; this translates to approximately 6.2 TFlops on the LINPACK [119] benchmark.

The complex make-up of the HPCx system can give rise to complex performance behaviour.

5.3 Measures of parallel performance

For the purposes of comparison and development it is important to ascertain the performance of a parallel program. The most common measures of performance are *speed-up* and *efficiency*.

The *parallel speed-up*, $S(n, P)$, is the ratio of the execution time of the parallel program run on one processor to that of the time taken on P processors; it is defined as:

$$S(n, P) = \frac{T(n, 1)}{T(n, P)} \tag{5.1}$$

where n is a measure of problem size.

The *parallel efficiency* is the speed-up divided by the number of processors.

$$E(n, P) = \frac{S(n, P)}{P} \tag{5.2}$$

To gauge the numerical efficiency of a parallel program it should be compared to the serial version of the program, this gives some indication of the quality of the parallel algorithm adopted. Measures for this are *total speed-up*, $S_{tot}(n, P)$, and *total efficiency*, $E_{tot}(n, P)$.

$$S_{tot}(n, P) = \frac{T_{serial}(n)}{T(n, P)} \tag{5.3}$$

$$E_{tot}(n, P) = \frac{S_{tot}(n, P)}{P} \tag{5.4}$$

where T_{serial} is the execution time of the serial version of the program. However it is not always possible to do this as a serial program may not be available due to the size of the problem, etc.

Amdahl's Law [120] refers to the maximum speed-up that can be achieved due to the inherent serial parts of any program. All programs have a mixture of serial parts and parallel parts. Speed-up is only relevant to the parallel portions and thus the serial portions provides the limit of *parallel efficiency.*

5.4 Vibrational Problem: PDVR3DJ

The Coriolis decoupled Hamiltonian, equation 2.42, is solved using the parallel program PDVR3DJ, giving eigenvalues η_i and eigenfunctions $\psi^{J,k,h}_{\alpha,\beta,\gamma}$. This program is more fully described in Mussa *et al* [13]. PDVR3DJ is largely based on the earlier version of DVR3DRJ suite of Tennyson *et al* [121] as opposed to the more recent version of the suite [43]. There are some notable differences in the versions of the suite which are outlined below. In addition a number of significant developments were made to the PDVR3DJ program during this work.

The general method of decomposing the vibrational problem over N_p processors with N_γ final grid points is to place N_γ/N_p points on each processor. Therefore the

Hamiltonian matrix is split on the final coordinate, such that each processor has a N^{3D}/n_γ segment of the whole Hamiltonian matrix, where N^{3D} is the size of the whole 3D Hamiltonian matrix. This requires that the Hamiltonian matrix is both constructed and solved in parallel.

The Hamiltonian is solved by a series of diagonalisations and truncations. Unlike the serial program there is no separate 1D and 2D step, this avoids load imbalance across processors [122]. If the coordinate ordering is $\theta \to r_1 \to r_2$, then each processor constructs the 2D Hamiltonian as given by,

$$^{(2D)}H^{\beta}_{\alpha,\alpha'} = L^{(1)}_{\alpha,\alpha',\gamma,\gamma'} + L^{(1)}_{\beta,\beta',\gamma,\gamma'} + V(r_{1\alpha}, r_{2\alpha}, \theta_\gamma) + K^{(1)}_{\alpha,\alpha'}\delta_{\beta,\beta'}\delta_{\gamma,\gamma'} \tag{5.5}$$

where the terms are given in section 2.9. The 2D Hamiltonian is solved by diagonalisation, giving eigenvectors, $C^{\beta}_{\alpha,l}$, for the l^{th} level, with eigenvalue ϵ^{β}_l at each grid point β. The diagonaliser used to solve the 2D Hamiltonian was ARPACK [123]. This was replaced by the LAPACK [124] routine DSYEV which is considerably faster, and has been proven by the serial program to give good eigenvectors and requires a simpler interface, making the code less cluttered.

The 2D eigenvalues and accompanying eigenvectors are selected by the size of the full 3D Hamiltonian, thus each γ point has the same number of 2D solutions. Again this is for load balancing.

Each processor constructs a strip of the Hamiltonian, $^{(3D)}H(N^{3D}, N^{3D}/N_p)$, using

$$^{(3D)}H_{\beta,\beta',l,l'} = \epsilon^{\beta}_l \delta_{\beta,\beta'}\delta_{l,l'} + \sum_{\alpha\gamma} C^{\alpha\beta}_{\gamma,l} C^{\alpha\beta'}_{\gamma,l'} K^{(2)}_{\beta,\beta'} \tag{5.6}$$

from equation (5.6). It can be seen that the kinetic $K^{(2)}$ matrix is replicated on each processor and each processor must broadcast its 2D solutions to all other processors. This distributed Hamiltonian matrix is solved using a parallel diagonaliser. A representation of this global 3D Hamiltonian matrix can seen in figure 5.6. The matrix was constructed such that the coordinate ordering was $\theta \to r_1 \to r_2$, with 32, 36, and 32 grid points for the θ, r_1 and r_2 coordinates respectively. The natural log of the absolute values of this 4800 × 4800 matrix were converted to a grayscale value in accordance to the PGM format [125]. Figure 5.6 clearly shows 32 × 32 smaller blocks within the larger matrix, this represents coupling between the 32 r_2 points which are used to construct the full 3D Hamiltonian.

The general algorithm of the vibrational calculation is as follows

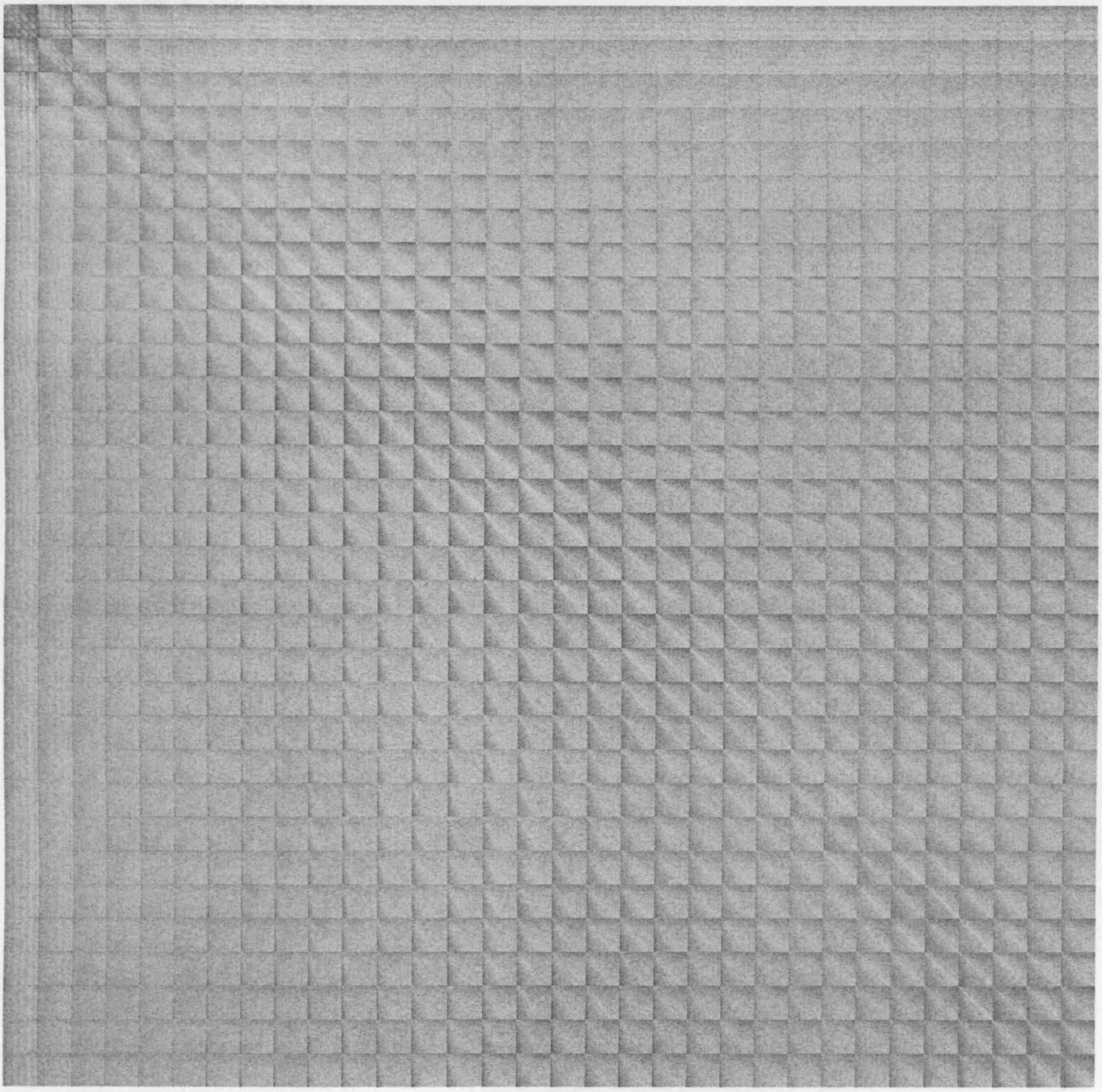

Figure 5.6: A representation of the global view of the $J = 0$ 3D Hamiltonian matrix. The natural log of the absolute values of the matrix values were taken and converted to a value of gray, where the darker the colour, the higher the value of the matrix element.(N=4800, n_{r_2}=32, n_{r_1}=36, $n_\theta = 32$)

1. Begin to loop over k
2. Each processor constructs and solves ${}^{(2D)}H^{\beta}_{\alpha,\alpha'}$ for a given γ, equation (5.5)
3. Each processor broadcasts the solutions of ${}^{(2D)}H^{\beta}_{\alpha,\alpha'}$
4. Each processor constructs a segment of the 3D Hamiltonian ${}^{(3D)}H(N^{3D}, N^{3D}/N_p)$, equation (5.6)
5. Solve ${}^{(3D)}H_{\beta,\beta',l,l'}$
6. Root process writes $\epsilon_h^{J,k}$ to disk
7. Each processor transforms the h/N_p eigenvectors back onto the DVR grid to form $\Psi^{J,k,h}_{\alpha,\beta,\gamma}$, equation (2.52)
8. Optionally save $\Psi^{J,k,h}_{\alpha,\beta,\gamma}$ to disk
9. Each processor Transform the h/N_p DVR eigenvectors, $\Psi^{J,k,h}_{\alpha,\beta,\gamma}$, to DVR^2-FBR^1 eigenvectors $\Psi^{J,k,h}_{\alpha,\beta,j}$, equation (2.53). Transformation matrix T_j^{γ} is replicated on each processor.
10. Save $\Psi^{J,k,h}_{\alpha,\beta,j}$ to disk
11. if k > 0 then form the $B^{k',k}$ off-diagonal Coriolis block, equation (5.12)
12. if k > 0 save $B^{k',k}$ to disk
13. Next k, i.e. **goto** 1

5.4.1 Diagonalisers

The purpose of a diagonaliser is to solve the eigenvalue equation

$$Ax = \lambda x \tag{5.7}$$

to give a set of eigenvalues λ_i and corresponding eigenvectors x_i; where for the purposes of this work A is a real symmetric Hermitian matrix. The general manner in which the eigenvalue equation is solved numerically can be summarised in three parts: Reduction of A to the tridiagonal form, T; diagonalisation of matrix T; back substitution to find the eigenvalues and eigenvectors of the full problem. The Hamiltonian matrix, ${}^{(3D)}H_{\beta,\beta',l,l'}$, which is solved by PDVR3DJ is dense and contains clusters. The diagonaliser used by PDVR3DJ needs to provide both the eigenvalues and eigenvectors which need to be orthonormal.

The diagonaliser implemented in PDVR3DJ had been PeIGS [126]. It was suggested that the ScaLAPACK diagonalisers [11, 12]: PDSYEV, PDSYEVX, PDSYEVD, may be considerably faster on the HPCx system. The ScaLAPACK library relies on the BLACS library for communication and the serial LAPACK library to perform that actual linear algebra; the LAPACK library in turn relies on the BLAS library. All three ScaLAPACK routines use a form of the Householder algorithm to reduce the matrix to the tridiagonal form. They then proceed from the tridiagonal matrix using their specific algorithm followed by a back transformation to obtain solutions for the full problem. PDSYEV implements the QR algorithm to solve the tridiagonal matrix; it gives all the eigenvalues and eigenvectors. While PDSYEVX uses bisection and inverse iteration to solve the tridiagonal matrix, thus allows for an arbitrary number of eigenvalues and eigenvectors to be calculated. As we are only interested in a few thousand such eigenvalue-eigenvector pairs from matrices possibly containing many times this number, this could prove efficient. PDSYEVD implements a divide and conquer algorithm [12] and currently gives all the eigenvalues and eigenvectors, although a version which only calculates a subset is under development.

Two dimensional blocks cyclic distribution

The ScaLAPACK diagonalisers requires that the matrix to be diagonalised, A, is distributed using the *two dimensional block cyclic* scheme. The scheme splits the matrix A into a number of contiguous blocks of size $M_B \times N_B$ and then maps these blocks onto processors. This distribution is chosen as it gives the best load balancing and efficient use of Level 3 BLAS library (serial version). The processors form a $P_r \times P_c$ grid where P_r and P_c are the number of rows and columns respectively. The size of each block is chosen such as to optimise computation with respect to considerations such as the size of Level 1 cache of the CPU. The mapping of element, (I, J), of global matrix A onto processor, (p_r, p_c), within block (l, m) at the position (x, y) is given by:

$$p_r = RSRC + integer\left(\frac{I-1}{M_B}\right) mod(P_r)$$
$$p_c = CSRC + integer\left(\frac{J-1}{N_B}\right) mod(P_c) \qquad (5.8)$$

$$l = integer\left(\frac{I-1}{P_r M_B}\right), \quad m = integer\left(\frac{J-1}{P_c N_B}\right) \tag{5.9}$$

$$x = mod(I-1, M_B) + 1, \quad y = mod(J-1, M_B) + 1 \tag{5.10}$$

where $RSRC$ and $CSRC$ are the row and columns coordinates of the processor to which the first block is assigned; $integer$ species integer arithmetic rounded towards zero. The distribution of a 9×9 matrix in the two dimensional block cyclic scheme is shown in figures 5.7 and 5.8. It is apparent that the data is distributed in a complex manner with each processor having different amounts of data.

A_{11}	A_{12}	A_{13}	A_{14}	A_{15}	A_{16}	A_{17}	A_{18}	A_{19}
A_{21}	A_{22}	A_{23}	A_{24}	A_{25}	A_{26}	A_{27}	A_{28}	A_{29}
A_{31}	A_{32}	A_{33}	A_{34}	A_{35}	A_{36}	A_{37}	A_{38}	A_{39}
A_{41}	A_{42}	A_{43}	A_{44}	A_{45}	A_{46}	A_{47}	A_{48}	A_{49}
A_{51}	A_{52}	A_{53}	A_{54}	A_{55}	A_{56}	A_{57}	A_{58}	A_{59}
A_{61}	A_{62}	A_{63}	A_{64}	A_{65}	A_{66}	A_{67}	A_{68}	A_{69}
A_{71}	A_{72}	A_{73}	A_{74}	A_{75}	A_{76}	A_{77}	A_{78}	A_{79}
A_{81}	A_{82}	A_{83}	A_{84}	A_{85}	A_{86}	A_{87}	A_{88}	A_{89}
A_{91}	A_{92}	A_{93}	A_{94}	A_{95}	A_{96}	A_{97}	A_{98}	A_{99}

Figure 5.7: The global view the 2D block cyclic distribution of a 9×9 global array with blocks of size 2×2 onto a 2×3 processor grid. The different colours represent the different processors. [11]

The method by which the Hamiltonian is constructed as outlined in section 5.4 is such that it is distributed in bands. Thus the matrix needs to be redistributed in the two dimensional block cyclic scheme. The matrix is symmetric, therefore only half the matrix needs to redistributed. After the matrix has been diagonalised the eigenvectors are distributed in the two dimensional block cyclic scheme and needs to be redistributed into bands such that an entire eigenvector resides on the same processor. This is accomplished using the Fortran subroutines of Munro [127]. These use considerably less memory then the equivalent ScaLAPACK routine PDGEMR2D [11].

Performance

To test the performance of the diagonalisers independently of PDVR3DJ; driver routines were written for the three diagonalisers: PDSYEV, PDSYEVX, PDSYEVD. These rou-

	0				1			2	
	A_{11}	A_{12}	A_{17}	A_{18}	A_{13}	A_{14}	A_{19}	A_{15}	A_{16}
	A_{22}	A_{22}	A_{27}	A_{28}	A_{23}	A_{24}	A_{29}	A_{25}	A_{26}
0	A_{51}	A_{52}	A_{57}	A_{58}	A_{53}	A_{54}	A_{59}	A_{55}	A_{56}
	A_{61}	A_{62}	A_{67}	A_{68}	A_{63}	A_{64}	A_{69}	A_{65}	A_{66}
	A_{91}	A_{92}	A_{97}	A_{98}	A_{93}	A_{94}	A_{99}	A_{95}	A_{96}
	A_{31}	A_{32}	A_{37}	A_{38}	A_{33}	A_{34}	A_{39}	A_{35}	A_{36}
	A_{41}	A_{42}	A_{47}	A_{48}	A_{43}	A_{44}	A_{49}	A_{45}	A_{46}
1	A_{71}	A_{72}	A_{77}	A_{78}	A_{73}	A_{74}	A_{79}	A_{75}	A_{76}
	A_{81}	A_{82}	A_{87}	A_{88}	A_{83}	A_{84}	A_{89}	A_{85}	A_{86}

Figure 5.8: The local distributed view the 2D block cyclic distribution of a 9×9 global array with blocks of size 2×2 onto a 2×3 processor grid. The different colours represent the different processors. [11]

tines would read in a Hamiltonian matrix constructed for H_3^+ $(J = 0)$ by PDVR3DJ and dumped to file. The drivers redistributed the Hamiltonian which when read in produces a banded data distribution to a two dimensional block cyclic data distribution. This matrix was then diagonalised giving eigenvalues and eigenvectors. All the eigenvalues and eigenvectors were calculated when using PDSYEV and PDSYEVD, while as PDSYEVX is able to calculate a subset, only 2400 eigenvalues and eigenvectors were requested. As the eigenvectors produced were block cyclically distributed, another redistribution to banded form was required so that the eigenvectors would be stored in columns locally. The two redistribution and diagonalisation were timed as a function of the number of processors and the size of the matrix/Hamiltonian. This data is tabulated in tables 5.1, 5.2, and 5.3. Plots comparing the performance of the diagonalisers are shown in figures 5.9 and 5.10.

It is clear from the data in tables 5.1, 5.2 and 5.3, and figures 5.9, 5.10 and 5.11 that PDSYEV is approximately 4 times slower then either PDSYEVX or PDSYEVD. The speed of both PDSYEVX and PDSYEVD result in the time for data redistribution to be significant contributer to the total time taken to solve the Hamiltonian matrix. This would indicate that if the Hamiltonian were built in a 2D block cyclic distribution significant time savings may be achieved through less data redistribution. PDSYEVX and PDSYEVD have comparable performance, however PDSYEVD should be preferred as it

Table 5.1: Time breakdown in seconds for the diagonalisation of an 12000×12000 matrix using the various ScaLAPACK [11, 12] routines. The time taken to redistribute the matrix from a banded to 2D block cyclic distribution, diagonalise the matrix, and redistribute from 2D block cyclic to banded.

	PDSYEV					PDSYEVX					PDSYEVD				
Number of Processors	32	64	96	128	160	32	64	96	128	160	32	64	96	128	160
Banded to 2D Block Cyclic	13.9	10.0	6.1	5.4	19.1	14.5	10.3	8.2	7.8	20.6	13.9	10.7	6.2	6.1	20.4
Diagonalisation	955.9	493.1	308.4	303.8	276.9	171.4	90.9	73.3	54.0	47.7	166.2	106.7	76.5	62.7	58.6
2D Block Cyclic to Banded	24.6	25.8	27.2	27.6	54.4	25.5	26.3	27.9	28.7	55.8	25.1	26.3	27.8	28.6	55.1
Total	983.8	513.2	320.5	314.7	315.1	200.4	111.4	89.8	69.6	88.9	194.0	128.1	88.8	74.9	99.5

Table 5.2: Time breakdown in seconds for the diagonalisation of an 24000×24000 matrix using the various ScaLAPACK [11, 12] routines. The time taken to redistribute the matrix from a banded to 2D block cyclic distribution, diagonalise the matrix, and redistribute from 2D block cyclic to banded.

	PDSYEV					PDSYEVX					PDSYEVD				
Number of processors	32	64	96	128	160	32	64	96	128	160	32	64	96	128	160
Banded to 2D Block Cyclic	-	57.2	43.2	45.8	85.7	-	59.3	46.2	53.8	89.6	-	59.4	44.3	47.8	89.3
Diagonalisation	-	3938.5	2546.4	1879.2	1843.5	-	691.5	569.6	366.5	306.2	-	856.6	513.7	392.0	357.8
2D Block Cyclic to Banded	-	104.3	110.8	113.7	222.8	-	106.2	111.7	115.7	218.9	-	106.1	112.3	117.7	221.4
Total	-	4052.9	2632.8	1970.7	2014.8	-	810.1	662.0	474.0	485.3	-	975.5	602.2	487.5	536.4

Table 5.3: Time breakdown in seconds for the diagonalisation of an 36000×36000 matrix using the various ScaLAPACK [11, 12] routines. The time taken to redistribute the matrix from a banded to 2D block cyclic distribution, diagonalise the matrix, and redistribute from 2D block cyclic to banded.

	PDSYEV					PDSYEVX					PDSYEVD				
Number of processors	64	96	128	160	192	64	96	128	160	192	64	96	128	160	192
Banded to 2D Block Cyclic	-	124.0	124.7	196.0	195.0	-	130.4	133.6	209.5	205.8	-	129.4	129.4	211.0	204.4
Diagonalisation	-	9785.2	8131.4	6641.2	5374.5	-	1927.9	1349.8	1149.0	976.4	-	1786.2	1382.3	1158.9	923.6
2D Block Cyclic to Banded	-	254.7	261.6	488.5	508.5	-	259.0	265.7	500.0	509.3	-	261.4	266.3	505.3	516.2
Total	-	10033.2	8380.8	7033.2	5764.4	-	2188.8	1617.1	1568.0	1388.1	-	2044.9	1641.0	1580.9	1332.3

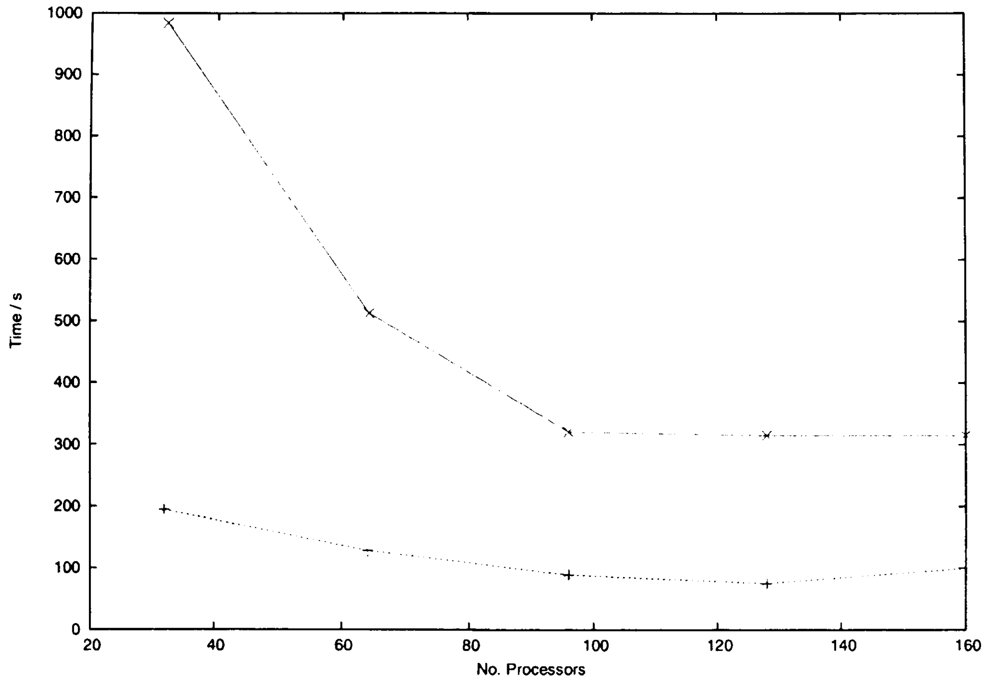

Figure 5.9: Total time taken to diagonalise 12000×12000 matrix as a function of number of processors using ScaLAPACK [11, 12] diagonalisation routines: *Crosses*, PDSYEV; *Diamonds*, PDSYEVX; *Pluses*, PDSYEVD.

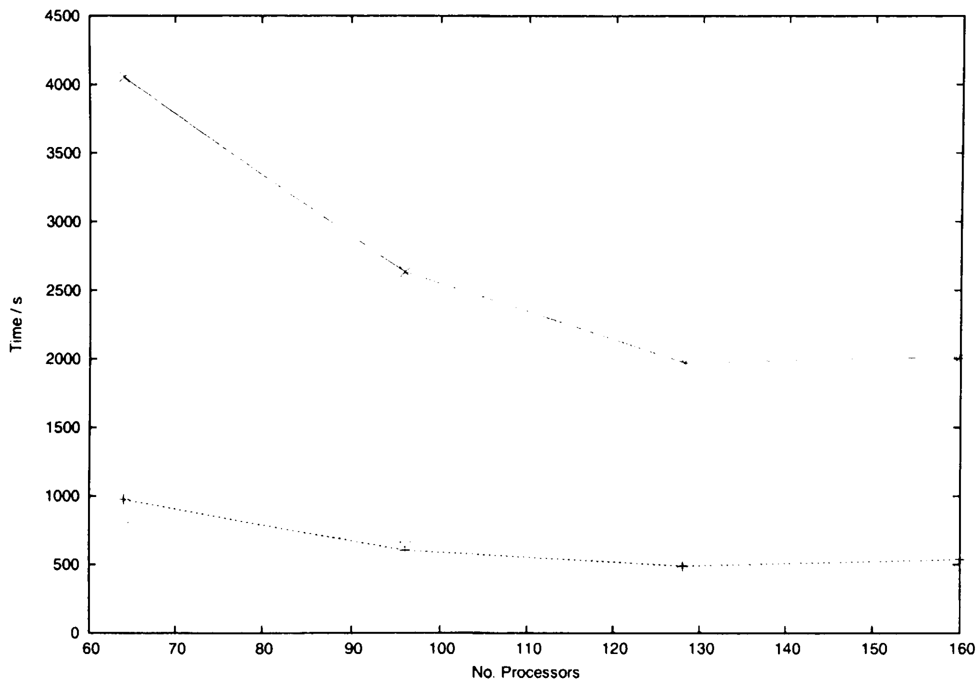

Figure 5.10: Total time taken to diagonalise 24000×24000 matrix as a function of number of processors using ScaLAPACK [11, 12] diagonalisation routines: *Crosses*, PDSYEV; *Diamonds*, PDSYEVX; *Pluses*, PDSYEVD.

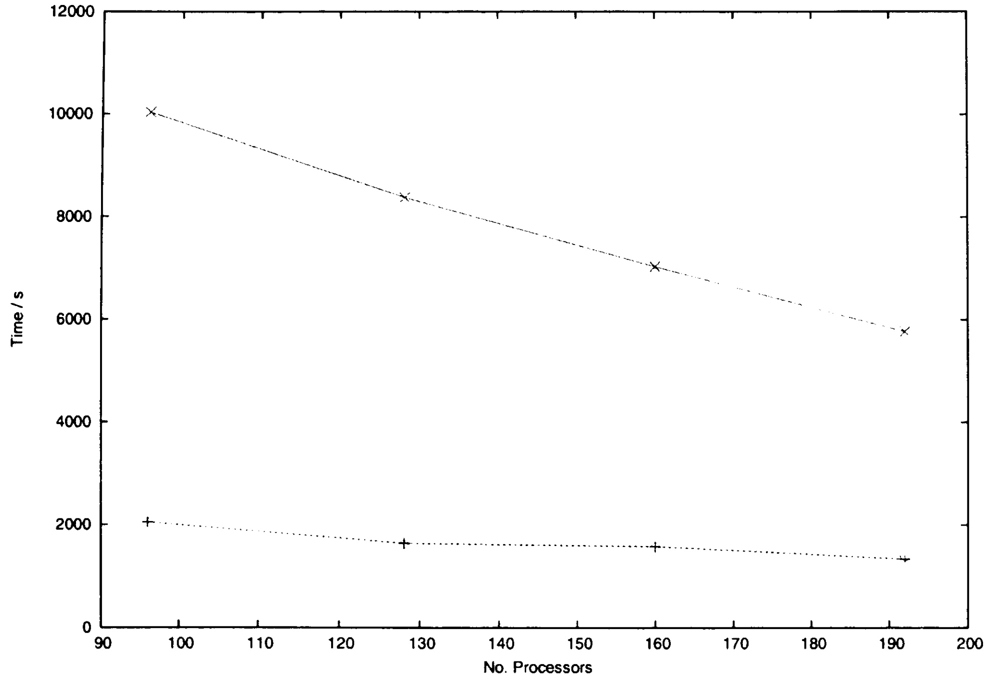

Figure 5.11: Total time taken to diagonalise 36000×36000 matrix as a function of number of processors using ScaLAPACK [11, 12] diagonalisation routines: *Crosses*, PDSYEV; *Diamonds*, PDSYEVX; *Pluses*, PDSYEVD.

calculates all the eigenvalues and eigenvectors, and also uses significantly less memory.

From figures 5.9 and 5.10 it can be seen that there is a relationship between matrix size and number of processors with respect to speed-up and parallel efficiency. In any parallel task in order to maximise the efficiency of the calculation the time spent calculating should be far greater then the time spent on communication and synchronisation, which are pure overhead with respect to parallel efficiency. With a 12000 matrix there is a near two fold speed up from 32 to 64 processors, but significantly less when going from 64 to 128. With the 24000 matrix there is a near two fold speed up going from 64 to 128 processors. However the total program execution time actually increases when the number of processors is increased from 128 to 160. The consequence of adding processors to a fixed size problem is that each processor has an increasingly smaller section of the global matrix, thus initially good speed-up begins to tail off. These inefficiencies result from each processors having too little computational work with respect to communication. Thus the cost of communication with a larger number of processor, with each processor doing less computational work, becomes too great to justify adding more processors. However there are occasions when a loss of efficiency must be made in order to actually tackle the problem, for example if there is insufficient memory. Thus the number of processors has to be increased so that each processors has a smaller section of the problem for which it has sufficient memory to handle. This represents one of the classic problems of parallel computing and the solution is to strike a balance between the matrix size, memory, number of processors, and the execution time of the program.

5.4.2 Calculating arbitrary number of k blocks

On the HPCx system the maximum wall clock time for any calculation is 12 hours. Thus for large runs of PDVR3DJ this may become a problem. To alleviate this problem a method by which an arbitrary number of k blocks could be calculated was devised. This splits running of PDVR3DJ program for a given J into $J+1$ possible runs. This is achieved by saving the DVR^{2}FBR^1 eigenvectors, $\Psi^{J,k,h}_{\alpha,\beta,j}$, to disk when the final k of the current run is reached. They are read back on the next run to form the off-diagonal block $B^{k,k'}$. The I/O is done in parallel using MPI-2 which makes it rapid.

5.4.3 Summary of changes to PDVR3DJ

I made a number of changes to the PDVR3DJ program, a summary of these changes are listed below:

- 2D diagonaliser changed from ARPACK [123] to LAPACK routine DSYEV [124]
- 3D diagonaliser changed from PeIGS [126] to ScaLAPACK routines PDSYEV, PDSYEVX, and PDSYEVD [11, 12]
- The ability to calculate an arbitrary number of k blocks on a single run
- The re-writing of all the I/O including the extensive use of MPI-2 I/O routines [116]
- Replacing the use Fortran common blocks with modules which are more conducive to complier optimisation.
- The addition of a file to which various pieces of data are written for use in PDIPOLE.

5.5 Rotational Problem: PROTLEV3

The eigenvalues, η_i, and eigenvectors, $\psi^{J,k,h}_{\alpha,\beta,\gamma}$, from the 3D Hamiltonian are used to solve the Coriolis coupled Hamiltonian where $J > 0$. These eigenvectors are transformed to the

DVR^2-FBR^1 representation, $\psi^{J,k,h}_{\alpha,\beta,j}$ by equation (2.53). This transformation is performed in parallel by PDVR3DJ. As the eigenvectors $\psi^{J,k,h}_{\alpha,\beta,\gamma}$ are distributed across processors, the transformation matrix, T^{γ}_{j}, is replicated and each eigenvector is transformed *in situ*, therefore the transformation can be carried out without the need for inter-processor communication.

The Coriolis fully coupled Hamiltonian is given by equation (2.54). It is apparent that the diagonal elements of the Hamiltonian are simply the eigenvalues η_i of the 3D Hamiltonian, thus the construction of the Hamiltonian becomes one of building the off-diagonal blocks in k, $B^{k,k'}(h,h')$, the second term in equation (2.54). Therefore each processor builds rows of each block $B^{k,k'}(h/N_p,h)$ using local eigenvectors $\psi^{J,k,h/N_p}_{\alpha,\beta,\gamma}$ and $\psi^{J,k',h'/N_p}_{\alpha,\beta,\gamma}$, and other non-local eigenvectors $\psi^{J,k',h'/N_p}_{\alpha,\beta,\gamma}$.

The off-diagonal block, $B^{k,k'}(h,h)$, in serial is given by

$$\begin{aligned} B^{k,k'}(h,h) = & - (1+\delta_{k,0}\delta_{k',0})^{\frac{1}{2}}\delta_{k',k\pm1} \\ & \times \sum_{\alpha,\beta,\gamma} \psi^{J,k,h}_{\alpha,\beta,j}\psi^{J,k',h'}_{\alpha,\beta,j} C^{\pm}_{J,k'} C^{\pm}_{j,k'} M^{(i)}_{\alpha,\alpha',\beta,\beta'} \end{aligned} \tag{5.11}$$

which in parallel becomes,

$$\begin{aligned} B^{k,k'}(h/N_p,h) = & - (1+\delta_{k,0}\delta_{k',0})^{\frac{1}{2}}\delta_{k',k\pm1} \\ & \times \sum_{\alpha,\beta,\gamma} \psi^{J,k,h/N_p}_{\alpha,\beta,j}\psi^{J,k',h'/N_p}_{\alpha,\beta,j} C^{\pm}_{J,k'} C^{\pm}_{j,k'} M^{(i)}_{\alpha,\alpha',\beta,\beta'} \end{aligned} \tag{5.12}$$

for a definition of the terms in equation (5.12) refer to section 5.11 and 2.9.1.

Both the DVR^2-FBR^1 transformation and the building of the off-diagonal blocks are performed in PDVR3DJ; the eigenvalues of the 3D Hamiltonian and the off-diagonal blocks are written to file. This was done to minimise I/O between PDVR3DJ and PROTLEV3, and also to reduce storage requirements. These I/O and storages restrictions were present on machines such as the Cray T3E and thus mainly historic; they are no longer significant problem. However the algorithm has remained unaltered. The parallel version of ROTLEV3 [121], PROTLEV3 [13], reads these eigenvalues and the off-diagonal blocks to build the distributed Coriolis coupled Hamiltonian, as shown in figure 5.12.

The fully coupled Coriolis Hamiltonian, $\hat{H}^{J,k}$, is then diagonalised using the parallel iterative diagonaliser PARPACK [14]. PARPACK is a parallel implementation of ARPACK [123] which uses the implicit restarted Arnoldi method for solving large sparse matrices. Solving $\hat{H}^{J,k}$ gives eigenvalues, η_l, and eigenfunctions, $\psi^{J,l}_{k,i}$. The eigenvectors

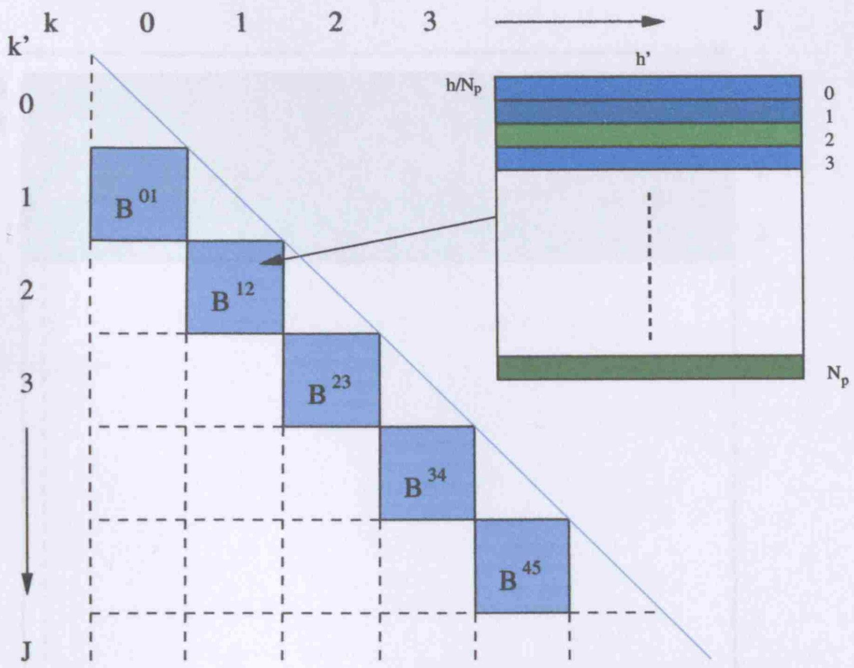

Figure 5.12: The structure of the Coriolis fully coupled Hamiltonian, $H^{J,k}$ which is constructed by PROTLEV3 [13]. The shaded regions, the diagonal and off-diagonal blocks, represent the only non-zero elements in this sparse matrix. The distribution of the off-diagonal block, $B^{k,k'}(h,h')$ across processors in shown in the enlargement. Each processor has a $B^{k,k'}(h/N_p,h')$ segment of each block.

as returned by PARPACK are such that each processor has $\psi^{J,l}_{(k,i)/N_p}$ segment, as illustrated in figure 5.13. In order to write the eigenvectors to file such that the eigenvectors are in sequential order MPI-2 I/O was utilised. Thus all N_p processors write simultaneously to different parts of a single file.

The general algorithm for PROTLEV3 is given below:

1. Root process reads diagonal elements η_i and broadcasts data to all processors
2. Root process reads in off-diagonal block $B^{k,k'}(h,h')$ and broadcast data to all processors
3. The $B^{k,k'}(h,h')$ block is distributed among processors, to create the global Hamiltonian matrix (figure 5.12)
4. The Hamiltonian is diagonalised to give rotation-vibration energy levels, η_l, and eigenfunctions, $\psi^{J,l}_{k,i}$.
5. Optionally save $\psi^{J,l}_{k,i}$ to disk.

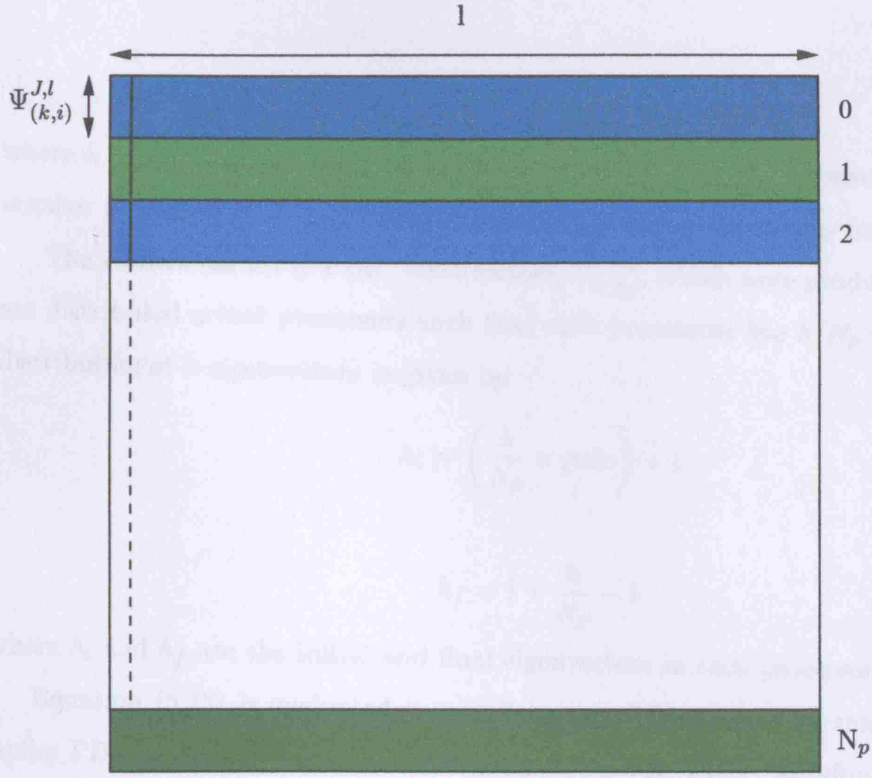

Figure 5.13: The distribution across, N_p, processors of, l, eigenvectors, $\psi^{J,l}_{k,i}$, produced by PARPACK [14].

6. Transform $\psi^{J,l}_{k,i}$ back onto a DVR grid to form $d^{J,k,h}_{k,\alpha,\beta,j}$

7. Save $d^{J,k,h}_{k,\alpha,\beta,j}$ to disk

5.5.1 Back transformation

The FBR eigenvectors $\psi^{J,l}_{k,i}$ need to be transformed onto the original DVR grid. This transformation is given by

$$d^{J,l}_{k,\alpha,\beta,j} = \sum_h \psi^{J,l}_{k,i} \psi^{J,k,h}_{\alpha,\beta,j} \tag{5.13}$$

A parallel algorithm was developed and implemented into PROTLEV3 to accomplish the above transformation in parallel.

The FBR rotational eigenvectors, $\psi^{J,l}_{k,i}$, are redistributed from the arrangement shown in figure 5.13 to one where each processor has l/N_p eigenvectors. The distribution of l eigenvectors is given by

$$l_i = \left(\frac{l}{N_p} \times proc \right) + 1 \tag{5.14}$$

$$l_f = i + \frac{l}{N_p} - 1 \tag{5.15}$$

where l_i and l_f are the initial and final eigenvectors in each processor, N_p is the total number of processors and *proc* is the process identifier, which goes from 0 to $N_p - 1$.

The vibrational DVR^{2}FBR^1 eigenvectors, $\psi^{J,k,h}_{\alpha,\beta,j}$, which were produced in PDVR3DJ are distributed across processors such that each processors has h/N_p eigenvectors. The distribution of h eigenvectors is given by

$$h_i = \left(\frac{h}{N_p} \times proc\right) + 1 \tag{5.16}$$

$$h_f = i + \frac{h}{N_p} - 1 \tag{5.17}$$

where h_i and h_f are the initial and final eigenvectors in each processor.

Equation (5.13) is evaluated in parallel using PBLAS parallel matrix-matrix multiplier PDGEMM [11]. This produces l $d^{J,l}_{k,\alpha,\beta,j}$ DVR^2-FBR^1 wavefunctions which are distributed such that each processor has l/N_p wavefunctions. The wavefunctions are written to file simultaneously using MPI-2 I/O.

The parallel algorithm is summarised below:

1. Redistribute rotational eigenvectors, $\psi^{J,l}_{k,i}$, such that each processor has l/N_p eigenvectors.

2. Begin loop over k

3. Read in vibrational DVR eigenvectors, $\psi^{J,k,h}_{\alpha,\beta,j}$, such that each processor has h/N_p eigenvectors

4. Perform transformation using parallel matrix-matrix multiplier PDGEMM [11] producing l/N_p DVR wavefunctions, $d^{J,l}_{k,\alpha,\beta,j}$, per processor.

5. Save $d^{J,l}_{k,\alpha,\beta,j}$ to disk

6. Next k, i.e. goto 2

5.5.2 Summary of changes to PROTLEV3

I made a number of changes to the PROTLEV3 program, a summary of these changes are listed below:

- Re-writing of diagonalisation routines for optimisation
- The re-writing of all the I/O including the extensive use of MPI-2 I/O routines [116]
- Rotation-vibration energy levels written to file for use with PDIPOLE
- The ability to back transform the rotation-vibration wavefunctions, $\psi^{J,l}_{k,i}$, to the DVR wavefunctions, $d^{J,l}_{k,\alpha,\beta,j}$, and write to disk.

5.6 Dipole Transition Moments: PDIPOLE

Dipole transition moments are calculated using a new parallel program PDIPOLE. PDIPOLE is based of the serial program of Tennyson *et al*, DIPOLE3 [43]. DIPOLE3 had been parallelised by Harris [128]. This parallelisation was done using OpenMP [117] for the shared memory architecture. Although OpenMP is particularly suited to the shared memory architecture, it had mixed success. This was thought to be because runs of the program required large amounts of memory which could not all be stored local to the processor, thus was distributed implicitly by OpenMP. This led to large amounts of communication in data transfer, giving unreliable and inefficient performance. A new algorithm has been developed which is suited to massively parallel architectures such as HPC*x*.

The parallel algorithm developed and used is relatively simple and requires minimal communication; this is important on a distributed memory system as inter processor communication is most likely to be the bottleneck in any program. The algorithm essentially involves parallelising two parts of the serial program, DIPOLE3 [43], the transformation of the wavefunctions, $d^{Jpl}_{kj\alpha\beta}$, (Equation (3.55)) and the actual intensity calculation (Equation (3.56)). The parallel decomposition of the problem is achieved by distributing the basis of each wavefunction across processors, such that each processor has k $(j,\alpha,\beta)/N_p$ segments of each wavefunction $d^{Jpl}_{kj\alpha\beta}$. The distribution is given by

$$i = \left(\frac{\alpha\beta j}{N_p} \times proc\right) + 1 \tag{5.18}$$

$$f = i + \frac{\alpha\beta j}{N_p} - 1 \tag{5.19}$$

where i and f are the initial and final grid points respectively on each processor, N_p is the total number of processors and $proc$ is the processor identifier, which goes from 0 to

$N_p - 1$. The transformation in parallel is therefore given by

$$c_{kz}^{Jpl} = \sum_n (w_n)^{\frac{1}{2}} P_{jk}(x_n) d_z^{J,k,l} \tag{5.20}$$

where z goes from i to f; the matrices w_n and $P_{jk}(x_n)$ are trivially calculated, thus can be replicated on each processor. This transformation is performed using BLAS matrix matrix multiplication routine DGEMM [129].

The evaluation of the line strength is performed in parallel by evaluating the matrix multiplication and summation $\sum_{\alpha\beta j} c_{k'\alpha\beta j}^{J'p'l'} c_{k''\alpha\beta j}^{J''p''l''} \mu_\nu^m(\alpha\beta j)$ on the local portion of the wavefunction. Therefore each processor performs the following

$$\sum_{z=i}^{f} c_{k'z}^{J'p'l'} c_{k''z}^{J''p''l''} \mu_\nu^m(z) \tag{5.21}$$

where z goes from i to f, as given by (5.18) and (5.19), each processor only works with the local portion of the wavefunction. The matrix $\mu_\nu^m(z)$ is replicated on each processor. Again the matrix-matrix multiplication is performed by BLAS routine DGEMM [129]. An MPI global reduction routine places the global sum on the root process, which completes the evaluation of equation (3.56) to give the line strength S($f - i$). The global reduction operation represents the only communication in the procedure; however this is a trivial amount of data, being only N_p double precision numbers. More significantly a slight load imbalance occurs as the root process alone evaluates the remaining portion of equation (3.56); Einstein A-coefficient, A_{if}; integrated absorption coefficient, $I(\omega_{if})$; and finally outputs all the transitions to disk.

The parallel algorithm is summarised below:

1. `All processors calculate dipole moment at the radial grid points and angular integration points`
2. `Begin to loop over k`
3. `Read in` $(j, \alpha, \beta)/N_p$ `segment of wavefunction` $d_{\alpha,\beta,j'}^{J',k',l'}$ `, and transform to common grid, equation (5.20).`
4. `Read in` $(j, \alpha, \beta)/N_p$ `segment of wavefunction` $d_{\alpha,\beta,j''}^{J'',k'',l''}$ `wavefunctions, and transform to common grid, equation (5.20)`
5. `Evaluate the following part of line strength equation`

$$\sum_{z=i}^{f} c_{k'z}^{J'p'l'} c_{k''z}^{J''p''l''} \mu_\nu^m(z)$$

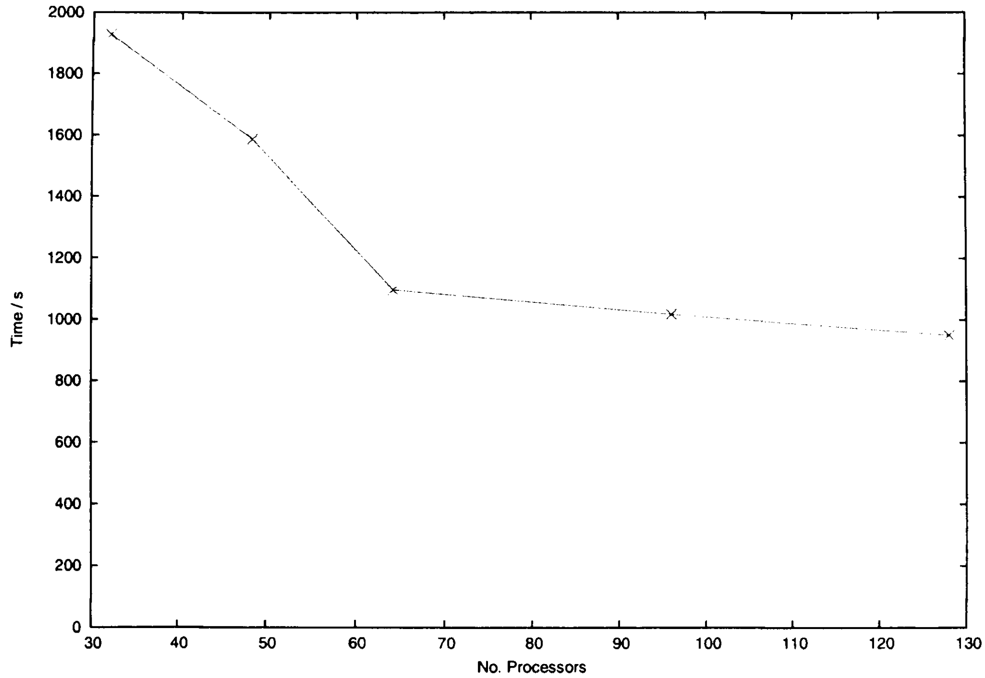

Figure 5.14: Total time taken by PDIPOLE to calculate all the transitions between 2112 $J = 2$ e and $J = 2$ f levels. The DVR grid consisted of n_{r_2}=96, n_{r_1}=36 and $n_\theta = 32$

6. Perform global sum placing the result on the root processor
7. Next k, i.e. goto 3
8. Root processor calculate S($f-i$) by completing the evaluation of line strength equation (3.56)
9. Root processor calculates A_{if} and $I(\omega_{if})$ (equations (3.60) and (3.61)) and outputs transitions.

5.6.1 Performance

The performance of the PDIPOLE program was determined from a $J = 2$ e to $J = 2$ f run for a varying number of processors. The results of this are plotted in figure 5.14

There is a near two fold speed up between using 32 and 64 processors, but virtually none from 64 to 128. This can be explained as a consequence of splitting a fixed size problem into ever smaller pieces. Thus each processor does increasingly less computation relative to communication. Also there is Amdahl's law; certain portions of PDIPOLE are inherently serial, such as the writing out of the transitions to file. No increase in the number of processors can speed these portions up; thus we reach a level where no speed-up can be achieved by adding additional processors. However as the problem size is increased it should increase the time the program spends in parallel parts of the program and thus make the program more scalable.

Chapter 6

Near-Dissociation Convergence

Performing rotation-vibration calculations which extend all the way to dissociation for the H_3^+ molecule is a formidable challenge. In this chapter I present the convergence testing of the basis sets used to calculate energy levels, wavefunctions, and dipole transitions in the high energy regime. All calculations pertaining to dissociation, that is all the calculation outlined in this section, use the dissociating potential energy surface of Polyansky *et al* [3].

Adequate convergence needs to be achieved all the way to dissociation, as this is the area of particular interest. For H_3^+ the dissociation energy is approximately 35 000 cm^{-1} [130, 131]. The dissociation energy of the Polyansky potential energy surface is calculated more precisely in this work.

The method used to solve the rotational-vibrational problem obeys the variational principle (refer to section 2). Thus by means of judicious choice of various parameters, the calculation can not only produce the best results but also minimise the cost of the calculation. The "cost of calculation", refers to the run-time of a calculation, the number of processors, the amount core memory needed, and the amount of disk space needed. There are several parameters used by PDVR3DJ and PROTLEV3 which affect the convergence of the energy levels and consequently the quality of the wavefunctions. The value these parameters may take to reach convergence must be weighed against any increase in computational cost.

6.1 Dissociation energy

The lowest dissociation channel for H_3^+ is the reaction

$$H_3^+ \rightarrow H_2(\nu = 0) + H^+ \tag{6.1}$$

There are two different definitions of the dissociation energy: the classical, D_e, and the quantum, $D_\circ$. Classically the dissociation energy is defined as the difference between the absolute bottom of the potential for the species of interest, and the energy at which it is no longer bound. Quantum mechanically the zero point energy must be considered. For H_3^+ the zero point energy is 4361.7 cm^{-1} (refer to section 4.1). The situation is further complicated for H_3^+ as the ground state is forbidden and the first occupied state is the J=1, K=1 level, 64.11 cm^{-1} above the ground state. The lowest dissociation channel for H_3^+ is that

The precise value of the dissociation energy is not known for certain. Cosby and Helm [130] determine from photo-ionisation and photo-dissociation of H_3 that $D_\circ$ for H_3^+ as 4.373 ± 0.021 eV (35270.6 cm^{-1}). This is the dissociation energy from the first occupied state to dissociation. While Lie and Frye [131] using *ab initio* techniques found $D_\circ$ from the zero point energy to dissociation to be 4.381 ± 0.002 eV (34980.3 cm^{-1}). These two energies are compared in figure 6.1 where the different definitions of $D_\circ$ are taken into account, there is a difference of some 350 cm^{-1} between theory and experiment. This discrepancy may be attributed to the fact that Cosby and Helm determine their value for H_3 and not a direct measurement on H_3^+.

The dissociation energy for the potential energy surface used in this work [3] was calculated in the following manner. If r_2 is taken to infinity then the H_3^+ molecule can be regarded as dissociated to H^+ and H_2. The first bound state of this H_2 then gives the H_3^+ dissociation limit for the potential energy surface. This can be calculated by solving the Schrödinger equation for this "diatomic" molecule. The potential for the "diatomic" is a cut through the full hyper-surface at an infinite r_2, arbitrary θ, and therefore r_1 represents the distance between the two hydrogen nuclei. The program LEVEL by Le Roy [132] was used to solve this "diatomic" problem via direct numerical integration and thus obtain the dissociation energy. The energy from the bottom of the potential to $H_2(\nu = 0)$ was calculated to be 4.869 eV (39273.24 cm^{-1}). From figure 6.1 this is approximately 70 cm^{-1} greater than the value given by Lie and Frye.

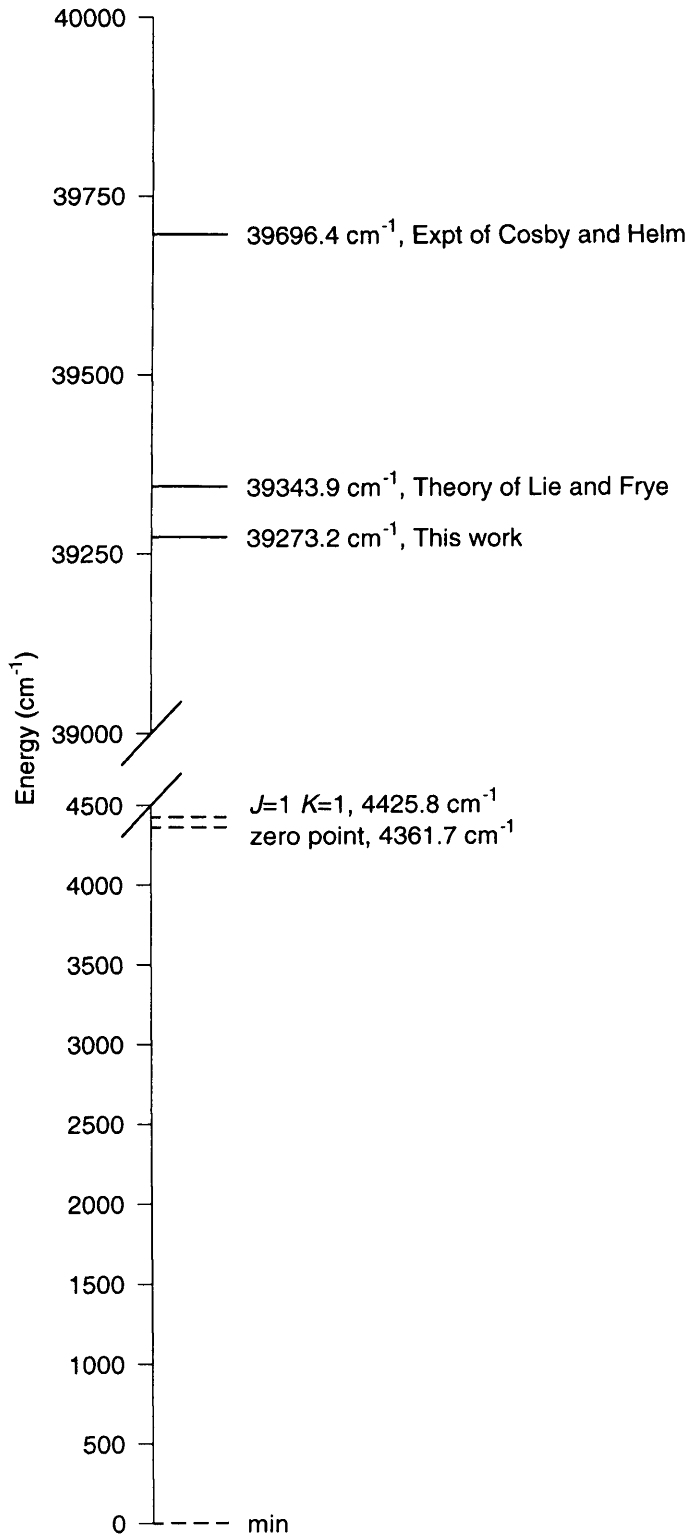

Figure 6.1: An energy diagram showing significant energies of H_3^+. Note the break in the scale of the y-axis.

6.2 Convergence of the Vibrational Problem: PDVR3DJ

There are various parameters which can be varied to improve convergence of the vibrational problem: the parameters for the basis functions, the number of points used for each coordinate, n_θ, n_{r_1} and n_{r_2} for θ, r_1, and r_2 respectively; the size of the final Hamiltonian, N.

For the purposes of convergence testing the energy levels are taken relative to the first $J = 0$ state which is 4361.60 cm^{-1} above the bottom of the potential. Thus the relative dissociation energy is 34911.64 cm^{-1}. It is known that the convergence characteristics of the even, $q = 0$, and odd, $q = 1$, vibrational states are different [15], therefore convergence testing needs to be performed on both.

6.3 Basis function optimisation

Spherical oscillator functions are used as the basis for the final coordinate, r_2. These take two parameters, α and ω. Morse oscillator functions are used to represent the r_1 coordinate, these take parameters r_e, D_e and ω_e. Legendre functions are used for the angular coordinate. Through numerical testing, Henderson *et al* [81] found that the optimal coordinate ordering with respect to convergence and computational cost for H_3^+ is $\theta \rightarrow r_1 \rightarrow r_2$. It has also been found that the basis parameters chosen for the final coordinate are most crucial to convergence; thus α and ω were optimised. The values of the Morse oscillator parameters used were $r_e = 2.1$ a$_\circ$, $D_e = 0.1$ E$_h$ and $\omega_e = 0.0118$ s^{-1}.

Calculations were performed with various values of ω and between the values of 0 and 1 for α. Henderson *et al* [15] used $\omega = 0.0095$, this was taken as a starting point for optimisation.

The mean energy differences between energy levels as a function of α are tabulated in tables 6.1 and 6.2. The differences between energy levels calculated with different values of α are shown in figures 6.2 and 6.3. It is evident that convergence improves with increasing α for even states, while the opposite is true for odd states. In order to perform dipole transition calculations the wavefunctions must be on the same radial grid. If transitions between odd and even states are to be calculated, as is the intention of this work, then the same value of α is needed for even and odd states; otherwise a costly transformation is required. As the variation for odd states is not as great as those

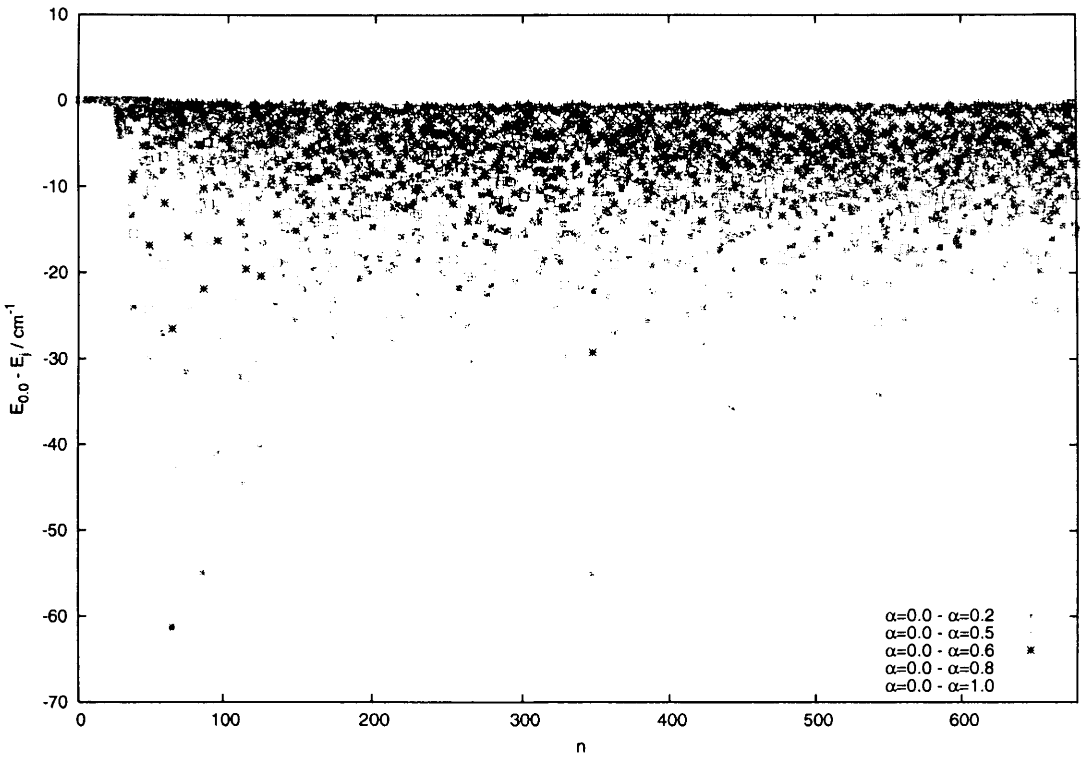

Figure 6.2: Convergence of $J = 0$ even band origins with respect to the value of α. The points indicate the difference of the n^{th} energy level calculated using a particular value of α relative to that calculated with $\alpha = 0.0$

for even states, $\alpha = 0.0$ is preferable. This gives convergence for states up to dissociation to approximately 0.5 cm^{-1} for even states and 1.3 cm^{-1} odd states.

From table 6.3 it is evident that the value of ω has little effect on the average convergence. However it is clear from figures 6.4 and 6.5 that its value has a great effect on high energy levels. Values of 0.0135, 0.0250, and 0.0500 are particularly bad for even states. Therefore a low value of 0.0075 seems appropriate giving convergence of approximately 0.14 cm^{-1} for even states and 0.28 cm^{-1} for odd states.

6.3.1 DVR grid optimisation

The computational cost increases approximately linearly with n_θ, n_{r_1} and n_{r_2}. It must be noted that the DVR is not strictly variational (refer to section 2.9) but can be assumed to be quasi variational, to a good approximation. That is states may converge from below or above with increasing a variational parameter. The general method of converging a DVR grid is to start with varying the first coordinate, while keeping the other parameters constant. When adequate convergence is attained, the second coordinate becomes the

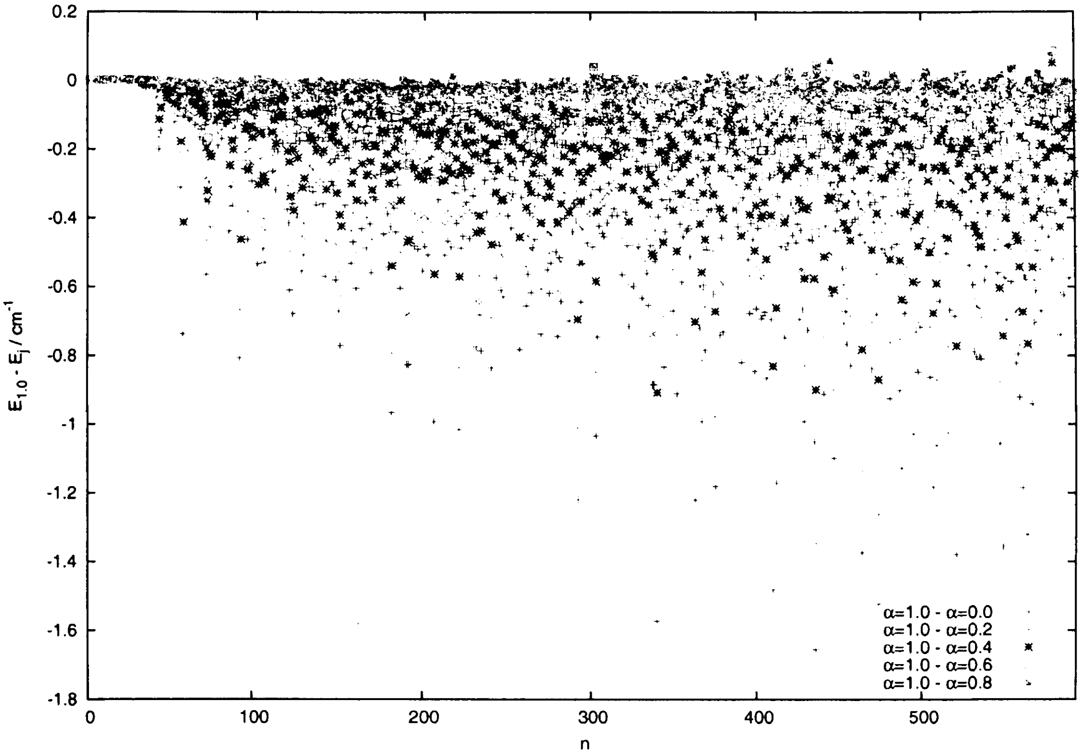

Figure 6.3: Convergence of $J = 0$ odd band origins with respect to the value of α. The points indicate the difference of the n^{th} energy level calculated using a particular value of α relative to that calculated with $\alpha = 0.0$

Table 6.1: The mean energy differences (cm^{-1}) between even energy levels calculated with various values of α and α = 0.0. The values of the other parameters are : N=29952, n_{r_2}=96, n_{r_1}=36, n_θ = 32 and ω = 0.0095.

	Max. Energy (cm^{-1})		
	15000	25000	Dissociation
mean($E_{0.0-0.1}$)	-0.04	-0.20	-0.25
mean($E_{0.0-0.2}$)	-0.14	-0.73	-0.87
mean($E_{0.0-0.3}$)	-0.28	-1.47	-1.77
mean($E_{0.0-0.4}$)	-0.45	-2.36	-2.85
mean($E_{0.0-0.5}$)	-0.64	-3.37	-4.07
mean($E_{0.0-0.6}$)	-0.84	-4.47	-5.39
mean($E_{0.0-0.7}$)	-1.06	-5.63	-6.79
mean($E_{0.0-0.8}$)	-1.28	-6.84	-8.25
mean($E_{0.0-0.9}$)	-1.51	-8.08	-9.76
mean($E_{0.0-1.0}$)	-1.74	-9.36	-11.30

Table 6.2: The mean energy differences (cm^{-1}) between odd energy levels calculated with various values of α and $\alpha = 1.0$. The values of the other parameters are : N=29952, n_{r_2}=96, n_{r_1}=36, $n_\theta = 32$ and $\omega = 0.0095$.

	Max. Energy (cm^{-1})		
	15000	25000	Dissociation
mean($E_{1.0-0.0}$)	0.00	0.01	0.03
mean($E_{1.0-0.1}$)	0.00	0.03	0.07
mean($E_{1.0-0.2}$)	0.00	0.06	0.12
mean($E_{1.0-0.3}$)	0.00	0.08	0.18
mean($E_{1.0-0.4}$)	0.00	0.11	0.23
mean($E_{1.0-0.5}$)	0.00	0.13	0.28
mean($E_{1.0-0.6}$)	0.00	0.15	0.32
mean($E_{1.0-0.7}$)	0.00	0.17	0.36
mean($E_{1.0-0.8}$)	0.00	0.18	0.38
mean($E_{1.0-0.9}$)	0.00	0.18	0.38

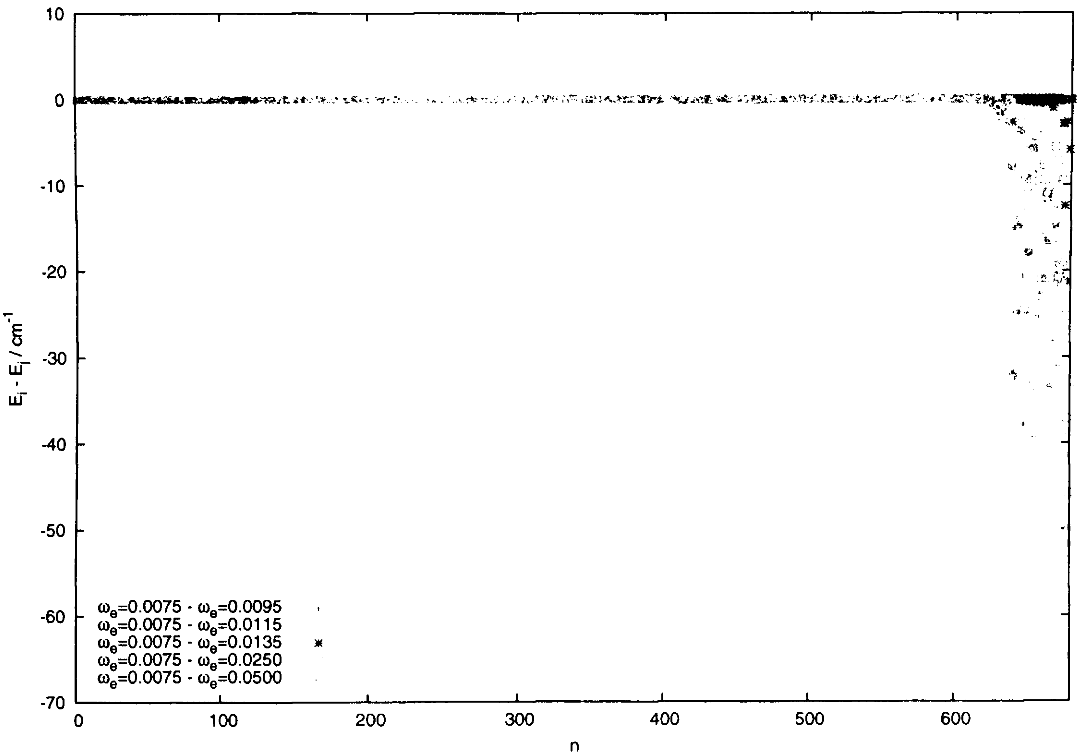

Figure 6.4: Convergence of $J = 0$ even band origins with respect to the value of ω. The points indicate the difference of the n^{th} energy level calculated using a particular value of ω relative to that calculated with $\omega = 0.0075$

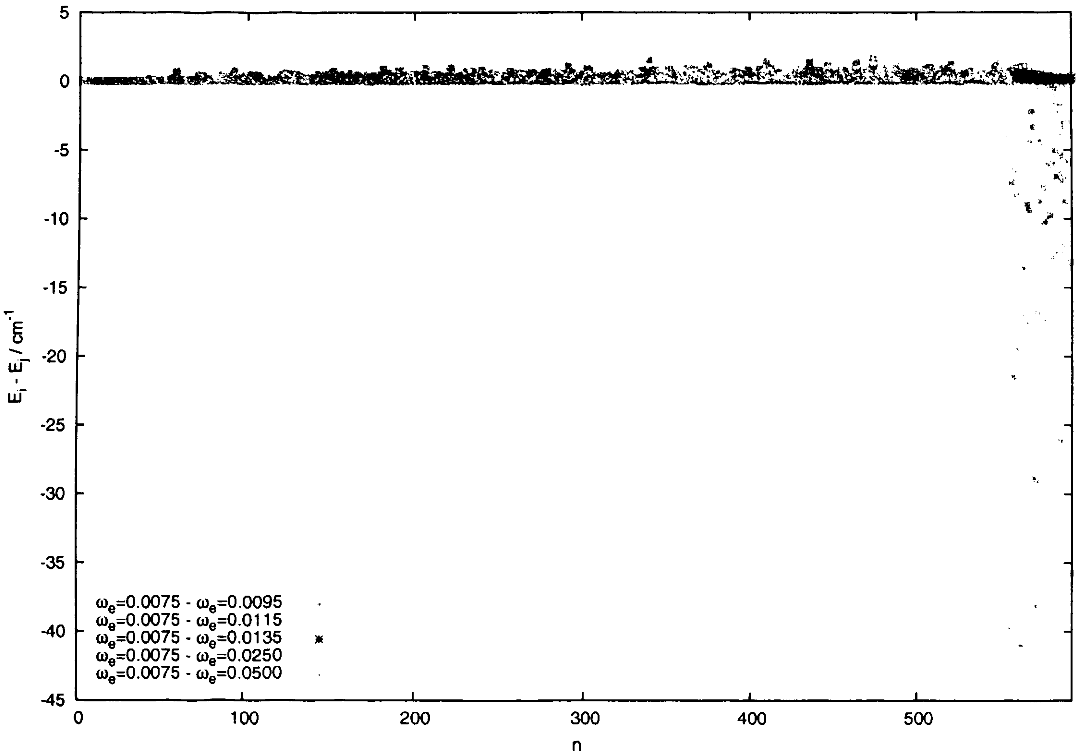

Figure 6.5: Convergence of $J = 0$ odd band origins with respect to the value of ω. The points indicate the difference of the n^{th} energy level calculated using a particular value of ω relative to that calculated with $\omega = 0.0075$

Table 6.3: The mean energy differences (cm^{-1}) between energy levels calculated with various values of ω and $\omega = 0.0075$. The values of the other parameters are : N=29952, n_{r_2}=96, n_{r_1}=36, $n_\theta = 32$ and $\alpha = 0.0$.

	EVEN			ODD		
Max. Energy (cm^{-1})	15000	25000	Dissociation	15000	25000	Dissociation
mean($E_{0.0075-0.0095}$)	0.00	0.00	0.00	0.00	0.04	0.08
mean($E_{0.0075-0.0115}$)	0.00	0.00	0.00	0.00	0.06	0.13
mean($E_{0.0075-0.0135}$)	0.00	0.00	0.00	0.00	0.08	0.18
mean($E_{0.0075-0.0250}$)	0.00	0.00	0.08	0.00	0.14	0.23
mean($E_{0.0075-0.0500}$)	0.00	0.00	-1.00	0.00	0.17	-0.55
mean($E_{0.0075-0.0750}$)	0.00	0.00	-1.41	0.00	0.19	-0.83

Table 6.4: The mean energy differences (cm^{-1}) between energy levels calculated with various values of n_{θ_1} and n_{θ_1} = 32. The values of the other parameters are : N=29952, n_{r_2}=96, n_{r_1} = 36, α = 0.0, and ω = 0.0075.

	EVEN			ODD		
Max. Energy (cm^{-1})	15000	25000	Dissociation	15000	25000	Dissociation
mean(E_{32-36})	0.00	0.00	0.00	0.00	0.00	0.00
mean(E_{32-42})	0.00	0.00	0.00	0.00	-0.04	-0.08
mean(E_{32-46})	0.00	0.00	0.00	0.00	-0.04	-0.09
mean(E_{32-50})	0.00	0.00	0.00	0.00	-0.04	-0.08

variational parameter. The procedure is then repeated for the third and final coordinate. There is an additional complication associated with the final coordinate becoming the variational parameter. The 3D Hamiltonian is built using a certain number of solutions from each 2D calculation per final grid point. Therefore to ensure that a fair comparison is made, the size of the final 3D Hamiltonian, N, must scale with the number of final grid points, such that equal numbers of 2D solutions are used per grid point.

For the θ coordinate it is clear from table 6.4 that there is little improvement in the mean convergence in using more than 32 points. Figures 6.6 and 6.7 show the differences between a calculation using n_θ = 32 and a calculation using a different value of n_θ. There is some non-variational behaviour as there are both positive and negative differences. Thus some of the states appear to be converging from below, as opposed to from above, which is the expected behaviour. This is most likely due to DVR calculations not being strictly variational, and thus are able to converge from above or below. There is little improvement in convergence for most states in using a n_θ greater then 32, some states, especially near dissociation, show marked improvement in using n_θ = 50. This value converges all the states to within 0.28 cm^{-1} for even states and 0.25 cm^{-1} for odd states.

The mean energy differences for the variation of n_{r_1}, table 6.5, do not clearly indicate the ideal value of n_{r_1}. Figures 6.8 and 6.9 show the difference of the n^{th} energy level calculated using a particular value of n_{r_1} relative to that calculated with n_{r_1} = 30; it is difficult to discern any significant trend. The number of r_1 grid points is limited by the nature of the Morse oscillator-like functions (2.58) used. Both y and r are valid in the range zero to infinity, however for certain values of y the corresponding value of r is negative, which is physically undefined.

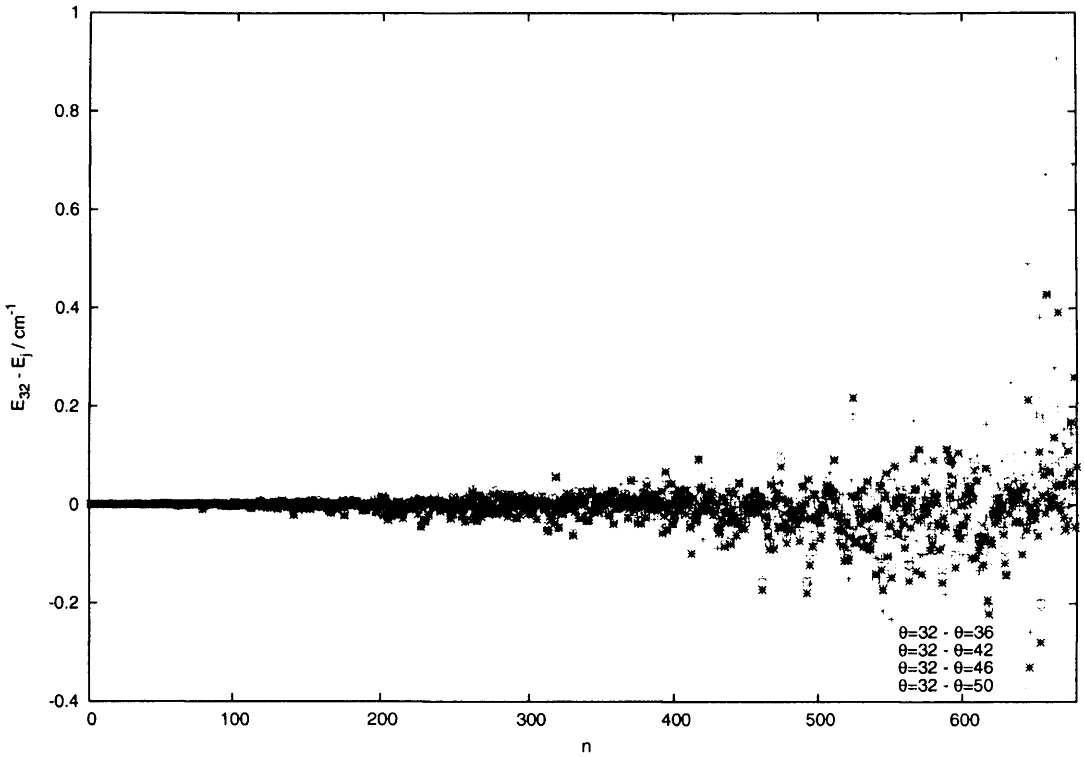

Figure 6.6: Convergence of $J = 0$ even band origins with respect to the value of n_θ. The points indicate the difference of the n^{th} energy level calculated using a particular value of n_θ relative to that calculated with $n_\theta = 32$

Table 6.5: The mean energy differences (cm^{-1}) between energy levels calculated with various values of n_{r_1} and $n_{r_1} = 30$. The values of the other parameters are : N=29952, n_{r_2}=96, $n_\theta = 32$, $\alpha = 0.0$, and $\omega = 0.0075$. Powers of 10 in parenthesis.

	EVEN			ODD		
Max. Energy (cm^{-1})	15000	25000	Dissociation	15000	25000	Dissociation
mean(E_{30-32})	0.00	-0.03	-0.92	0.00	-0.03	-0.57
mean(E_{30-34})	0.00	-0.01	-0.26	0.00	-0.01	0.16
mean(E_{30-36})	0.00	0.03	0.35	0.00	0.03	0.48

As r_2 is the final coordinate, the Hamiltonian needs to be scaled. Hamiltonian sizes of 19968, 29952, 39273, 49920, and 60000 were used for n_{r_2}=88, 96, 104, 112 and 120. The situation is further complicated by the need for parallel computing and the HPCx system, both are discussed in more detail in sections 5.4 and 5.2.5 respectively. To summarise, PDVR3DJ requires that the number of processors used be a multiple of n_{r_2}; HPCx is most efficiently used if multiples of 32 processors are used.

The band origins with respect to n_{r_2} are shown in figures 6.10 and 6.11. Abnormal

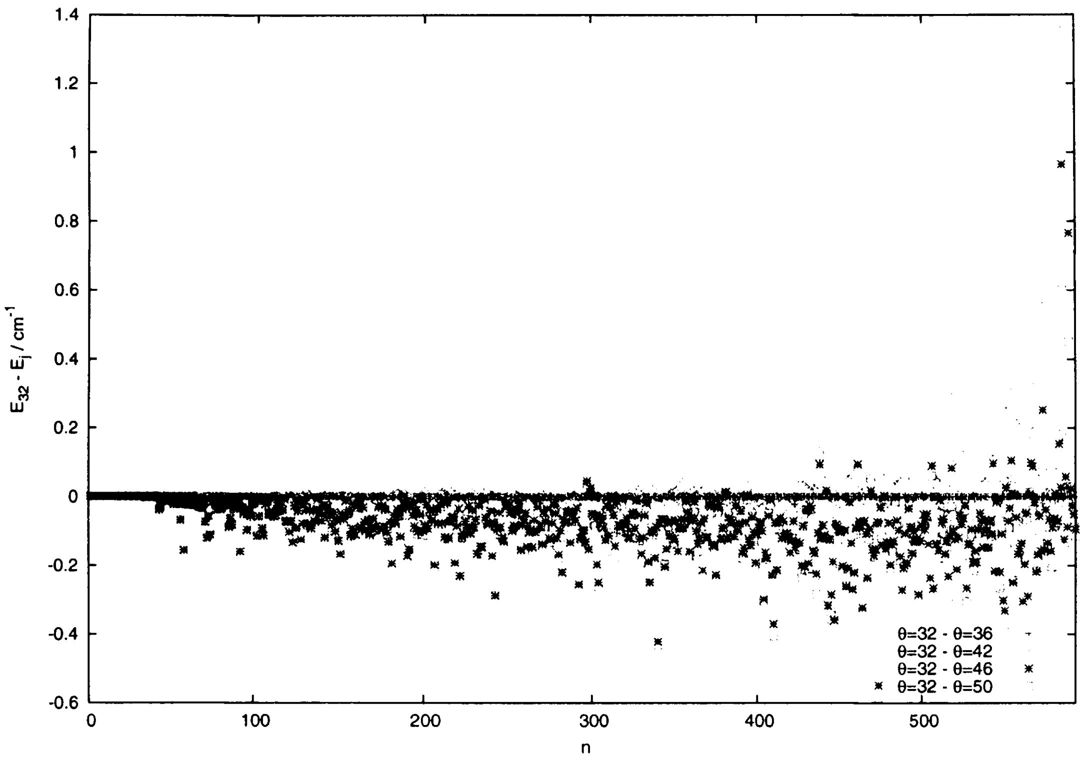

Figure 6.7: Convergence of $J = 0$ odd band origins with respect to the value of n_θ. The points indicate the difference of the n^{th} energy level calculated using a particular value of n_θ relative to that calculated with $n_\theta = 32$

behaviour is shown for n_{r_2}=104, 112, and 120 near dissociation, especially for the even states. This is caused by some of the weights, ω_η, for these values of n_{r_2} underflowing on the machine and being set zero. These weights are used in the kinetic energy terms, (2.44) to build the Hamiltonian (2.42) and are a source of numerical instability. If 96 r_2 grid points are used all states are converged to 0.12 cm^{-1} and 0.42 cm^{-1} for even and odd states respectively, which was judged to be sufficient given the errors in the individual DVR expansions discussed above.

6.3.2 Hamiltonian size optimisation

The size of the Hamiltonian approximately scales quadratically with the amount of core memory and cubically with the runtime. Table 6.7, and figures 6.12 and 6.13 show the convergence as a function of Hamiltonian size. The largest Hamiltonian gave convergence within 2×10^{-6} cm^{-1} for even states and 1×10^{-4} cm^{-1} for odd states. However this comes at a great computational cost, N = 39273 converges states within 0.12 cm^{-1} and 0.08 cm^{-1} for even and odd states respectively.

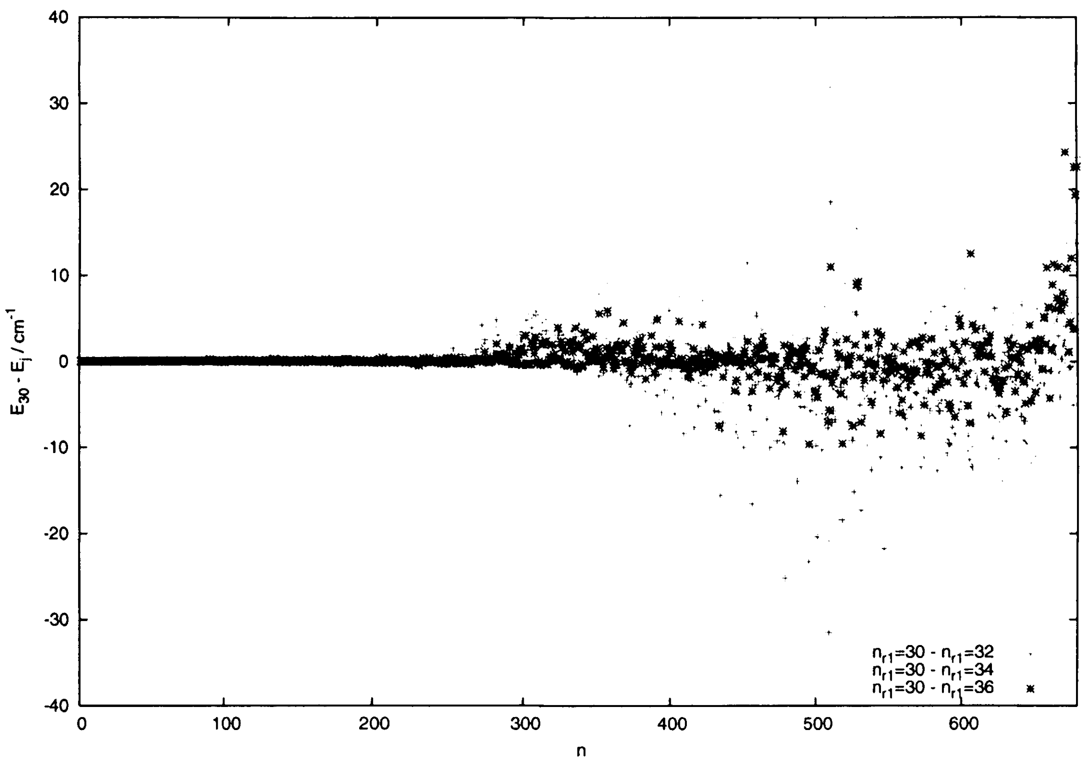

Figure 6.8: Convergence of $J = 0$ even band origins with respect to the value of n_{r_1}. The points indicate the difference of the n^{th} energy level calculated using a particular value of n_{r_1} relative to that calculated with $n_{r_1} = 36$

Table 6.6: The mean energy differences (cm^{-1}) between energy levels calculated with various values of n_{r_2} and $n_{r_2} = 88$. The values of the other parameters are : n_{r_1}=36, $n_\theta = 32$, $\alpha = 0.0$, and $\omega = 0.0075$.

	EVEN			ODD		
Max. Energy (cm^{-1})	15000	25000	Dissociation	15000	25000	Dissociation
mean(E_{88-96})	0.00	0.00	0.00	0.00	0.03	0.08
mean(E_{88-104})	0.00	0.00	0.02	0.00	0.06	0.13
mean(E_{88-112})	0.00	0.00	0.03	0.00	0.08	0.17
mean(E_{88-120})	0.00	0.00	0.08	0.00	0.10	0.22

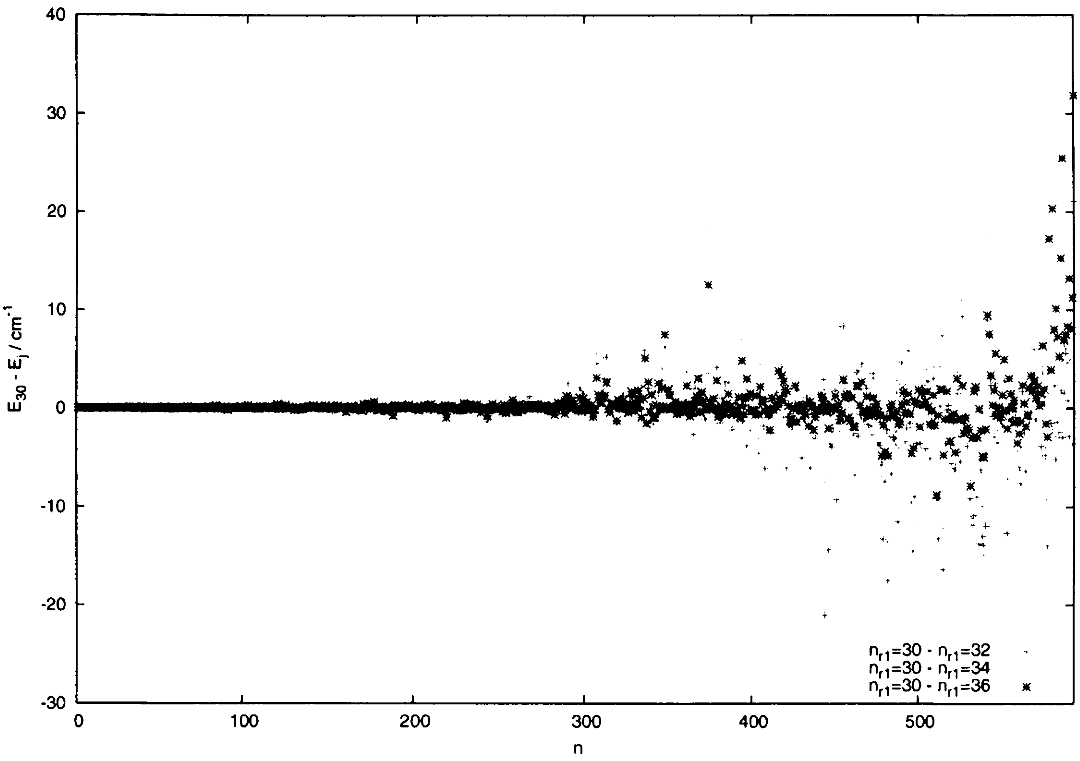

Figure 6.9: Convergence of $J = 0$ odd band origins with respect to the value of n_{r_1}. The points indicate the difference of the n^{th} energy level calculated using a particular value of n_{r_1} relative to that calculated with n_{r_1}

Table 6.7: The mean energy differences (cm^{-1}) between energy levels calculated with various values of N and $N = 19968$. The values of the other parameters are : n_{r_2}=96, n_{r_1}=36, $n_\theta = 32$, $\alpha = 0.0$, and $\omega = 0.0075$.

	EVEN			ODD		
Max. Energy (cm^{-1})	15000	25000	Dissociation	15000	25000	Dissociation
mean($E_{19968-29952}$)	0.00	0.01	0.21	0.00	0.00	0.17
mean($E_{19968-39273}$)	0.00	0.01	0.23	0.00	0.02	0.18
mean($E_{19968-49920}$)	0.00	0.01	0.23	0.00	0.01	0.18
mean($E_{19968-60000}$)	0.00	0.01	0.23	0.00	0.01	0.18

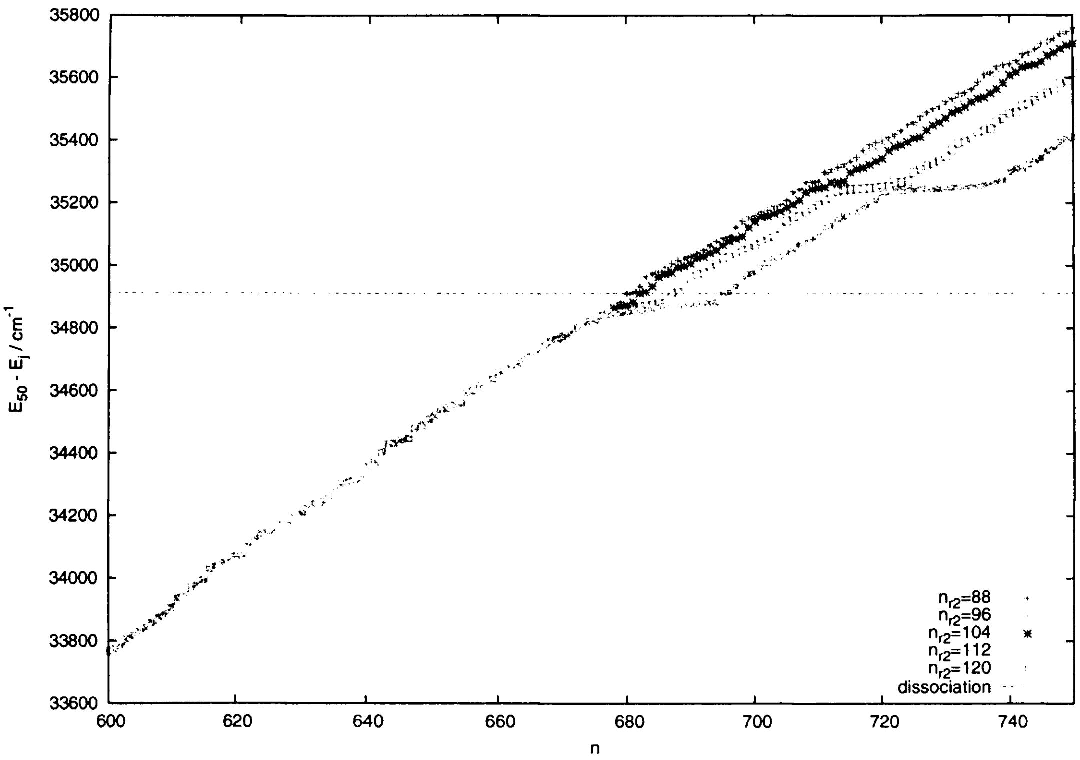

Figure 6.10: Convergence of $J = 0$ even band origins with respect to the value of n_{r_2}. The values of the other parameters are : n_{r_1}=36, $n_\theta = 32$, $\alpha = 0.0$, and $\omega = 0.0075$.

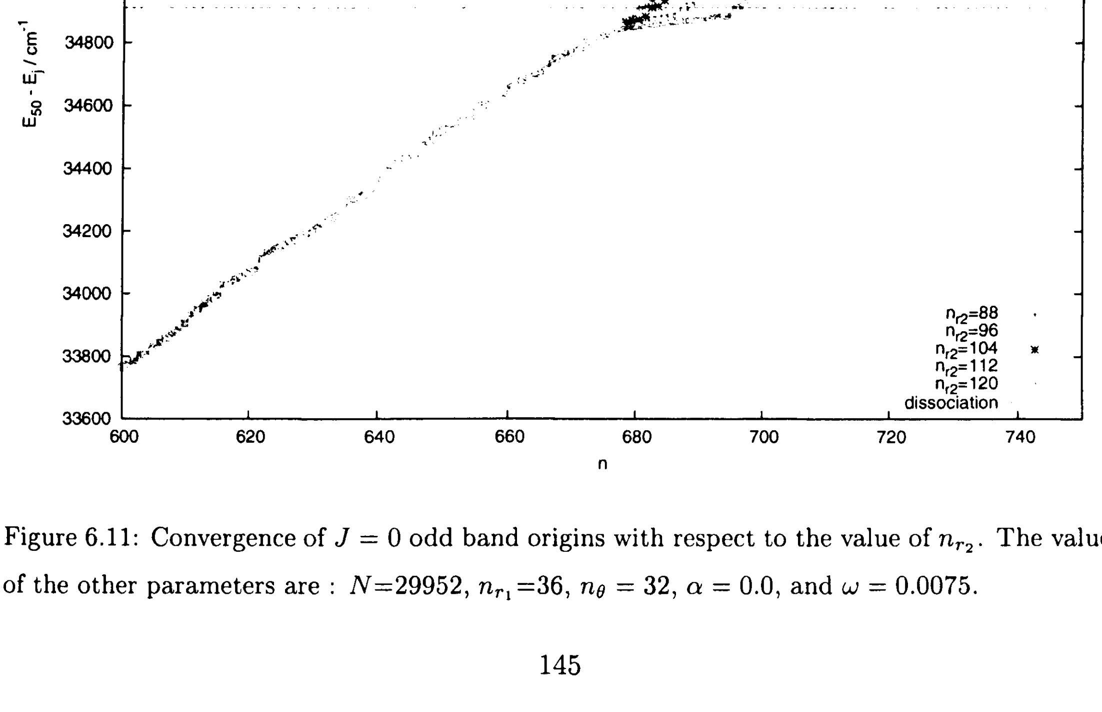

Figure 6.11: Convergence of $J = 0$ odd band origins with respect to the value of n_{r_2}. The values of the other parameters are : N=29952, n_{r_1}=36, $n_\theta = 32$, $\alpha = 0.0$, and $\omega = 0.0075$.

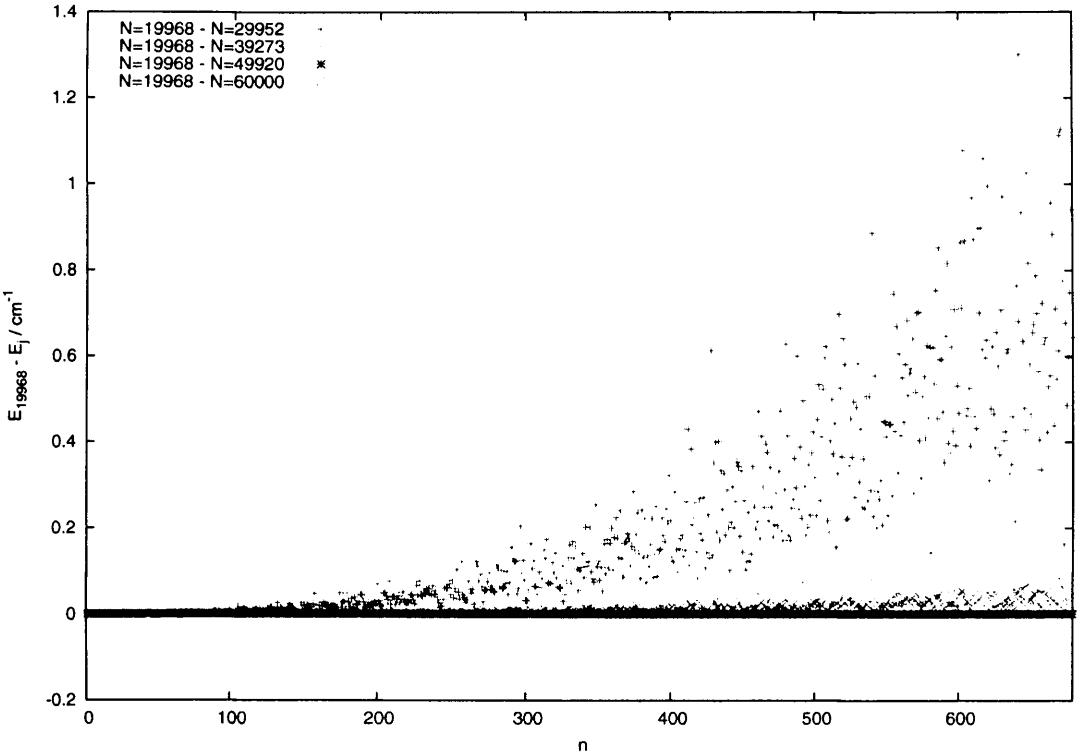

Figure 6.12: Convergence of $J = 0$ even band origins with respect to the Hamiltonian size, N. The values of the other parameters are: n_{r_2}=96, n_{r_1}=36, $n_\theta = 32$, $\alpha = 0.0$, and $\omega = 0.0075$.

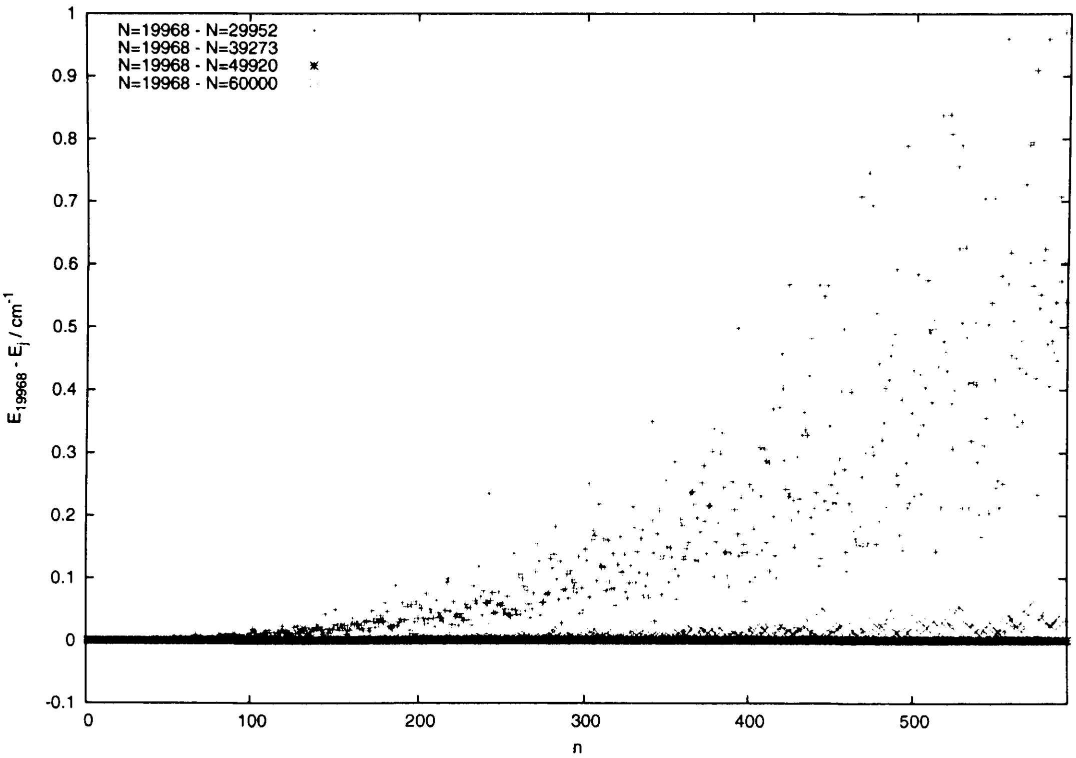

Figure 6.13: Convergence of $J = 0$ odd band origins with respect to the Hamiltonian size, N. The values of the other parameters are: n_{r_2}=96, n_{r_1}=36, $n_\theta = 32$, $\alpha = 0.0$, and $\omega = 0.0075$.

Table 6.8: The mean energy differences (cm^{-1}) between J = 1 energy levels calculated using various values of h and h = 2016. The values of other parameters are : N =29952, n_{r_2}=96, n_{r_1}=36, n_θ = 32, α = 0.0, and ω = 0.0075.

	EVEN		ODD	
p	e	f	e	f
mean($E_{2016-2976}$)	0.02	0.00	0.02	0.00
mean($E_{2016-3936}$)	0.03	0.00	0.03	0.00
mean($E_{2016-4800}$)	0.03	0.00	0.03	0.00

6.4 Convergence of the Rotational Problem: PROTLEV3

The convergence of the rotational problem is largely governed by the number of solutions, h, from the vibrational problem used in the construction of the Hamiltonian. The number of solutions used is directly related to the size of the Hamiltonian, thus the cost of the calculation. The number of solutions, rotational-vibrational energy levels and wavefunctions required must be less then h (refer to section 2.9). Again the needs of parallel computing limits the value h may take to a multiple of the number of processors used by PROTLEV3. The convergence is also dependent of the rotational parity, p, which is 0 or 1 for e and f states respectively.

The energy levels are taken relative to first $J = 0$ state which is 4361.60 cm^{-1} above the bottom of the potential. Thus the relative dissociation energy is 34911.64 cm^{-1}.

The mean energy differences between $h = 2016$ and $h = 2976, 3976, 4800$ for $J = 1$ are shown in table 6.8; they are also plotted in figures 6.14 to 6.17. The convergence of the f states is clearly not dependent on h and thus a value of h which gives enough solutions should be used. For the e states there is an improvement in convergence with increasing h for both the even and odd parities. However the improvement in using 3936 solutions as opposed to be 2976 is not sufficient to justify the increased cost of the calculation.

For $J = 2$ the mean energy differences between $h = 2880$ and $h = 3840, 4880, 5760$ are shown in table 6.9. The energy differences are also plotted in figures 6.18, to 6.21. Both the e and f states show improvement in mean convergence with h. The improvement in the f states is slight and no greater then 0.03 cm^{-1}, therefore not justifying the cost of using more than 2880 solutions. The e states show greater improvement in the high energy regime, with the maximum differences near 0.25 cm^{-1}. The difference in using $h = 5760$ instead of $h = 4880$ is slight, so a value of $h = 4880$ should be considered to

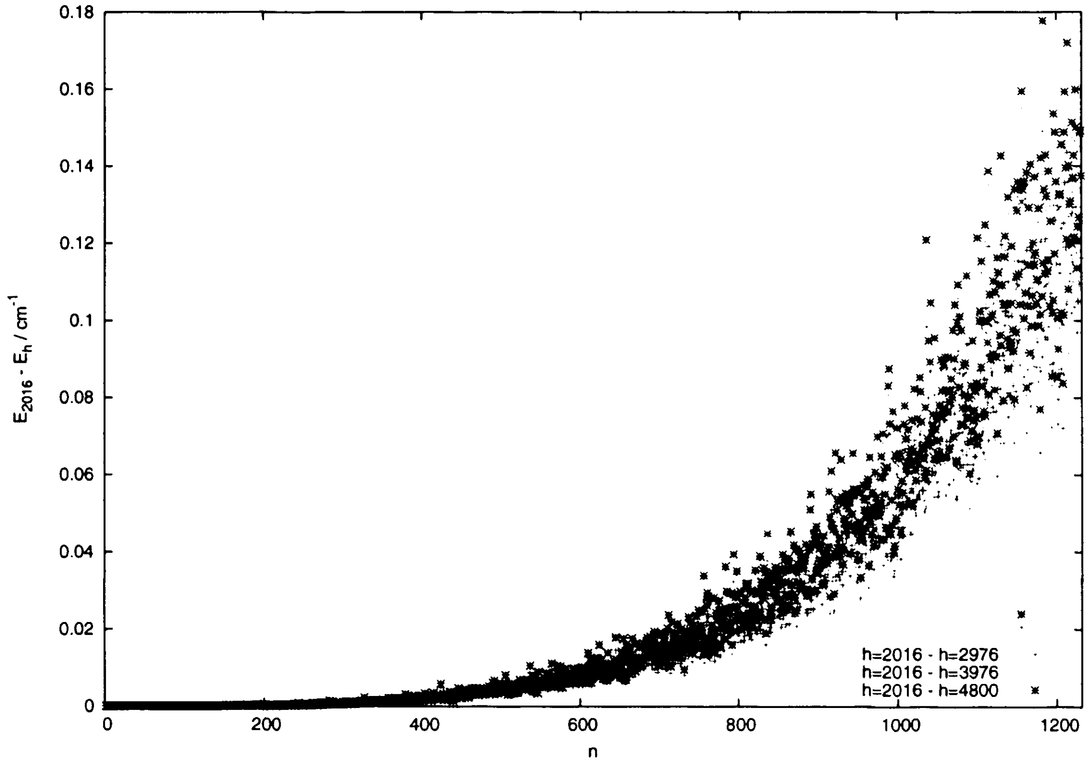

Figure 6.14: The convergence of $J = 1$, even, e states. The points indicate the difference between the n^{th} energy level calculated with $h = 2016$ and other values of h.

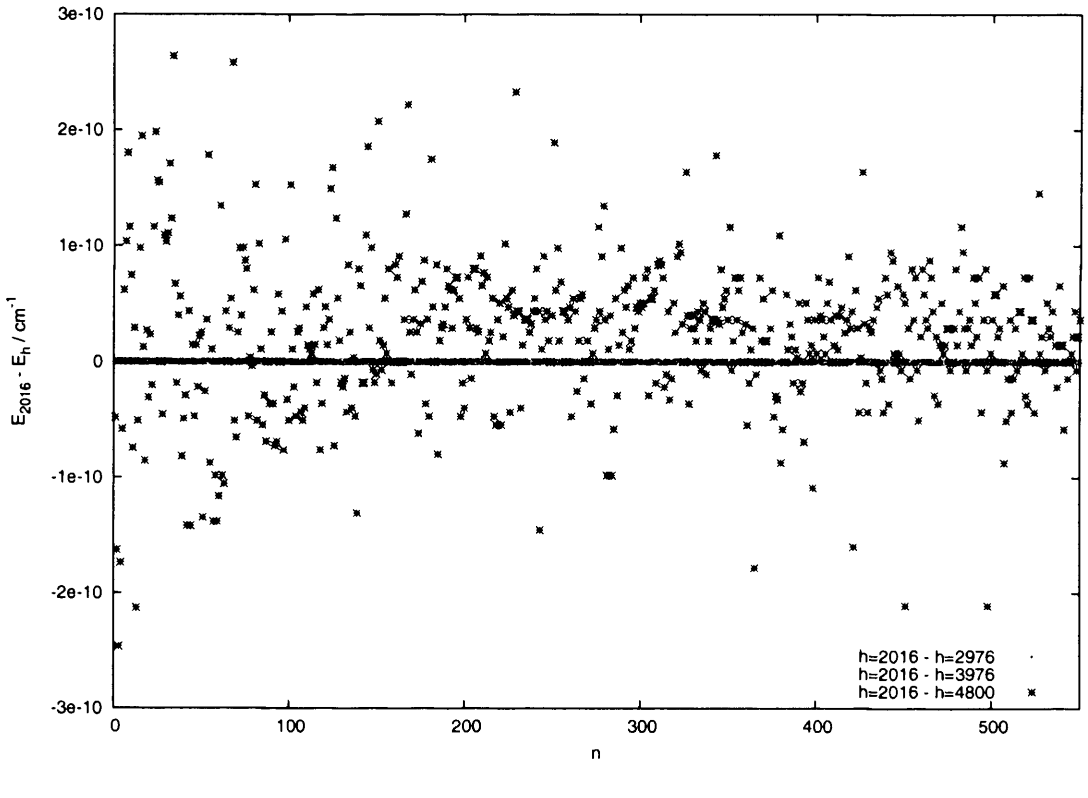

Figure 6.15: The convergence of $J = 1$, even, f states. The points indicate the difference between the n^{th} energy level calculated with $h = 2016$ and other values of h.

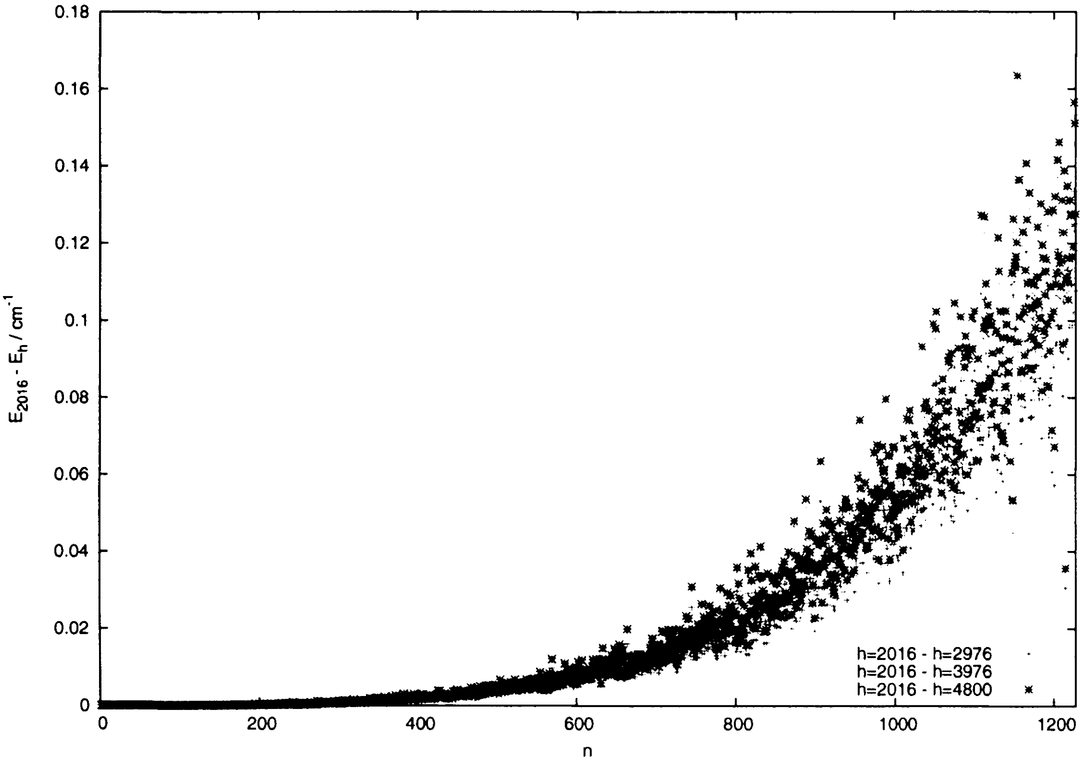

Figure 6.16: The convergence of $J = 1$, odd, e states. The points indicate the difference between the n^{th} energy level calculated with $h = 2016$ and other values of h.

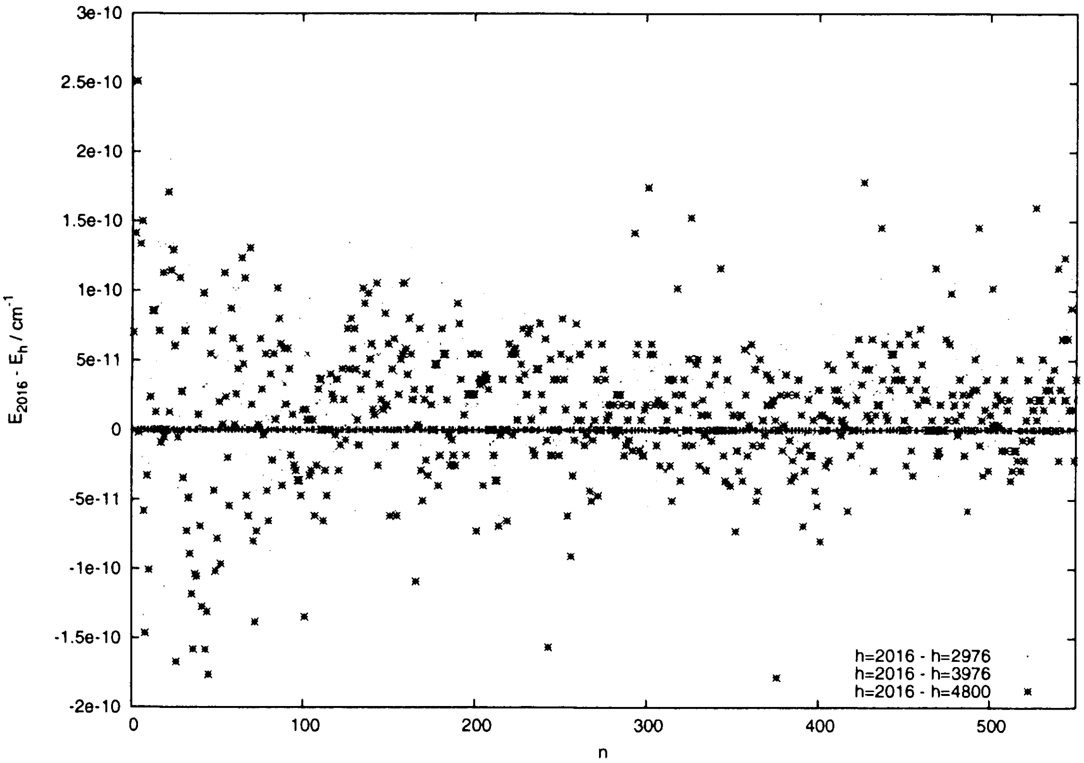

Figure 6.17: The convergence of $J = 1$, odd, f states. The points indicate the difference between the n^{th} energy level calculated with $h = 2016$ and other values of h.

Table 6.9: The mean energy differences (cm^{-1}) between $J = 2$ energy levels calculated using various number of vibrational solutions. The values of other parameters are : N =29952, n_{r_2}=96, n_{r_1}=36, $n_\theta = 32$, $\alpha = 0.0$, and $\omega = 0.0075$.

	EVEN		ODD	
	e	f	e	f
mean($E_{2880-3840}$)	0.02	0.00	0.03	0.00
mean($E_{2880-4880}$)	0.03	0.00	0.03	0.00
mean($E_{2880-5760}$)	0.03	0.00	0.03	0.00

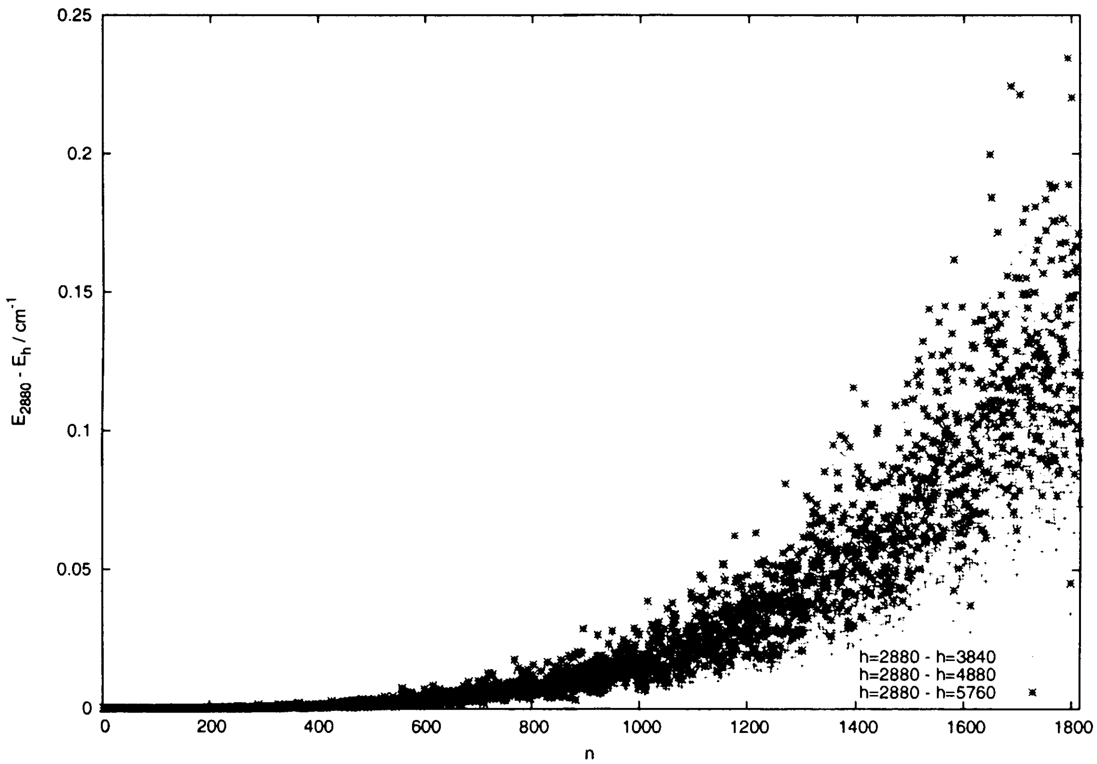

Figure 6.18: The convergence of $J = 2$, even, e states. The points indicate the difference between the n^{th} energy level calculated with $h = 2016$ and other values of h.

converge the high lying states.

In order to ascertain a trend in the value of h needed to adequately converged a rotation-vibration calculation for a given J, a $J = 5$ calculation was performed. The mean energy differences between $h = 2880$ and $h = 3840, 4880, 5760$ are shown in table 6.9. The convergence with respect to h is plotted in figures 6.18 to 6.21.

The $h = 6912$ calculation was near the boundary of what was computationally feasible with the PROTLEV3 program on the HPCx system. This gave convergence within 0.32 cm^{-1} for the e states and 0.07 cm^{-1} for the f states. The convergence of the e

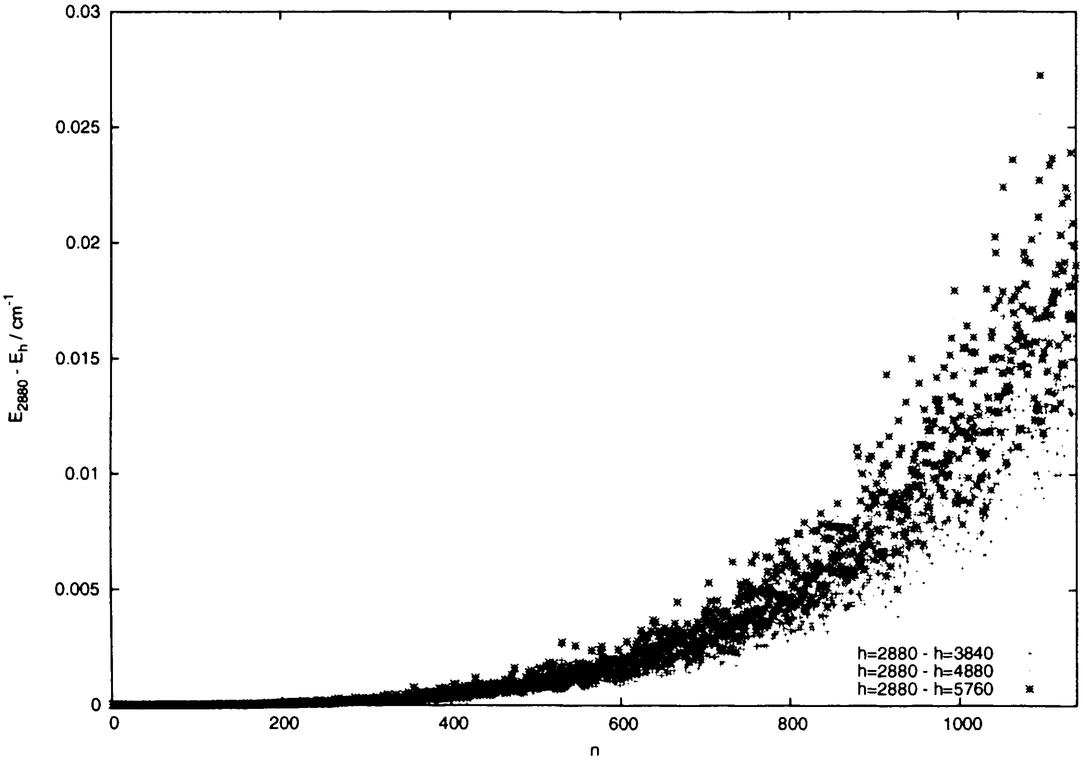

Figure 6.19: The convergence of $J = 2$, even, f states. The points indicate the difference between the n^{th} energy level calculated with $h = 2016$ and other values of h.

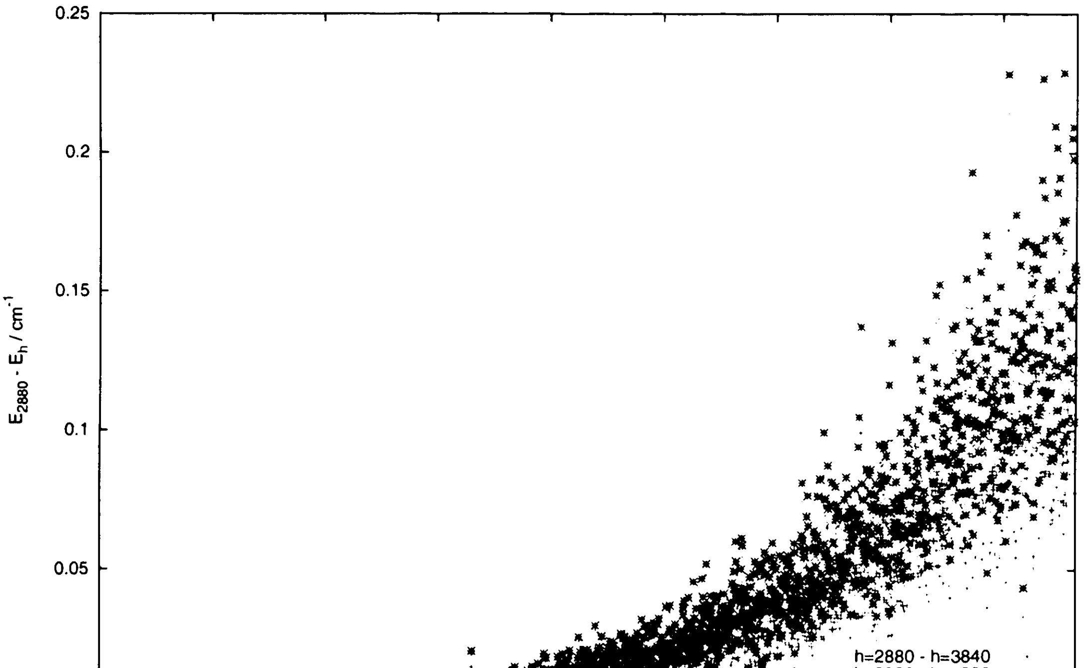

Figure 6.20: The convergence of $J = 2$, odd, e states. The points indicate the difference between the n^{th} energy level calculated with $h = 2016$ and other values of h.

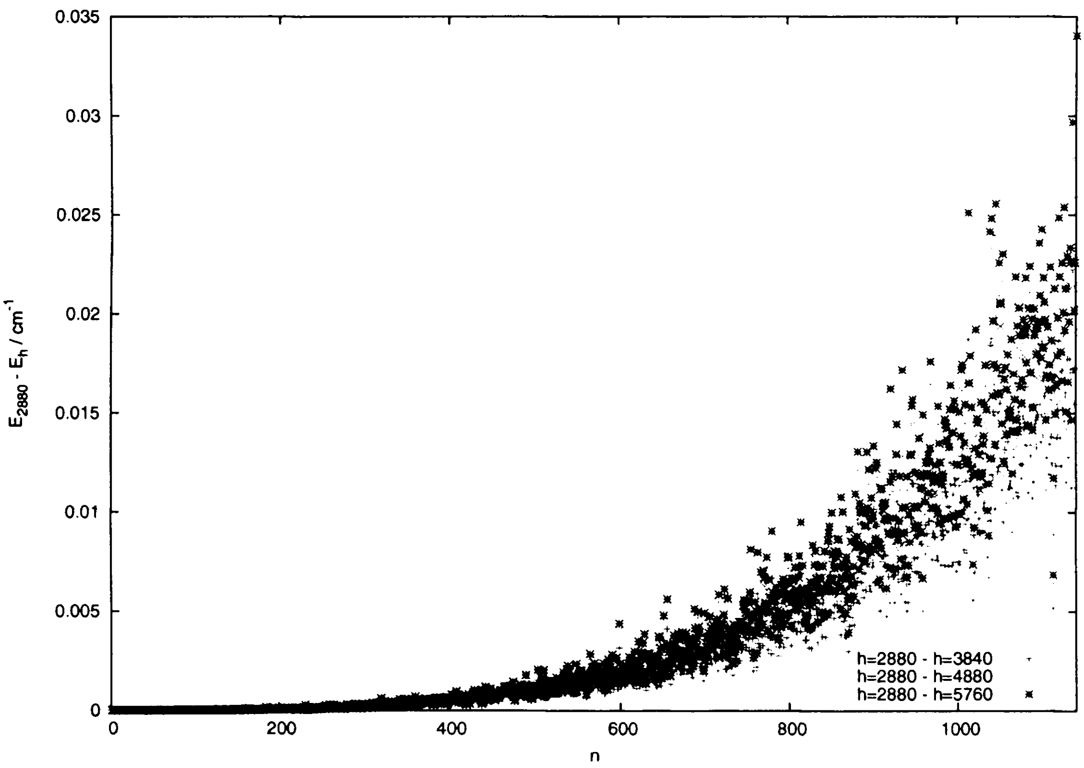

Figure 6.21: The convergence of $J = 2$, odd, f states. The points indicate the difference between the n^{th} energy level calculated with $h = 2016$ and other values of h.

Table 6.10: The mean energy differences (cm^{-1}) between $J = 5$ energy levels calculated using various values of h and $h = 2880$. The values of other parameters are : N =29952, n_{r_2}=96, n_{r_1}=36, $n_\theta = 32$, $\alpha = 0.0$, and $\omega = 0.0075$.

	EVEN		ODD	
	e	f	e	f
mean($E_{2880-3840}$)	0.83	0.25	0.82	0.24
mean($E_{2880-4992}$)	1.15	0.33	1.14	0.33
mean($E_{2880-5952}$)	1.26	0.36	1.24	0.35
mean($E_{2880-6912}$)	1.30	0.37	1.28	0.36

states is worse then that for the e states with $J = 1$ and $J = 2$. This indicates that 6912 solutions may not be enough to converge $J = 5$ e states to the same level as those of $J = 1$ and $J = 2$ calculations.

It was found that the empirical equation $h = (J+2) \times 1000$ was sufficient to converge all the states to dissociation to within 0.32 cm^{-1}. Convergence for the f states is markedly better at 0.06 cm^{-1}, therefore a lower value of h could be used for calculating f states to the same level of convergence as the e states.

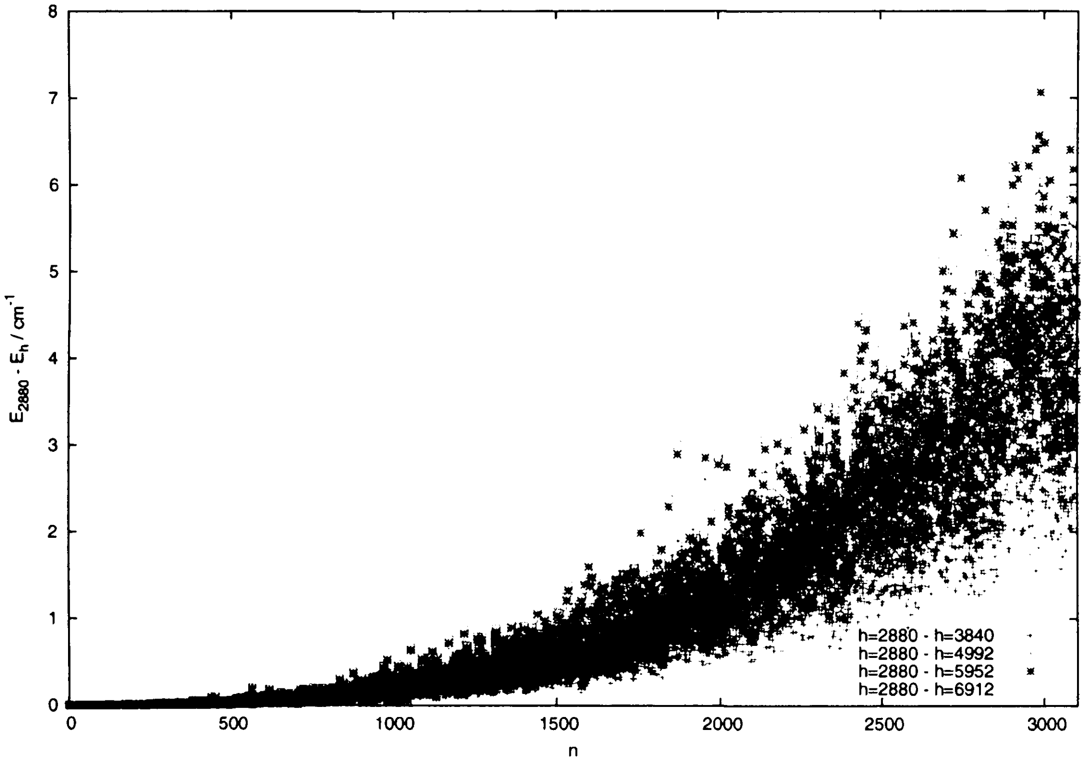

Figure 6.22: The convergence of $J = 5$, even, e states. The points indicate the difference between the n^{th} energy level calculated with $h = 2016$ and other values of h.

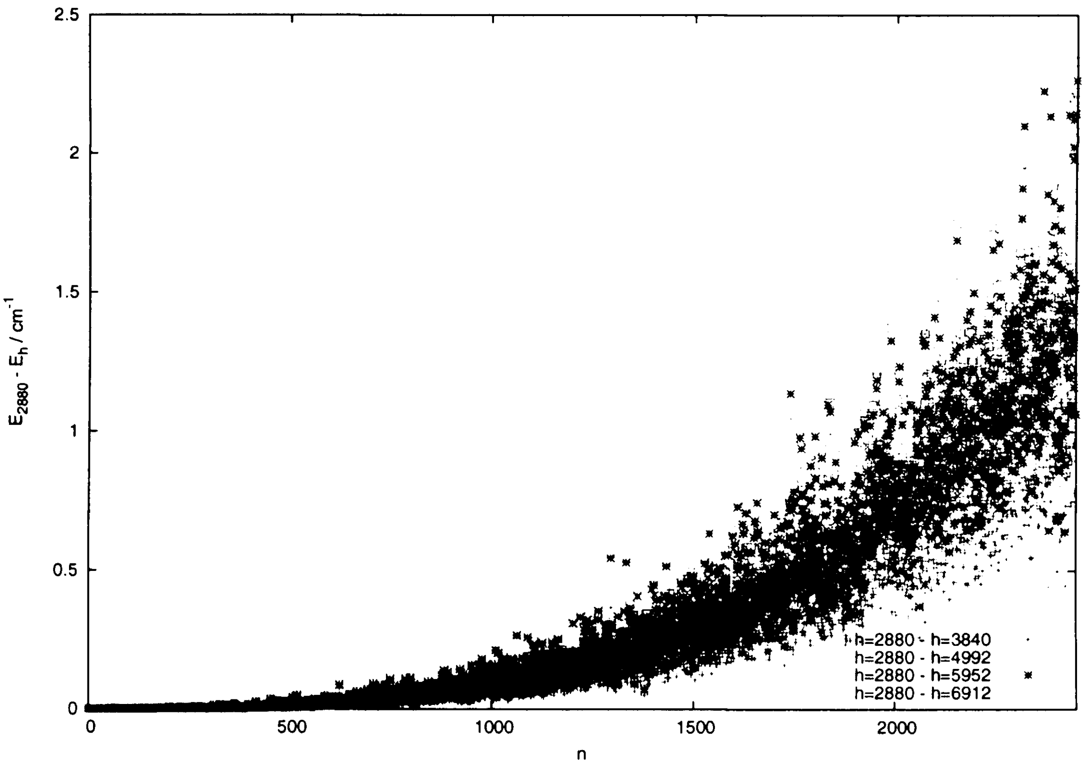

Figure 6.23: The convergence of $J = 5$, even, f states. The points indicate the difference between the n^{th} energy level calculated with $h = 2016$ and other values of h.

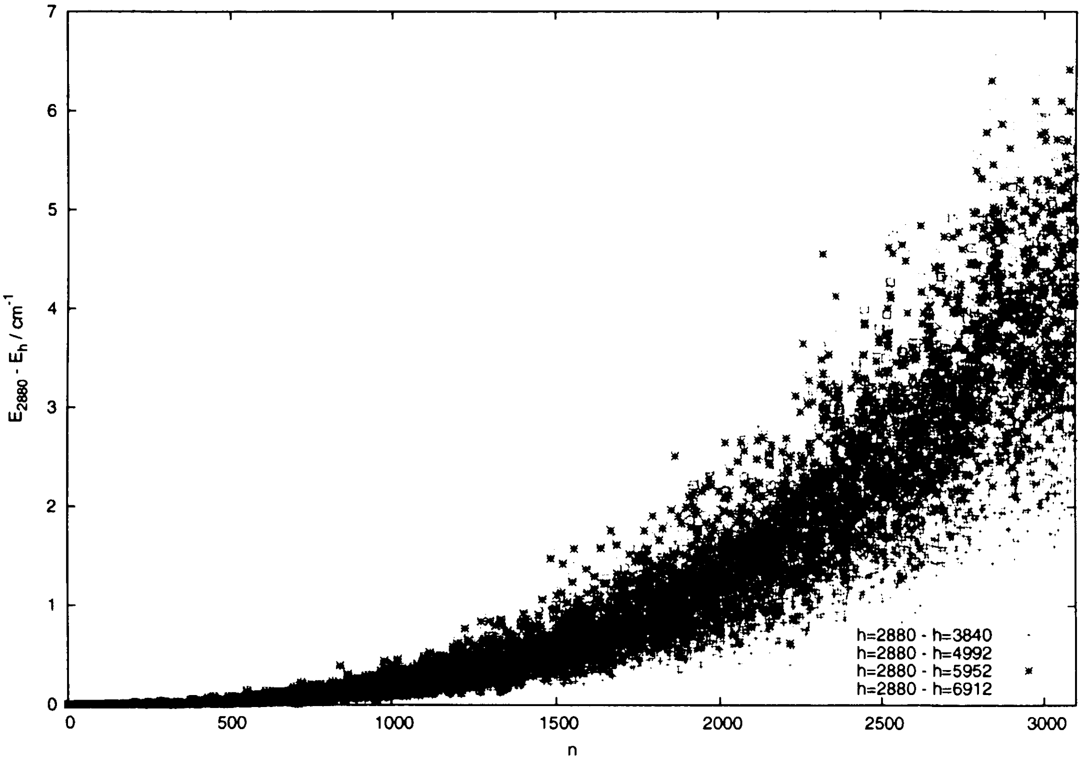

Figure 6.24: The convergence of $J = 5$, odd, e states. The points indicate the difference between the n^{th} energy level calculated with $h = 2016$ and other values of h.

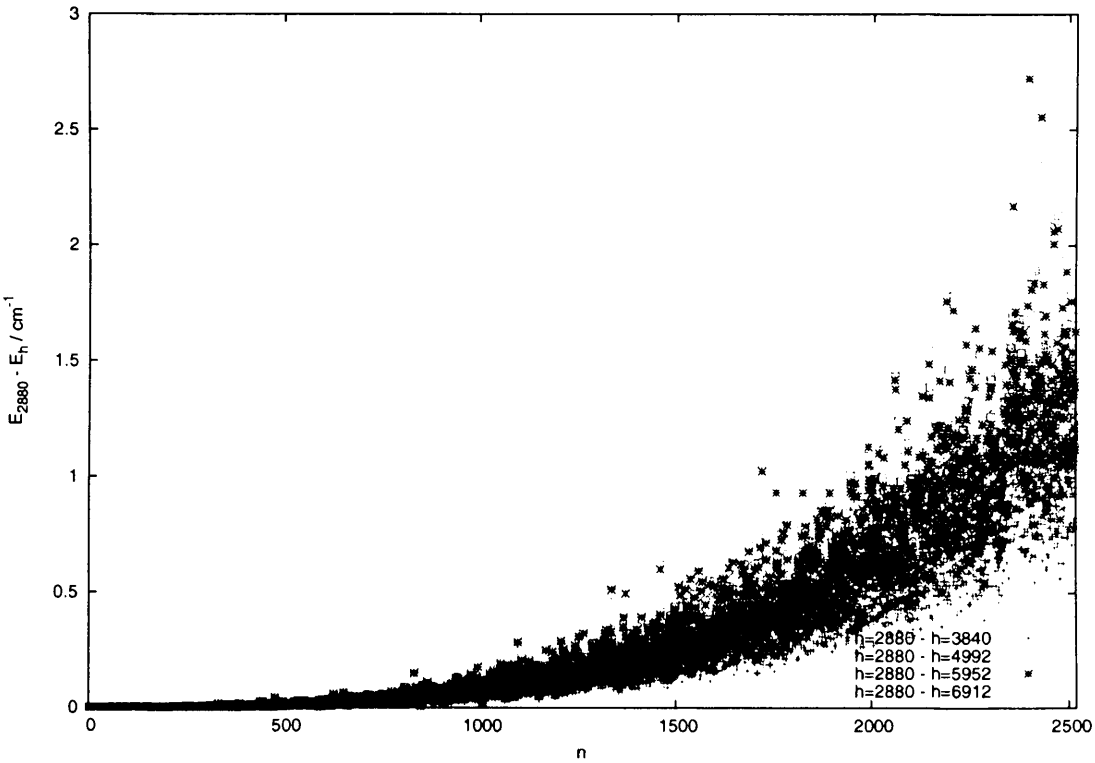

Figure 6.25: The convergence of $J = 5$, odd, f states. The points indicate the difference between the n^{th} energy level calculated with $h = 2016$ and other values of h.

6.5 Summary

If the values taken for the variational parameters are $n_\theta = 50$, $n_{r_1} = 36$, $n_{r_2} = 96$, $N = 39273$ and $h = (J + 2) \times 1000$, this gives rotational-vibrational energy levels converged to within 1 cm^{-1}, with the majority of states converged to a much greater level.

Chapter 7

Near-Dissociation Results and Discussion

In this chapter wavefunctions and a partial calculation of the dipole transition intensities pertinent to Carrington-Kennedy near-dissociation spectrum are presented.

7.1 Rotation-vibration wavefunctions

Using the PDVR3DJ and PROTLEV3 programs the H_3^+ wavefunctions were calculated for $J = 0$ to $J = 2$. The parameters used are outlined more fully in chapter 6. The coordinates were treated in the order $\theta \rightarrow r_1 \rightarrow r_2$ with 50, 36 and 96 points respectively. Morse oscillator-like functions were used for the r_1 coordinate with basis parameters $r_e =$ 2.1 a_o, $D_e = 0.1$ E_h and $\omega_e = 0.0118$ a.u. The r_2 coordinate was represented by spherical oscillator functions with parameters $\alpha = 0.0$ and $\omega = 0.0075$. A final Hamiltonian size of 39273 was used for the vibrational problem while the size of the rotation-vibration Hamiltonian was determined from the empirical relation $h = (J + 2) \times 1000$, where h is the number of vibrational solutions used to build the full Coriolis coupled Hamiltonian.

The $J = 0$ even ($q = 0$) DVR wavefunctions were examined by taking two dimensional cuts. The θ coordinate was fixed at 88.2°, the last θ grid point, and plotting contours as a function of r_1 and r_2 coordinates. All $J = 0$ even wavefunctions were examined in this manner, giving 679 plots which are shown in figures 7.1 to 7.17

This is the first time that wavefunctions calculated from a correctly dissociating H_3^+ potential have been analysed. From figures 7.1 to 7.17 it is clear that most of the plots show highly irregular structure, this is more prevalent as the energy is increased. Berblinger *et al* [133] performed a classical mechanical study of the H_3^+ system at $J = 0$.

Figure 7.1: H_3^+ $J = 0$ even ($q = 0$) wavefunctions in Jacobi (r_1, r_2, θ) coordinates for states 1 to 42 with θ taken to be 88.2°. Contours are taken at 8%, 16%, 32% and 64% of the maximum amplitude. The dashed line enclosing each state indicates the classical turning point for that state. r_1 and r_2 are along the x and y axes respectively, with ranges from 0 to 6 a_o.

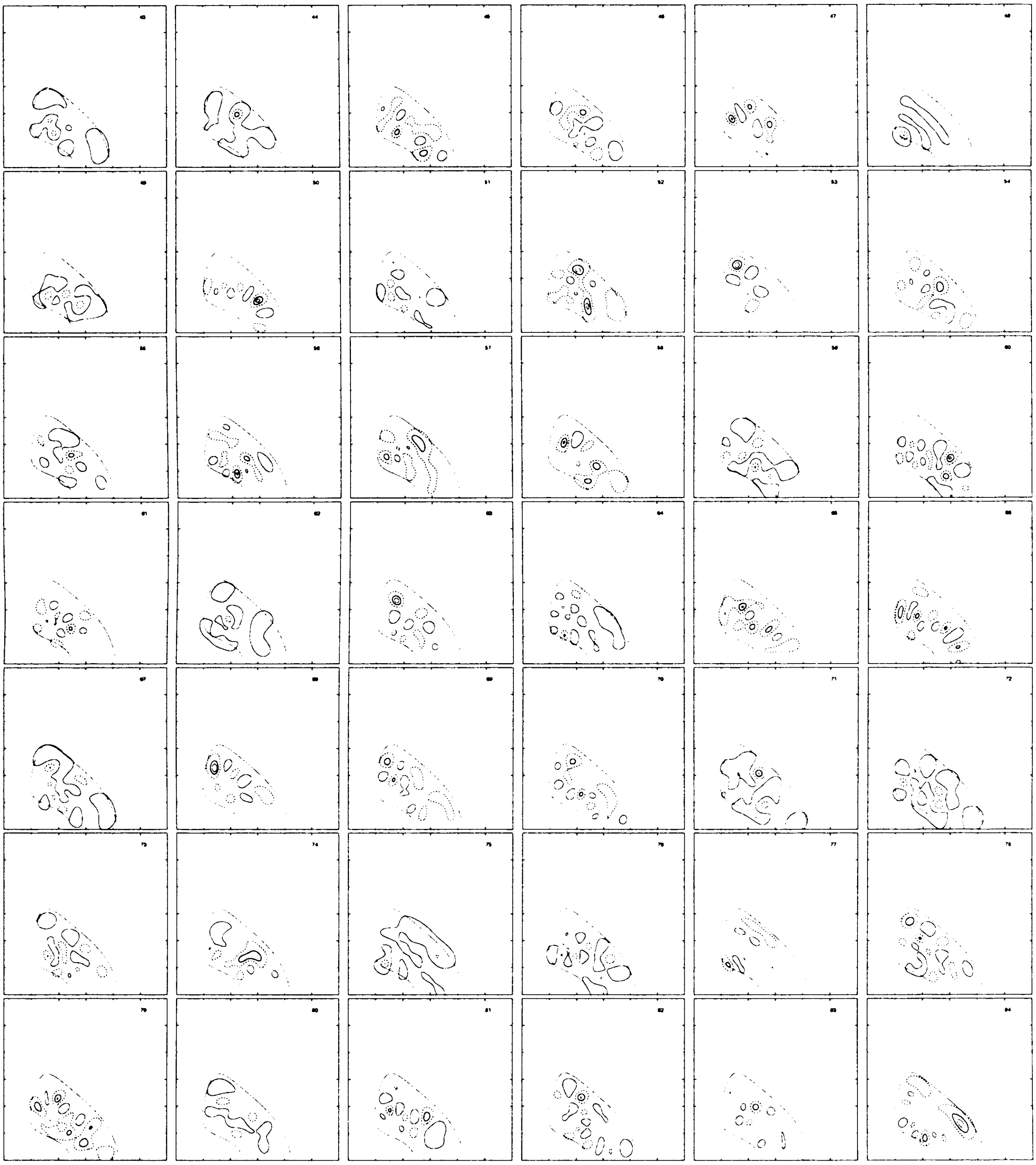

Figure 7.2: H_3^+ $J = 0$ even ($q = 0$) wavefunctions in Jacobi (r_1, r_2, θ) coordinates for states 43 to 84 with θ taken to be 88.2°. Contours are taken at 8%, 16%, 32% and 64% of the maximum amplitude. The dashed line enclosing each state indicates the classical turning point for that state. r_1 and r_2 are along the x and y axes respectively, with ranges from 0 to 6 a_0.

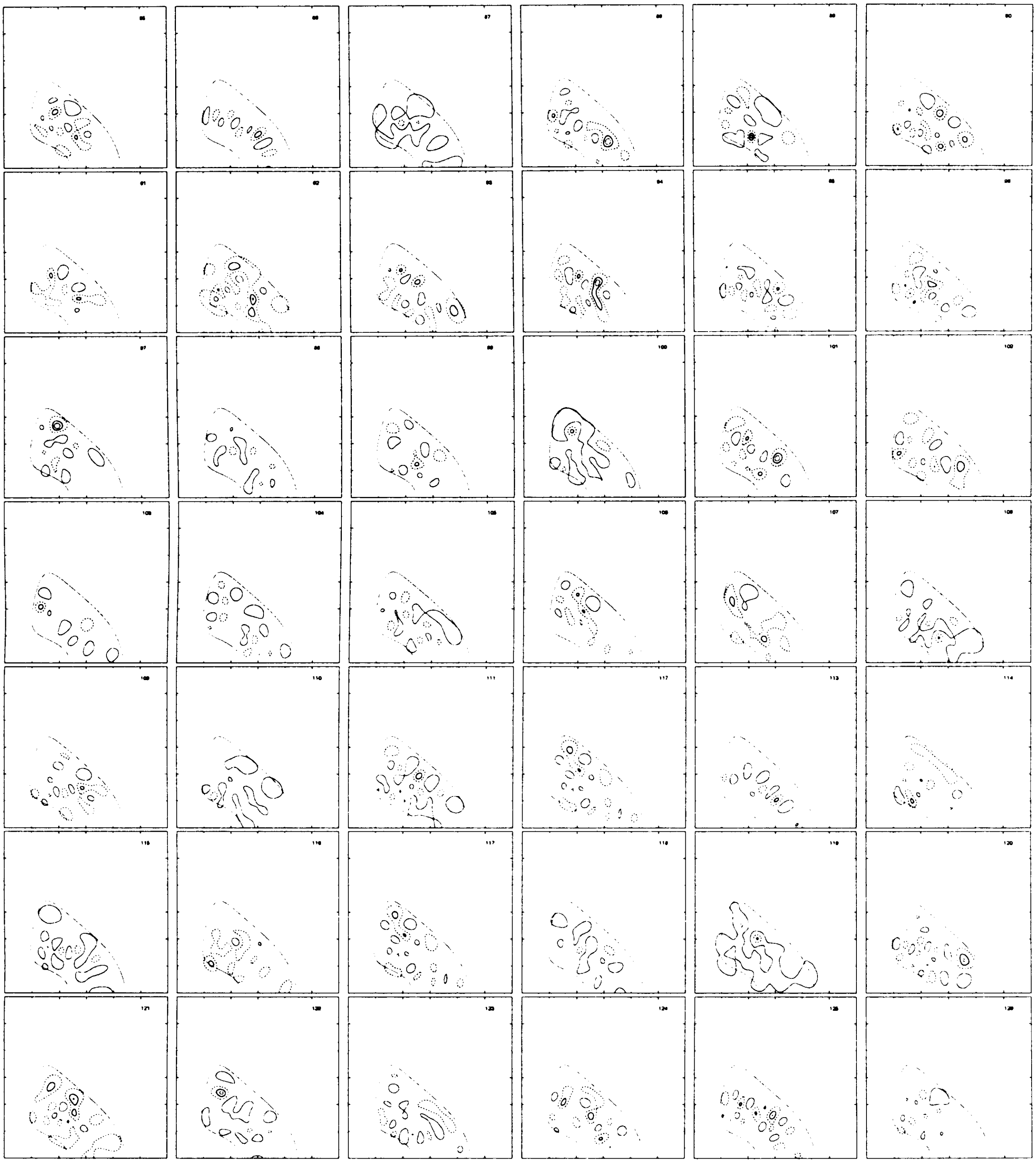

Figure 7.3: H_3^+ $J = 0$ even ($q = 0$) wavefunctions in Jacobi (r_1, r_2, θ) coordinates for states 85 to 126 with θ taken to be 88.2°. Contours are taken at 8%, 16%, 32% and 64% of the maximum amplitude. The dashed line enclosing each state indicates the classical turning point for that state. r_1 and r_2 are along the x and y axes respectively, with ranges from 0 to 6 a_o.

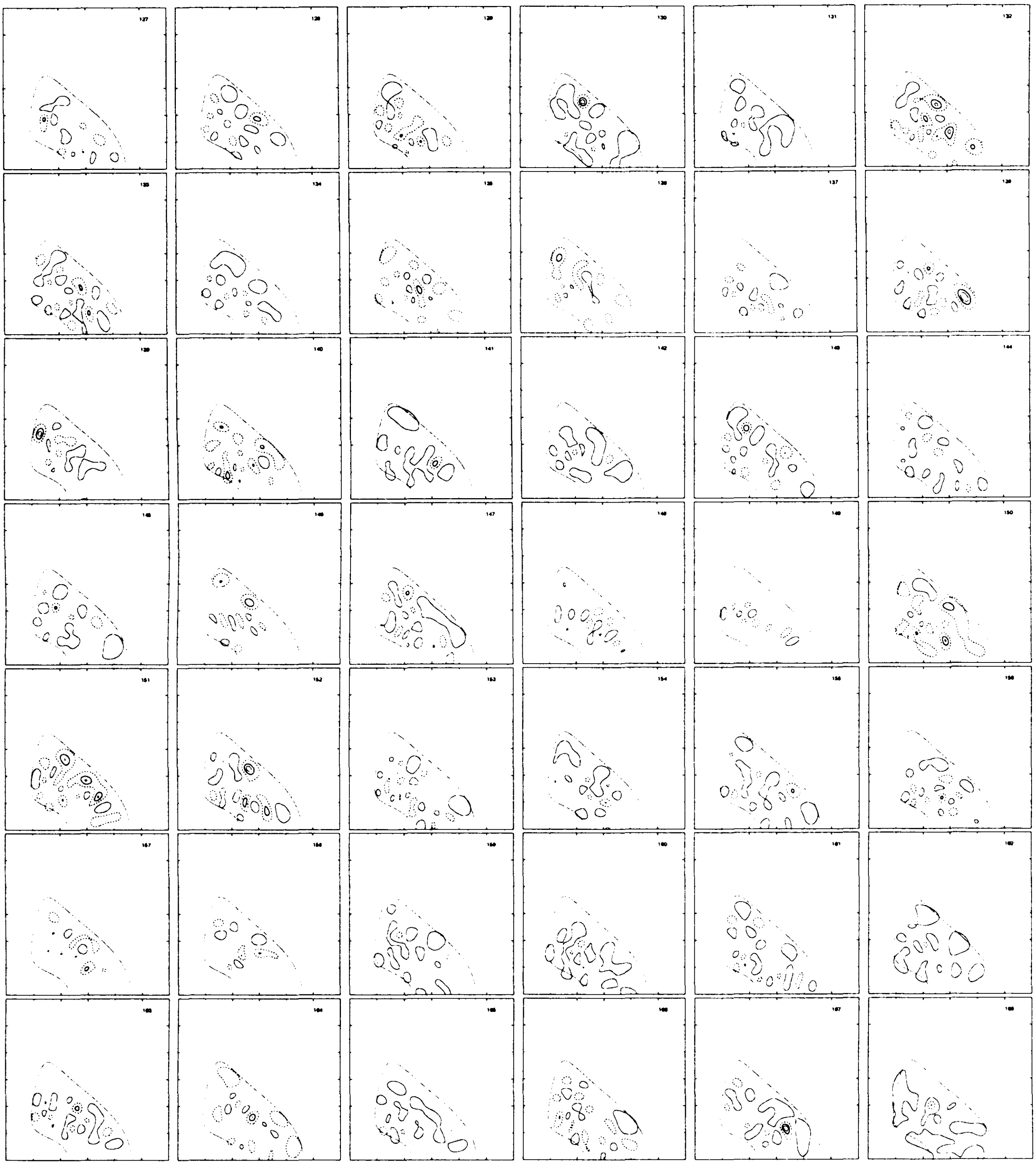

Figure 7.4: H_3^+ $J = 0$ even ($q = 0$) wavefunctions in Jacobi (r_1, r_2, θ) coordinates for states 127 to 168 with θ taken to be 88.2°. Contours are taken at 8%, 16%, 32% and 64% of the maximum amplitude. The dashed line enclosing each state indicates the classical turning point for that state. r_1 and r_2 are along the x and y axes respectively, with ranges from 0 to 6 a_o.

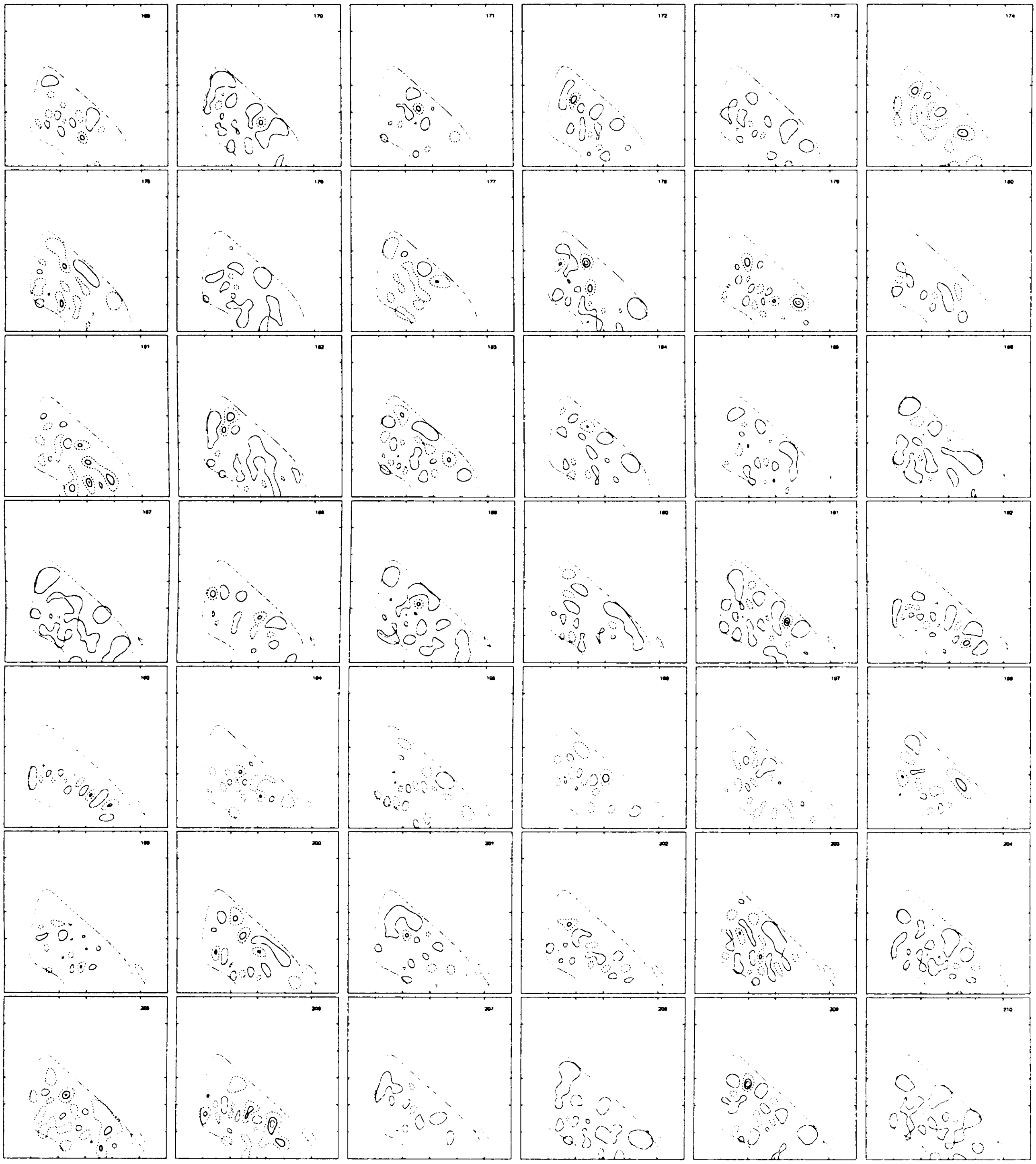

Figure 7.5: H_3^+ $J = 0$ even ($q = 0$) wavefunctions in Jacobi (r_1, r_2, θ) coordinates for states 169 to 210 with θ taken to be 88.2°. Contours are taken at 8%, 16%, 32% and 64% of the maximum amplitude. The dashed line enclosing each state indicates the classical turning point for that state. r_1 and r_2 are along the x and y axes respectively, with ranges from 0 to 6 a_o.

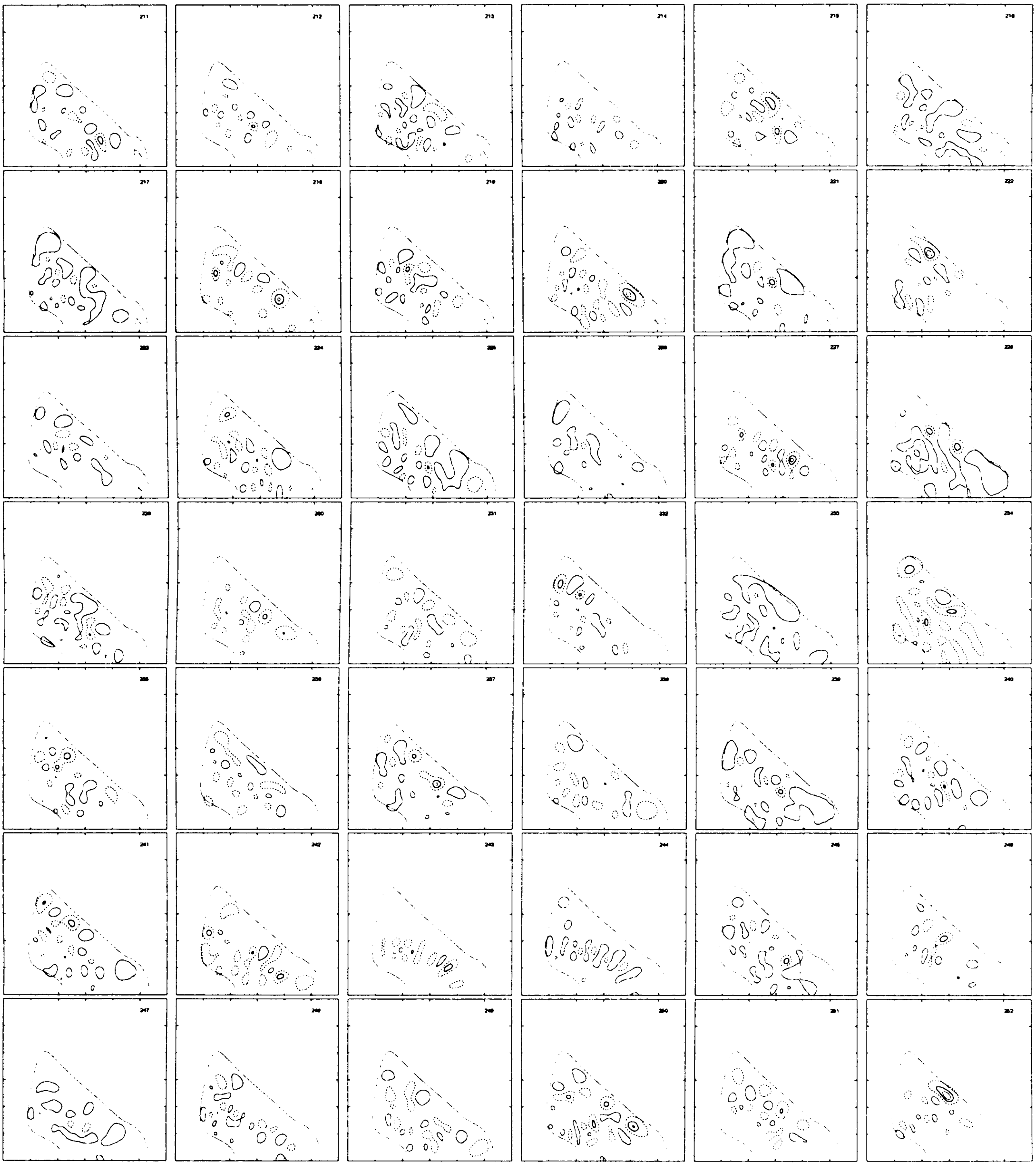

Figure 7.6: H_3^+ $J = 0$ even ($q = 0$) wavefunctions in Jacobi (r_1, r_2, θ) coordinates for states 211 to 252 with θ taken to be 88.2°. Contours are taken at 8%, 16%, 32% and 64% of the maximum amplitude. The dashed line enclosing each state indicates the classical turning point for that state. r_1 and r_2 are along the x and y axes respectively, with ranges from 0 to 6 a_o.

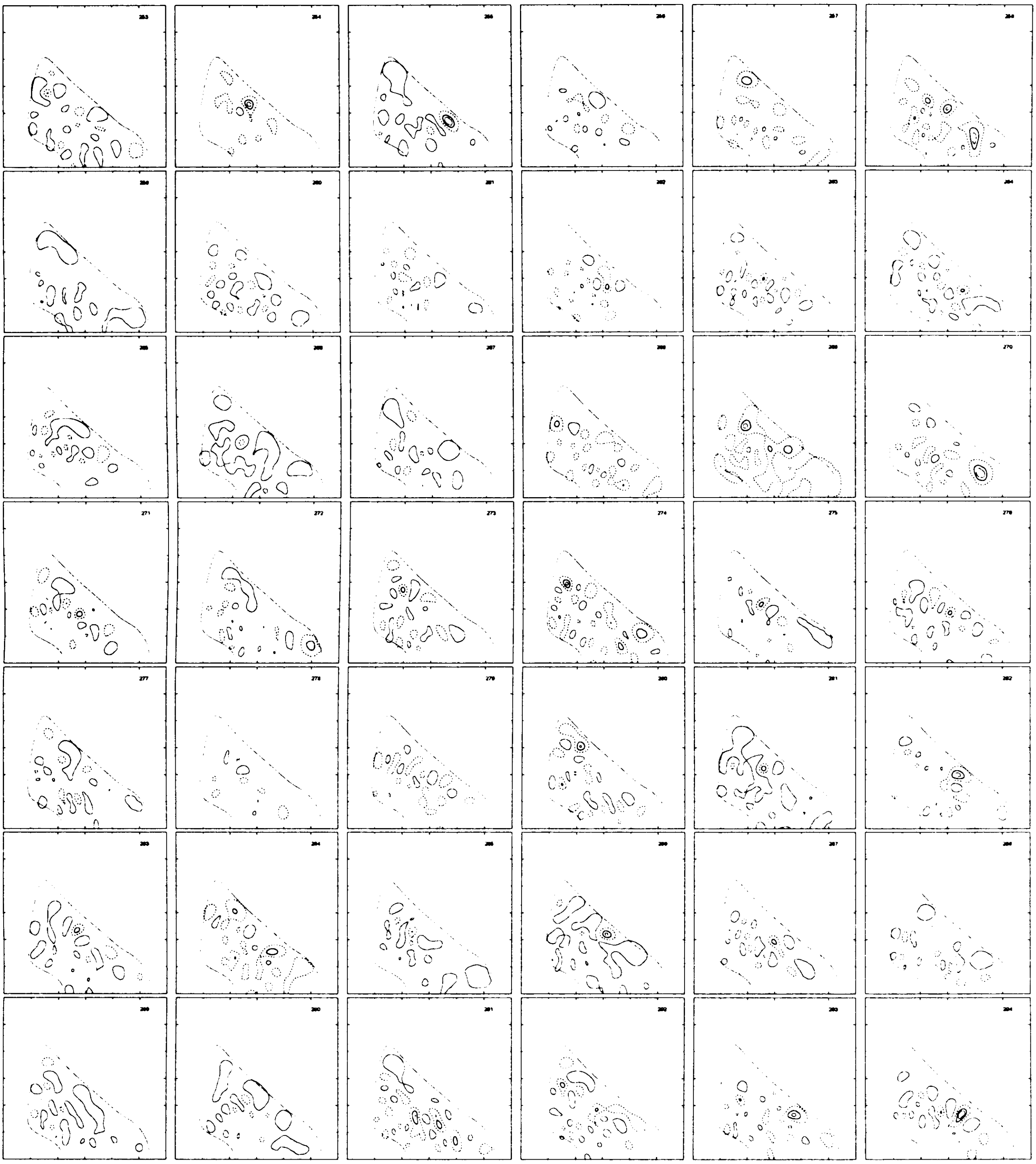

Figure 7.7: H_3^+ $J = 0$ even ($q = 0$) wavefunctions in Jacobi (r_1, r_2, θ) coordinates for states 253 to 294 with θ taken to be 88.2°. Contours are taken at 8%, 16%, 32% and 64% of the maximum amplitude. The dashed line enclosing each state indicates the classical turning point for that state. r_1 and r_2 are along the x and y axes respectively, with ranges from 0 to 6 a_o.

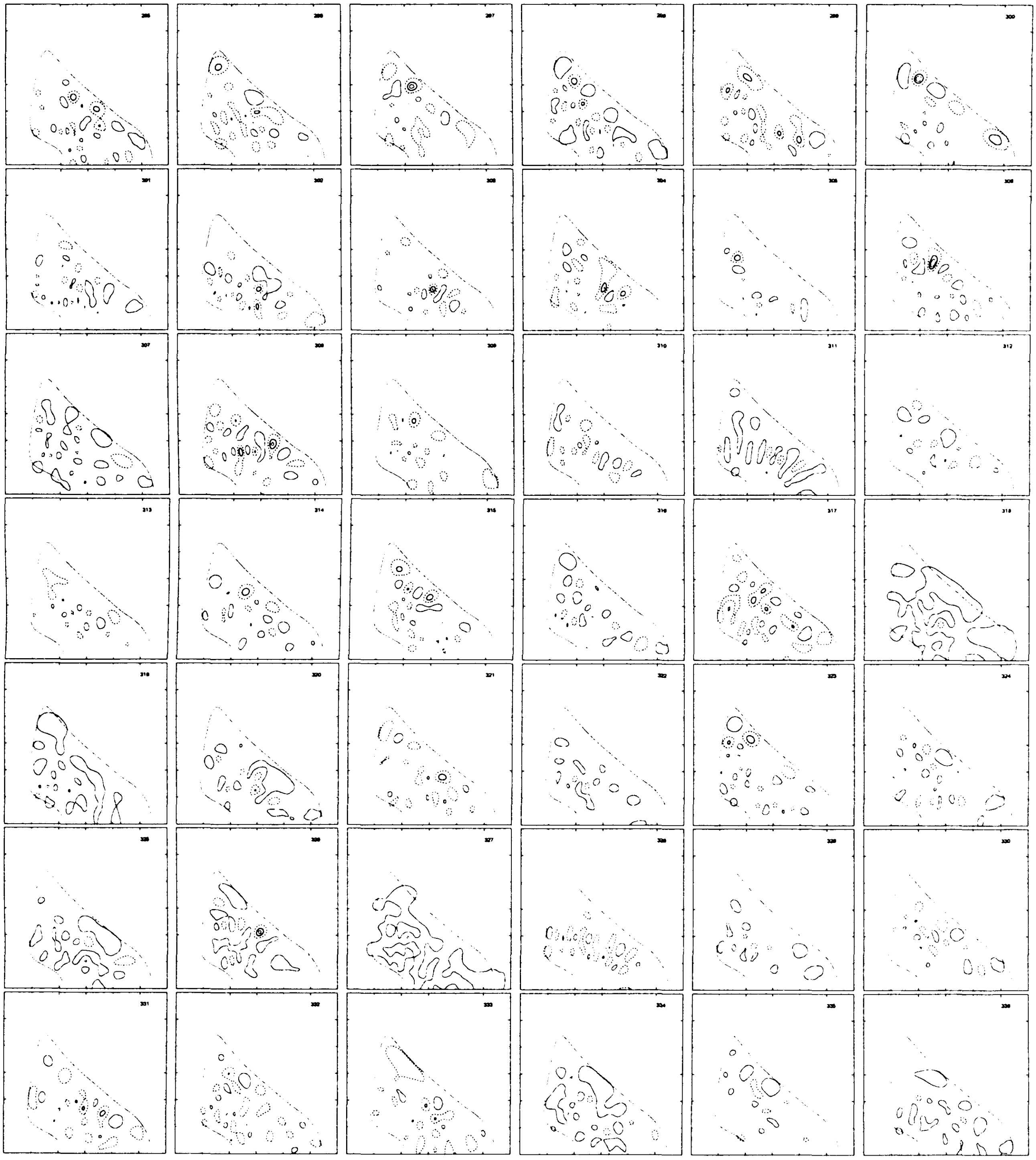

Figure 7.8: H_3^+ $J = 0$ even ($q = 0$) wavefunctions in Jacobi (r_1, r_2, θ) coordinates for states 294 to 336 with θ taken to be 88.2°. Contours are taken at 8%, 16%, 32% and 64% of the maximum amplitude. The dashed line enclosing each state indicates the classical turning point for that state. r_1 and r_2 are along the x and y axes respectively, with ranges from 0 to 6 a_o.

Figure 7.9: H_3^+ $J = 0$ even ($q = 0$) wavefunctions in Jacobi (r_1, r_2, θ) coordinates for states 337 to 378 with θ taken to be 88.2°. Contours are taken at 8%, 16%, 32% and 64% of the maximum amplitude. The dashed line enclosing each state indicates the classical turning point for that state. r_1 and r_2 are along the x and y axes respectively, with ranges from 0 to 6 a_o.

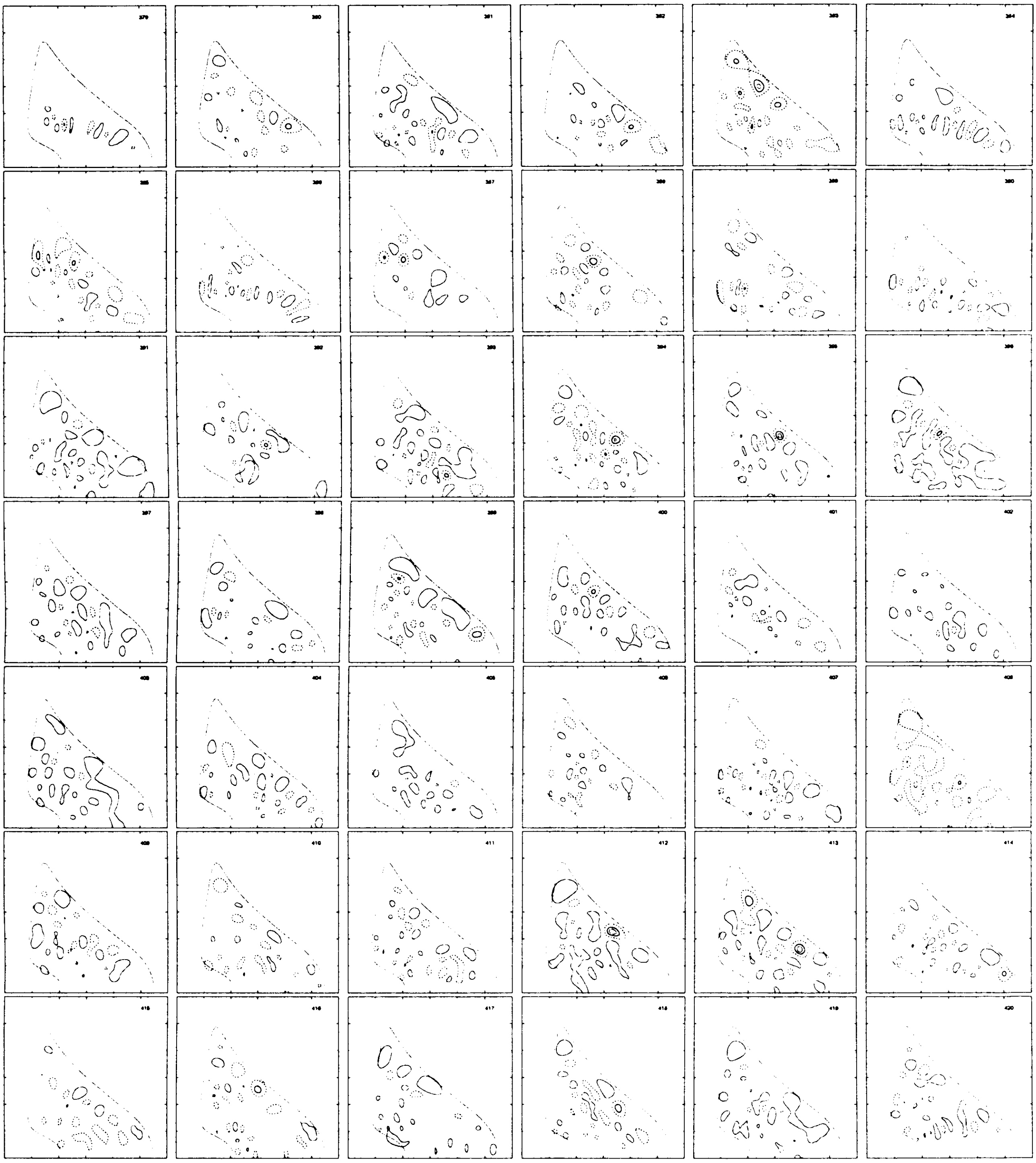

Figure 7.10: H_3^+ $J = 0$ even ($q = 0$) wavefunctions in Jacobi (r_1, r_2, θ) coordinates for states 379 to 420 with θ taken to be 88.2°. Contours are taken at 8%, 16%, 32% and 64% of the maximum amplitude. The dashed line enclosing each state indicates the classical turning point for that state. r_1 and r_2 are along the x and y axes respectively, with ranges from 0 to 6 a_o.

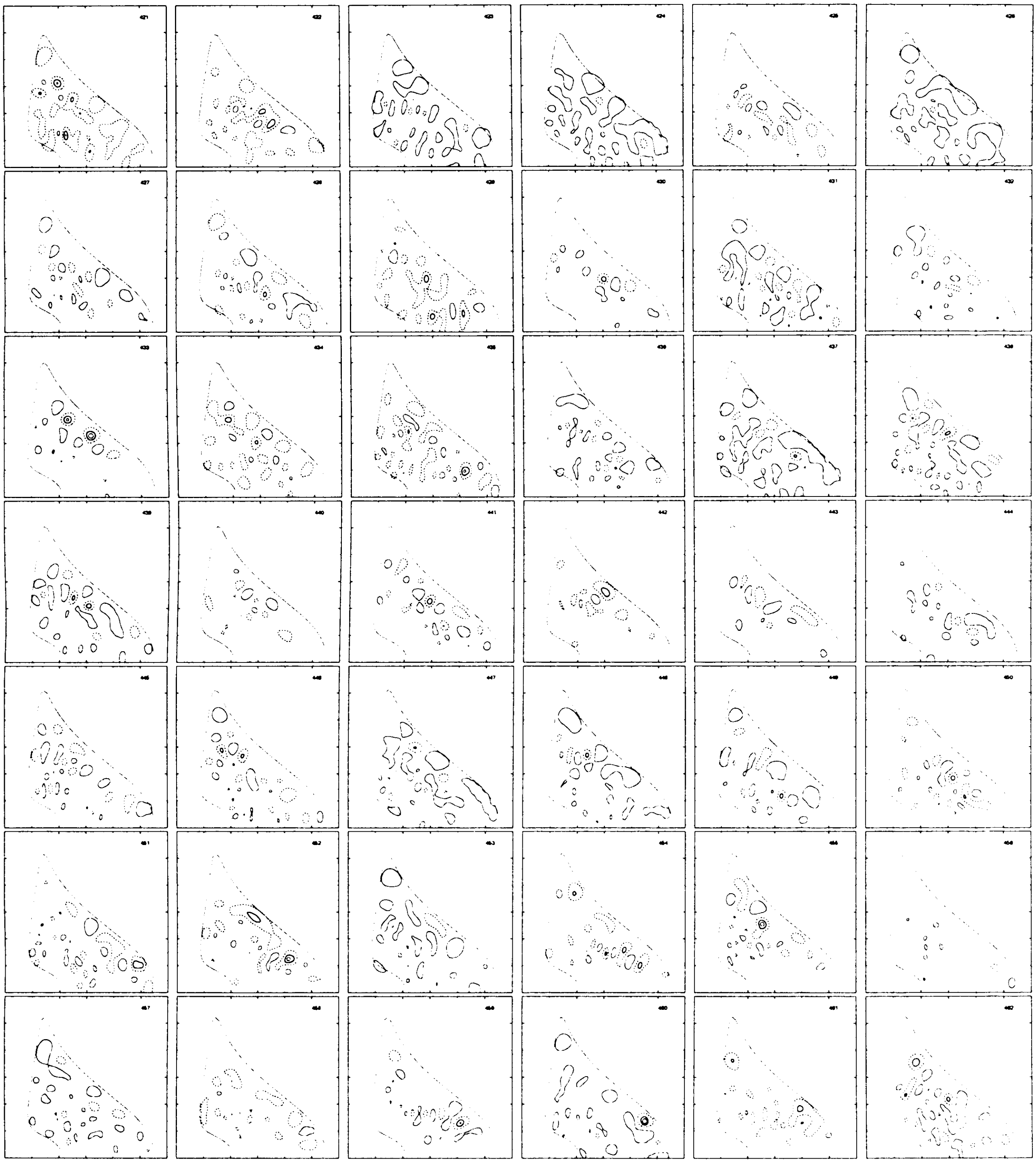

Figure 7.11: H_3^+ $J = 0$ even ($q = 0$) wavefunctions in Jacobi (r_1, r_2, θ) coordinates for states 421 to 462 with θ taken to be 88.2°. Contours are taken at 8%, 16%, 32% and 64% of the maximum amplitude. The dashed line enclosing each state indicates the classical turning point for that state. r_1 and r_2 are along the x and y axes respectively, with ranges from 0 to 6 a_o.

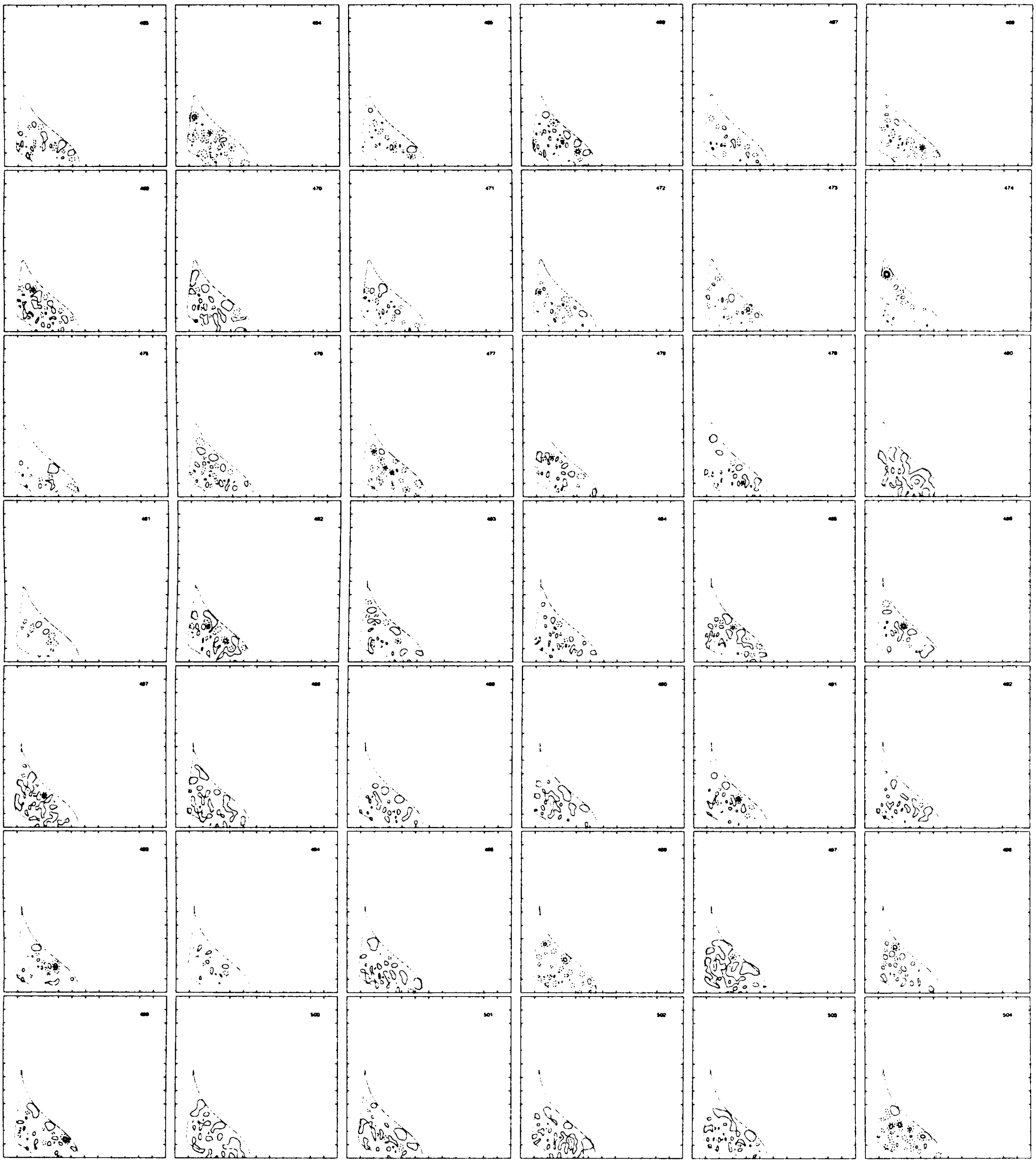

Figure 7.12: H_3^+ $J = 0$ even ($q = 0$) wavefunctions in Jacobi (r_1, r_2, θ) coordinates for states 463 to 504 with θ taken to be 88.2°. Contours are taken at 8%, 16%, 32% and 64% of the maximum amplitude. The dashed line enclosing each state indicates the classical turning point for that state. r_1 and r_2 are along the x and y axes respectively, with ranges from 0 to 12 a_o.

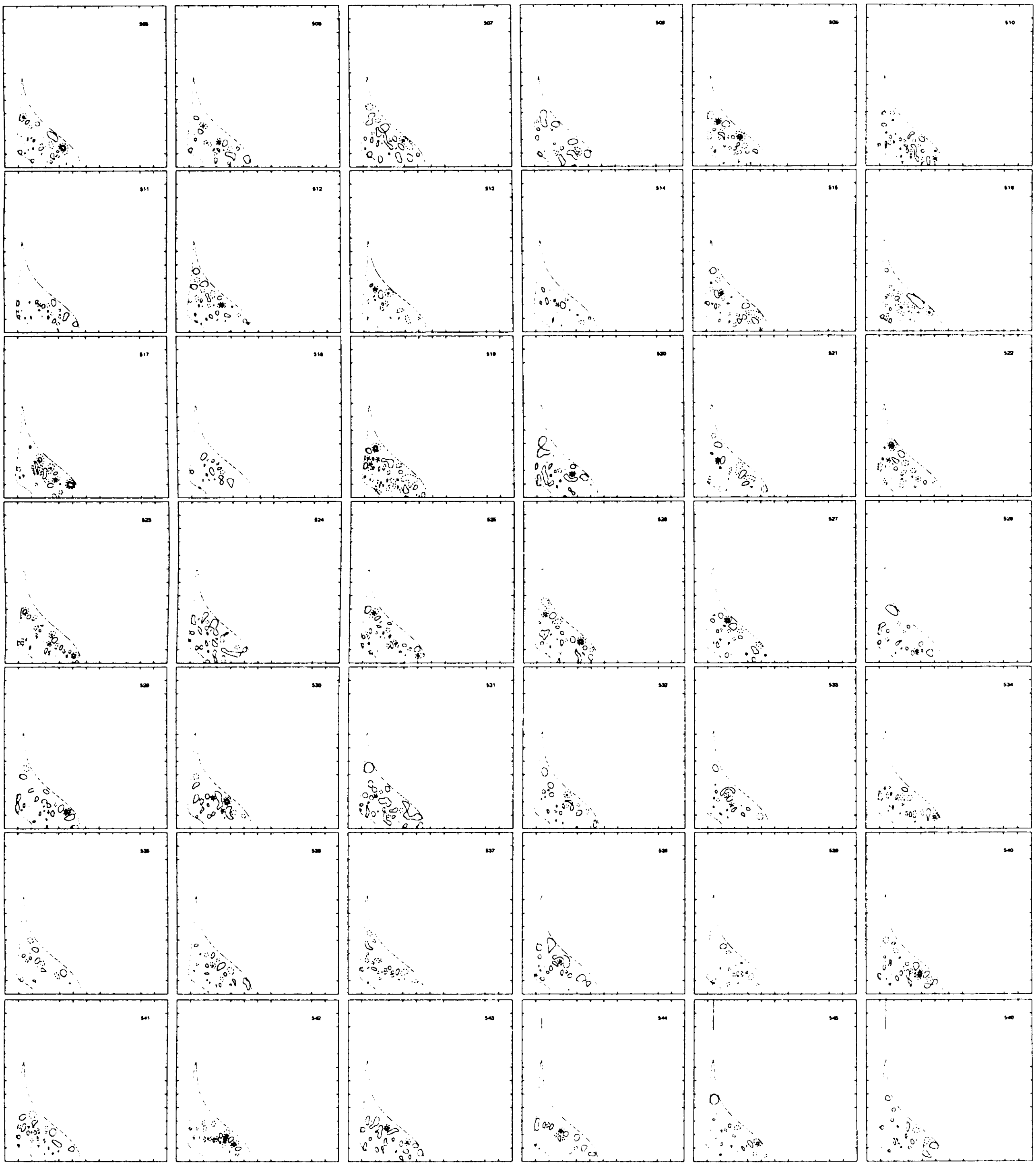

Figure 7.13: H_3^+ $J = 0$ even ($q = 0$) wavefunctions in Jacobi (r_1, r_2, θ) coordinates for states 505 to 546 with θ taken to be 88.2°. Contours are taken at 8%, 16%, 32% and 64% of the maximum amplitude. The dashed line enclosing each state indicates the classical turning point for that state. r_1 and r_2 are along the x and y axes respectively, with ranges from 0 to 12 a_o.

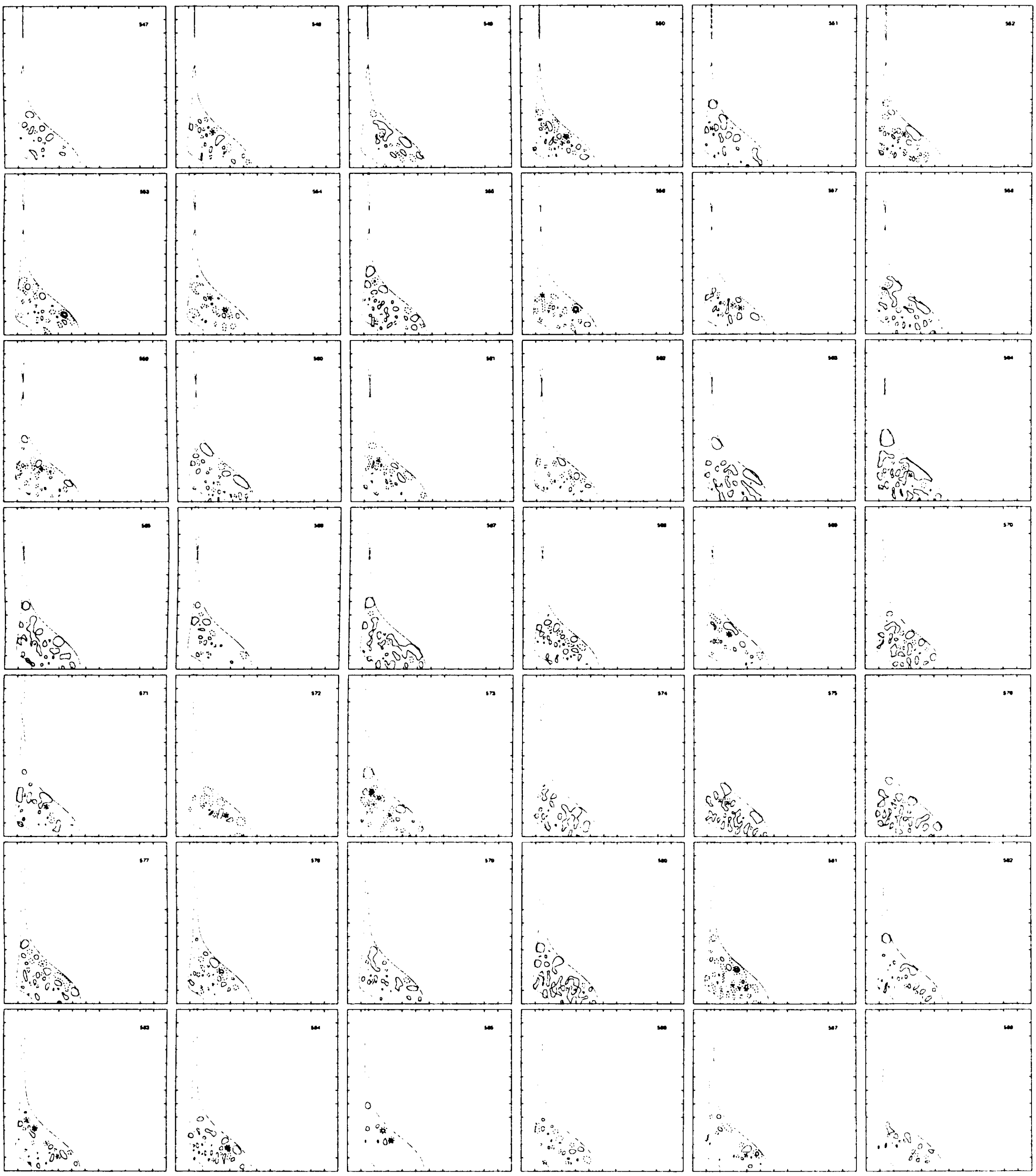

Figure 7.14: H_3^+ $J = 0$ even ($q = 0$) wavefunctions in Jacobi (r_1, r_2, θ) coordinates for states 547 to 588 with θ taken to be 88.2°. Contours are taken at 8%, 16%, 32% and 64% of the maximum amplitude. The dashed line enclosing each state indicates the classical turning point for that state. r_1 and r_2 are along the x and y axes respectively, with ranges from 0 to 12 a_o.

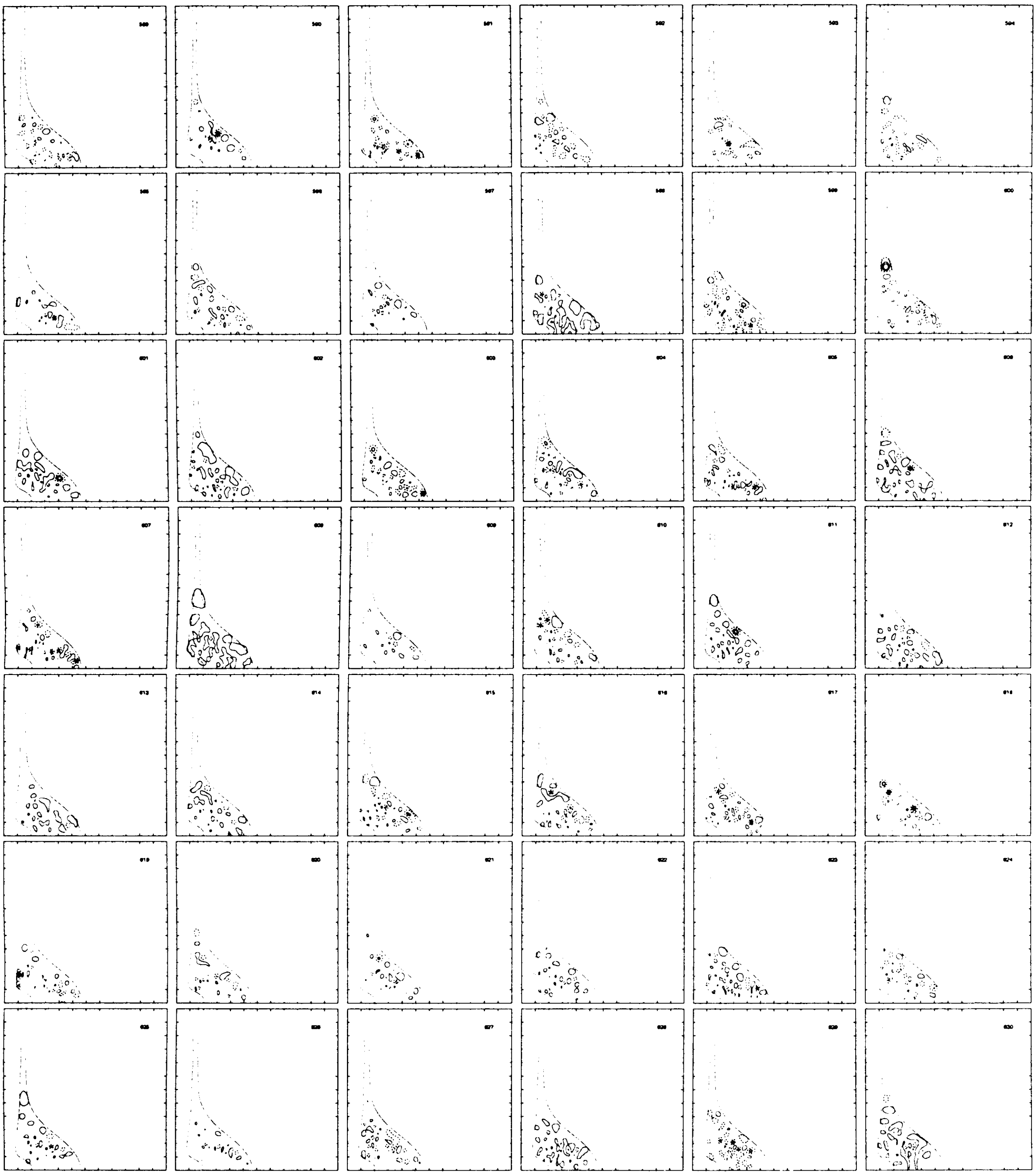

Figure 7.15: H_3^+ $J = 0$ even ($q = 0$) wavefunctions in Jacobi (r_1, r_2, θ) coordinates for states 589 to 630 with θ taken to be 88.2°. Contours are taken at 8%, 16%, 32% and 64% of the maximum amplitude. The dashed line enclosing each state indicates the classical turning point for that state. r_1 and r_2 are along the x and y axes respectively, with ranges from 0 to 12 a_o.

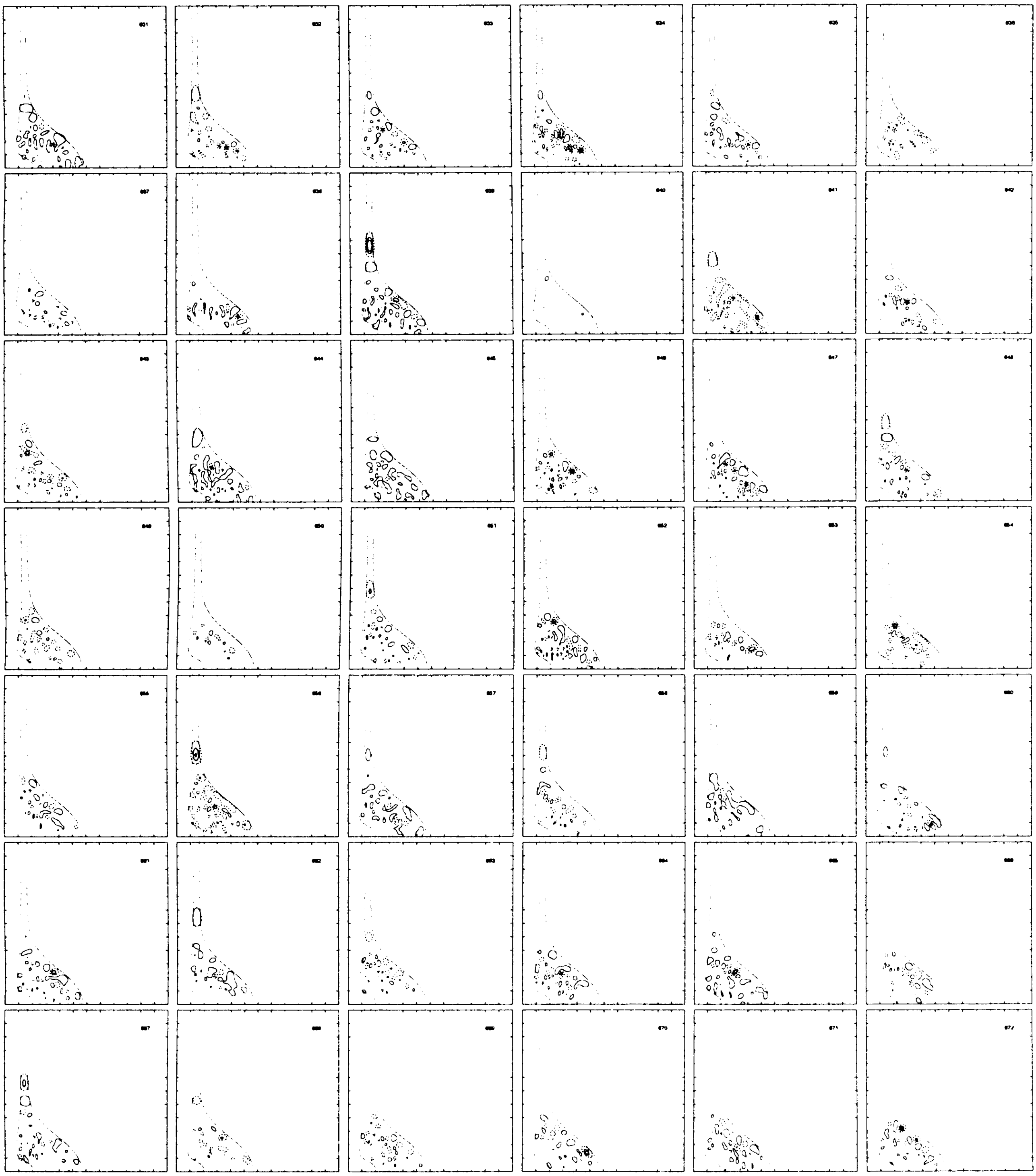

Figure 7.16: H_3^+ $J = 0$ even ($q = 0$) wavefunctions in Jacobi (r_1, r_2, θ) coordinates for states 631 to 672 with θ taken to be 88.2°. Contours are taken at 8%, 16%, 32% and 64% of the maximum amplitude. The dashed line enclosing each state indicates the classical turning point for that state. r_1 and r_2 are along the x and y axes respectively, with ranges from 0 to 12 a_o.

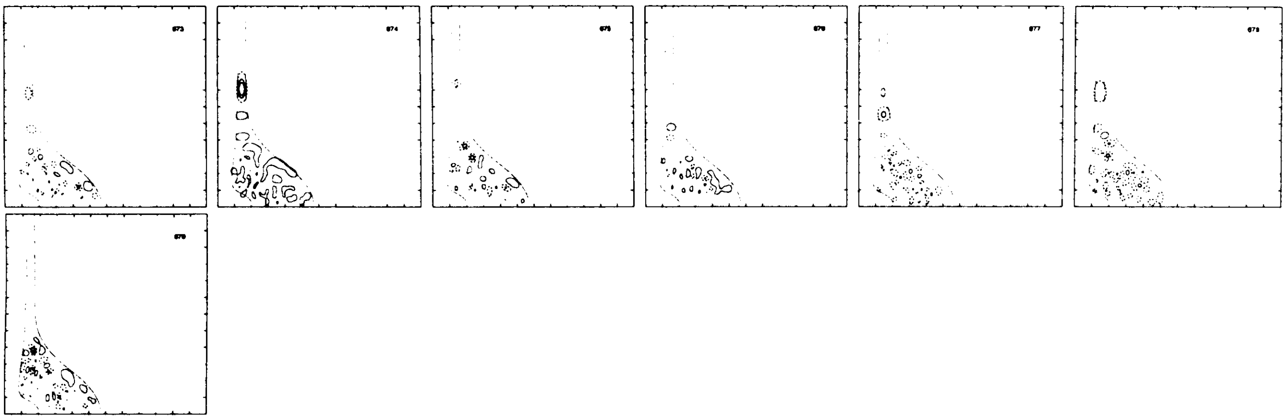

Figure 7.17: H_3^+ $J = 0$ even ($q = 0$) wavefunctions in Jacobi (r_1, r_2, θ) coordinates for states 631 to 679 with θ taken to be 88.2°. Contours are taken at 8%, 16%, 32% and 64% of the maximum amplitude. The dashed line enclosing each state indicates the classical turning point for that state. r_1 and r_2 are along the x and y axes respectively, with ranges from 0 to 12 a_o.

They discovered stable periodic orbit, which they named "horseshoe" orbits. This motion can be considered as a highly excited bending motion in a quasi-linear molecule. These structures have been found within the wavefunctions of other triatomic species, such as Ar_3 [134] and Na_3 [135]; thus they are not unique to H_3^+. Le Sueur *et al* [136] calculated vibrational band intensities for the H_3^+ system. They found that "horseshoe" states were responsible for high intensities. Furthermore they found that these "horseshoe" states were invariant to the potential energy surface used, being produced with both the Meyer *et al* [57] and Jensen *et al* [137] potentials. Thus it would be expected that these states should exist in the present calculation, which uses a significantly improved potential, that correctly dissociates. Le Sueur *et al* [136] identified 20 "horseshoe" states, the last two are above the dissociation energy of this calculation. One can convince oneself that states 2, 5, 8, 14, 21, 28, 38, 50, 66, 86, 115, 149 193, 243, 311 and 386 correspond to the first 16 states identified by Le Sueur *et al.* However the correspondence of the next 2 states is less clear, this could be due to the generally more chaotic nature of phase space shown at higher energies.

The plots for states 600, 639, 656 and 674 show an interesting feature at approximately $r_2 = 5a_o$ This increase in amplitude along $H_3^+ \rightarrow H_2 + H^+$ dissociation channel may be due to loosely coupled H^+–H_2 complexes. Such states have been suggested to exist in the Carrington-Kennedy spectra before by Pfeiffer and Child [138], albeit for much higher rotational excitation. These features could also be an artifact of the potential created when the potential energy surface was fitted. For diatomic molecules the near-dissociation and long-range behaviour is well known [139]. The H^+–H_2 complexes found lie above the classical dissociation energy D_e, lying in the region between D_e and D_o, and therefore are a purely quantal phenomenon. Unlike diatomic states near-dissociation, the zero point energy and potential energy of the products, H_2 in this case, have to be accounted for. For H_3^+ dissociation the potential for H_2 lies orthogonal to the dissociating H_3^+ coordinate. Thus analogies to the one dimensional diatomic case are not possible. These long-range bonded complexes exhibit interesting behaviour and definitely warrant further investigation.

7.2 Density of states

The Polyansky *et al* [3] potential energy used is the first that dissociates H_3^+ correctly. This potential includes long range attractive terms which should increase the number of bound states with respect to previous potentials. To test this all the H_3^+ band origins of this work are compared to those of Henderson *et al* [15] up to dissociation (figure 7.18). Henderson *et al* used the potential energy surface of Meyer *et al* [57] which is known not to dissociates correctly. Therefore a greater density states would be expected in this work compared to that of Henderson *et al.*

It is apparent from figure 7.18 that the opposite of the expected behaviour is shown, that is Henderson *et al* in fact have a higher density of states then this work. The significant difference in the densities begins at approximately 22500 cm^{-1}. A possible reason for this contradiction may lie in convergence with the Henderson *et al* band origins being less well converged then those in this work. Henderson *et al* found that their band origins were converging from below and thus a lack of convergence could result in a lowering in the density of states.

7.3 Dipole calculations

The PDIPOLE program was used with the afore mentioned rotation-vibration wavefunctions to calculate line strengths. Using the dipole surface of Röhse *et al* [56], the line strengths for *all* transition allowed by the rigorous dipole selection rules were calculated for the given rotational states.

The wavefunctions, $\psi^{J',k}_{\alpha,\beta,j'}$, have an angular dependence on k and need to be transformed to a common DVR grid (refer to chapter 3). A slightly larger number of FBR

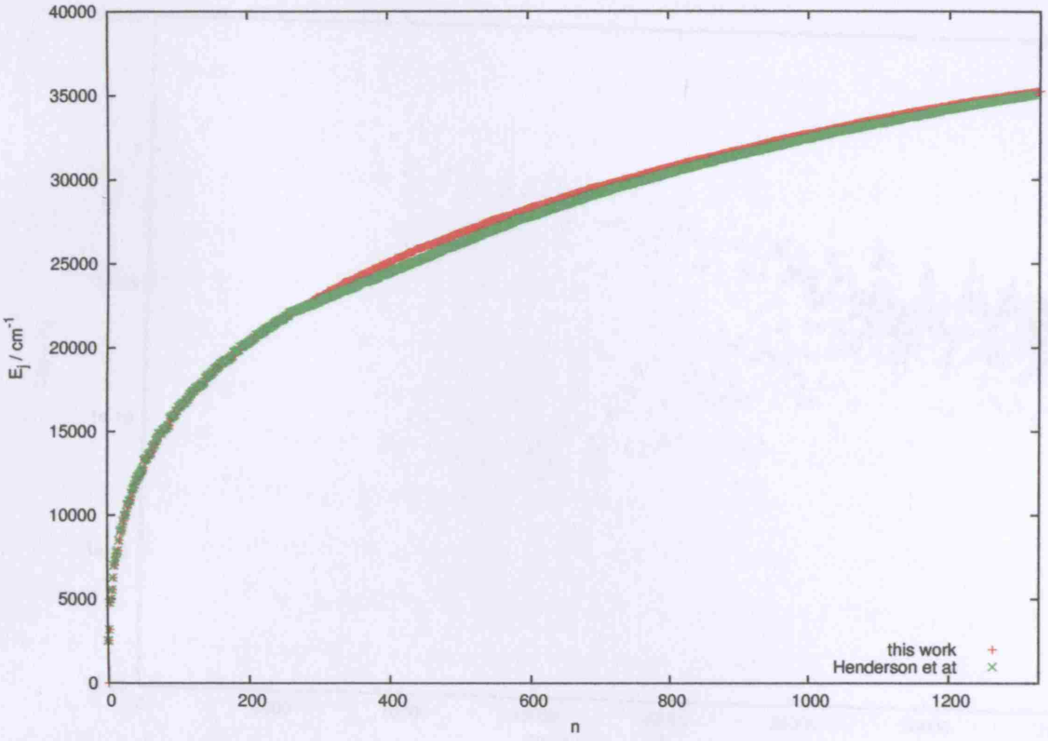

Figure 7.18: A comparison of all the H_3^+ band origins of this work and that of Henderson *et al* [15]. The E states are not degenerate and thus counted twice in each data set.

angular functions γ need to be used. The smaller the grid size the lower the computational cost of the dipole transition calculation. Thus a value γ was varied to determine a stable value, $\gamma = 64$.

A total of approximately 12.8 million transitions were computed. It should be noted that as the full D_{3h} symmetry of the H_3^+ molecule is not fully exploited and as such the E states are not degenerate across the even ($q = 0$) and odd ($q = 1$) calculations; this leads to doubling of transitions and transitions with zero line strength.

7.4 Analysis of spectra

The number of transitions, for even this limited calculation, are too large for any analysis of individual transitions to be made; alternative methods must be used. The Einstein A_{if} coefficients for transitions to the vibrational ground states ($J = 0$) were plotted as a function of band origin, figure 7.19.

This figure (7.19) compares well to one produced by Le Sueur *et al* [136] using the potential energy surface Meyer *et al* [57]. As previously mentioned, Le Sueur *et al*

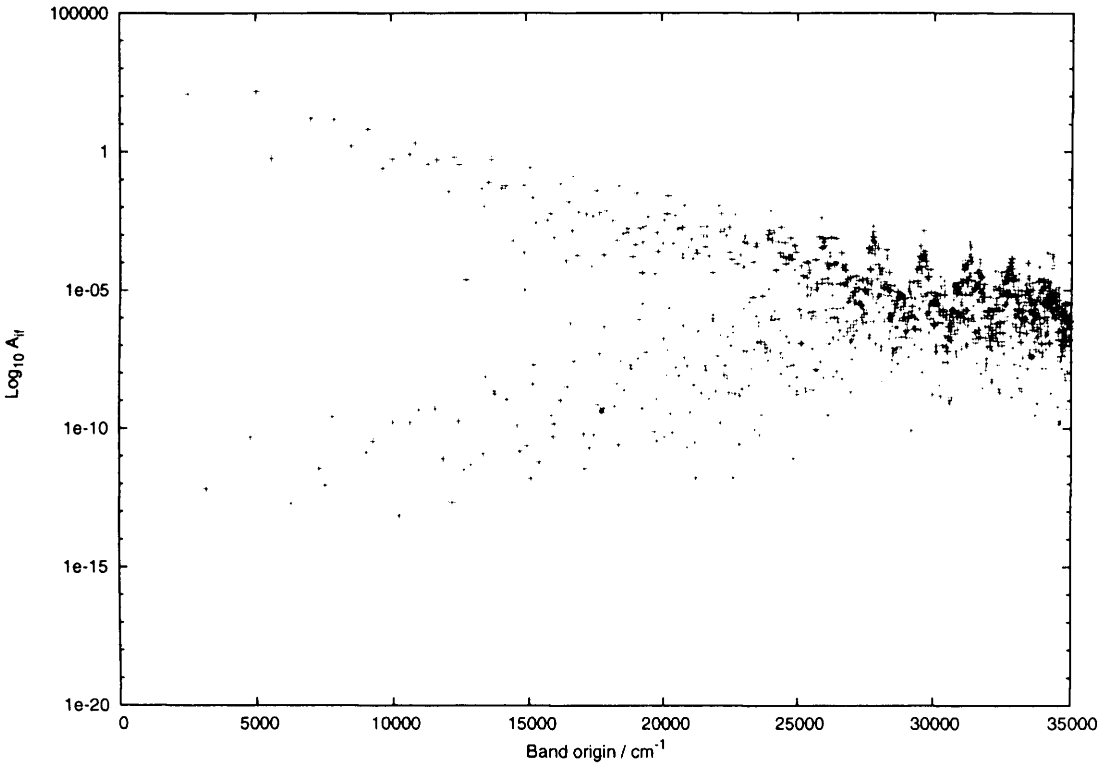

Figure 7.19: Einstein A_{if} coefficients for transitions to the vibrational ground states ($J = 0$) as a function of band origin. Note the log scale for the A_{if} coefficients

found that the horseshoe states produced high intensities. The peaks in figure 7.19 also correspond to the horseshoes tentatively identified in section 7.1. This leads one to believe that although the horseshoe states are less clear in this calculation than previous ones, they are still present. Thus it is reasonable to believe that these states and the series of intensity peaks produced by them have a significant effect on the near-dissociation spectrum.

Also in the manner of Carrington *et al* [42, 140] and Henderson *et al* [141] a convoluted spectrum was produced in an attempt to discern some structure. Each transition was given a Gaussian profile, Γ, using equation (7.1) and the resulting intensity, $I(\omega)$ binned into boxes of 1 cm^{-1}.

$$S(f-i)(\omega) = \sum_{n=1}^{N} S(f-i)_n \left[2\frac{(\ln 2)^{1/2}}{\pi\Gamma} \exp\left(-4\ln 2 \frac{(\omega_n - \omega)^2}{\Gamma^2} \right) \right] \qquad (7.1)$$

where N are the number of transitions satisfying certain criteria; $S(f-i)_n$ and ω_n are the line strength and frequency, in D^2 and cm^{-1} respectively, of the nth transition considered; Γ is the full width at half maximum in cm^{-1}.

Only absorption transitions into a 33000–34911.64 cm^{-1} energy window with frequencies, ω, between 0 and 2000 cm^{-1} were analysed. Spectra with Γ values of 2 cm^{-1} and 4 cm^{-1} were produced. To examine the effects of the strongest transition, additional spectra were produced using only transition whose line strength was greater than 0.08 D^2; this reduced the number of transitions into the energy window to approximately 1.4% of the original. The convoluted spectra are shown in figures 7.20 and 7.21.

It is apparent from 7.20 and 7.21 that the difference in using a value of Γ of 2 cm^{-1} and 4 cm^{-1} is marginal, with $\Gamma = 4$ cm^{-1} giving a slightly smoother spectrum. Not all the features of the spectra using all the transitions are replicated in spectra with a reduced number of the strongest transitions in both frequency ranges. The intensity is also reduced by some 75% in the reduced strongest transitions spectra. This indicates that all transitions may need to be considered with respect to determining some structure to the near-dissociation spectrum. It is also clear that there is no real resemblance between these spectra and the spectra of produced by Henderson *et al* [141] using the incorrectly dissociating potential of Meyer *et al* [57]. Thus the near-dissociation spectrum has changed significantly in this work which has better convergence and uses a correctly dissociating potential [3]. Thus a much fuller calculation is needed for further investigation.

Carrington and Kennedy [42] were able to establish that for some of the H_3^+ ions, the transitions involved upper and lower energy levels which lay above dissociation; that is the levels were quasi-bound. These quasi-bound states are thought to be trapped by rotational barriers in the system (shape resonance). The Carrington-Kennedy experiment can be regarded as a measurement of the transition intensities between bound states and dissociation. Thus any fuller calculation would need to be extended to these quasi-bound states and transition intensities to these states from bound states. States with higher rotational excitation would also need to be considered. Relatively little work on high-lying rotational states has been done in comparison to the equivalent vibrational states. However such calculations would be computationally, very expensive. If the Carrington-Kennedy experimental spectra are to be replicated then the experiment itself must be considered, especially with regard to lifetimes. The experiment was only able to measure transitions satisfying certain lifetime constraints (refer to chapter 1). Finally, Carrington-Kennedy also repeated the H_3^+ experiment on the H_3^+ isotopomers. It would be desirable if the calculation could be extended to include these isotopomers.

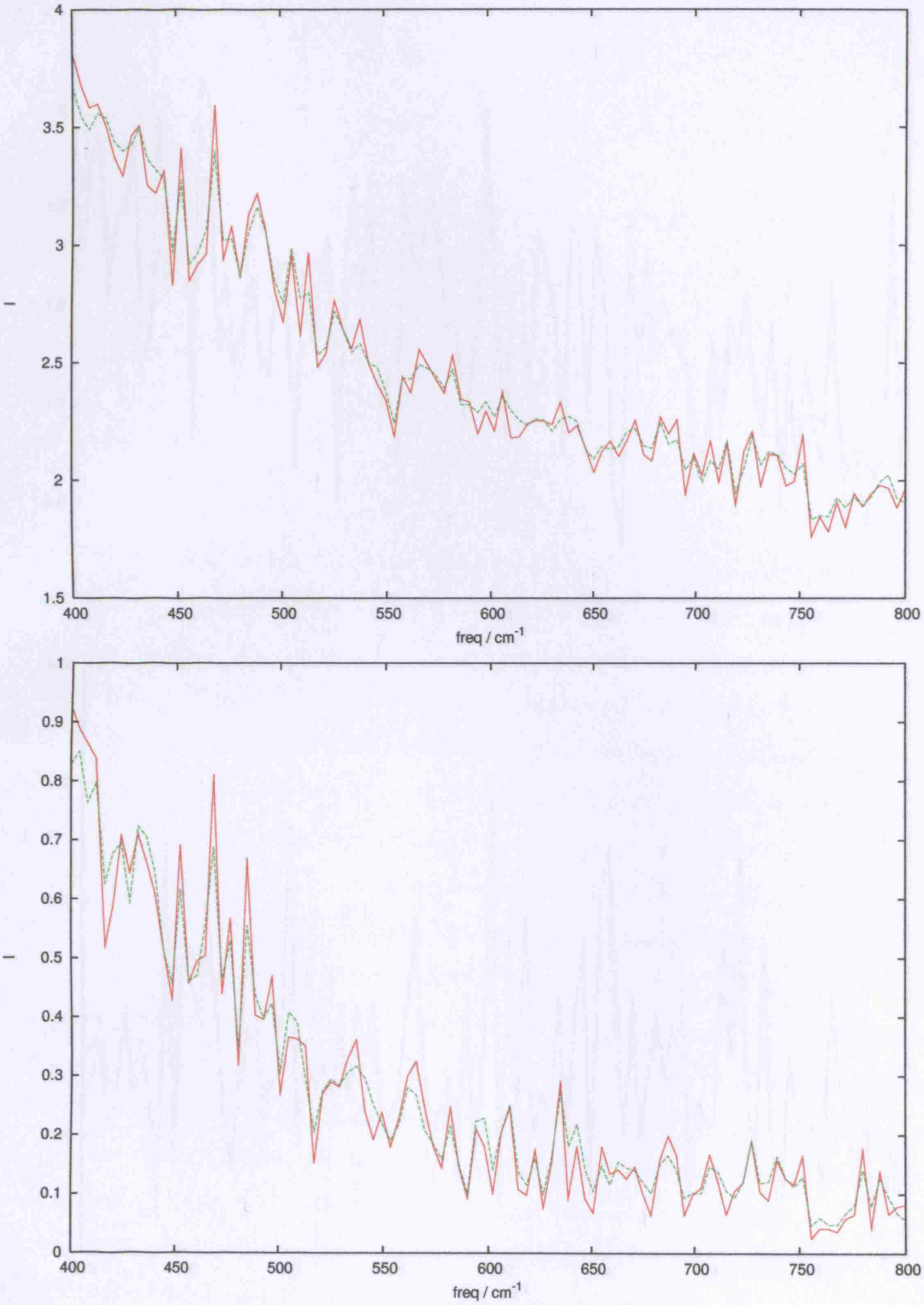

Figure 7.20: Convoluted H_3^+ spectrum at frequencies of 400 to 800 cm^{-1}. The spectrum was synthesised by using equation 7.1 with all transitions into the energy window 33000–34911.64 cm^{-1}. *Solid curve*, $\Gamma = 2$ cm^{-1}; *dashed curve*, $\Gamma = 4$ cm^{-1}. *Top* figure includes all transitions; *Bottom* figure includes transitions with $S(f-i) \geq 0.08$ D^2 only.

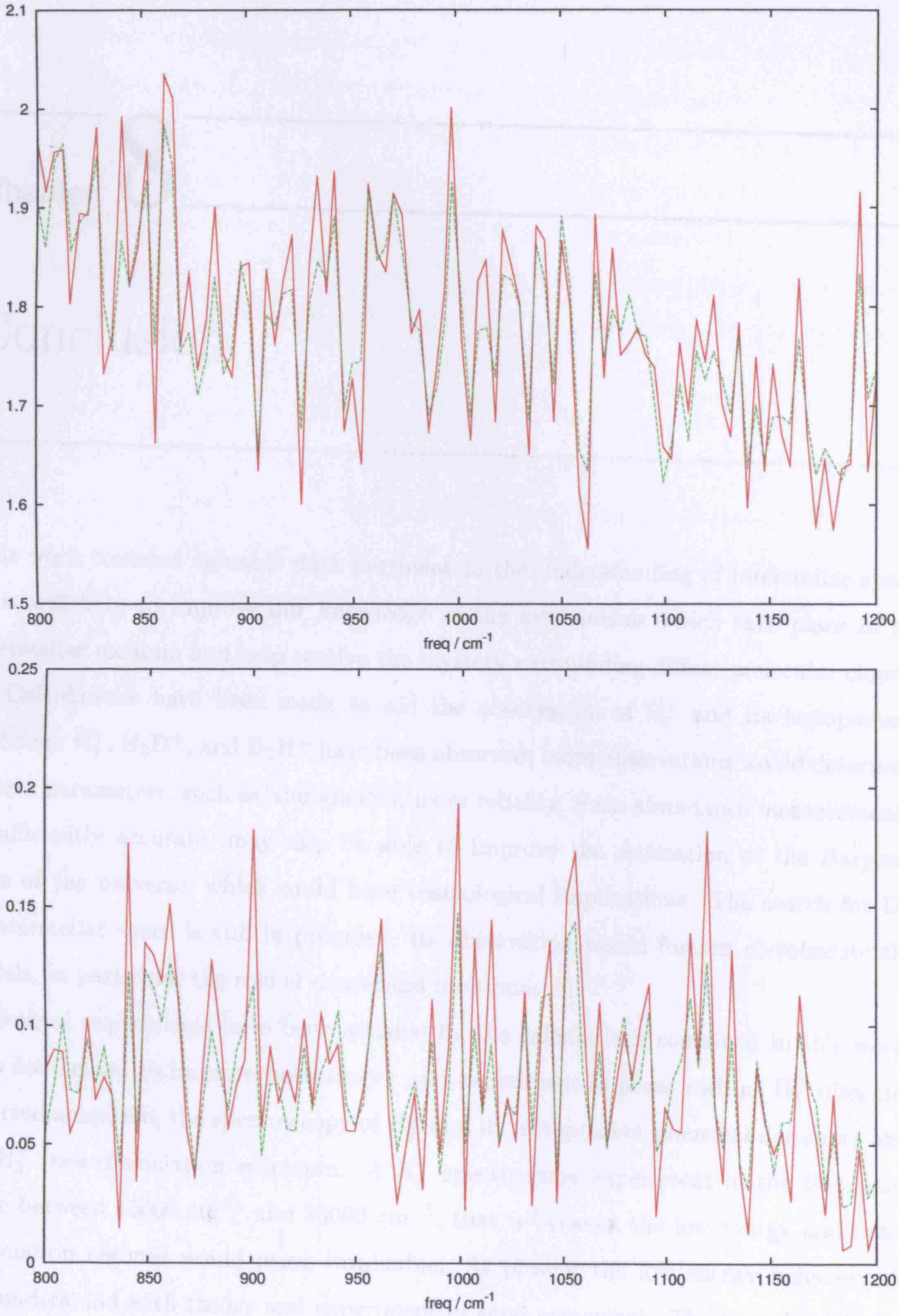

Figure 7.21: Convoluted H_3^+ spectrum at frequencies of 800 to 1200 cm^{-1}. The spectrum was synthesised by using equation 7.1 with all transitions into the energy window 33000–34911.64 cm^{-1}. *Solid curve*, $\Gamma = 2$ cm^{-1}; *dashed curve*, $\Gamma = 4$ cm^{-1}. *Top* figure includes all transitions; *Bottom* figure includes transitions with $S(f-i) \geq 0.08$ D^2 only.

Chapter 8

Conclusion

This work contains valuable data pertinent to the understanding of interstellar space. This will help to improve our knowledge of the mechanisms which take place in the interstellar medium and help resolve the mystery surrounding diffuse molecular clouds.

Calculations have been made to aid the observation of H_3^+ and its isotopomers. Although H_3^+, H_2D^+, and D_2H^+ have been observed; more observations would determine certain parameters, such as abundances, more reliably. Such abundance measurements, if sufficiently accurate, may also be able to improve the estimation of the Baryonic mass of the universe; which could have cosmological implications. The search for D_3^+ in interstellar space is still in progress. Its observation would further corroborate the models, in particular the role of deuterium fractionation.

Several experiments have been assisted by the calculations contained in this work. This has helped to improve both theory and experiment in areas such as H_3^+ dissociative recombination, the spectroscopy of H_3^+ and its isotopomers, chemical dynamics and the H_3^+ near-dissociation spectrum. A H_3^+ spectroscopy experiment in the frequency range between 15000 cm^{-1} and 25000 cm^{-1}, that is between the low energy and near-dissociation regimes would prove invaluable. At present the low energy behaviour is well understood with theory and experiment in good agreement. The near-dissociation behaviour remains poorly understood by theory. Experiments between the two regimes would allow theory to understand the behaviour of H_3^+ at higher energies in more progressive manner.

All the H_3^+ states to dissociation for $J = 0$ to $J = 2$ using a correctly dissociating potential energy surface have been calculated for the first time. The convergence of these states, although much improved from previous works, still remains an issue. Convergence may be improved by using a different coordinate system, such as Radau coordinates with the z-axis perpendicular to the frame of the molecule or hyperspherical coordinates. The use hyperspherical coordinates would allow symmetry labels to be attached to states and thus nuclear degeneracy weights could be used more easily to produce realistic synthetic spectra. Of great interest is the discovery of loosely coupled H^+–H_2 complexes which could prove to be crucial to explaining the Carrington-Kennedy near-dissociation experiment.

A new more efficient algorithm for dipole transitions has been derived and implemented in both serial and parallel programs. H_3^+ dipole transitions to dissociation between states with $J = 0$ to $J = 2$ have been calculated. This has indicated that there is structure in the near-dissociation spectrum with regard to horseshoe states. That is intensity peaks are still associated with these states when a correctly dissociating potential is used.

To date, the manner by which attempts to explain the Carrington-Kennedy experiment by theory have been to perform successively larger calculations. That is taking advantage of the advances in computing to perform ever more converged calculations. The utility of this approach may now be coming to an end. A more careful study of the key aspects of the H_3^+ spectrum may prove to be more fruitful. This would involve a study of the vibrational horseshoe states and H^+–H_2 complexes. That is a calculation of transitions from these states to both bound and quasi-bound states and an answer to whether these states remain when rotation takes place.

Bibliography

[1] A. Carrington, J. Buttenshaw, and R. A Kenedy. Observation of the infrared spectrum of H_3^+ ion at its near dissciation limit. *Mol. Phys.*, 45:753, 1982.

[2] O. L. Polyansky and J. Tennyson. Ab initio calculation of the rotation-vibration energy levels of H_3^+ and its isotopomers to spectroscopic accuracy. *J. Chem. Phys.*, 110:5056–5064, 1999.

[3] O. L. Polyansky, R. Prosmiti, W. Klopper, and J. Tennyson. An accurate, global, *ab initio* potential energy surface for the H_3^+ molecule. *Mol. Phys.*, 98:261–273, 2000.

[4] J.K.G Watson. Vibration-rotation calculations for H_3^+ using a morse-based discrete variable representation. *Can J. Phys.*, 72:238, 1994.

[5] J. Tennyson and B. T. Sutcliffe. On the rovibrational levels of the H_3^+ and H_2D^+ molecules. *Mol. Phys.*, 51:887–906, 1984.

[6] B. T. Sutcliffe and J. Tennyson. A general treatment of vibration-rotation coordinates for triatomic molecules. *Intern. J. Quantum Chem.*, 39:183–196, 1991.

[7] K. S. Sidhu, S. Miller, and J. Tennyson. Partition functions and equilibrium constants for H_3^+ and H_2D^+. *Astro. Astrophys.*, 255:453–456, 1992.

[8] L. Neale and J. Tennyson. A high temperature partition function for H_3^+. *Astrophys. J.*, 454:L169–L173, 1995.

[9] J. Glosík and P. Hlavenka. private communication, 2004.

[10] M.J. Flynn. Very high speed computing systems. *Proceedings of the IEEE*, 54:1901, 1966.

[11] L. S. Blackford, J. Choi, A. Cleary, E. D'Azevedo, J. Demmel, I. Dhillon, J. Dongarra, S. Hammarling, G. Henry, A. Petitet, K. Stanley, D. Walker, and R. C. Whaley. *ScaLAPACK Users' Guide* `http://www.netlib.org/scalapack/slug/`.

[12] F. Tisseur and J. Dongarra. A parallel divide and conquer algorithm for the symmetric eigenvalue problem on distributed memory architectures. *Siam Journal on Scientific Computing*, 20:2223, 1999.

[13] H. Y. Mussa, J. Tennyson, C. J. Noble, and R. J. Allan. Rotation-vibration calculations using massively parallel computers. *Computer Phys. Comms.*, 108:29–37, 1998.

[14] K. J. Maschhoff and D. C. Sorensen. Parpack: An efficient portable large scale eigenvalue package for distributed memory parallel architectures. Technical Report CRPC-TR96659, Rice University, 1996.

[15] J. R. Henderson, J. Tennyson, and B. T. Sutcliffe. All the bound vibrational states of H_3^+: a reappraisal. *J. Chem. Phys.*, 98:7191–7203, 1993.

[16] J. K. G. Watson. Higher-Order Vibration-Rotation Energies of the X_3 Molecule. *J. Mol. Spectrosc.*, 103:350, 1984.

[17] I. R. McNab. The Spectroscopy of H_3^+. *Advances in Chemical Physics*, 1993.

[18] O. L. Polyansky and J. Tennyson. Ab initio calculation of the rotation-vibration energy levels of H_3^+ and its isotopomers to spectroscopic accuracy. *J. Chem. Phys.*, 110:5056–5064, 1999.

[19] K.P. Huber and G. Herzberg. *Constants of Diatomic Molecules.* Van Nostrand Reinhold Company, 1979.

[20] K. Giles, N. G. Adams, , and D. Smith. A study of the reactions of H_3^+, H_2D^+, HD_2^+ and D_3^+ with H_2, HD, and D_2, using a variable-temperature selected ion flow tube. *J. Phys. Chem*, 96:7645, 1992.

[21] N. G. Adams and D. Smith. A laboratory study of the reaction H_3^+ + HD $\rightleftharpoons$ H_2D^+ + H_2: The electron densities and the temperatures in interstellar clouds. *Astrophys. J.*, 248:373–379, 1981.

[22] E. Herbst. The temperature dependence of the HCO^+/DCO^+ abundance ratio in dense interstellar clouds. *Astro. Astrophys.*, 111:76–80, 1982.

[23] M. Fárník, S. Davis, M. A. Kostin, O. L. Polyansky, J. Tennyson, and D. J. Nesbitt. Beyond the Born-Oppenheimer approximation: High-resolution overtone spectra of H_2D^+ and D_2H^+. *J. Chem. Phys.*, 116:6146–6158, 2002.

[24] P. Drossart, J. P. Mailard, J. Caldwell, S. J. KIM, J. K. G. Watson, W. A. Majewski, J. Tennyson, S. Miller, S. Atreya, J. Clarje, J. H. Waite, and R. Wagener. Detection of H_3^+ on Jupiter. *Nature*, 340:539, 1989.

[25] T. R. Geballe, M. F. Jagod, and T. Oka. Detection of H_3^+ infrared emission lines in Saturn. *Astrophys. J.*, 408:L109–L112, 1993.

[26] L. M. Trafton, T. R. Geballe, S. Miller, J. Tennyson, and G. E. Ballester. Detection of H_3^+ from Uranus. *Astrophys. J.*, 405:761–766, 1993.

[27] T. R. Geballe and T. Oka. Detection of H_3^+ in interstellar space. *Nature*, 384:334, 1996.

[28] B. J. McCall, T. R. Geballe, K. H. Hinkle, and T. Oka. Detection of H_3^+ in the diffuse interstellar medium toward Cygnus OB2 No. 12. *Science*, 279:1910, 1998.

[29] T. R. Geballe. H_3^+ between the stars. *Royal Society of London Philosophical Transactions Series A*, 358:2503–2513, 2000.

[30] S. Miller, J. Tennyson, S. Lepp, and A. Dalgarno. Identification of features due to H_3^+ in the infrared spectrum of supernova 1987a. *Nature*, 355:420–422, 1992.

[31] G. J. Harris, A. E. Lynas-Gray, S. Miller, and J. Tennyson. The effect of the electron donor H_3^+ on the pre main-sequence and main-sequence evolution of low-mass, zero-metallicity stars. *Astrophys. J.*, 600:1025–1034, 2004.

[32] E. Herbst and W. Klemperer. The formation and depletion of molecules in dense interstellar clouds. *Astrophys. J.*, 185:505, 1973.

[33] W. D. Watson. The Rate of Formation of Interstellar Molecules by Ion-Molecule Reactions. *Astrophys. J.*, 183:L17, 1973.

[34] B. J. McCall, T. R. Geballe, K. H. Hinkle, and T. Oka. Observations of H_3^+ in dense molecular clouds. *Astrophys. J.*, 522:338, 1999.

[35] D. R. Bates, M. F. Guest, and R. A. Kendall. Enigma of H_3^+ dissociative recombination. *Planetary and Space Science*, 41:9, 1993.

[36] B. J. McCall, K. H. Hinkle, T. R. Geballe, G. H. Moriarty-Schieven, N. J. Evans II, K. Kawaguchi, S. Takano, V. V. Smith, and T. Oka. Observations of H_3^+in the diffuse interstellar medium. *Astrophys. J.*, 537:391, 2002.

[37] A. Dalgarno and S. Lepp. Deuterium fractionation mechanisms in interstellar clounds. *Astrophys. J.*, 287:L47–L50, 1984.

[38] L. Loinard, A. Castets, C. Ceccarelli, E. Caux, and A. G. G. M. Tielens. Doubly deuterated molecular species in protostellar environments. *Astrophys. J.*, 552:163–166, 2001.

[39] C. Ceccarelli. Millimeter and infrared observations of deuterated molecules. *Planet Space Sci.*, 50:1267–1273, 2002.

[40] C. Vastel, T. G. Phillips, and H. Yoshida. Detection of D_2H^+ in the dense interstellar medium. *Astrophys. J.*, 606:L127–L130, 2004.

[41] C. M. Lindsay and B. J. McCall. Comprehensive Evaluation of H_3^+ Spectroscopy. *J. Mol. Spectrosc.*, 210:60, 2001.

[42] A. Carrington and R. A. Kennedy. Infrared predissociation limit of the H_3^+ ion. *J. Chem. Phys.*, 81:91, 1984.

[43] J. Tennyson, M. A. Kostin, P. Barletta, G. J. Harris, J. Ramanlal, O. L. Polyansky, and N. F. Zobov. DVR3D: a program suite for the calculation of rotation-vibration spectra of triatomic molecules. *Computer Phys. Comm.*, 163:85, 2004.

[44] Lord Rayleigh. *Theory of Sound*, volume 1. Macmillan, London, 1937.

[45] W. Ritz. Über eine neue methode zur lsung gewisser variations probleme der mathematischen physik. *Reine Angew Math.*, 135:1, 1908.

[46] J. K. L. MacDonald. Successive approximations by the Rayleigh-Ritz variation method. *Phys. Rev.*, 43:830, 1933.

[47] M. Born and J.P. Oppenheimer. Zur quantentheorie der molekeln. *Ann. Phys.*, 84:457, 1927.

[48] M.Born and K.Huang. *Dynamical Theory of Crystal Lattices.* Oxford University Press, 1955.

[49] H. C. Longuet-Higgins. *Advances in spectroscopy II*, page 429. Interscience, London, 1961.

[50] B. M. Dinelli, C. R. Le Sueur, J. Tennyson, and R. D. Amos. *Ab initio* rovibrational levels of H_3^+ beyond the Born-Oppenheimer approximation. *Chem. Phys. Lett.*, 232:295–300, 1995.

[51] A. G. Ioannou, R.D. Amos, and N. C. Handy. The diagonal Born-Oppenheimer corection for He_2^+ and F + H_2. *Chem. Phys. Lett.*, 251:52, 1996.

[52] N. C. Handy and A. M. Lee. The adiabatic approximation. *Chem. Phys. Letts.*, 252:425, 1996.

[53] N. C. Handy, Y. Yamaguchi, and H. F. Schaefer III. The diagonal correction to the Born-Oppenheimer approximation: Its effect on the singlet-triplet splitting of CH_2 and other molecular effects. *J. Chem. Phys.*, 84:4481, 1986.

[54] W. Cencek, J. Rychlewski, R. Jaquet, and W. Kutzelnigg. Sub-microhartree accuracy potential energy surface for H_3^+ including adiabatic and relativistic effects. I. Calculation of the potential points. *J. Chem. Phys.*, 108:2831, 1998.

[55] R. Schinke, M. Dupuis, and W. A. Lester. Proton-H_2 scattering on an *ab initio* CI potential energy surface. I. Vibrational excitation at 10 eV. *J. Chem. Phys.*, 72:3909–3915, 1980.

[56] R. Röhse, W. Kutzelnigg, R. Jaquet, and W. Klopper. Potential energy surface of the H_3^+ ground state in the neighborhood of the minimum with microhartree accuracy and the vibration frequencies derived from it. *J. Chem. Phys.*, 101:2231, 1994.

[57] M. Meyer, P. Botschwina, and P.G. Burton. *Ab initio* calculation of near-equilibrium potential and multipole moment surfaces and vibrational frequencies of the H_3^+ and its isotopomers. *J. Chem. Phys.*, 84:891, 1986.

[58] C. Eckart. Some studies concerning rotating axes and polyatomic molecules. *Phys. Rev.*, 47:552, 1935.

[59] H. Wei and T. Carrington, Jr. The triatomic Eckart-frame kinetic energy operator in bond coordinates. *J. Chem. Phys.*, 107:9493, 1997.

[60] H. Wei and T. Carrington, Jr. An exact Eckart-embedded kinetic energy operator in Radau coordinates for triatomic molecules. *Chem. Phys. Lett.*, 287:289, 1998.

[61] V. Špirko, P. Jensen, P.R. Bunker, and A. Čejchan. The development of a new morse-oscillator based rotation-vibration Hamiltonian for H_3^+. *J. Mol. Spectrosc.*, 112:183, 1985.

[62] C. L. Pekeris. Ground state of two-electron atoms. *Phys. Rev.*, 112:1649, 1958.

[63] E.R. Davidson. Global topology of triatomic potential surfaces. *J. Am. Chem. Soc.*, 99:397, 1977.

[64] A. J. C. Varandas. *Advances in Chemical Physics*, volume LXXIV. Wiley, New York, 1988.

[65] B. T. Sutcliffe. The use of perimetric coordinates in the vibration-rotation Hamiltonian for triatomic-molecules. *Mol. Phys.*, 75:1233, 1992.

[66] A. Callegari, P. Theule, R. N. Tolchenov, N. F. Zobov, O. L. Polyansky, J. Tennyson, J. S. Muenter, and T. R. Rizzo. Dipole moments of highly vibrationally excited water. *Science*, 297:993–995, 2002.

[67] O. L. Polyansky, A. G. Császár, S. V. Shirin, N. F. Zobov, P. Barletta, J. Tennyson, D. W. Schwenke, and P. J. Knowles. High accuracy *ab initio* rotation-vibration transitions of water. *Science*, 299:539–542, 2003.

[68] M. A. Kostin, O. L. Polyansky, and J. Tennyson. Calculations of rotation-vibration states with the z-axis perpendicular to the plane: high accuracy results for H_3^+. *J. Chem. Phys.*, 116:7564–7573, 2002.

[69] M. A. Kostin, O. L. Polyansky, J. Tennyson, and H. Y. Mussa. Rotation-vibration states of H_3^+ at dissociation. *J. Chem. Phys.*, 118:3538–3542, 2003.

[70] B. R. Johnson. The quantum dynamics of three particles in hypersherical coorinates. *J. Chem. Phys.*, 79:1916, August 1983.

[71] R. M. Whitnell and J. C. Light. Efficient pointwise representations for vibrational wave-functions-eigenfunctions of H_3^+. *J. Chem. Phys.*, 90:1774, 1989.

[72] P. Bartlett and P. J. Howard. The Rotational-Vibrational spectrum of symmetrical nonrigid triatomics in hyperspherical coordinates - the H_3^+ molecule. *Mol. Phys.*, 70:1001, 1990.

[73] S. Carter and W. Meyer. A variational method for the calculation of vibrational energy levels of triatomic molecules using a Hamiltonian in hyperspherical coordinates. *J. Chem. Phys.*, 93:8902, 1990.

[74] L. Wolniewicz and J. Hinze. Rotation-vibrational states of H_3^+ computed using hyperspherical coordinates and harmonics. *J. Chem. Phys.*, 101:9817, 1994.

[75] M. J. Bramley, J. W. Tromp, T. Carrington, Jr, and G. C Corey. Efficient calculation of highly excited vibrational levels of floppy molecules: the band origins of H_3^+ up to 35 000 cm^{-1}. *J. Chem. Phys.*, 100:6175, 1994.

[76] B. M. Dinelli, L. Neale, O. L. Polyansky, and J. Tennyson. New assignments for the infrared spectrum of H_3^+. *J. Mol. Spectrosc.*, 181:142–150, 1997.

[77] J. C. Light, I. P. Hamilton, and J. V. Lill. Generalised discrete variable approximation in quantum-mechanics. *J. Chem. Phys.*, 82:1400, 1985.

[78] A. S. Dickinson and P. R. Certain. Calculation of matrix elements for one-dimensional quantum-mechanical problems. *J. Chem. Phys.*, 49:4204, 1968.

[79] Z. Bačić and J. C. Light. Theoretical methods for rovibrational states of floppy molecules. *Annu. Rev. Phys. Chem.*, 40:469, 1989.

[80] J. C. Light, R. M. Whitnell, T. J. Pack, and S. E. Choi. In A. Laganà, editor, *Supercomputer Algorithms for Reactivity, Dynamics and Kinetics of Small Molecules*, volume 277 of *NATO ASI series C*, page 187. Kluwer, Dordrecht, 1989.

[81] J. R. Henderson, C. R. Le Sueur, S. G. Pavett, and J. Tennyson. Coordinate ordering in the discrete variable representation. *Computer Phys. Comms.*, 74:193–198, 1993.

[82] J. Tennyson and B. T. Sutcliffe. Variationally exact ro-vibrational levels of the floppy CH_2^+ molecule. *J. Mol. Spectrosc.*, 101:71–82, 1983.

[83] J. Tennyson and B. T. Sutcliffe. The *ab initio* calculation of the vibration-rotation spectrum of triatomic systems in the close-coupling approach with KCN and H_2Ne as examples. *J. Chem. Phys.*, 77:4061–4072, 1982.

[84] P.R. Bunker and R.E. Moss. The breakdown of the Born-Oppenheimer approximation: the effective vibration-rotation hamiltonian for a diatomic molecule. *Molec. Phys.*, 33:417, 1977.

[85] S. Miller, J. Tennyson, and B. T. Sutcliffe. First principles calculation of rotational and ro-vibrational line strengths: spectra for H_2D^+ and D_2H^+. *Mol. Phys.*, 66:429–456, 1989.

[86] D. M. Brink and G. R. Satchler. *Angular Momentum.* Clarendon Press, Oxford, 1979.

[87] A. H. Stroud and D. Secrest. *Gaussian Quadrature Formulas.* Prentice-Hall, London, 1966.

[88] A. E. Lynas-Gray, S. Miller, and J. Tennyson. Infra red transition intensities for water: a comparison of *ab initio* and fitted dipole moment surfaces. *J. Mol. Spectrosc.*, 169:458–467, 1995.

[89] M. Lemoine, J. Audouze, L. B. Jaffel, P. Feldman, R. Ferlet, G. Hebrard, E. B. Jenkins., C. Mallouris, W. Moos, K. Sembach, G. Sonneborn, A. Vidal-Madjar, and D. G. York. Deuterium abundances. *New Astronomy*, 4:231–243, 1999.

[90] H. Roberts, E. Herbst, and T. J. Millar. Enhanced Deuterium fractionation in dense interstellar cores resulting from multiply deuterated H_3^+. *Astrophys. J.*, 591:L41, 2003.

[91] C. M. Walmsley, D. R. Flowers, and G. Pineau des Forêts. Complete depletion in prestellar cores. *Astro. Astrophys.*, 2004. submitted.

[92] G. D. Carney. Rotation energies for deuterated H_3^+ oscillators in zero-point states of vibrartion. *Chem. Phys.*, 54:103–107, 1980.

[93] P. Jensen, V. Špirko, and P.R. Bunker. A new morse-oscillator based hamiltonian for H_3^+: Extension to H_2D^+ and D_2H^+. *J. Mol. Spectrosc.*, 115:269–293, 1986.

[94] H.J.G. Hayman. *Statistical thermodynamics : an introduction to its foundations.* Elsevier, 1967.

[95] A. W. Irwin. Polynomial partition function approximations of 244 atomic and molecular species. *Astrophysical Journal Supplement Series*, 45:621, 1981.

[96] R. L. Kelly. Atomic and ionic spectrum lines of hydrogen through Kryton. *J. Phys. Chem. Ref. Data*, 16, 1987.

[97] D. Gerlich, E. Herbst, and E. Roueff. H_3^+ + HD $\rightleftharpoons$ H_2D^+ + H_2: low-temperature laboratory measurements and interstellar implications. *Planetary and Space Science*, 50:1275–1285, 2002.

[98] D. Smith, N. G. Adams, and E. Alge. Some H/D exchange reactions involved in the deuteration of intersellar molecules. *Astrophys. J.*, 263:123, 1982.

[99] H. Roberts, E. Herbst, and T.J. Millar. The chemistry of multiply deuterated species in cold, dense interstellar cores. *Astro. Astrophys.*, 424:905–917, 2004.

[100] T. Oka. Observation of the infrared spectrum of H_3^+. *Physical Review Letters*, 45:531–534, August 1980.

[101] T. Oka. A search for interstellar H_3^+. *Royal Society of London Philosophical Transactions Series A*, 303:543–549, December 1981.

[102] J.K.G. Watson, S.C. Foster, and A.R.W. Mckellar. The infrared-spectrum of the v_2 fundamental-band of the D_3^+ molecular ion. *Can. J. Phys.*, 65:38–46, 1987.

[103] T. Amano, M.C. Chan, S. Civiš, A.R.W McKellar, W.A Majewski, D. Sadovsií, and J.K.G Watson. The infrared vibration-rotation spectrum of the D_3^+ molecular ion: extension to higher vibrational and rotational quantum numbers. *Can J. Phys.*, 72:1007–1015, 1994.

[104] S. C. Foster, A. R. W. McKellar, I. R. Peterkin, J. K. G. Watson, and F. S. Pan. Observation and analysis of the ν_2 and ν_3 fundamental bands of the H_2D^+ ion. *J. Chem. Phys.*, 84:91–99, January 1986.

[105] I. N. Kozin, O. L. Polyansky, and N. F. Zobov. Improved analysis of the experimental data on the H_2D^+ and D_2H^+ absorption spectra. *Journal of Molecular Spectroscopy*, 128:126–134, March 1988.

[106] O.L. Polyansky and A.R.W. McKellar. Improved analysis of the infrared spectrum of D_2H^+. *J. Chem. Phys.*, 92:4039, 1989.

[107] A. Zavagno, L. Deharveng, D. Nadeua, and J. Caplan. Near-infrared imaging of RAFGL7009S. *Astro. Astrophys.*, 394, 2002.

[108] D.S Shepard and E. Churchwell. High-velocity molecular gas from high-mass star formation regions. *Astrophys. J.*, page 267, 1996.

[109] L. Bronfman, L. A. Nyman, and J. May. A CS(2-1) survey of IRAS point sources with color characteristics of ultra-compact H II regions. *Astro. Astrophys.*, 81:1693, 1996.

[110] M. A. Biondi and S. C. Brown. Measurement of electron-ion recombination. *Phys. Rev.*, 76, 1949.

[111] J. Glosík, R Plašil, V. Poterya, P Kudrna, M. Tichý, and A. Pysanenko. Experimental study of recombintion of H_3^+ ions with electrons relevant for interstellar and planetary plasmas. *Journal of Physics B*, 34:L485–L494, 2001.

[112] D. Smith and N. G. Adams. Ionic reactions in thermal plasmas. *J. Chem. Soc. Faraday Trans II*, 83:149, 1987.

[113] N. G. Adams and D. Smith. *Dissociative Recombination: Theory, Experiment and Applications*, pages 124–140. World Scientific, Singapore, 1989.

[114] R. Plašil, J. Glosík, V. Poterya, P. Kudrna, J. Rusz, M. Tichý, and A. Pysanenko. Advanced integrated stationary afterglow method for the experimental study of recombintion process of H_3^+ and D_3^+ ions with electrons. *Int. J. Mass Spectrom*, 218:105, 2002.

[115] L. Lammich, H. Kreckel, S. Krohn, M. Lange, D. Schwalm, D. Strasser, A. Wolf, and D. Zajfman. Breakup dynamics in the dissociative recombination of H_3^+ and its isotopomers. *Radiation Physics and Chemistry*, 68:175–179, 2003.

[116] *Message Passing Interface Forum, http://www.mpi-forum.org/.*

[117] *openMP consortium. 2002, http://www.openmp.org.*

[118] *BLACS (Basic Linear Algebra Communication Subprograms) , http://www.netlib.org/blacs/.*

[119] J Donagarra, J. Bunch, C. Moler, and G.W. Stewart. *LINPACK User's Guide.* Philadelphia, 1979.

[120] G. Amdahl. Validity of the Single Processor Approach to Achieving Large-Scale Computing Capabilities. In *AFIPS Conference Proceedings*, volume 30, page 483, 1967.

[121] J. Tennyson, J. R. Henderson, and N. G. Fulton. DVR3D: programs for fully pointwise calculation of ro-vibrational spectra of triatomic molecules. *Computer Phys. Comms.*, 86:175–198, 1995.

[122] H. Y. Mussa and J. Tennyson. Bound and quasi-bound rotation-vibrational states using massively parallel computers. *Computer Phys. Comms.*, 128:434–445, 2000.

[123] R. Lehoucq, K. Maschhoff, D. Sorensen, and C. Yang. *ARPACK, http://www.caam.rice.edu/software/ARPACK/*, 1996.

[124] E. Anderson, Z. Bai, C. Bischof, S. Blackford, J. Demmel, J. Dongarra, J. Du Croz, A. Greenbaum, S. Hammarling, A. McKenney, and D. Sorensen. *LAPACK Users' Guide.* Society for Industrial and Applied Mathematics, Philadelphia, PA, third edition, 1999.

[125] *Netpbm user manual.* http://netpbm.sourceforge.net/doc/.

[126] D. Elwood, G. Fann, and R. Littlefield. *PeIGS Parallel Eigensystem Solver.* Pacific Northwest Laboratory, 2.1 edition.

[127] J. Munro. To be published.

[128] G. J. Harris. *An Ab Initio HCN/HNC Rotational-Vibrational Line List and Opacity Function for Astronomy.* PhD thesis, University of London, 2002.

[129] BLAS (basis linear algebra subprograms) , http://www.netlib.org/blas/.

[130] P. C. Cosby and H. Helm. Experimental determination of the H_3^+ band dissociation energy. *Chem. Phys. Lett.*, 151:71, 1988.

[131] G. C. Lie and D. Frye. Vibrational analysis of a Hylleraas-configuration interaction potential for H_3^+. *J. Chem. Phys.*, 96:6784–6790, 1992.

[132] R .J. Le Roy. LEVEL 7.5. Chemical Physics Research Report CP-655, University of Waterloo, 2002.

[133] M. Berblinger, E. Pollak, and C. Schlier. Bound states embedded in the continuum of H_3^+. *J. Chem. Phys.*, 88:5643, 1988.

[134] N. J. Wright and J. M. Hutson. Regular and irregular vibrational states: Localized anharmonic modes in Ar_3. *J. Chem. Phys.*, 110:902, 1999.

[135] N. J. Wright and J. M. Hutson. Regular and irregular vibrational states: Localized anharmonic modes in Na_3. *J. Chem. Phys.*, 112:3214, 2000.

[136] C. R. Le Sueur, J. R. Henderson, and J. Tennyson. Gateway states and bath states in the vibrational spectrum of H_3^+. *Chem. Phys. Lett.*, 206:429–436, 1993.

[137] P. Jensen and V. Špirko. A new Morse-oscillator based Hamiltonian for H_3^+: Calculation of line strengths. *J. Mol. Spectrosc.*, 118:208, 1986.

[138] R. Pfeifer and M.S. Child. Towards an understanding of the predissociation exiciation spectrum of H_3^+. *Mol. Phys.*, 60:1367, 1987.

[139] R.J. LeRoy and B. Bernstein. Dissociation Energy and Long-Range Potential of Diatomic Molecules from Vibrational Spacings of Higher Levels. *J. Chem. Phys.*, 52:3869, 1970.

[140] Alan Carrington, Iain R. McNab, and Yvonne D. West. Infrared predissociation spectrum of the H_3^+ ion. II. *J. Chem. Phys.*, 98:1073, 1993.

[141] J. R. Henderson and J. Tennyson. Calculated spectrum for near-dissociation H_3^+: a first attempt. *Mol. Phys.*, 89:953–963, 1996.